# Searching for Signs of Habitability and Life in the Era of Extremely Large Telescopes

Miles Harrison Currie

A dissertation
submitted in partial fulfillment of the
requirements for the degree of

Doctor of Philosophy

University of Washington

2024

Reading Committee:
Victoria S. Meadows, Chair
Eric Agol
Sarah Tuttle

Program Authorized to Offer Degree:
Astronomy

University of Washington

## Abstract

Searching for Signs of Habitability and Life in the Era of Extremely Large Telescopes

Miles Harrison Currie

Chair of the Supervisory Committee:
Victoria S. Meadows
Department of Astronomy

We are entering an exciting era for astrobiology, with terrestrial exoplanet characterization studies now underway with the JWST and the next generation of ground-based Extremely Large Telescopes (ELTs) expected to be online by the end of the decade. However, the prospects for searching for signs of habitability and life with the upcoming 30 m class ELTs are not yet thoroughly explored. Specifically, it is not well understood the extent to which the high resolution spectroscopy and high contrast imaging capabilities of the ELTs can be leveraged to characterize terrestrial exoplanet atmospheres. Previous theoretical studies on ELT capabilities have focused on the detectability of the biosignature gas $O_2$ in Earth-twin atmospheres, but have not rigorously considered the environmental context gained by detecting other molecules. Models that produce atmospheres that are photochemically self-consistent with their host stars can be used to show how additional molecules reveal more about the planet and its processes, either strengthening the interpretation of $O_2$ as a biosignature, or ruling in or out biosignature false positive mechanisms that can generate abiotic $O_2$. Furthermore, our ability to use future ELT observations to observationally constrain the composition of nearby transiting and non-transiting terrestrial exoplanets is uncertain, and could provide independent avenues for determining the origin of $O_2$ in particular.

The goal of this dissertation is to explore and define the terrestrial exoplanet characterization capabilities of the upcoming ELTs, which can complement and support JWST and the future Habitable Worlds Observatory (HWO) NASA flagship mission. To that end, this work provides recommendations and observational protocols that will enhance and maximize the science of the ELTs to search for signs of habitability and life in terrestrial exoplanet atmospheres, laying the foundation for ground-based terrestrial exoplanet science in the near term, and space-based characterization studies in the future. In this work, we develop and apply techniques for analyzing simulated high-resolution ground-based spectra and retrieving molecular abundances in simulated ELT data.

Our approach extends well beyond current approaches for characterizing terrestrial exoplanet atmospheres with the ELTs by considering the detectability of a suite of molecular species that can help constrain the origin of atmospheric $O_2$, and provide further environmental context for a potential biosignature detection. We simulated ELT detectability of atmospheric molecules for a range of different inhabited and uninhabited terrestrial atmosphere types, as well as a sub-Neptune atmosphere, for planets orbiting M dwarf host stars. We found that $CH_4$, $CO_2$, $H_2O$, and CO are all potentially detectable for both transiting and non-transiting terrestrial exoplanets, and that two biosignature pairs ($O_2/CH_4$ and $CO_2/CH_4$) may be detectable for nearby Earth-like worlds in $\sim$ 10 hours of observing for Proxima Centauri b, the nearest non-transiting target. Furthermore, we may be able to discriminate biosignature false positive environments using the direct imaging capabilities of the ELTs by detecting CO, an indicator gas for several false positive cases, in as little as 10 hours for nearby targets. We could also identify false positives by searching for signs of significant abiotic $O_2$ buildup via $H_2O$ photolysis, which may be possible in $<$ 100 hours of observing time. Discriminating the atmospheres of non-transiting planets as either terrestrial- or sub-Neptune-like may also be possible via spectral characterization in $\sim$ 1 hour of observing with the ELTs to detect absorption from hydrogen-bearing species such as $NH_3$. We also explore our ability to measure the abundance of $O_2$ in habitable Proxima Centauri b atmospheres using atmospheric retrieval methods for high-resolution cross-correlation spectroscopy for the first time, and we find that we may be able to measure Earth-like $O_2$ abundances or lower ($\leq 21\%$ $O_2$) in 100 hours of observing the $O_2$ A-band; however, retrieving high $O_2$ abundances in post-ocean loss scenarios with thick atmospheres may be challenging due to significant saturation of the $O_2$ A-band. Considering other $O_2$ bands that are less prone to saturation or searching for the spectral features of $O_2$–$O_2$ collisionally-induced absorption may instead be used to identify this scenario. This dissertation proposes future ELT observing protocols and observational strategies for characterizing terrestrial exoplanets. The tools we have developed will continue to be relevant in the preparation for the analysis of the first ELT transit transmission and reflected light observations of nearby terrestrial exoplanets, as well as for the development of future ground- and space-based instrumentation and science strategies. The code and methodology developed in this work are available to the exoplanet and astrobiology communities.

# TABLE OF CONTENTS

# LIST OF FIGURES

# LIST OF TABLES

Table Number Page

# ACKNOWLEDGMENTS

As I reflect on my life's journey at this point, I am immensely proud of how far I have come, and I owe the majority of my gratitude to the people I have met along the way who have made this all possible. First and foremost, I would like to thank my advisor and mentor, Vikki Meadows, for fostering my curiosity, challenging me, and imparting foundational research and writing skills that I will carry with me for the rest of my life. Thank you, Vikki, for believing in me and for turning me into a scientist. I could not have done this without your support and the support of the Virtual Planetary Laboratory and the NINS Astrobiology Center of Japan. I look forward to our future collaborations.

I would also like to thank the other members of my dissertation committee: Sarah Tuttle, who imparted foundational knowledge on astronomical observing both in class and at the Apache Point Observatory; Eric Agol, whose deep knowledge of all things exoplanet related and beyond was an immense resource at the beginning and throughout my graduate research career; Miguel Morales, for serving as my graduate school representative, and whose statistical science course left a lasting impression on how I do research; and finally Cecilia Bitz, for serving as the astrobiology program representative for both my general and final exams.

Furthermore, this work has benefited greatly from the expertise and advice from other members of the Virtual Planetary Laboratory community, including Drake Deming, Mike Line, and Dave Crisp. Thank you all for your availability as a resource and for your guidance throughout this work.

Since my undergraduate years, I have worked with many wonderful people who have mentored me and helped me navigate my choice to pursue science as a career, and I am especially thankful for these early scientific influences: David Rubin, Susan Mullally (Thompson), Fergal Mullally, Susana Deustua, Andy Fruchter, Bryan Quaife, and Kevin Speer.

My family has fostered my intense love for the natural world from the beginning, and so I owe them a debt of gratitude for always encouraging me to stay curious. To Chris and Merrilee Currie, and to my sister, Willow: thank you for all of your support.

Many others I met during my graduate school years deserve my heartfelt gratitude, and I specifically want to call out the following people for making a particularly large impact on my life: Chris Stark, for being an extraordinary secondary mentor; Liza Young, for your hard work on the administrative side and for always having confidence in me; and finally all of the UW astronomy and astrobiology graduate students and others who have made this experience enjoyable.

I am also grateful for the opportunities to travel around the world to present my research. My work has brought me to three different continents (four if you count North America!), and the people and experiences during these travels have made me a more worldly human both academically and personally.

After years of toiling over words to describe the most complex scientific concepts, I am forever at a loss for words when trying to write about my feelings for my partner, Hali Dzigurski. Hali, you have stood by my side through the highs and the lows; you've been there for me when I've felt like giving up on myself; you've built me back up and encouraged me to keep going; we've celebrated every single achievement together—both small and large—for six long years. Finally, here we are at the last hurdle. I am so excited to start the next chapter of our lives together.

# DEDICATION

To Hali, for everything.

*Portions of this dissertation were originally published or have been submitted for publication in collaboration with Victoria S. Meadows and Kaitlin C. Rasmussen in The Planetary Science Journal (Currie et al., 2023a, PSJ, Vol. 4, 5; DOI: 10.3847/PSJ/accf86. Currie et al. 2024a, PSJ, submitted. Currie et al. 2024b, PSJ, in prep.), and are reproduced in this dissertation with the permission of the American Astronomical Society–Institute of Physics Publishing.*

# Chapter 1

# INTRODUCTION

Nearly three decades ago, the field of astronomy was fundamentally changed when 51 Pegasi b, a Jupiter-mass planet, was discovered orbiting a Sun-like star (Mayor & Queloz, 1995). This discovery sparked a new sub-field of observational astronomy that would evolve toward building highly sensitive and dedicated instruments that may soon allow humanity to answer the grand question: "Are we alone?"

Since the discovery of 51 Pegasi b, techniques and instrumentation used to characterize exoplanet environments have continued to develop for both ground- and space-based observatories, and we are now entering an era where characterizing terrestrial, rocky, potentially habitable worlds is within our grasp. Atmospheric characterization studies for large exoplanets are currently underway with both space- and ground-based telescopes (e.g. Hoeijmakers et al., 2020b; Rustamkulov et al., 2023), and teams have begun to use the JWST to characterize the atmospheres of the smaller, rocky exoplanets of the TRAPPIST-1 system (Gillon et al., 2016; Greene et al., 2023; Ducrot et al., 2024; Ih et al., 2023; Lincowski et al., 2023; Zieba et al., 2023). However, new ground-based extremely large telescopes (ELTs) will begin to come online within the next decade, and characterizing multiple terrestrial exoplanet atmosphere targets is a major driving science goal of these new facilities (e.g. López-Morales et al., 2019).

The ELTs will have the sensitivity to probe the atmospheres of smaller, more Earth-like exoplanets, and will provide a novel near-term opportunity to search terrestrial exoplanet environments for signs of habitability and life (e.g. Snellen et al., 2013; López-Morales et al., 2019; Serindag & Snellen, 2019; Hardegree-Ullman et al., 2023; Currie et al., 2023; Vaughan et al., 2024; Currie & Meadows, submitted). Over the past several decades, ground-based telescopes have proven themselves to be powerful tools for addressing the challenges of large exoplanet characterization (e.g. Snellen et al., 2010; Brogi et al., 2012; de Kok et al., 2014; Brogi et al., 2016; Birkby, 2018). Applying the cumulative lessons learned from these pioneering studies, we are now able to consider the possibility of probing the atmospheres of smaller, more Earth-like exoplanets with the upcoming ELTs, which may become invaluable tools in the search for habitability and life outside the Solar System (e.g. López-Morales et al., 2019). In particular the ELTs, with sensitivity in the visible and near infrared wavelength regions, may present the best near-term opportunity to detect $O_2$ in terrestrial exoplanet atmospheres (e.g. Snellen et al., 2013; Rodler & López-Morales, 2014; Serindag & Snellen, 2019; López-Morales et al., 2019), which can be a strong biosignature if its origin is known (e.g. Meadows, 2017).

However, the overall performance of the ELTs as tools for searching for signs of habitability and life has not been comprehensively assessed, and in particular our ability to detect molecules in terrestrial planetary atmospheres and interpret their origin given environmental context has not been adequately explored. For example, $O_2$ is likely not exclusive to planets hosting life, and theoretical models suggest it may be created by abiotic processes such as atmospheric escape and photochemistry (e.g. Domagal-Goldman et al., 2014; Tian et al., 2014; Wordsworth & Pierrehumbert, 2014; Harman et al., 2015; Gao et al., 2015; Luger & Barnes, 2015; Tian, 2015; Hu et al., 2012; Meadows et al., 2018; Ranjan et al., 2023). The performance of the ELTs to detect other molecules that can contextualize $O_2$ by either strengthening its interpretation as biological in origin, or by indicating that it has an abiotic planetary (escape or photochemistry) source (Meadows, 2017) has not been assessed. In addition, molecular detectability with the ELTs has previously only been addressed in an Earth-twin scenario, but terrestrial exoplanet targets will likely have atmospheres photochemically altered by their unique host stars, possibly lengthening atmospheric lifetimes and increasing the abundance of important biosignature gases like $CH_4$ (e.g. Segura et al., 2005; Lincowski et al., 2018; Meadows et al., 2023). Searching for other gases, like $CH_4$, in addition to $O_2$ can also support the interpretation of $O_2$ as biological in origin (e.g. Hitchcock & Lovelock, 1967; Lovelock & Kaplan, 1975; Sagan et al., 1993; Meadows et al., 2018). Furthermore, the possibility of retrieving the abundances of the detected species in ELT spectra of terrestrial atmospheres to constrain surface fluxes of key biosignature gases has not yet been investigated.

In this dissertation work, we develop an analysis and retrieval pipeline to predict the performance of the ELTs for searching for signs of habitability and life using simulated ELT observations. The tools, methods, and observing protocols we develop will help maximize the science return from the upcoming ELTs, and help us understand how ground-based observations may be complementary to space-based observations. The following sections of this chapter present a brief review of the current state of observational exoplanet astrobiology, with a specific emphasis on ground-based techniques, to frame the research conducted in this dissertation. We then outline the structure for the following chapters of this dissertation in Section 1.4.

## *1.1 Spectral Characterization of Exoplanet Atmospheres: An Overview*

While the spectral characterization of exoplanet atmospheres is a relatively new field of study, scientists have been studying the atmospheres of Solar System bodies for over a century (e.g. Slipher, 1908; John & Nicholson, 1922), providing the basis and provenance for modern spectroscopic analysis techniques. Through the last century, we have learned a great deal about the physics and chemistry of these closest planetary neighbors, generally separating them into three distinct categories: gas giants ($>\sim$ 100 $M_\oplus$ and $> 9R_\oplus$), ice giants (14-17 $M_\oplus$ and $\sim 4R_\oplus$), and terrestrials ( $\leq 1$ $R_\oplus$ and $\leq 1$ $M_\oplus$) (Lodders & Fegley, 1998). The atmospheres of gas and ice giants are likely primary atmospheres captured by a rocky core during the planet formation phase, as shown by the significant H and He species in Solar-like abundances that make up the bulk of their atmospheres (Inaba & Ikoma, 2003). On the other hand, terrestrial planet atmospheres are secondary atmospheres likely outgassed from the surface of the planet well after formation, as evidenced by plentiful oxidizing molecular species (e.g. Kite & Barnett, 2020). While our understanding of planetary atmospheres has previously been limited to the Solar System bodies over the last century, new observational facilities now make characterizing the atmospheres of exoplanets a possibility, and the diversity of known exoplanets presents opportunities to learn much more about the physics, chemistry, and geology that influence planetary atmosphere formation and evolution.

Today, over 5,500 exoplanets have been discovered (Akeson et al., 2013; Christiansen, 2022), with a more diverse range of sizes and masses than our Solar System ($1 - 10^4$ $M_\oplus$ and $0.5 - 20R_\oplus$) (Akeson et al., 2013; Christiansen, 2022), and we expect the atmospheres of these exoplanets to be similarly spectroscopically diverse (Seager & Deming, 2010; Burrows, 2014; Madhusudhan et al., 2016; Jontof-Hutter, 2019). For example, through the study of exoplanet atmospheres, a new class of gas giant planets that reside close to their host stars has been discovered, called "hot Jupiters" (Mayor & Queloz, 1995; Butler et al., 1997). These hot Jupiter atmospheres are observationally favorable targets and are now highly amenable to spectroscopic atmospheric characterization (e.g. Hawker et al., 2018; Harada et al., 2021; Bell et al., 2024), although they were initially studied via photometric thermal phase curves (e.g. Knutson et al., 2007) and with 3D general circulation models (e.g. Showman et al., 2008). Exoplanet discovery missions, such as Kepler (Koch et al., 2010) and TESS (Guerrero et al., 2021) have also discovered many smaller, more terrestrial sized exoplanets (Akeson et al., 2013; Christiansen, 2022), presenting opportunities for spectroscopic followup to understand their habitability and to search for signs of life.

### *1.1.1 Methods for Spectral Characterization*

The method used to obtain spectroscopic observations of exoplanet atmospheres varies depending on the geometry of the observed system, namely whether or not the planet transits its host star from our vantage point (the transit transmission and direct imaging techniques, respectively).

Planets that transit their host star can be characterized by either transit transmission or secondary eclipse spectroscopy (Seager & Sasselov, 2000; Charbonneau et al., 2002; Richardson et al., 2003; Deming et al., 2007; Seager, 2008). In transit transmission observations, the planet passes in front of its host star, blocking light proportional to the projected geometric area of the planet. The apparent radius of a planet is a function of wavelength because the stellar light can be scattered or absorbed by the atmosphere at different wavelengths. The transmission spectrum of the exoplanet atmosphere can therefore be obtained by measuring the depth of a transit lightcurve as a function of wavelength— observable increases in the planet's apparent radius can indicate molecular absorption in the planet atmosphere (Seager & Sasselov, 2000; Charbonneau et al., 2002). The second method for characterizing transiting exoplanet atmospheres is to measure thermal emission through a secondary eclipse (Richardson et al., 2003; Deming et al., 2007). In this method, a spectrum of the entire unresolved planetary system is taken before or after the planet passes behind the host star, and then compared to a spectrum taken at secondary eclipse, during which the planet's emission is blocked by the star. This allows us to separate the missing planetary emission spectrum from the stellar spectrum (Richardson et al., 2003; Deming et al., 2007). For the purposes of this dissertation, we will focus on the transit transmission method, which can be used for ELT observations of terrestrial exoplanets orbiting M dwarf stars in the visible–NIR (see Chapter 3 in Part I).

For planets that do not transit their host star, the direct imaging technique can be used to obtain spectra of an exoplanet atmosphere. This method hinges on our ability to resolve and/or isolate the light directly from the planet (Kalas et al., 2008; Marois et al., 2008; Lagrange et al., 2010; Traub & Oppenheimer, 2010). This is typically accomplished by measuring either the stellar light reflected off the planet's atmosphere (e.g. Robinson et al., 2016), or by directly measuring the planet's thermal emission in the infrared (e.g. Kalas et al., 2008; Marois et al., 2008; Lagrange et al., 2010). In either case, light from the star must be suppressed to prevent the stellar light from overwhelming the planetary light, and this is done through coronagraphic and adaptive optics instruments (e.g. Guyon, 2018). In reflected light observations, the stellar light is reflected off the planet, which produces its own inherent reflectance spectrum due to absorbers in the planetary atmosphere and, if present, on its surface (Traub & Oppenheimer, 2010): the reflected stellar light passes through a terrestrial planet's atmosphere and may reach the surface, and is attenuated by the wavelength-dependent surface albedo and cloud reflectivity, and absorption/scattering from molecules/aerosols in the atmosphere, which we then are able to measure to study the planetary atmospheric and surface properties (Rugheimer et al., 2013; Robinson et al., 2014; Schwieterman et al., 2015; Arney et al., 2017, 2018). On the other hand, thermal emission observations of exoplanets do not rely on reflected stellar light, and instead thermal radiation emitted by the planet is directly measured (e.g. Kalas et al., 2008; Marois et al., 2008; Lagrange et al., 2010). For this dissertation, we focus on reflected light observations (see Chapters 4 and 5).

### *1.1.2 The Current and Future State-of-the-Art*

The substantial size and mass of gas giant planets have more pronounced observational effects, such as significant transit depths, radial velocity signals, and planet flux, making them observationally favorable targets for both ground (e.g. Brogi et al., 2014; Piskorz et al., 2017; Hoeijmakers et al., 2018a; Birkby, 2018; Hoeijmakers et al., 2020b) and space based (e.g. Line et al., 2016; Stevenson et al., 2017; Mansfield et al., 2018; Rustamkulov et al., 2023) observatories, and thus these objects have been the most well-studied in recent years (e.g. Fortney et al., 2021). Ground-based observations of gas giant planets have revealed information about their composition and structure via the detection of molecular features (e.g. Brogi et al., 2014; Piskorz et al., 2017; Hoeijmakers et al., 2018a; Birkby, 2018; Hoeijmakers et al., 2020b), aerosols including clouds (e.g. Marley et al., 1999; Sing et al., 2016; Gao et al., 2020), and weather patterns (e.g. Snellen et al., 2010; Louden & Wheatley, 2015; Ehrenreich et al., 2020). Simultaneously, theoretical models have become increasingly sophisticated, incorporating complex chemistry, cloud formation, and circulation patterns to predict atmospheric properties (e.g. Showman et al., 2010; Heng & Showman, 2015; Showman et al., 2020; Zhang, 2020), and are essential for interpreting observational data and guiding future observations. Through observations of these giant exoplanets, we have begun to explore the diversity of exoplanet atmospheres, examining how different planetary masses, orbital distances, and host star types influence atmospheric composition and behavior (e.g. Fortney et al., 2021), allowing us to understand the complex processes guiding planet formation and evolution.

Looking forward, JWST is expected to revolutionize the field by providing even deeper insights into both giant and terrestrial exoplanet atmospheres through its powerful infrared capabilities. For giant planets, JWST has for the first time revealed evidence of active photochemistry in the atmosphere of exoplanet WASP-39 b (Rustamkulov et al., 2023). The sensitivity of JWST allows for the detection of a broader range of molecules and the exploration of planets cooler and smaller than gas planets, moving closer to characterizing Earth-like exoplanets (e.g. Lustig-Yaeger et al., 2019a), and the seven transiting planets in the TRAPPIST-1 system are currently the best known terrestrial Earth-sized exoplanet targets for astrobiology with JWST. Their orbits span interior, within, and exterior to the habitable zone, and the small size of their host star makes them amenable to transit spectroscopy (e.g. Gillon et al., 2016; Lincowski et al., 2018; Lustig-Yaeger et al., 2019a). Observers have begun to target the planets in the TRAPPIST-1 system, and current analyses are starting to constrain whether or not the inner planets have atmospheres, and the possible nature of those atmospheres. For example, analysis of TRAPPIST-1 b secondary eclipse data has suggested that the planet either has little to no planetary atmosphere redistributing incoming stellar radiation to the nightside and thereby cooling the dayside (Greene et al., 2023; Ducrot et al., 2024; Ih et al., 2023), or is consistent with a thick pure $CO_2$ atmosphere with photochemical haze (Ducrot et al., 2024). For TRAPPIST-1 c, studies have suggested that based on JWST data, the atmosphere is likely thin and not enriched in $CO_2$ (Zieba et al., 2023), although further work by Lincowski et al. (2023) shows that denser atmospheres, including 3-bar steam atmospheres are not inconsistent with the current data to 1.8-$\sigma$. With these atmospheric constraints, Gialluca et al. (2024) used stellar evolution and planetary escape models to estimate the initial volatile abundance for the TRAPPIST-1 planets to be close to 8 terrestrial oceans, increasing the likelihood that the habitable zone (HZ) planets still retained an ocean. However, all studies highlight the need for more data to further constrain these atmospheres, and at the time of writing further observations are planned and being proposed for these planets and others in the TRAPPIST-1 system.

In the near term, the ELTs offer complementary terrestrial exoplanet science to JWST, especially for biogenic $O_2$ detection, and are likely the only near-term class of observatories sensitive to both transiting and non-transiting terrestrial exoplanets (Snellen et al., 2015), expanding the number of accessible terrestrial worlds. Using advancements in high-contrast, high-resolution spectroscopy (Section 1.2), the ELTs will provide a near-term opportunity to detect biosignature gases as well as molecular species that can provide wider environmental context (e.g. Snellen et al., 2013; López-Morales et al., 2019; Currie et al., 2023; Currie & Meadows, submitted). In comparison, JWST targets are limited to a handful of transiting HZ exoplanets around smaller stars, including the TRAPPIST-1 system, as larger stars produce weaker planetary atmospheric signals (Lustig-Yaeger et al., 2019a). However, the ELTs will also be capable of observing the TRAPPIST-1 system (Currie et al., 2023; Hardegree-Ullman et al., 2023). The seven planets in this system will offer the first opportunity to both follow up and complement JWST observations of exoplanet atmospheres. JWST is primarily sensitive to the IR, and considering ELT spectra in the visible-NIR allows us to probe a broader wavelength range to search for novel molecular features and observe multiple bands of a molecule to constrain abundances. The ELTs will be sensitive to the wavelength regions where $O_2$ absorbs, and, despite some challenges—including instrument sensitivity and seasonable observability of the targets (Hardegree-Ullman et al., 2023)—they may be our best near term tools for searching for $O_2$ (e.g. Rodler & López-Morales, 2014; Snellen et al., 2015; López-Morales et al., 2019; Serindag & Snellen, 2019; Currie et al., 2023), particularly for the TRAPPIST-1 system. Furthermore, the ELTs are being designed to characterize the atmospheres of non-transiting terrestrial planets in the habitable zone, a capability that will be unique to the ground-based observatories in the near term (e.g. Lovis et al., 2017; López-Morales et al., 2019) until the launch of NASA's flagship Habitable Worlds Observatory mission (National Academies of Sciences, Engineering, and Medicine, 2021). Observing planets in reflected light, the ELTs will provide our first glimpse at the compositions of multiple nearby potentially terrestrial exoplanet atmospheres, and may have the ability to thoroughly characterize the atmospheres of the very best nearby targets (see Chapter 4; Currie & Meadows, submitted).

Beyond JWST and the ELTs in the near term, whose targets are primarily M dwarfs, the Astro2020 Decadal Survey (National Academies of Sciences, Engineering, and Medicine, 2021) recommended the development of the Habitable Worlds Observatory (HWO), a direct imaging flagship mission with an astrobiological goal: to expand the characterization of non-transiting Earth-like planets to those orbiting around more Sun-like stars. Although HWO is planned to launch in the 2040s, mission design and trade studies are already underway to realize this timeline, and direct imaging studies completed in the near term with the ELTs will be particularly complementary to both the design and science goals of HWO. HWO and the ELTs will observe in the same wavelength region, and the overlap in targets—which will be planets orbiting M or K type host stars—will likely be on the order of ten if we select for K or M dwarf HWO targets within 5 pc (Mamajek & Stapelfeldt, 2023). HWO will primarily be designed for FGK systems, which require coronagraphic stellar suppression to beyond $10^{-10}$ contrast (National Academies of Sciences, Engineering, and Medicine, 2021). On the other hand, the ELTs will likely only be sensitive to M and possibly K dwarf systems because their coronagraphic capabilities will be limited to the $10^{-5}$ range; the time delay between the wavefront sensor and adaptive optics system for the ELT ground-based instruments will limit the contrast achieved by their coronagraphs (e.g. Guyon, 2018). The ELTs may play a vital role in vetting HWO M dwarf targets in the near term by performing preliminary atmospheric characterization studies that can be used to inform target selection when HWO is online (Currie et al., 2019). A major challenge of HWO observations will be resolving a degeneracy in the size/albedo of an exoplanet: a small, high-albedo planet may have the same brightness as a large, low-albedo planet, and discriminating between the two is not trivial. The ELTs will offer a near-term solution for this by observing HWO targets in the decade before HWO launches, providing initial characterization efforts to identify and discriminate sub-Neptune type planets with H envelopes from terrestrial planets with higher molecular weight secondary atmospheres (Chapter 4; Currie & Meadows, submitted).

## *1.2 High-Resolution Cross-correlation Spectroscopy*

Soon after the discovery of 51 Pegasi b (Mayor & Queloz, 1995) via the radial velocity technique, the high-resolution spectroscopy technique for atmospheric characterization began to take shape, allowing us to begin to characterize the atmospheres of large exoplanets (Snellen et al., 2010). The high-resolution cross-correlation spectroscopy technique that was developed to characterize exoplanet atmospheres with ground-based telescopes is based on the radial velocity method of exoplanet discovery, where observations of a planet's host star are taken with precise high-resolution spectrometers, and the planet's presence is inferred from small Doppler shifts in the stellar spectrum over a series of observations (e.g. Perryman, 2011; Birkby, 2018). Modern techniques extend the use of these high-resolution spectrometers to obtain observations of combined planet and star emission spectrum, or the planet spectrum itself, with either the transit transmission or direct imaging methods, taking advantage of the planetary Doppler shift over time to isolate the planetary signal from the stellar and telluric contamination (Birkby, 2018). This new technique along with higher precision instrumentation enabled a breakthrough when the first robust detection of a molecule in the atmosphere of hot Jupiter HD 209458 b was made by Snellen et al. (2010). This pioneering study led a deluge of other foundational work that would allow us to investigate the atmospheric composition of both transiting and non-transiting close-in giant planets (e.g. Brogi et al., 2012; Rodler et al., 2012; Birkby et al., 2013; De Kok et al., 2014; Rodler et al., 2013; Brogi et al., 2013; Lockwood et al., 2014; Brogi et al., 2014; Schwarz et al., 2015; Hoeijmakers et al., 2015; Brogi et al., 2016; Piskorz et al., 2016; Birkby et al., 2017a; Allart et al., 2017; Brogi et al., 2017; Piskorz et al., 2017; Nugroho et al., 2017; Brogi et al., 2018; Brogi & Line, 2019; Hoeijmakers et al., 2020b), as well as some mini-Neptune and super-Earth atmospheres (Crossfield et al., 2011; Esteves et al., 2017).

As the high-resolution technique and instrumentation has matured, observers have started to observe and characterize smaller and/or cooler exoplanets (e.g. Crossfield et al., 2011; Esteves et al., 2017). Among these, the mini-Neptune GJ 1214 b (e.g. Crossfield et al.,

2011) and the super Earth 55 Cnc e (e.g. Esteves et al., 2017) stand out as some of the most well studied due to their relative accessibility with current observatories. Using the high-resolution technique, studies have suggested that GJ 1214 b may have a cloudy/hazy atmosphere dominated by H and He species (e.g. Crossfield et al., 2011; Orell-Miquel et al., 2022; Spake et al., 2022); however, detections of He I in particular have been tenuous (Spake et al., 2022). Many studies have used transmission spectroscopy to attempt to characterize the atmosphere of the smaller super-Earth sized planet 55 Cnc e, with growing consensus that the planet likely has a high molecular weight atmosphere (Demory et al., 2016; Tsiaras et al., 2016; Angelo & Hu, 2017; Esteves et al., 2017; Bourrier et al., 2018) or none at all (Deibert et al., 2021; Zhang et al., 2021). Jindal et al. (2020) ruled out low molecular weight or clear-sky water-rich atmospheres with a non-detection of TiO and water, although the results were also consistent with cloudy atmosphere or no atmosphere. High-resolution spectroscopy was also used to search for traces of a mineral atmosphere, but very little or no evidence was found (Ridden-Harper et al., 2016; Keles et al., 2022; Rasmussen et al., 2023). More recent JWST results have suggested that 55 Cnc e may actually have a secondary atmosphere rich in $CO_2$ (Hu et al., 2024), but this has not yet been confirmed by ground-based high-resolution observations. However, current and future facilities offer abundant opportunities to improve on instrumentation or observing techniques to access more information on smaller exoplanet atmospheres.

The rapid progression of characterization studies from giant planets to mini-Neptunes and super Earths over the course of less than a decade has also sparked initial studies on how this technique can be applied to smaller, more Earth-like planets in the near future (e.g. Snellen et al., 2013; Rodler & López-Morales, 2014; Snellen et al., 2015; Lovis et al., 2017; Wang et al., 2017; López-Morales et al., 2019; Serindag & Snellen, 2019; Hawker & Parry, 2019; Lovis et al., 2022; Currie et al., 2023; Hardegree-Ullman et al., 2023; Vaughan et al., 2024; Currie & Meadows, submitted). Using both transmission and reflected light high-resolution spectroscopy, theoretical studies have shown that characterization of Earth-like terrestrial planets orbiting M dwarf stars may be possible in the near future with upcoming instruments and telescopes (e.g. Snellen et al., 2013; Rodler & López-Morales, 2014; Snellen et al., 2015; Lovis et al., 2017; López-Morales et al., 2019; Serindag & Snellen, 2019; Hawker & Parry, 2019; Lovis et al., 2022; Currie et al., 2023; Hardegree-Ullman et al., 2023). In particular, upcoming improvements to the instrumentation on the Very Large Telescope (VLT) may allow observers to begin to characterize Proxima Centauri b (Lovis et al., 2017; Lovis et al., 2022), the nearest known potentially rocky exoplanet at 1.3 pc from Earth (Anglada-Escudé et al., 2016). Furthermore, multiple nearby Earth-like targets may be amenable to atmospheric characterization with the ELTs in the near term (Wang et al., 2017; Zhang et al., 2023). For further discussion of this topic, see Section 1.3.4.

We describe the high-resolution cross-correlation spectroscopy technique, current and future facilities amenable to using this technique, and its applications in the following sections.

### *1.2.1 Current Facilities*

Since the inception of the high-resolution spectroscopy technique for characterizing exoplanet atmospheres, many instruments have been developed and/or applied for the purpose of characterizing exoplanet atmospheres. Among the most notable instrument/telescope combinations are iterations of the CRIRES instrument (R=100,000) on ESO's VLT (Kaeufl et al., 2004). From 2010 to 2014, the original CRIRES instrument (Kaeufl et al., 2004) was used to investigate the atmospheres of hot Jupiter planets before being removed for upgrades (Follert et al., 2014). In 2022, a new iteration of CRIRES returned to the VLT (Follert et al., 2014; Holmberg & Madhusudhan, 2022), and the enhanced high-resolution data from CRIRES+ has since allowed observers to perform retrieval studies to begin to determine the abundance of molecules in large exoplanet atmospheres (e.g. Holmberg & Madhusudhan, 2022; Maimone et al., 2022; Lesjak et al., 2023; Landman et al., 2024), and has been a proving ground for instrumentation that will be capable of observing smaller, terrestrial planets such as RISTRETTO on the VLT (Lovis et al., 2022) and future ELT instrumention. Other recent high-resolution instrument/telescope systems, particularly in the infrared, include iSHELL/IRTF (Rayner et al., 2022), CARMENES/CAHA (Quirrenbach et al., 2016), GIANO/TNG (Oliva et al., 2006), SPIRou/CFHT (Thibault et al., 2012), ARIES/MMT (McCarthy et al., 1998), IGRINS/Gemini (Park et al., 2014), HPF/HET (Kanodia et al., 2018), IRD/Subaru (Kotani et al., 2018), iLocator/LBT (Crass et al., 2023), CRIRES+/VLT (Follert et al., 2014; Holmberg & Madhusudhan, 2022), and NIRSPEC/Keck (Martin et al., 2018). Optical instrumentation includes ESPRESSO/VLT (Pepe et al., 2021) and EXPRES/DCT (Fischer et al., 2017).

The RISTRETTO instrument concept on the VLT will revolutionize our current capabilities before the ELTs come online by observing the first spectrum of the potentially rocky planet Proxima Centauri b (Lovis et al., 2017; Lovis et al., 2022). RISTRETTO is an optical high-resolution spectrograph paired with an extreme adaptive optics system, with a science goal of characterizing the atmosphere of Proxima Centauri b. Construction on this instrument concept began in 2022, and prototypes are currently being tested before the science instrument is commissioned on the VLT in the near future. RISTRETTO may provide near-term demonstrations of ELT technology by observing the atmosphere of Proxima Centauri b, and possibly detecting $O_2$ and $H_2O$ if its atmosphere is Earth-like (Lovis et al., 2017).

### *1.2.2 Upcoming Facilities*

The innovations in the high-resolution technique and instrumentation over the previous decade have shaped the science goals of future facilities capable of high-resolution spectroscopy, which include three extremely large telescopes: The Giant Magellan Telescope (Johns et al., 2012; Fanson et al., 2022), the Thirty Meter Telescope (Nelson & Sanders, 2008; Chisholm et al., 2020), and the European Extremely Large Telescope (Gilmozzi & Spyromilio, 2007; Ramsay et al., 2020). The large apertures of the ELTs will be key for enabling the characterization of smaller, terrestrial exoplanets (Snellen et al., 2013, 2015), and they will all have instruments capable of making these observations (e.g. Szentgyorgyi et al., 2022; Marconi et al., 2022; Palle et al., 2023; Konopacky et al., 2023). The ELTs will begin to come online within the next decade, and will be our most powerful visible–NIR ground-based tools to date.

The Giant Magellan Telescope (GMT) will feature a unique design consisting of seven 8.4-meter mirrors that together create a telescope with an effective aperture of 24.5 meters, along with several instruments—both first-light and future—that can be used for characterizing terrestrial exoplanet atmospheres. The GMT Consortium Large Earth Finder (G-CLEF) (Mueller et al., 2022; Szentgyorgyi et al., 2022) will be the first instrument installed on the GMT with the primary objective of detecting and characterizing terrestrial exoplanet atmospheres. G-CLEF is designed as a fiber-fed, optical Echelle spectrograph, and will operate at R $\sim 100,000$, which will allow spectral characterization of transiting terrestrial exoplanets. Later, the GMagAO-X extreme adaptive optics system will be installed on the GMT, which can suppress stellar light for investigations of nearby non-transiting exoplanet atmospheres in reflected light (Males et al., 2022).

The Thirty Meter Telescope (TMT) will have a primary mirror diameter of 30 meters, which will consist of 492 hexagonal segments, and the Multi-Objective Diffraction-limited High-Resolution Infrared Spectrograph (MODHIS) (Konopacky et al., 2023) first light instrument will be capable of the R $\sim 100,000$ observations required for high-resolution spectroscopy. While the MODHIS first-light instrument will not have the ability to suppress stellar light, required for reflected light observations of non-transiting targets, it will be powerful enough for characterizing the atmospheres of nearby transiting terrestrial exoplanets (Chapter 3; Currie et al., 2023). In the future, the planned Second Earth Imager (Matsuo & Tamura, 2010; Matsuo et al., 2012) and Planetary Systems Imager (PSI) (Jensen-Clem et al., 2021) on the TMT will combine an extreme adaptive optics system with a high resolution spectrometer to capture spectra and characterize nearby non-transiting exoplanets.

The European Extremely Large Telescope (E-ELT) is the largest of the ELTs with a primary mirror diameter of 39 m and a total collecting area of 987 $\mathrm{m}^2$. Instrumentation relevant for terrestrial exoplanet characterization is currently being developed, and includes the High Angular Resolution Monolithic Optical and Near-infrared Integral field (HARMONI) spectrograph (Thatte et al., 2016; Vaughan et al., 2024), the Mid-infrared ELT Imager and Spectrograph (METIS) (Brandl et al., 2014), and the ArmazoNes high Dispersion Echelle

Spectrograph (ANDES) (Marconi et al., 2022; Palle et al., 2023) instruments. HARMONI and METIS will be first light instruments, while ANDES, which will be most powerful for terrestrial exoplanet characterization (Marconi et al., 2022; Palle et al., 2023), will be a second-generation instrument designed to be coupled to a high-contrast imager to take spectra of non-transiting terrestrial exoplanets.

### *1.2.3 Telluric Line Mitigation*

The crux of observing exoplanet atmospheres from the ground, and the reason that such high resolution (R $\sim$100,000) spectrometers are required, is that the Earth's atmosphere has its own telluric absorption spectrum that a planetary signal must pass through before arriving at the detector— the planetary spectrum must be separated from the telluric spectrum using post-processing techniques (e.g. Birkby, 2018). This is especially relevant for observing other potentially Earth-like worlds, which may have atmospheric compositions similar to our own (Rodler et al., 2012; López-Morales et al., 2019; Currie et al., 2023; Hardegree-Ullman et al., 2023) and may be challenging to discriminate from our own atmosphere. The high-resolution spectroscopy technique depends on our ability to leverage the Doppler shift of the system (i.e. star+exoplanet+barycentric radial velocity offsets from our rest frame) over the course of a time series of observations to separate the exoplanet spectrum from the telluric spectrum, and resolving individual spectral lines at high resolution allows us to achieve this separation with post-processing techniques (Birkby, 2018). Commonly used methods for separating the spectrum of an exoplanet atmosphere from the telluric lines use a principal component analysis (PCA) algorithm (e.g. Brogi et al., 2018). Because the telluric lines do not Doppler shift with the planet spectrum, these removal algorithms isolate spectral features that are stationary (or quasi-stationary) in time (i.e. the star and telluric lines) on the detector from the spectral features that shift in wavelength space over time (i.e. the planet spectrum). However, these PCA-type methods can be challenging to apply to observations of terrestrial exoplanets (Chapter 3; Currie et al., 2023) because they typically require a total wavelength shift of $> 1$ spectral channel on the detector per observation (e.g. Birkby, 2018; Brogi et al., 2018), and terrestrial planets typically shift less than this as they transit their host star (Currie et al., 2023; Hardegree-Ullman et al., 2023). Velocity shifts for small planets during a typical observation may be insufficient to effectively isolate the planet spectrum from static telluric lines via PCA (Chapter 3; Currie et al., 2023), however, promising steps have been made to mitigate this effect by investigating our ability to remove telluric contamination on the sub-pixel level (Cheverall & Madhusudhan, 2024).

Other telluric removal techniques that will become particularly relevant to terrestrial exoplanet observations include applying radiative transfer tools to model and subtract the Earth's telluric contribution from the observation. These tools include Molecfit (Smette et al., 2015) and the online TAPAS service (Bertaux et al., 2014). Molecfit as a telluric line removal tool has been demonstrated to successfully remove the telluric lines down to the photon noise limit in high resolution of $H_2O$ lines in the atmosphere of HD 189733b (Allart et al., 2017). More recently, the web-based telluric transmission calculation service TAPAS has been used on ESPRESSO data of HD 40307 to remove telluric lines in wavelength regions with significant telluric absorption traditionally excluded by precision radial velocity surveys, improving the precision of the resulting stellar spectrum by up to 25% (Ivanova et al., 2023). While these telluric removal techniques have not been thoroughly demonstrated for simulated observations of Earth-like exoplanets, they show significant promise to mitigate the telluric contamination for future studies and ELT observations.

### *1.2.4 The Cross-Correlation Method*

After the static telluric and stellar lines are removed from a series of observations as detailed in Section 1.2.3, the planetary lines themselves are relatively low signal-to-noise, and a cross-correlation method is employed to combine the contributions from each absorption line in the spectrum to boost the overall signal (e.g. Snellen et al., 2010; Birkby, 2018). In the cross-correlation method, first used for this application by Snellen et al. (2010), a template spectrum that is a plausible model of the planetary atmosphere is convolved with the series of observed spectra to attempt to match the template to the observation at the radial velocity of the planet spectrum (Snellen et al., 2010). Early studies used template spectra simply composed of lists of absorption line locations (e.g. Snellen et al., 2010), but methods have evolved to use more complex radiative transfer models as template spectra (Brogi & Line, 2019), and in this work we additionally include the effects of the climate and photochemistry in our template spectra. The template spectrum is generally computed by running an atmospheric model through a radiative transfer algorithm that can compute spectra considering absorption and emission properties of the atmosphere (e.g. SMART; Meadows & Crisp, 1996; Crisp, 1997). Because every atmospheric constituent absorbs and emits light at unique wavelength bands, cross-correlating the template spectrum with the observed spectra can reveal the presence of specific molecules if a high correlation is found at the Doppler velocity of the planetary target.

Mathematically, given an observed spectrum $O(\lambda)$ and a model spectrum $M(\lambda)$, where $\lambda$ represents the wavelength, the cross-correlation function $C(v)$ as a function of radial velocity $v$ is computed by convolving the model (template) spectrum with the observed spectrum across velocity space and calculating the correlation coefficient at each velocity in a grid of velocities The mathematical formulation of the cross-correlation function is given by:

$$C(v) = \int O(\lambda)M(\lambda, v), d\lambda, \tag{1.1}$$

where $M(\lambda, v)$ is the model spectrum shifted by a velocity $v$. Peaks in the cross-correlation function indicate the presence of molecular signatures in the exoplanet's atmosphere that match the molecules in the model spectrum. This technique is particularly effective because it amplifies the signal of the molecular features by combining information across the entire spectrum, making it possible to detect the signatures of molecules even in noisy data. The cross-correlation technique effectively enhances the achieved stellar suppression contrast ratio by as much as a multiplicative factor of $10^{-5}$ (Snellen et al., 2015).

### *1.2.5 Molecular Abundance Determination*

The cross-correlation method is used in many studies to detect the presence of a molecule in an atmosphere (e.g. Brogi et al., 2012; Rodler et al., 2012; Birkby et al., 2013; De Kok et al., 2014; Rodler et al., 2013; Brogi et al., 2013; Lockwood et al., 2014; Brogi et al., 2014; Schwarz et al., 2015; Hoeijmakers et al., 2015; Brogi et al., 2016; Piskorz et al., 2016; Birkby et al., 2017a; Allart et al., 2017; Brogi et al., 2017; Piskorz et al., 2017; Nugroho et al., 2017; Brogi et al., 2018; Brogi & Line, 2019; Hoeijmakers et al., 2020b), but determining the abundance of a molecule can be more challenging (de Kok et al., 2014; Pino et al., 2018; Birkby, 2018). However, this is achievable for large planets with the latest generation of instrumentation, and has been demonstrated in recent studies (e.g. Holmberg & Madhusudhan, 2022; Maimone et al., 2022; Lesjak et al., 2023; Landman et al., 2024). For example, Landman et al. (2024) used the upgraded CRIRES+ instrument to retrieve a sub-solar C/O ratio for $\beta$ Pictoris b, confirming previous results, and also improved constraints on the planetary rotation via their retrieval framework. Obtaining the abundance of molecules in an exoplanet atmosphere can help provide a more thorough understanding of the atmosphere, including the chemistry and bulk composition that can help determine the formation and evolutionary pathways that a planet has undergone (e.g. Brogi & Line, 2019). In the context of terrestrial exoplanets, gaining abundance information can provide more compelling arguments for determining the nature of an atmosphere, especially for making claims of a biosignature detection, by constraining surface fluxes and abundances for key biosignature gases (e.g. Lustig-Yaeger et al., 2022; Krissansen-Totton et al., 2018b), or ruling out biosignature false positive scenarios (Krissansen-Totton et al., 2016; Meadows, 2017; Meadows et al., 2018; Leung et al., 2020; Krissansen-Totton et al., 2018b; Meadows et al., 2023). See section 1.3 for a discussion on biosignatures and their false positives.

To constrain the properties of an exoplanet atmosphere, including molecular abundances, observed spectra can be analyzed with statistical model inference frameworks (i.e. atmospheric retrievals) that constrain the parameters of a forward model of the planetary system properties (e.g. Lustig-Yaeger et al., 2022). Atmospheric retrieval analyses for ground-based high-resolution observations construct plausible models of exoplanet atmospheres and simulate spectra that are compared with the observed spectrum via cross-correlation analysis (e.g. Rodgers, 2000; Irwin et al., 2008; Madhusudhan & Seager, 2009). Often there is not a unique simulated spectrum that corresponds to the observation, and a Bayesian approach is applied to infer probability distributions of the atmospheric properties (e.g. Line et al., 2013). Spectral retrievals can include a customized list of parameters to fit, such as atmospheric molecular mixing ratios and planetary properties that can alter the spectrum beyond atmospheric properties(e.g. Madhusudhan & Seager, 2009; Lee et al., 2012). Many current exoplanet retrieval frameworks stem from models developed for ground-based observations of gas giants, and have been applied to both space-based (e.g. Nayak et al., 2017; Feng et al., 2018; Damiano et al., 2020; Damiano & Hu, 2022; Lustig-Yaeger et al., 2023b) and ground-based high-resolution (e.g. Brogi et al., 2017; Pino et al., 2018; Brogi & Line, 2019; Roche et al., 2021; Line et al., 2021; Seidel et al., 2023; Landman et al., 2024) observations. These state-of-the-art models show promising atmospheric retrieval capabilities, providing constraints on atmospheric composition in simulated (e.g. Damiano et al., 2020) and observed (e.g. Lustig-Yaeger et al., 2023b; Landman et al., 2024) spectra. However, a retrieval framework has not yet been tested for simulated ELT observations of terrestrial exoplanets.

Abundance retrieval is more challenging for ground-based observations than for space-based observations, because the best techniques for removing telluric contamination from the observation require the spectra to be normalized, losing the spectral continuum information used to gain absolute measurements of spectral line depths (Birkby, 2018); however, our ability to retrieve molecular abundances for terresrial planets with the ELTs has not been explored. Without knowing the continuum, degeneracies can arise from using models of different temperature–pressure profiles and molecular abundances which can alter the continuum and gas abundances (Birkby, 2018). Despite this, simultaneous detections of multiple molecules, or multiple bands of a single molecule, may provide pathways to retrieving the relative molecular abundances by comparing line depths relative to one another (de Kok et al., 2014; Brogi et al., 2017; Pino et al., 2018; Brogi et al., 2018; Brogi & Line, 2019; Roche et al., 2021; Line et al., 2021; Seidel et al., 2023; Landman et al., 2024), therefore spectrographs with wide wavelength coverage will be more suited to this technique (Pino et al., 2018). Additionally, the use of low-resolution spectroscopy (LRS) in conjunction with HRS has been shown to provide tighter constraints on atmospheric composition for ground-based observations of larger exoplanets (Brogi et al., 2017; Pino et al., 2018; Brogi & Line, 2019), and a formal retrieval framework for combining low and high resolution observations was introduced in Brogi & Line (2019); however Brogi & Line (2019) also shows that abundance retrieval is also possible with high-resolution observations alone. It is not clear whether we will be able to retrieve molecular abundances for terrestrial exoplanets with the ELTs, and in this work we apply a retrieval framework to simulated ELT observations of terrestrial exoplanets for the first time (see Chapter 5).

## *1.3 The Search for Signs of Habitability and Life in Exoplanet Atmospheres*

Searching for signs of habitability and life in nearby exoplanet atmospheres is inherently challenging due to the sheer diversity of possible planetary evolutionary outcomes that may mimic potential habitability or biosignature indicators (e.g. Meadows, 2017), and our understanding of the conditions that can lead to the evolution of biological metabolisms on other planets is based in our understanding of Earth processes (e.g. Kiang et al., 2018; Meadows et al., 2018; Schwieterman et al., 2018). Broadly speaking, the habitability of a planet is governed by abiotic planetary or astrophysical processes (e.g. Kopparapu et al., 2013; Shields et al., 2016; Meadows & Barnes, 2018); however, for a living world, abiotic and biological properties are interconnected, and searching for signs of habitability is important to understand whether the environment is capable of hosting life, or to support a claim that life was detected (Schwieterman et al., 2018). While the capacity for a planet to host life depends on whether the planet is habitable, a habitable planet does not necessarily imply the presence of extant life (e.g. Kopparapu et al., 2013; Meadows, 2017; Schwieterman et al., 2018; Meadows et al., 2018). Below we discuss habitability as it relates to life, as well as the associated detectable effects we seek to observe in Earth-like exoplanet atmospheres.

### *1.3.1 Habitability: Liquid Surface Water in the Habitable Zone*

A habitable planet is one that has the necessary conditions for life to evolve and exist (Cockell et al., 2016), and one of the pillars of planetary habitability is the existence of liquid water, which is believed to be a critical solvent used to develop and evolve life (e.g. Franks & Jones, 1987; Pohorille & Pratt, 2012). Terrestrial exoplanet environments may have climates and surface temperatures that allow liquid water to exist on their surfaces, and this property is the result of a complex web of both astrophysical and planetary processes, including the instellation the planet receives and the stability of the planetary orbit, atmospheric chemistry/dynamics, geochemistry, and surface processes (Meadows & Barnes, 2018). The habitable zone—the region around a host star where liquid water could exist—is a useful concept to readily evaluate the habitability of a planet (Kasting et al., 1993; Kopparapu et al., 2013); however, we acknowledge that habitability is not exclusive to planets in the habitable zone, as liquid water can exist beneath icy shells on planets or moons well outside of the habitable zone, as we find in our own Solar System (e.g. Gaidos et al., 1999). However, for this work we consider only planets in the habitable zone of their host stars, and below we discuss habitability and life only in the context of planets capable of having liquid surface water.

The location of the habitable zone is dependent on the host star type, and the range is defined by atmospheric processes limiting the existence of stable liquid surface water (Kopparapu et al., 2013). The host star and location of the planet dictates the level of instellation the planet receives, which is a main driver along with greenhouse gases that helps to control the temperature of the planet (Walker et al., 1981; Kasting et al., 1993; Kopparapu et al., 2013). Planets with $CO_2/H_2O/N_2$ atmospheres can buffer the planetary climate by controlling the atmospheric greenhouse gas inventory, which absorb then re-emit heat from the host star to warm the climate, with an active carbonate–silicate feedback cycle (Walker et al., 1981; Kasting et al., 1993; Kopparapu et al., 2013). In the carbonate–silicate cycle, atmospheric $CO_2$ dissolves in rainwater creating carbonic acid, which falls onto silicate rocks, dissolving them into bicarbonate among other products via weathering processes. The products of weathering eventually make it into the ocean via streams, where they are buried and subducted by plate tectonics, and are eventually outgassed as $CO_2$ into the atmosphere. Higher/lower climatic temperatures (coupled to higher/lower instellation) increase/decrease water evaporation, rainfall, and weathering, which causes removal/accumulation of $CO_2$ in the atmosphere, and a cooling/heating effect (Walker et al., 1981; Kasting et al., 1993; Kopparapu et al., 2013). The inner edge of the habitable zone is defined by the runaway greenhouse limit, and is the point at which the atmosphere becomes hot enough for liquid surface water to rapidly evaporate and contribute to the greenhouse inventory in a runaway effect (Kopparapu et al., 2013). On the other hand, the outer edge of the habitable zone is defined by the maximum greenhouse effect, where the greenhouse effect caused by adding more $CO_2$ into the atmosphere becomes overwhelmed by the cooling effect of Rayleigh scattering of the $CO_2$, causing runaway cooling (Kopparapu et al., 2013). The habitable zone provides a readily observable metric we can use to search for terrestrial exoplanets that could potentially host life, and key observables include the host star type and distance of the planet to the star, and the presence and abundance of the greenhouse gases $CO_2$, $H_2O$, and $CH_4$ that can help keep the planet temperate (Walker et al., 1981; Kasting et al., 1993; Kopparapu et al., 2013).

### *1.3.2 Biosignatures: Environmental Context is Key*

Observing the atmospheres of terrestrial exoplanets offers us one of the best opportunities to search for life beyond Earth in the form of biosignatures, and there are known biosignature gases that may be detectable via remote sensing with ground or space based observatories (e.g. Lovis et al., 2017; Kiang et al., 2018; Lustig-Yaeger et al., 2019a). Biosignatures can be any detectable phenomenon that is produced by life, and can include objects, substances, and patterns indicative of life (Marais & Walter, 1999; Des Marais et al., 2008; Seager et al., 2012; Schwieterman et al., 2018). Biosignatures are considered to be robust when they are unequivocally byproducts of life that remain in the atmosphere and are readily detectable (Meadows, 2017; Meadows et al., 2018). One approach to detecting biosignatures is to search for chemical disequilibria in the atmosphere, which would imply active fluxes of gases into the system, that, depending on their nature and amount, could potentially be due to life, or to planetary surface geology and atmospheric photochemistry (Hitchcock & Lovelock, 1967; Lovelock, 1965; Lovelock & Kaplan, 1975; Sagan et al., 1993; Krissansen-Totton et al., 2016, 2018b; Meadows et al., 2023). Below we describe the biosignature gases $O_2$ and $CH_4$, as well as two possible biosignature disequilibrium pairs, $O_2$/$CH_4$ (e.g. Hitchcock & Lovelock, 1967; Sagan et al., 1993; Meadows et al., 2018) and $CO_2$/$CH_4$ (Krissansen-Totton et al., 2016, 2018b; Meadows et al., 2023) .

On Earth, $O_2$ and $CH_4$ are the products of two separate biospheres, and if they are detected in the atmospheres of other worlds their simultaneous presence can enhance the likelihood that these gases originated via biology (e.g. Hitchcock & Lovelock, 1967; Meadows et al., 2018). $O_2$ is one of the major constituents in the Earth's atmosphere (21% volume mixing ratio) and is the byproduct of oxygenic photosynthesis, which uses $CO_2$ and $H_2O$ to produce organic sugars, with $O_2$ as a byproduct (Leslie, 2009). The great oxidation event 2.3 billion years ago (Ga) marked a turning point in the Earth's atmospheric composition, where the significant biological flux of $O_2$ over geologic timescales overwhelmed the major $O_2$ sinks, including the burial of oxidized iron and sulfur compounds (Lyons et al., 2014). This led to the eventual buildup of $O_2$ in our atmosphere to an abundance of 21% in the modern day (Lyons et al., 2014). Abiotic mechanisms that create $O_2$ via the photolysis of oxygen-bearing molecular species such as $CO_2$ and $H_2O$ may be able to produce detectable $O_2$ levels for planets in the habitable zones of especially M dwarf host stars (Wordsworth & Pierrehumbert, 2014; Luger & Barnes, 2015; Gao et al., 2015; Tian, 2015; Meadows, 2017; Schwieterman et al., 2018); however, known abiotic $O_2$ production mechanisms on Earth have low fluxes compared to the biological $O_2$ flux, making $O_2$ a robust biosignature gas for our atmosphere (e.g. Hitchcock & Lovelock, 1967), but not necessarily for any exoplanet atmosphere containing $O_2$. $O_2$ has strong absorption bands in the visible and near infrared wavelength regimes, and its high abundance in Earth's atmosphere provides an additional advantage for using this gas as a biosignature (Meadows, 2017).

The methanogenesis metabolism is the dominant source of non-anthropogenic $CH_4$ in Earth's atmosphere (e.g. Wuebbles & Hayhoe, 2002), and this has been suggested as a biosignature on Earth (Hitchcock & Lovelock, 1967; Sagan et al., 1993; Meadows et al., 2018) for an entirely different biosphere (archaea) than organisms using oxygenic photosynthesis as their metabolism. Using the methanogenesis metabolism, organisms generate energy by reacting $CO_2$ with $H_2$, leaving $CH_4$ and $H_2O$ as major byproducts (Woese & Fox, 1977; Ueno et al., 2006; Lyu et al., 2018). The abundance of $CH_4$ has varied throughout Earth's history, from thousands of ppm in the Archean Eon (Reinhard et al., 2017) to 1.8 ppm in the modern Earth atmosphere, and its atmospheric abundance could be enhanced for planets orbiting M dwarf stars (Segura et al., 2005). However, there are also abiotic $CH_4$-generating mechanisms which involve water–rock interactions, and our ability to use $CH_4$ as a biosignature depends on whether we can determine its origin (e.g. Etiope & Sherwood Lollar, 2013; Krissansen-Totton et al., 2018b). Considering $O_2$ and $CH_4$ together as an atmospheric disequilibrium pair may enhance the likelihood that these gases are biological in origin because large $CH_4$ fluxes are required to explain its persistence in a highly oxidized atmosphere (Hitchcock & Lovelock, 1967; Lovelock, 1965; Lovelock & Kaplan, 1975; Sagan et al., 1993; Krissansen-Totton et al., 2016; Meadows, 2017; Meadows et al., 2018; Krissansen-Totton et al., 2018b). Large fluxes of $CH_4$ are incompatible with known abiotic $CH_4$-producing mechanisms (e.g. Wogan et al., 2020), and the simultaneous detection of $CH_4$ and $O_2$ may be a strong biosignature (e.g. Krissansen-Totton et al., 2016, 2018b; Meadows et al., 2018), indicating the presence of two separate, and active, biospheres.

We can also consider other gas disequilibria as an indicator for life: $CO_2$ and $CH_4$ may be an alternative pair of biosignature disequilibrium gases that were first proposed for Earth's $O_2$-poor ancient Archean atmosphere (Krissansen-Totton et al., 2018b; Meadows et al., 2023). Similar to the $O_2$/$CH_4$ pair, a high abundance of $CH_4$ in the presence of significant $CO_2$ requires a high flux of $CH_4$ to maintain a detectable abundance in the atmosphere against atmospheric oxidation via $CO_2$ (Krissansen-Totton et al., 2018b; Meadows et al., 2023). If the $CH_4$ flux can be quantified, it can be assessed as to whether it is more or less likely to be due to less productive abiotic processes like serpentinization, when water runs over ultramafic (e.g. basaltic) rock (Guzmán-Marmolejo et al., 2013; Etiope & Sherwood Lollar, 2013), or more productive biological processes such as methanogenesis (Krissansen-Totton et al., 2018b; Meadows et al., 2023). Although originally proposed for the Archean Earth (Krissansen-Totton et al., 2016), the $CO_2/CH_4$ biosignature pair may also be detectable in transmission for M dwarf planets with a modern Earth photosynthetic biosphere and methanogenesis, even when the dominant oxygenic biosphere is not detectable (Meadows et al., 2023; Currie et al., 2023). This makes the $CO_2/CH_4$ disequilibrium biosignature significantly more persistent throughout Earth's history when compared to the $O_2/CH_4$ pair, which may have been detectable only within the last 1 billion years (Planavsky et al., 2018), and a prime target for observational studies of terrestrial exoplanet atmospheres (Meadows et al., 2023).

### *1.3.3 Biosignature False Positives*

Although the $O_2$ and $CH_4$ present in Earth's atmosphere is the byproduct of oxygenic photosynthesis (e.g. Lyons et al., 2014) and methanogenesis (Wuebbles & Hayhoe, 2002), respectively, other abiotic pathways exist that can generate detectable levels of these gases. Terrestrial atmosphere environments can be habitable, but uninhabited, with temperate climates that allow for the buildup of liquid surface water and detectable levels of $O_2$ and/or $CH_4$, and we refer to these atmospheres as biosignature false positive environments (Meadows, 2017; Meadows et al., 2018; Schwieterman et al., 2018). In these environments, $O_2$ can be generated via the photolysis of oxygen-bearing molecules like $CO_2$ or $H_2O$ (Wordsworth & Pierrehumbert, 2014; Luger & Barnes, 2015; Gao et al., 2015; Meadows et al., 2018; Ranjan et al., 2023), and these abiotic production pathways may be especially relevant for planets orbiting M dwarf stars, which have enhanced UV flux that can drive photochemical reactions and molecular lifetimes in the atmosphere, potentially also building up higher abundances of supporting gases like $CH_4$ (Segura et al., 2005). One proposed, but now understood to be less concerning (Ranjan et al., 2023), scenario for detectable abiotic-origin $O_2$ may arise for atmospheres that have significant $CO_2$ abundance, which gets photolyzed by the host star's flux and the oxygen atoms combine into $O_2$ at a $\sim 5\%$ level (e.g. Harman et al., 2015). This process may also produce detectable CO, the presence of which may indicate this biosignature false positive scenario (Meadows et al., 2018); however, the original calculations predicting significant $O_2$ buildup via $CO_2$ photolysis may be an overestimate due to model artifacts, and the $O_2$ produced from this process is more likely to be a trace gas, potentially eliminating this $O_2$ false positive scenario from consideration (Harman et al., 2018; Ranjan et al., 2023). Another case of abiotic $O_2$ buildup may result from planets with significant surface water that boils into steam in the atmosphere (Luger & Barnes, 2015; Tian, 2015; Schwieterman et al., 2016), and the buildup of water vapor is photolyzed, resulting in significant $O_2$ abundances that may, after planetary sinks are considered, reach 3 to thousands of bars (Schaefer et al., 2016; Meadows et al., 2018); however, this biosignature false positive mechanism may be indicated by significant suppression in $O_2$ spectral features, apparent in high-resolution spectra (Leung et al., 2020), and tested in this work for simulated ELT observations. $O_2$ can also build up to the $\sim 20\%$ level for desiccated planets (Gao et al., 2015) or for planets with a low noncondensable gas inventory (Wordsworth & Pierrehumbert, 2014); therefore, detecting the presence of $O_2$, or even measuring the abundance of $O_2$, alone may not be sufficient to discriminate these cases. In lifeless environments such as the prebiotic Earth, significant volcanism could potentially generate high abundances of $CH_4$ that may be detectable in atmospheres with significant $CO_2$, which can be a false positive for the $CO_2/CH_4$ biosignature pair (Krissansen-Totton et al., 2016; Wogan et al., 2020; Thompson et al., 2022; Meadows et al., 2023). In this prebiotic Earth scenario, the volcanism would also generate large abundances of CO in that atmosphere, which would be the discriminant for this false positive, as CO is not prevalent in a biological Earth-like scenario (Krissansen-Totton et al., 2016).

### *1.3.4 Searching for Habitability and Life with the ELTs*

The majority of targets accessible to the ELTs will orbit around M dwarf stars, which may provide interesting comparisons of planetary evolutionary processes, as well as expand the search for habitability and life to non-Earth-like systems (Gialluca et al., 2024). The stellar environments of M dwarf systems can significantly alter the composition and evolution of terrestrial planet atmospheres (e.g. Segura et al., 2005; Meadows et al., 2018; Gialluca et al., 2021), and these effects have not yet been accounted for in ELT detectability studies, which have historically used modern Earth analog targets (e.g. Rodler & López-Morales, 2014). On M dwarf planets, even with the same assumed surface fluxes of gases, the spectral energy distribution (SED) of the host star can affect molecular destruction and production rates, altering photochemical lifetimes of gas species, potentially enhancing the abundance of key gases in the atmosphere such as $CH_4$ (Segura et al., 2005; Rugheimer et al., 2013; Rugheimer et al., 2015). Planets in the habitable zone may also receive different irradiances than Earth depending on their orbital geometries (Kopparapu et al., 2013) which may act to cool or warm the planet relative to Earth. However, the carbonate–silicate cycle, which is presumed to be active on a planet with liquid water and plate tectonics, may stabilize the surface temperature by buffering the $CO_2$ abundance in the planetary atmosphere (Walker et al., 1981). Thus planets receiving less irradiance from their host star may have a buildup of $CO_2$ in their atmospheres to keep the surface temperate. These different abundances and distributions of atmospheric species due to the action of photochemistry and climate buffers can significantly alter their detectability, and thus these effects must be accounted for when estimating their detectability in terrestrial exoplanet atmospheres (Meadows et al., 2023).

The feasibility of detecting $O_2$ in ground-based observations of terrestrial exoplanets is relatively well studied. The main challenge is separating exoplanet $O_2$ absorption from Earth's $O_2$ absorption—which also applies to other molecules that appear both in a target atmosphere and Earth's atmosphere (see Section 1.2.3). However, with well-constrained radial velocity measurements from high-resolution ($R \sim 100{,}000$) ELT spectrometers (Szentgyorgyi et al., 2014; Marconi et al., 2016; Mawet et al., 2019; SANNA et al., 2021), this challenge can be overcome using a cross-correlation method (Snellen et al., 2010) (see Section 1.2). Using this method, significant emphasis has been placed on estimating the detectability of $O_2$ in Earth-like atmospheres for both transit transmission (i.e. HRS-only) (e.g. Rodler & López-Morales, 2014; López-Morales et al., 2019; Snellen et al., 2013; Currie et al., 2023; Hardegree-Ullman et al., 2023) and reflected light (HDC) (e.g. Hawker & Parry, 2019; Lovis et al., 2017; Wang et al., 2017; Zhang et al., 2023; Vaughan et al., 2024) simulations, and some studies suggest that strong atmospheric $O_2$ features may be detected through the Earth's atmosphere for nearby Earth-twin targets (Snellen et al., 2013; Rodler & López-Morales, 2014; Serindag & Snellen, 2019; López-Morales et al., 2019), making $O_2$ a prime biosignature gas to target for upcoming ground-based telescopes. Snellen et al. (2013) pioneered the use of cross-correlation analysis to simulate how to untangle the telluric oxygen lines from exoplanet oxygen, and found that $O_2$ is detectable at $3.8\sigma$ with the European–ELT in 30 transits for a hypothetical Earth twin in the GJ 1214 (M5V) system $\sim 14.6$ pc away. Rodler & López-Morales (2014) later refined this study by adding red noise and atmospheric refraction effects to the simulated observations, and found that it would instead take about twice as many transits to detect oxygen at the same significance. To simulate even more realistic observations, Serindag & Snellen (2019) injected an $O_2$ signal into real observations of Proxima Centauri using the Ultraviolet and Visual Echelle Spectrograph (UVES) instrument on the Very Large Telescope (VLT), and found that $O_2$ would be detectable in 20–50 transits for an Earth twin orbiting an M5 star 7pc away, which is consistent with Snellen et al. (2013) and Rodler & López-Morales (2014). López-Morales et al. (2019) sought to optimize instrumentation and observing strategies for detecting $O_2$, and found that increasing the spectral resolution to $R = 300,000$ more than doubles the $O_2$ line depths compared to $R = 100,000$ spectra, and the higher spectral resolution lowers the number of transits to detect $O_2$ at $3\sigma$ by 34%. Furthermore, early studies by Wang et al. (2017) and Hawker & Parry (2019) have investigated the detectability of $O_2$ for reflected light ELT observations for an Earth-like Proxima Centauri b, and found that it may be detectable in $30 - 100$ hours of observing.

While the ground-based high-resolution cross-correlation spectroscopy technique is well explored for $O_2$ detection, similarly thorough investigations for other molecules that can help interpret $O_2$ in the context of its planetary environment are required to understand whether a planet is habitable or inhabited. Lin & Kaltenegger (2020) suggested that in addition to $O_2$, ELTs may be used to search for potential biosignature or climate-indicator gases like $CH_4$, $CO_2$, and $H_2O$ in Earth-like atmospheres around late-type M dwarfs, but did not simulate observations to quantify the detectability of these molecules. Furthermore, Lovis et al. (2017) explored $O_2$, $CH_4$, and $H_2O$ detectability using instrumentation on the Very Large Telescope (VLT), and found that $O_2$ and $H_2O$ may be accessible in an Earth-like Proxima Centauri b atmosphere in $\sim 60$ nights of observing, but their limited access to high-accuracy line list data in their wavelength region (600-780 nm) limited their ability to estimate $CH_4$ detectability; however the broader wavelength range we study in this work (0.5–2$\mu$m) includes regions where high-accuracy $CH_4$ lines are available, allowing us to study the detectability of $CH_4$. Wang et al. (2017), Lovis et al. (2017), Hawker & Parry (2019), Zhang et al. (2023), and Vaughan et al. (2024) simulate direct imaging observations of Proxima Centauri b, and predict that subsets of $H_2O$, $O_2$, $CO_2$, and/or $CH_4$ may also be detectable with future ELT instrumentation for modern Earth-like atmospheres within $\sim 100$ hours of observation, however considerations for the detectability of these molecules in the astrobiological context of both inhabited and false positive abiotic environments has not yet been explored.

While previous studies have established that it may be possible to detect the presence of $O_2$ for nearby terrestrial targets with the ELTs (Rodler & López-Morales, 2014; López-Morales et al., 2019; Hawker & Parry, 2019; Serindag & Snellen, 2019; Hardegree-Ullman et al., 2023), they have not explored how to constrain the abundances of molecules in simulated ELT spectra using a retrieval framework. Determining the abundances of molecules in terrestrial atmospheres will be critical for characterizing the environment and providing contextual clues constraining whether the environment can both support life or if it is currently inhabited. In particular, over the course of Earth's history, the $O_2$ abundance has fluctuated— $O_2$ was a trace gas in the Archean, and after oxygenic photosynthesis evolved the $O_2$ abundance fluctuated between 1% and 21% (Lyons et al., 2014; Reinhard et al., 2017). For brief periods in the Paleozoic, $O_2$ levels may have risen above 24% and were accompanied by evidence of extensive forest fires due to the high atmospheric combustion potential associated with high $O_2$ levels (Glasspool et al., 2015; Lenton, 2013). Therefore, planets with $O_2$ abundances in excess of 21% may be inhospitable to life on the land surfaces. To rule out this scenario and increase the likelihood of a habitable environment, as well as understand what false positive mechanisms may be at work, constraining the $O_2$ abundance via atmospheric retrieval is the next step in the progression of characterizing terrestrial atmospheres with the ELTs. One of the goals of this work is to provide an exploratory first step toward understanding our ability to constrain atmospheric abundances in terrestrial exoplanet atmospheres using the ELTs, beginning with our ability to constrain $O_2$ abundance in simulated observations of our nearest potentially terrestrial exoplanet neighbor, Proxima Centauri b (Anglada-Escudé et al., 2016).

## *1.4 Purpose and Structure of Dissertation*

The goal of this dissertation work is to identify the capabilities of the ELTs and how they may be optimized to support the search for habitability and life on terrestrial exoplanets over the course of their operating lifetimes. The methods we use to accomplish this are presented in Chapter 2, and we present results and discussions for our work in Parts I through III, outlined below.

In Part I, we analyze the detectability of molecular species in the atmospheres of both terrestrial and sub-Neptune atmospheres orbiting M dwarf stars. We simulate realistic ELT observations using a novel noise calculator, and perform a cross-correlation analysis for a broad range of atmospheres and systems. Chapter 3 covers exoplanets that transit their host star, and we use simulated transit transmission spectra to study the detectability of molecular species. Chapter 4 considers non-transiting exoplanets, and as such focuses on reflected light observations. These works help to lay the foundation for the retrieval analyses developed and demonstrated in Part II.

In Part II, we upgrade an existing retrieval framework to consider high-resolution ELT data, incorporating a cross-correlation analysis into a retrieval framework for terrestrial exoplanets for the first time. We explore how well we may be able to constrain the abundance of $O_2$ in simulated ground-based, high spectral resolution observations of the nearest non-transiting potentially terrestrial exoplanet Proxima Centauri b to understand the capabilities and limitations of the ELTs (see Chapter 5).

In Part III, we summarize key insights relevant to maximize the science of future ELT observations, and synthesize the results from this dissertation, discussing them in the context of the broader scientific landscape. Chapter 6 provides an overview of the impact of this dissertation on the fields of terrestrial exoplanet characterization and astrobiology, and reports on how our findings have shaped the future outlook and optimal approaches for characterizing terrestrial exoplanets and searching for signs of habitability and life with the ELTs. Finally, we conclude in Chapter 7.

## Chapter 2

# METHODS FOR TERRESTRIAL EXOPLANET CHARACTERIZATION USING THE ELTS

*Portions of this chapter were originally published in collaboration with Victoria S. Meadows and Kaitlin C. Rasmussen in the May 2023 edition of The Planetary Science Journal (Currie et al., 2023a, PSJ, Vol. 4, 5; DOI: 10.3847/PSJ/accf86), or submitted for publication in The Planetary Science Journal on June 19, 2024, and is reproduced below with the permission of the American Astronomical Society.*

## ***Summary***

To understand and define the utility of the ELTs for characterizing terrestrial exoplanet atmospheres for nearby targets, we have devised a research program that thoroughly explores the prospects for detecting a suite of molecular features in simulated high-resolution spectra of a range of different atmosphere types. In this chapter, we present the methods and analysis pipelines we have developed and/or implemented to understand the capabilities of the ELTs and formulate initial observing protocols for when these observatories come online. At the core of our methods is the high-resolution cross-correlation technique, discussed in detail in Section 1.2 of Chapter 1, and in the following sections we present how we applied this method to simulated ELT observations of terrestrial exoplanets to estimate the detectability of individual molecular species, and measure the abundance of molecular oxygen. The research arc of this dissertation is divided into three distinct projects: (1) estimating the detectability of molecular species in *transiting* terrestrial exoplanets using simulated transit transmission observations, (2) estimating the detectability of molecular species in *non-transiting* terrestrial exoplanets using simulated high-contrast reflected light observations, and (3) exploring how we may be able to use the ELTs to constrain molecular abundances using a retrieval framework. The following sections of this chapter map onto the results presented in Chapters 3, 4, and 5, and this mapping is summarized directly below.

We begin by describing the development of a novel pipeline for estimating the detectability of a suite of molecules expected in transiting terrestrial exoplanet atmospheres. We consider a suite of different atmosphere types, including worlds that are inhabited and worlds that are habitable, but uninhabited, and calculate the relative detectability of molecular species

in these atmospheres for simulated observations using the upcoming ELTs. The details of this pipeline, including a discussion of the provenance of the atmosphere models we tested, how the spectra were generated, how the ELT observations were simulated, and how we applied the high-resolution cross-correlation method to arrive at detectability estimates for transiting planets are presented below in Section 2.1. The results corresponding to this section are presented and discussed in Chapter 3.

Next, we upgrade the detectability pipeline we developed in Section 2.1 to encompass non-transiting planets. Contrary to transiting planets, observations of non-transiting planets require the use of high-contrast coronagraphic imaging (see Section 1.2), which necessitates upgrades to our detectability model to simulate these observations. In Section 2.2, we describe these upgrades and how we implemented them in our detectability model, and apply this upgraded model to simulated observations of nearby non-transiting exoplanets, including the most favorable nearby target Proxima Centauri b. In addition to testing the same atmospheres of Section 2.1 for a direct comparison of transmission vs. reflected light observations, we also include a sub-Neptune type atmosphere because there is a $>10\%$ likelihood that Proxima Centauri b is not terrestrial (Bixel & Apai, 2017). We present the results and a discussion of this project in Chapter 4.

The final project of this research arc focuses on our ability to measure molecular abundances from simulated ELT observations. This requires pairing the detectability pipeline developed in Sections 2.1 and 2.2 to a retrieval framework. For consistency in radiative transfer calculations, we chose to use an existing retrieval framework that is based around the same radiative transfer code we use in our detectability pipeline. However, this existing retrieval framework was initially designed for space-based observations, therefore upgrades were necessary to analyze ground-based high-resolution spectra with the cross-correlation method. In Section 2.3, we describe these upgrades and how they were implemented to the pre-existing retrieval framework. We test this new capability by attempting to retrieve molecular abundances in simulated ELT observations of terrestrial exoplanets, and present the results and a discussion in Chapter 5.

In summary, the following sections of this chapter describe in detail the methods used to predict the performance of the ELTs for characterizing terrestrial-sized exoplanets by expanding the application of the high-resolution cross-correlation spectroscopy technique to simulated observations of both transiting and non-transiting terrestrial exoplanets using the upcoming ELTs. Each section corresponds to the results presented in the following three chapters: Section 2.1 describes the development and application of a novel ELT detectability pipeline created specifically for transiting terrestrial exoplanet observations, with the results presented in Chapter 3. Section 2.2 describes upgrades made to the detectability pipeline that are necessary to explore the detectability of non-transiting planetary atmospheres, and the results appear in Chapter 4. Finally, in Section 2.3 we present upgrades to an existing retrieval framework for constraining the abundance of molecular species in ground-based high-resolution spectra of terrestrial exoplanets, with initial results presented in Chapter 5.

## *2.1 SPECTR: A Novel ELT Detectability Pipeline for Terrestrial Exoplanets*

In this work, we develop a novel pipeline for estimating the detectability of molecular bands in transiting terrestrial exoplanet atmospheres using cross-correlation analysis (Figure 2.1). The model takes simulated high-resolution (R=100,000) transit transmission spectra of a variety of terrestrial environments as its input, adds appropriate noise for ground-based high-resolution spectroscopy, and performs a cross-correlation analysis on the synthetic observation and a model spectrum. We use the resulting cross-correlation function to determine the detectability of a molecular band as a function of the number of transits observed.

### *2.1.1 Model inputs*

Our novel detectability pipeline (Figure 2.1) requires high-resolution transit transmission spectra as its input. We generate high-resolution spectra using a radiative transfer model applied to 1-D atmospheric profiles that describe the pressure, temperature and mixing ratio of key gases as a function of altitude (pressure). To generate atmospheres that are self-consistent with the host star SEDs, we use results from previous coupled climate–photochemical models.

#### *2.1.1.1 System selection*

We test the detectability of multiple absorption bands for seven molecules (Table 2.1) in four atmosphere classes derived from the climate/photochemistry models of other studies (Table 2.2) orbiting five different M dwarf host stars, at 5 and 12 pc away from Earth. To inform the development of future instrumentation, the detectability is calculated for individual absorption bands of each molecule, as López-Morales et al. (2019) found no advantage to combining molecular bands in observations when accounting for red noise. The four atmosphere classes include pre-industrial Earth (PIE) and Archean Earth (ARE) (Meadows et al., 2018; Davis et al., in prep.), a scenario with abiotic $O_2$ buildup from $CO_2$ photolysis (referred to as $CO_2$ photolysis) for both lightning on and lightning off cases (Harman et al., 2018), and scenarios for 10 bar $O_2$ atmospheres that result from both complete ocean loss

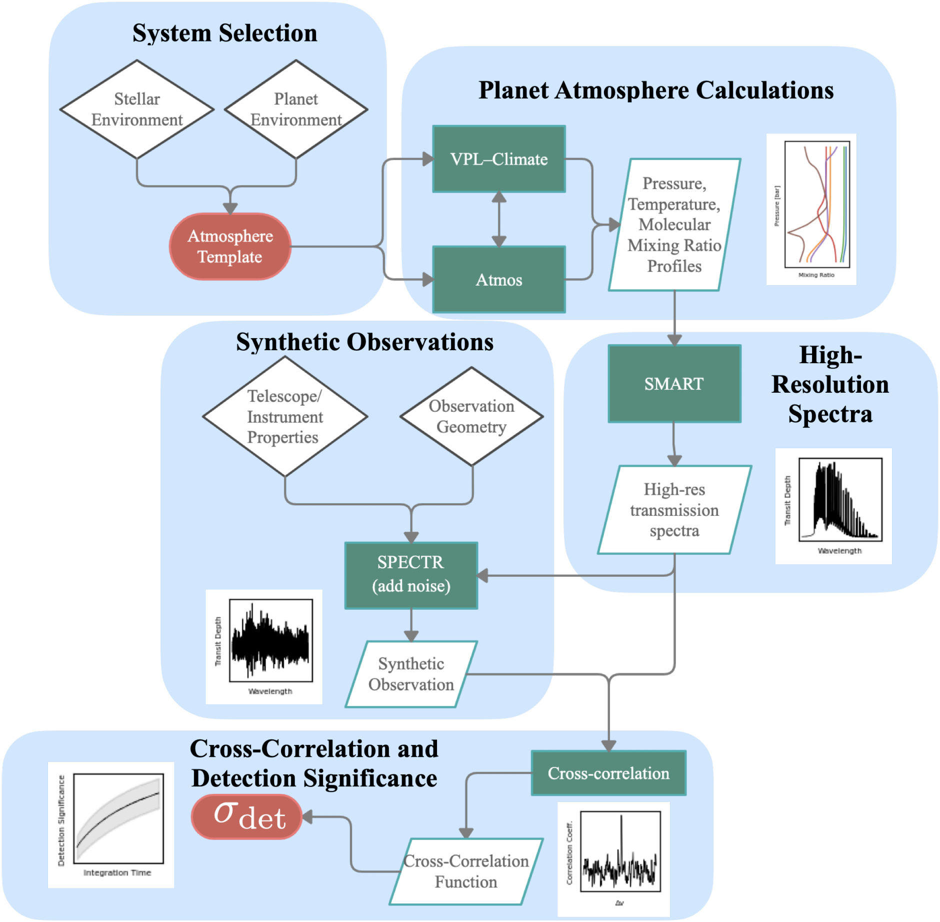

Figure 2.1 Overview of methods pipeline. The red round boxes represent the start and end points of the pipeline. The solid green boxes represent models or software pipelines, the white parallelograms represent input or output data products, and the rhombuses represent user-specified metadata or parameters. Cartoon examples of the data products are shown next to each data product node.

Table 2.1. Molecular bands explored in this study

| Molecule | Bands [$\mu m$] |
|---|---|
| $O_2$ | 0.69, 0.76, 1.27 |
| $CH_4$ | 0.89, 1.1, 1.3, 1.6 |
| $CO_2$ | 1.59, 2.0 |
| $H_2O$ | 0.94, 1.1, 1.3 |
| $O_3$ | 0.63, 0.65, 3.2 |
| CO | 1.55, 2.3 |
| $C_2H_6$ | 3.33 |

(referred to as ocean-loss) with internal desiccation, and ongoing ocean loss with subsequent interior outgassing (referred to as ocean outgassing) (Meadows et al., 2018; Leung et al., 2020). All planets are one Earth radius in size. We place the PIE and ARE planets in orbit around M2V, M3V, M4V, M6V, and M8V dwarf host stars, and use outputs from previous studies that produced self-consistent photochemical and climatic simulations for calculating our spectra. The $CO_2$ photolysis and 10 bar $O_2$ ocean loss/outgassing atmospheres are self-consistent with only M4V and M6V dwarf hosts, respectively, and thus detectability for these planets orbiting other M dwarf hosts is not considered. For our pre-industrial Earth-like atmospheres, we include both clear sky and cloudy scenarios. In total, there are 14 unique planet/star systems in this study, outlined in Table 2.2. As an example of a potential real ELT target, we calculate the detectability of species in our Earth-sized PIE and ARE atmospheres with TRAPPIST-1 e's orbit (M8V host) at its canonical distance of 12 pc (Gillon et al., 2016) using the atmosphere models of Davis et al. (in prep).

Table 2.2. Atmosphere classes and host stars

| Atmosphere | Host Star(s) | Atm. Ref. |
|---|---|---|
| Pre-industrial Earth (PIE) | M2V, M3V, M4V, M6V, M8V | Davis et al. (in prep) |
| Archean Earth (ARE) | M2V, M3V, M4V, M6V, M8V | Davis et al. (in prep) |
| $CO_2$ photolysis, lightning ON | M4V | Harman et al. (2018) |
| $CO_2$ photolysis, lightning OFF | M4V | Harman et al. (2018) |
| 10 bar $O_2$ complete ocean loss | M6V | Meadows et al. (2018) |
| 10 bar $O_2$ ongoing ocean outgassing | M6V | Meadows et al. (2018) |

Table 2.3. Planet orbital properties

| Host Spectral Type | Transit duration [hr] | Time between transits [hr] | Orbital Period [day] | Semi-major axis [AU] |
|---|---|---|---|---|
| M2V | 4.7 | 1153 | 48 | 0.24 |
| M3V | 3.6 | 793 | 33 | 0.19 |
| M4V | 3.4 | 692 | 29 | 0.16 |
| M6V | 1.2 | 152 | 6.4 | 0.041 |
| M8V | 0.99 | 96 | 6.0 | 0.027 |

Table 2.4. Host star properties

| Spectral Type | Example star | Radius [$R_\odot$] | $T_{\rm eff}$ K | Synthetic Spectrum Ref. | $m_I$ (5 pc) [mag] | $m_J$ (5 pc) [mag] | $m_I$ (12 pc) [mag] | $m_J$ (12 pc) [mag |
|---|---|---|---|---|---|---|---|---|
| M2 | GJ 832 | 0.499[a] | 3657 | Peacock et al. (2019b) | 6.2 | 5.0 | 8.1 | 6.9 |
| M3 | GJ 436 | 0.464[b] | 3416 | Peacock et al. (2019b) | 6.8 | 5.4 | 8.7 | 7.3 |
| M4 | GJ 876 | 0.3761[c] | 3129 | Peacock et al. (2020) | 7.1 | 5.8 | 9.0 | 7.7 |
| M6 | Proxima Centauri | 0.141[d] | 3050 | Davis et al. (in prep) | 10.7 | 8.6 | 12.6 | 10.5 |
| M8 | TRAPPIST-1 | 0.114[e] | 2516 | Peacock et al. (2019a) | 12.2 | 9.3 | 14.1 | 11.2 |

Note. — Stellar radii references: [a]Houdebine (2010), [b]Torres (2007), [c]von Braun et al. (2014), [d]Bonfils et al. (2005), [e]Filippazzo et al. (2015). The magnitudes are calculated for each example star placed at 5 and 12 pc away from Earth.

### *2.1.1.2 Planet atmosphere calculations*

For the self-consistent planetary atmospheres used as input to the simulator, we use previously generated results from a 1-D coupled climate–photochemistry model—which includes the effects of the host star SED on the photochemistry and climate of each planet atmosphere. The model couples the atmospheric chemistry component of *Atmos*, a publicly available model based on Kasting et al. (1979) and Zahnle et al. (2006), with VPL-Climate, a general-purpose, 1D radiative–convective equilibrium, terrestrial planet climate model (Meadows et al., 2018; Robinson & Crisp, 2018). The coupled model is described in detail in Lincowski et al. (2018), including validations for both Earth and Venus.

Davis et al. (in prep) updated the coupled climate–photochemistry model to include new $H_2O$ cross-sections, and ran globally-averaged PIE and ARE atmospheres orbiting M2V, M3V, M4V, M6V, and M8V dwarf stars to convergence, which we use for our PIE and ARE atmosphere classes in this study. Each planet is placed in orbit around its host star such that it receives 0.66 times the irradiance that Earth receives, and the accompanying orbital properties are given in Table 2.3. This irradiance is approximately the same as that received by the M dwarf habitable zone planets TRAPPIST-1e (Gillon et al., 2017) and Proxima

Centauri b (Anglada-Escudé et al., 2016). The host star properties and spectra are given in Table 2.4, and their synthetic spectra are plotted in Figure 2.2 (degraded to R = 50 for clarity). For each spectral type, we use publicly available synthetic high-resolution stellar spectra for the stars GJ832, GJ436, GJ876, Proxima Centauri, and TRAPPIST-1 (Peacock et al. (2019a,b, 2020), Davis et al. in prep.). These spectra serve as analog examples for M2V, M3V, M4V, M6V, and M8V dwarf stars, respectively. The vertical gas abundance and temperature profiles for the self-consistent PIE and ARE atmosphere calculations are shown as solid lines in Figures 2.3 and 2.4, respectively; we include true Earth profiles in dashed lines as a comparison. The habitable PIE and ARE atmospheres considered here contain 10% $CO_2$, which is required to raise the global mean surface temperatures above the freezing point of water (Meadows et al., 2018). This abundance is not unreasonable if we assume that the surface temperature of a planet within the habitable zone is buffered by a carbonate-silicate feedback, as proposed by Walker et al. (1981). With the carbonate-silicate feedback working, a planet may have an atmospheric $CO_2$ abundance of up to several bars of $CO_2$ near the HZ outer edge (Kopparapu et al., 2013).

The Harman et al. (2018) $CO_2$ photolysis atmospheres, which, with lightning turned off, can generate up to 6% $O_2$ from $CO_2$ photolysis are self-consistent with our M4V stellar host, and the corresponding molecular and temperature profiles are presented in Figure 2.5. The two red lines show the effects of turning lightning off (dotted) and on (solid). NO produced by lightning catalyzes the recombination of CO and O, decreasing oxidizing species and increasing reducing species in the atmospheres. Again, true Earth is shown for comparison in the blue dashed lines.

The 10-bar $O_2$ atmospheres from Leung et al. (2020) are self-consistent with our M6V stellar host, and the corresponding molecular and temperature profiles are presented in Figure 2.6, with ocean-loss profiles as the solid lines and ocean-outgassing profiles as the dashed lines. True Earth profiles are shown for comparison as the blue dashed lines.

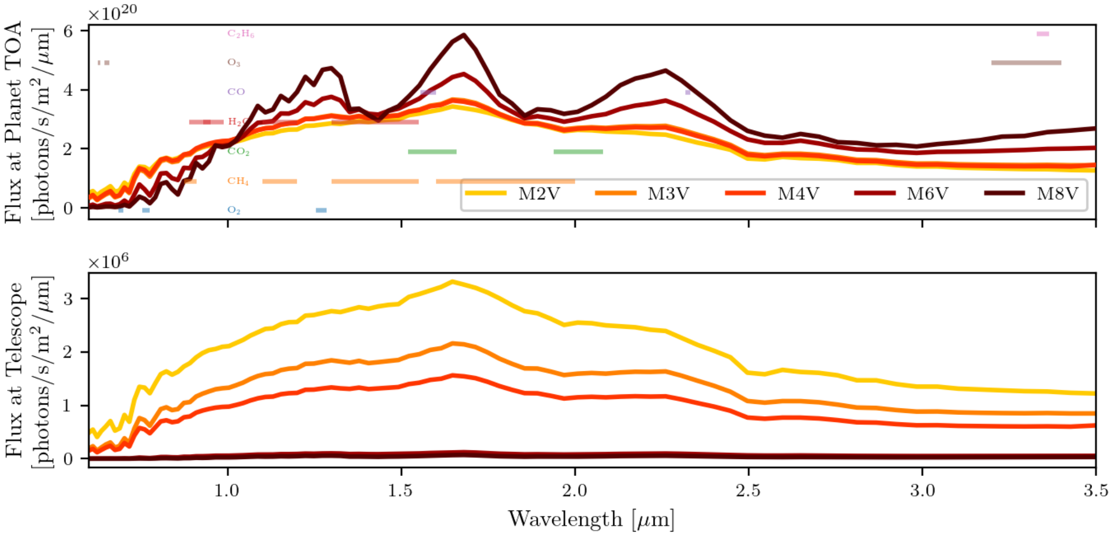

Figure 2.2 **Upper panel:** Spectral energy distributions of the M dwarf host stars in this study incident at the top of the planets' atmospheres. **Lower panel:** The stellar fluxes as seen by an observer 12 pc away. The spectral resolution is binned down to $R = 50$ for clarity. The colored horizontal lines are selected molecular absorption bands we investigate in our planetary atmospheres.

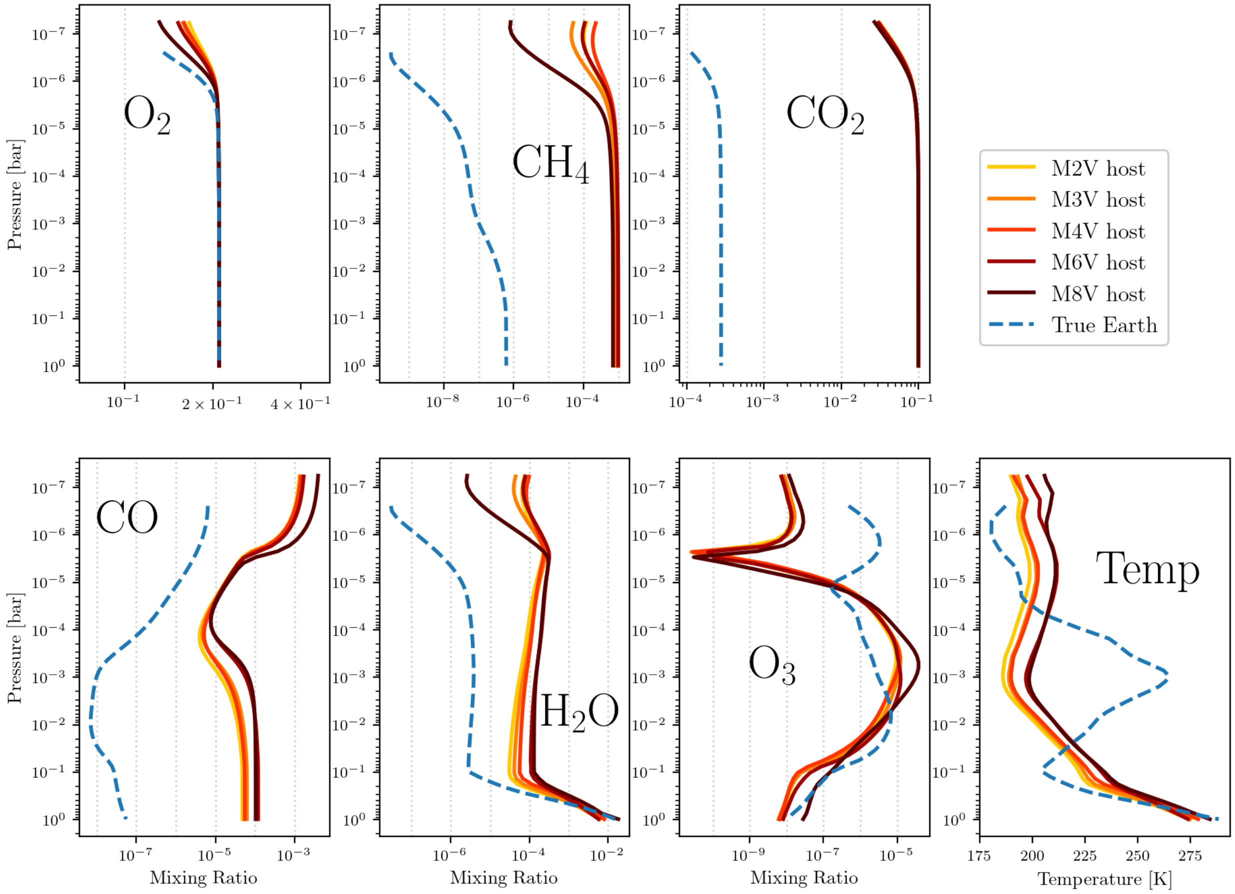

Figure 2.3 Mixing ratios for the major species in the pre-industrial Earth-like (PIE) atmospheres and temperature profiles. Each line represents a self-consistent Earth-like atmosphere orbiting a stellar host. Earlier-type M dwarf hosts are lighter and later-type M dwarf hosts are darker. The dashed blue line represents profiles for the Earth orbiting the Sun for comparison.

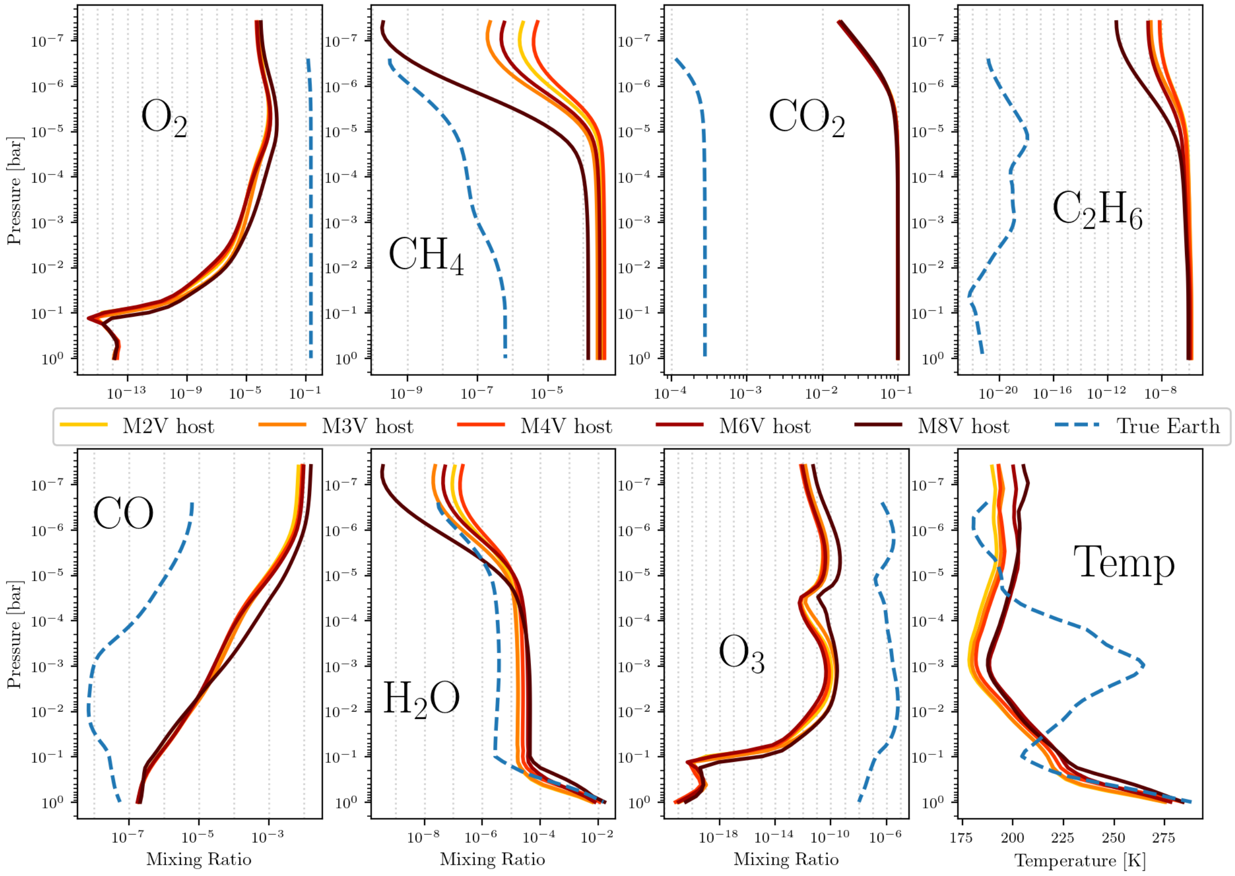

Figure 2.4 Mixing ratios for the major species in the Archean Earth-like (ARE) atmospheres and temperature profiles. Each line represents a self-consistent Earth-like atmosphere orbiting a stellar host. Earlier-type M dwarf hosts are lighter and later-type M dwarf hosts are darker. The dashed blue line represents profiles for the Earth orbiting the Sun for comparison.

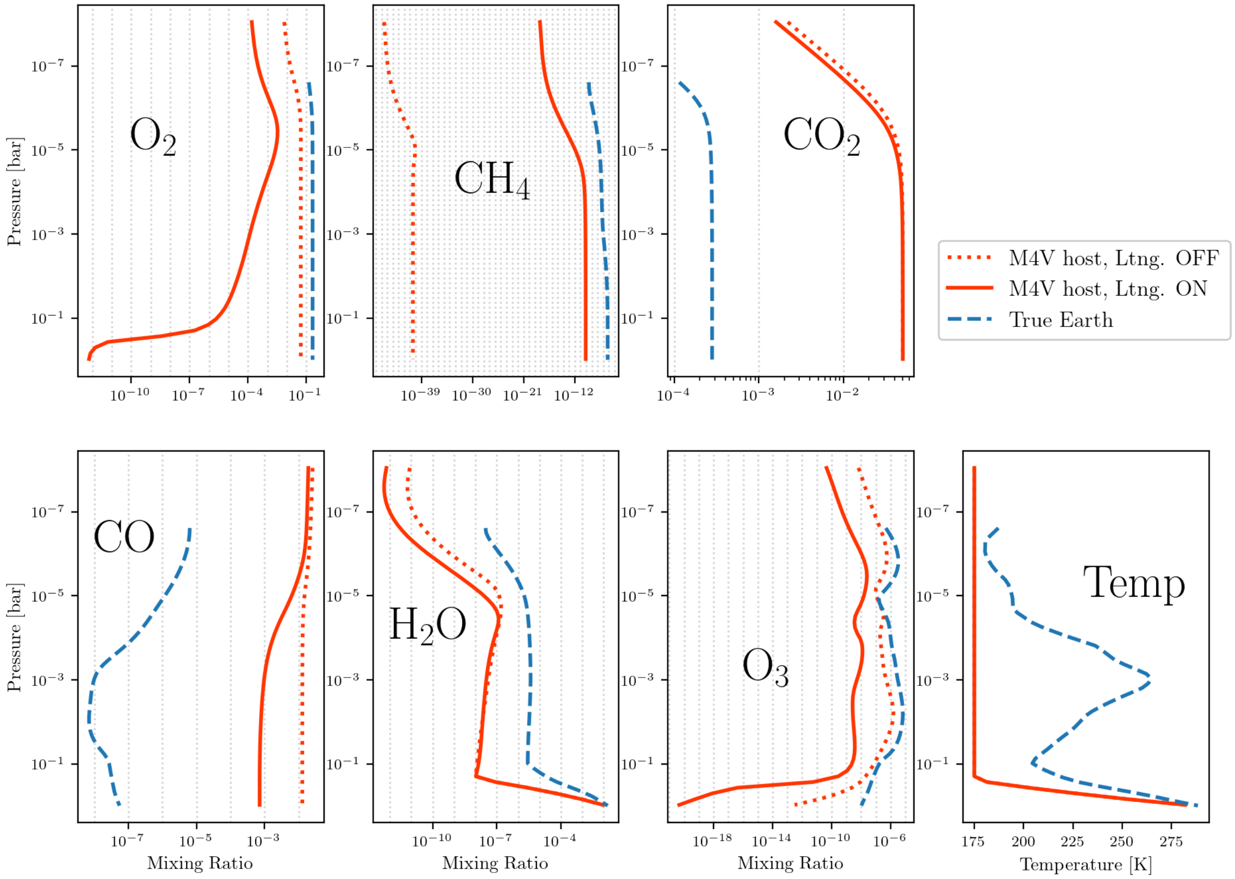

Figure 2.5 Mixing ratios for the major species in the abiotic $O_2$ buildup from $CO_2$ photolysis atmospheres and temperature profiles. The solid and dotted red lines represent profiles for a $CO_2$ photolysis atmosphere with lightning turned on and off, respectively, orbiting an M4V-type stellar host. The dashed blue line represents profiles for the Earth orbiting the Sun for comparison.

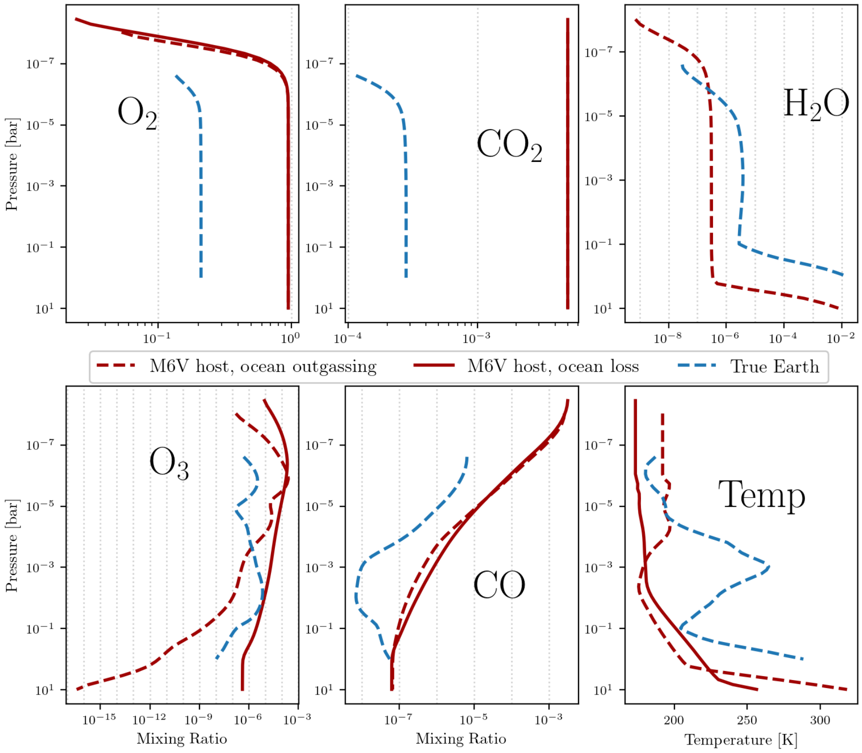

Figure 2.6 Mixing ratios for the major species in the 10-bar $O_2$ ocean outgassing (dashed) and ocean-loss (solid) atmospheres and temperature profiles. The dashed blue line represents profiles for the Earth orbiting the Sun for comparison. There is no $H_2O$ in the ocean-loss atmosphere.

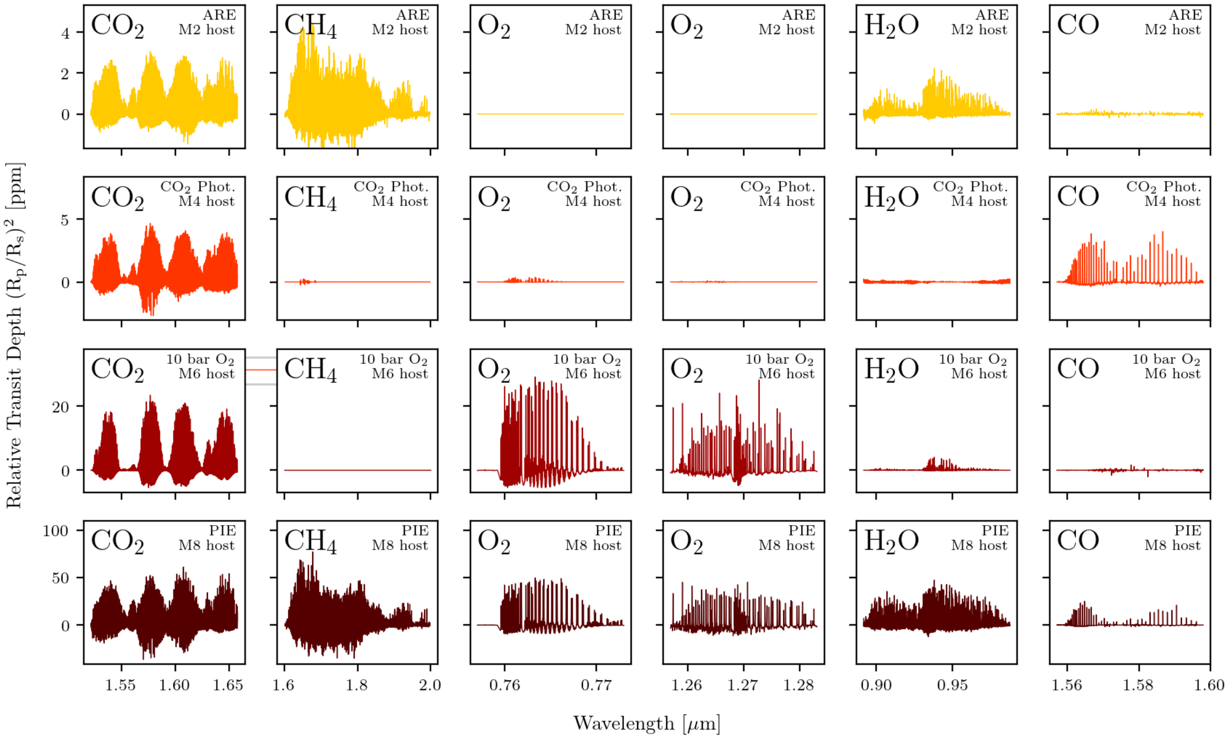

Figure 2.7 Selected molecular bands in this work. Each molecular band is plotted at $R = 100,000$ and is continuum subtracted using a high-pass filter (see Section 2.1). Note the scale in each row: planets transiting later type M dwarf hosts typically have larger relative transit depths than planets transiting early type hosts.

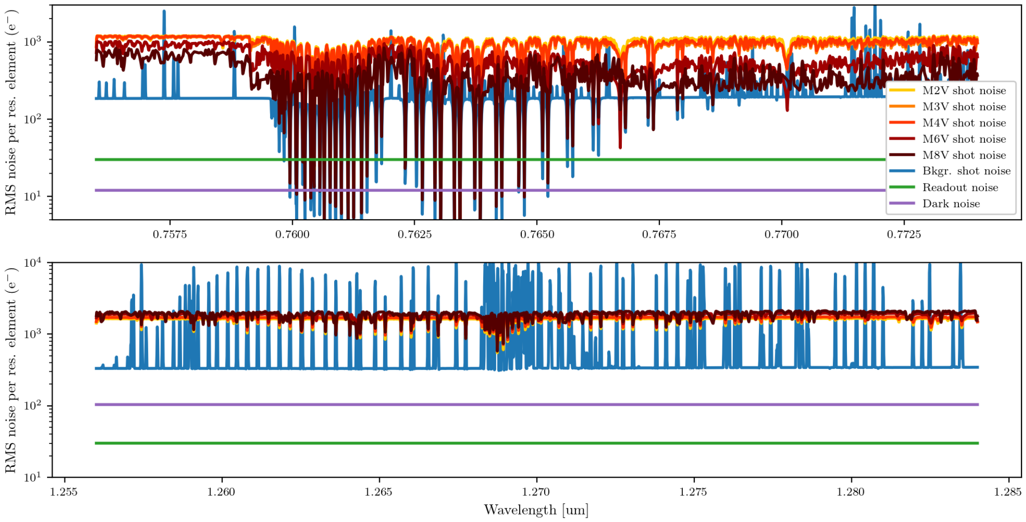

Figure 2.8 Noise sources per resolution element considered in this work for a band in the visible (top panel) and a band in the NIR (bottom panel) for a 2 hr exposure at R = 100,000. The background shot noise is comprised of zodiacal light, telluric emission, airglow, and telescope/instrument thermal emission, and the airglow continuum dominates the background continuum. The shot noise is plotted for all stars at 12 pc, and includes attenuation from the Earth's telluric transmission. Photon (shot) noise from the M2V and M8V stars exceeds the combined readout and dark noise by a factor of 25 and 8, respectively, for the visible, and 12 and 15, respectively, for the NIR, for the generic detectors used in this work described in Section 2.1.2.2.

#### *2.1.1.3 High-resolution spectra*

We calculated high-resolution spectra of our transiting planet atmospheres using SMART, a 1D, line-by-line radiative transfer model (Stamnes et al., 1988; Meadows & Crisp, 1996; Crisp, 1997). SMART calculates the spectra using stellar sources, and solves the radiative transfer equation for each atmospheric constituent in discrete layers in the atmosphere. In each layer, SMART calculates extinction due to vibrational and rotational transitions, and collisionally-induced absorption for each absorbing gas. It also calculates the effects of aerosols, Rayleigh scattering, and wavelength-dependent surface albedo. SMART outputs top-of-atmosphere planetary radiances and transmission spectra, and has been validated for Earth in reflected light at low-resolution in Robinson et al. (2011), and for Earth in transmission at high-resolution in Lustig-Yaeger et al. (2022). We calculated each spectrum at a resolution of $R = 1,000,000$ for both clear and cloudy sky scenarios, which we then convolve with a Gaussian profile to achieve a resolution of $R = 100,000$ for this study. As in López-Morales et al. (2019), we find that increasing the resolution of our spectra to $R = 300,000$ roughly doubles (100% increase) the average line depths for the $O_2$ A-band and NIR band. However, this effect is dependent on the molecular band, and we see different increases in line depth ranging from 50% (O3, 0.65 um) to nearly 200% (CO, 2.3 um). We simulate cloudy-sky scenarios as 50% clear sky, 25% Earth-like cirrus clouds, and 25% and Earth-like stratocumulus clouds for the pre-industrial Earth-like atmospheres. The clouds are assumed to be uniformly-spaced around the planet, and the cirrus and stratocumulus clouds are placed at 0.331 bar and 0.847 bar, respectively. Figure 2.7 show clear-sky high-resolution spectra for selected molecular bands in this study.

### *2.1.2 Simulated observations*

We upgraded an existing, sophisticated noise model, `coronagraph`—which is designed for simulating observations of space-based telescopes (Robinson et al., 2016; Lustig-Yaeger et al., 2019b)—and modified it to produce synthetic observations of ground-based ELTs. Because we are simulating transmission spectra for the ELTs, we turn off the coronagraph mode in our ground-based upgrade of `coronagraph`. To avoid confusion, we hereafter refer to our coronagraph-free version of the `coronagraph` code as the Spectral Planetary ELT Calculator for Terrestrial Retrieval (SPECTR) pipeline[1]. To estimate the wavelength-dependent signal-to-noise ratio for a ground-based observation, we use SPECTR to calculate the incoming photon count from the exoplanet/star system, and the background photon count from zodiacal, exo-zodiacal, telescope, instrument, detector, and atmospheric (telluric) sources.

#### *2.1.2.1 Modeling the Sky*

To simulate ground-based observations, SPECTR has a built-in interface to the Cerro Paranal Advanced Sky Model (SykCalc Noll et al., 2012; Jones et al., 2013), a highly customizable telluric atmosphere model built by the European Southern Observatory (ESO) for observation planning. Within SPECTR, the user can choose parameters that describe the observatory site, season, time, target coordinates, and moon phase/location, which are passed to the SkyCalc command line interface. SkyCalc returns the wavelength-dependent background and telluric transmittance at the native resolution of the instrument. We assume an airmass of 1.2. The background component is comprised of moonlight, starlight, zodiacal light, telluric emission, airglow, and telescope/instrument thermal emission. We find that the dominant component of the background is the airglow continuum, which is comprised of radiation from chemiluminsecent reactions between atmospheric constituents (e.g. Khomich et al., 2008; Kenner & Ogryzlo, 1984) as well as pseudo-continua from many closely spaced molecular lines (e.g. Saran et al., 2011). We use Paranal as our observatory site, with precipitable water vapor of 3.5 mm, and do not include scattered moonlight in these simulations.

---

[1] https://github.com/curriem/spectr

#### *2.1.2.2 Telescope and instrument properties*

We simulate $R = 100,000$ observations for European ELT (E-ELT), Thirty Meter Telescope (TMT), and Giant Magellan Telescope (GMT) configurations, with collecting areas of and 978 $m^2$, 707 $m^2$, and 368 $m^2$, respectively. These collecting areas correspond to a 39 m E-ELT with a central hole to accommodate its secondary mirror[2], a 30 m diameter TMT, and the total expected collecting area of all mirror segments of the GMT[3]. We expect our E-ELT aperture to yield a 1.39x higher flux than our TMT aperture. The required equivalent observation time with our E-ELT configuration is $\sim 30\%$ less than our TMT configuration to yield the same flux. The E-ELT aperture yields a 2.66x higher flux than our GMT aperture, and the required equivalent E-ELT observation time is $\sim 60\%$ less than for the GMT. The ELTs will be equipped with high-resolution spectrometers capable of R = 100,000 in visible and/or near-infrared wavelengths with estimated throughputs of 10%, typical dark current values of 0.0002 $e^-$/pix/s and 0.015 $e^-$/pix/s for the visible and NIR, respectively, and read noise of 3 $e^-$/pix for the E-ELT, TMT, and GMT (Marconi et al., 2022; Mawet et al., 2019; Szentgyorgyi et al., 2014). We use these values for our E-ELT, TMT, and GMT configurations for this study, and assume 100 detector pixels per resolution element. In particular, we note that the term $T$ in Equation 2.1 is the 10% throughput multiplied by the telluric absorption. One can approximate the effect of varying the total efficiency by multiplying our detection significance calculation by the square root of the ratio of a new efficiency and the 10% efficiency we use in our calculations.

We briefly investigate the effect of varying the spectral resolution of our simulated observations by calculating the number of transits required to detect the $O_2$ 1.27 $\mu$m band for a PIE planetary atmosphere transiting M2V–M8V host stars 5 pc away from Earth, and present the results in Figure 2.9. We find that decreasing the spectral resolution to $R = 50,000$ roughly doubles the required number of transits, while increasing the resolu-

---

[2] https://elt.eso.org/about/facts/

[3] https://giantmagellan.org/explore-the-design/

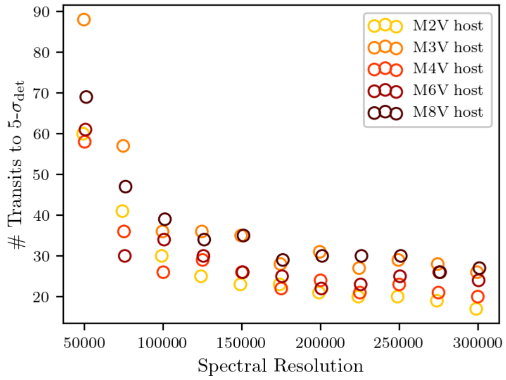

Figure 2.9 Number of transits required to detect the $O_2$ 1.27 $\mu$m band as a function of spectral resolution for a PIE atmospheres transiting M dwarf stars 5 pc away from Earth. We note that these targets at 5 pc do not exist, but we include this for comparison to previous work that uses the 5 pc distance as a metric. The benefits of increasing the spectral resolution are marginal for resolutions greater than $R \sim 150,000$.

tion to $R \geq 150,000$ only marginally decreases the required number of transits. We note that while average line depth roughly doubles when increasing the spectral resolution from $R = 100,000$ to $R = 300,000$, this only translates to a 35% decrease in the number of transits required for a detection, which is consistent with López-Morales et al. (2019). The dominant factor controlling the number of transits required for a detection as a function of resolving power is the average SNR of the resolution elements. Assuming the wavelength range remains constant, an increase in spectral resolution requires an increase in the number of pixels per observation, thus the signal is spread over more pixels, and the average SNR of the individual resolution elements decreases. We expect the other molecular bands to roughly follow this trend, and we look forward to completing a more in-depth analysis in our future work.

#### *2.1.2.3 Synthetic spectra*

Our SPECTR pipeline generates synthetic observations by calculating the incoming photon count from the planetary system for both in-transit and out-of-transit observations, and the background photon count from atmospheric molecular emission, airglow, scattered light, zodiacal light, dark current, and read noise sources. We appropriately Doppler shift the planet spectrum over the course of the transit, and multiply each exposure by the corresponding high-resolution telluric transmittance spectrum obtained from SkyCalc.

The stellar photon count rate in counts per unit time is given by:

$$c_s = TF_s(\lambda)\frac{\lambda}{hc}d\lambda\pi\left(\frac{D}{2}\right)^2 \tag{2.1}$$

where $T$ is the total efficiency of the telescope/instrument/detector system multiplied by the wavelength-dependent telluric absorption, $F_s(\lambda)$ is the stellar flux at the top of Earth's atmosphere, $h$ is the Planck constant, $c$ is the speed of light, $d\lambda$ is the spectral element width, and $D$ is the diameter of the telescope. The stellar photon count rate is scaled to simulate an in-transit observation by multiplying by one minus the wavelength-dependent transit depth:

$$c_{\mathrm{in-transit}} = c_s\left(1-\left(\frac{R_p}{Rs}\right)^2\right) \tag{2.2}$$

The atmospheric molecular emission, airglow, scattered light, zodiacal light backgrounds are calculated using the ESO SkyCalc interface, and the dark current and read noise are taken to be typical quoted values for ELT detectors (see Section 2.1.2.2). The thermal contribution to photon count rate is the sum of thermal emission from Earth's atmosphere and the thermal emission of the telescope and instrument, which we set as standard across both telescope/instrument configurations: 273 K for the telescope mirror and 90 K for the instrument/detector, typical standard values for a high-altitude telescope/instrument setup. The noise sources are shown in Figure 2.8. To minimize the contribution of readout noise to the total noise budget, we fix the exposure time to equal the transit duration for each target. Our planets have relatively short transit durations, and the planetary orbital velocities relative to the host stars are sufficiently small such that any smearing effects on the detector are negligible during the transit.

Finally, we simulate random Poisson noise in our spectra. We add the signal, background, and dark current to obtain total signal for each resolution element, and total shot noise follows by taking the square root of the total signal. Total noise is then the total shot noise and readout noise added in quadrature. We randomly draw values from Poisson distributions defined by the total noise for each resolution element, and add this to our spectra to simulate noise.

We assume all transit spectra in this study to have a system velocity shift of 22 km/s relative to Earth (including all sources of velocity shift) to shift the target spectrum away from the telluric transmission lines. This is within the optimal range for reducing blending between telluric and exoplanet $O_2$ lines at the $0.76\mu m$ absorption feature (Rodler & López-Morales, 2014). A non-optimal Doppler shift for the system may increase blending of the planetary and telluric absorption lines by 50% or more (Rodler & López-Morales, 2014).

#### *2.1.2.4 A note on host star properties*

Modeling how the properties of a host star affect exoplanet characterization is complex and often unique to each individual system, thus we make simplifications to generalize our study. In particular, we leave out the effects of stellar rotation and star spots. We also do not model the effects of stellar or planetary rotation, but we acknowledge that stellar rotation in particular can make stellar line removal more difficult in transmission via the Rossiter-McLaughlin effect (e.g. Brogi et al. (2016)).

While some studies have addressed the possibility of star spots interfering with transit studies (Pont et al., 2007, 2008), Brogi et al. (2016) showed that the appearance of star spots, at least in the scenario of the hot Jupiter HD 189733 b, was negligible due to the small fraction of spectra which include the spot. However, HD 189733 is a K dwarf, and is thus not as active as the class of star we study in this work. In fact, other studies (e.g. Czesla et al., 2009; Désert et al., 2011; Silva-Valio & Lanza, 2011; Bruno et al., 2016) found that both occulted and non-occulted star spots can cause a wavelength-dependent increase or decrease in transit depth, and that in some regions of the spectrum, stellar features can actually be imprinted onto the transmission spectrum (Bruno et al., 2020). This is especially problematic for cool and low-mass stars (e.g. Rackham et al., 2017, 2018; Wakeford et al., 2018), which are known to have $H_2O$ and CO in their spectra (Allard et al., 1997) that can overlap with the spectral lines of identical molecules in the planetary atmosphere. This molecular overlap effect is likely less problematic for $O_2$, $CO_2$, $CH_4$, which are weak or nonexistent in low-mass stellar spectra (Allard et al., 1997). While this potential stellar contamination is a further complication to consider when attempting to observe terrestrial exoplanet atmospheres at high spectral resolution, the specific impact is not yet well constrained, and we currently do not include these effects in our simulations.

### *2.1.3 Telluric line removal*

To remove telluric lines from our spectra, we assume that there exists a "perfect" corresponding out-of-transit observation at the same airmass for each in-transit observation such that the ratio of the in-transit to out-of-transit spectra leaves only the planetary transmission spectrum and noise. We then construct an outlier mask to flag data in areas of extremely low signal-to-noise (e.g. where the telluric transmittance falls to near zero) by performing a running sigma clip with a width of 100 pixels. All values more than $3\sigma$ from the median were flagged and not considered in the cross-correlation analysis. To remove low frequency variations associated with the spectral continuum in the template and observed spectra, we apply a high-pass filter with an arbitrarily chosen bin width of 100 wavelength steps.

However, for real terrestrial exoplanet data, the removal of telluric transmission lines using techniques initially developed for hot Jupiter observations is less likely to be effective, although several other avenues show promise. Although the radial velocity of the planetary system will Doppler shift the planetary lines away from the telluric lines (López-Morales et al., 2019), the high sensitivity required for these observations suggests additional techniques may be needed to refine telluric subtraction. The current state-of-the-art methods for hot Jupiter telluric transmission line removal employ either a principal component analysis (PCA) algorithm (e.g. Brogi et al., 2018), or a radiative transfer model (e.g. Allart et al., 2017) to remove Earth's transmission spectrum. However, for transiting habitable zone terrestrial planets, PCA will be less effective because the planetary velocity shifts during a transit are likely insufficient to effectively isolate the planet spectrum from static telluric lines, resulting in the subtraction of the planet spectrum itself. Therefore, blind analysis techniques like PCA or PCA-like algorithms that do not use existing knowledge of molecular absorption and the Earth's atmospheric properties to subtract tellurics will be less effective for observations of transiting Earth-like planets.

More promising techniques relevant to terrestrial exoplanet observations include applying radiative transfer tools like Molecfit (Smette et al., 2015) or the online TAPAS service (Bertaux et al., 2014) to model the Earth's atmospheric transmission. Molecfit as a telluric line removal tool is demonstrated in Allart et al. (2017), where it is used to fit and subtract the telluric lines down to the noise level in high-resolution observations of water lines in the atmosphere of HD 189733b. More recently, TAPAS has been used on ESPRESSO data of HD 40307 to fit and remove telluric lines in wavelength regions with significant telluric absorption traditionally excluded by precision radial velocity surveys, improving the precision of the resulting stellar spectrum by up to 25% (Ivanova et al., 2023). While using a radiative transfer tool to fit the telluric lines of our synthetic data would be more realistic, here we have chosen to present the ideal case with perfect subtraction; however, we look forward to including a more realistic telluric removal process in future iterations of this work.

### *2.1.4 Cross-correlation and detection significance*

To estimate the detectability of the molecular absorption bands, we employ a cross-correlation technique similar to that described in Brogi et al. (2016) for its sensitivity to line locations, line shapes, and relative line depths, and robustness against small perturbations to the radial velocity due to stellar or planetary processes when applied to real data. With the cross-correlation technique, it is not necessary to identify the precise wavelength position of the band before co-adding the flux. We cross-correlate our simulated transmission spectra with a model template of the molecular absorption band based on the techniques tested and used by similar studies (e.g. Snellen et al., 2010, 2013; Rodler & López-Morales, 2014; Brogi et al., 2016; Serindag & Snellen, 2019; López-Morales et al., 2019; Spring et al., 2022), and report detections as the significance at the expected signal location in the resulting cross-correlation functions.

The cross-correlation technique works by comparing an observed spectrum ($f(n)$) to a range of Doppler-shifted template spectra ($g(n-s)$). We remove the spectral features of molecules other than the one in question from the template spectrum to reduce contamination, which, left in the spectrum, can lead to inaccurate boosts in the detection significance. For each observation–template comparison, the potential match is quantified with a correlation coefficient, where a more positive coefficient indicates a better match. The Doppler velocity of the template spectrum is allowed to vary over ±150 km/s on an evenly spaced grid of 101 elements. For the grid of velocity shifts, $s$, a cross-correlation function $C(s)$ is calculated from the variance of the observed spectrum ($s_f^2$), the variance of the template (model) spectrum ($s_g^2$), and the cross-covariance $R(s)$. To remove low-frequency variations in the spectral continuum, it is crucial to apply a high-pass filter to the model and observed spectra before the variance, cross-covariance, cross-correlation function are calculated to remove low frequency continuum variations. We adopt the notation of Brogi & Line (2019) and define:

$$s_f^2 = \frac{1}{N}\sum_n f^2(n) \tag{2.3}$$

$$s_g^2 = \frac{1}{N}\sum_n g^2(n-s) \tag{2.4}$$

$$R(s) = \frac{1}{N}\sum_n f(n)g(n-s) \tag{2.5}$$

where $n$ is the bin or pixel number, $s$ is a bin or wavelength shift due to the relative velocity, N is the total number of pixels, $f(n)$ is the synthetic observed spectrum, and $g(n-s)$ is the template spectrum with a wavelength shift of $s$. The cross-correlation function is then defined as

$$C(s) = \frac{R(s)}{\sqrt{s_f^2 s_g^2}}. \tag{2.6}$$

This results in a cross-correlation function which peaks at a relative velocity of zero if a signal can be detected through the noise. To estimate the detection significance of the resulting cross-correlation function, we follow the $\chi^2$ analysis of (Brogi et al., 2016): We define a non-detection as zero planet signal and zero correlated noise, such that the corresponding distribution of cross-correlation function values is a Gaussian with a mean of zero. Thus, a non-detection is best fit with a flat line with zero offset. To test for a signal, we compare our cross-correlation function to a flat line with zero offset:

$$\chi^2_{\mathrm{CCF}} = \sum_s \frac{(C(|s| < s_0) - 0)^2}{\sigma^2_{C(|s|>s_0)}}. \tag{2.7}$$

In Equation 2.7, the sum is only calculated for velocity shifts $|s| < s_0$, where $s_0$ is 5 km/s and chosen to reflect the width of a typical cross-correlation peak in this study, to include only values that could correspond to the planet signal, and exclude any aliasing patterns or spurious matches with other spectral features. Similarly, $\sigma^2_{C(|s|>s_0)}$ is the variance excluding possible planet signal. We convert this $\chi^2_{\mathrm{CCF}}$ value to a p-value using the cumulative distribution function of a $\chi^2$ distribution, and finally convert the p-value to a sigma interval using the inverse survival function of a normal distribution to arrive at a measure of how much our cross-correlation function deviates from a Gaussian distribution, $\sigma_{\mathrm{det}}$.

In this detection significance estimation scheme, a non-detection would be consistent with a detection significance of $\sim 1$, which differs from a traditional signal-to-noise ratio non-detection of 0. To confirm this, we calculated the detection significance of a "cross-correlation function" consisting of randomly drawn values from a standard normal distribution. After a million iterations of drawing random CCFs and estimating their detection significances, the median detection significance was 1.04. Therefore, we expect non-detections in our results to have detection significances consistent with 1.04, and this value is seen at a low number of observed transits or for molecules that are challenging to detect in several of our cases in e.g. Figure 3.3. Furthermore, there exists a fundamental upper limit to the detection significance that is unique to each molecular band. Because we estimate detection significance from a cross-correlation function, the largest detection significance possible corresponds to the detection significance of the cross-correlation of the template spectrum and a noiseless observed spectrum. Therefore, instead of obeying a $\sqrt{N_{\text{transits}}}$ trend indefinitely as a traditional signal-to-noise vs. number of transits observed curve would, we expect our detection curves to "saturate" at the detection significance upper limit. Indeed, this trend arises in strong, readily detectable molecular bands in Figure 3.3.

For $N$ transits observed, we integrate $N$ in-transit spectra with random noise and N out-of-transit spectra with random noise, remove the telluric lines via the procedure in Section 2.1.3, and calculate the cross-correlation detection significance. We then repeat this process for 500 iterations. We report the median detection significance with uncertainties corresponding to the standard deviation of the detection significance iterations.

## *2.2 Upgrading SPECTR for ELT Reflected Light Observations*

In this work, we modify the high-resolution, cross-correlation detectability pipeline of Section 2.1 and Currie et al. (2023) to include treatment of non-transiting planets orbiting M dwarf host stars. As input to the detectability pipeline, we use high-resolution ($R \sim 100,000$) spectra of climatically and photochemically self-consistent terrestrial and sub-Neptune planet environments. We simulate observations of these atmospheres for a range of observational and instrumental configurations, and compute cross-correlation functions to search for a range of molecular absorption bands for 1000 realizations of noise. We finally estimate the detection significance for each molecular absorption band as a function of exposure time. Below, we first describe how we generate synthetic planetary spectra for the planets considered here, and then describe the SPECTR observation simulator, including its upgrades, cross-correlation mechanism, and noise sources.

### *2.2.1 Planetary Spectra*

For the terrestrial planetary atmospheres considered in this study, we use a similar suite of previously generated photochemically self-consistent temperature and molecular mixing ratio profiles used in Section 2.1 and Currie et al. (2023), with the addition of a $CO_2/CH_4$ biosignature false positive environment (Prebiotic Earth)(Meadows et al., 2023), and a sub-Neptune type atmosphere (Charnay et al., 2015). These atmospheric profiles are passed to the 1D radiative transfer model SMART (Meadows & Crisp, 1996; Crisp, 1997)to calculate high resolution reflected light spectra, which are subsequently used as input to our cross-correlation detectability pipeline (Section 2.1; Currie et al., 2023).

We consider four distinct classes of terrestrial planet atmospheres in this study, and a sub-Neptune world for comparison. The inhabited environments we consider include the pre-industrial Earth-like (modern Earth with a photosynthetic biosphere and without anthropogenic fluxes) and Archean Earth-like atmospheres from Davis et al. (in prep), both of which have active biospheres. These atmospheres were also used in Chapter 3 and Currie et al. (2023) to test molecular detectability for transiting terrestrial planets, and their atmospheric profiles are plotted in Figures 3 and 4 of Chapter 3 and Currie et al. (2023). These planets are placed in orbit around M2V, M3V, M4V, M6V, or M8V host stars and driven to climate-photochemical equilibrium. We leverage this diversity of atmospheres and stellar hosts to understand how M dwarf host star type may affect the detectability of spectral features in non-transiting terrestrial planets. The compositions of our atmosphere environments are listed in Table 2.5.

We also consider habitable, but uninhabited, biosignature false positive atmospheres that can build up potentially detectable levels of gases that are also generated by life. In this work, we consider a false positive scenario for both the pre-industrial and Archean Earth like atmospheres. For our pre-industrial photosynthetic biosphere false positive, we use the high-$O_2$, ocean retaining planet from Meadows et al. (2018). A planet that undergoes significant ocean loss when its younger star is more luminous, could build up tens to 1000s of bars of

Table 2.5. Composition of terrestrial atmospheric cases

| Atmosphere template | Surface | Atmospheric gases | Surface Temperature [K] |
|---|---|---|---|
| Pre-industrial Earth | Earth Composite | 68% $N_2$, 21% $O_2$, 10% $CO_2$, 0.2% $H_2O$, 700-800 ppm $CH_4$, trace $O_3$, CO | 275 |
| Archean Earth | Earth no vegetation | 78% $N_2$, 10% $CO_2$, 0.2% $H_2O$, 100-400 ppm $CH_4$, 2 ppm $C_2H_6$, trace $O_2$, $O_3$, CO | 275 |
| Ocean Loss | Earth no vegetation | 95% $O_2$, 4% $N_2$, 0.5% $CO_2$, 0.3% $H_2O$, trace $O_3$, CO, $NO_2$ | 318 |
| Prebiotic Earth* | Earth no vegetation | 89% $N_2$, 1.9% $CO_2$, 4.4% CO, 4.8% $H_2$, 14 ppm $CH_4$, trace $O_2$, $H_2O$ | 262 |

*low redox volcanism, 200× enhanced

abiotic $O_2$ via the photolysis of evaporated $H_2O$ and the subsequent loss of hydrogen to space (Luger & Barnes, 2015; Schaefer et al., 2016; Meadows et al., 2018; Gialluca et al., 2024). For a false positive for the $CO_2/CH_4$ biosignature we use the modeled version of a prebiotic Earth with enhanced volcanic outgassing from a more reducing mantle from Meadows et al. (2023). In this scenario, both $CO_2$ and abiotic $CH_4$ are volcanically outgassed, and build up in the atmosphere (Krissansen-Totton et al., 2018b; Meadows et al., 2023).

For comparison, we also consider a sub-Neptune type atmosphere in thermochemical equilibrium, as calculated by Charnay et al. (2015) for GJ 1214 b. Figure 2.10 shows the molecular and temperature vertical profiles for the sub-Neptune atmosphere. The GJ 1214 b atmosphere is a significantly reducing atmosphere, containing high levels of $H_2$ and $NH_3$, as well as molecules that are found in terrestrial atmospheres, including $CH_4$, $CO_2$, and $H_2O$. The molecular bands we study are listed in Table 2.7. We note that this planet is closer to its star than the habitable zone, with an equilibrium temperature close to 500K (Figure 2.10)

Planet and host star properties are given in Table 2.6. For the M dwarf terrestrial planets, we use the same stellar spectra as in Section 2.1 and Currie et al. (2023), which also includes

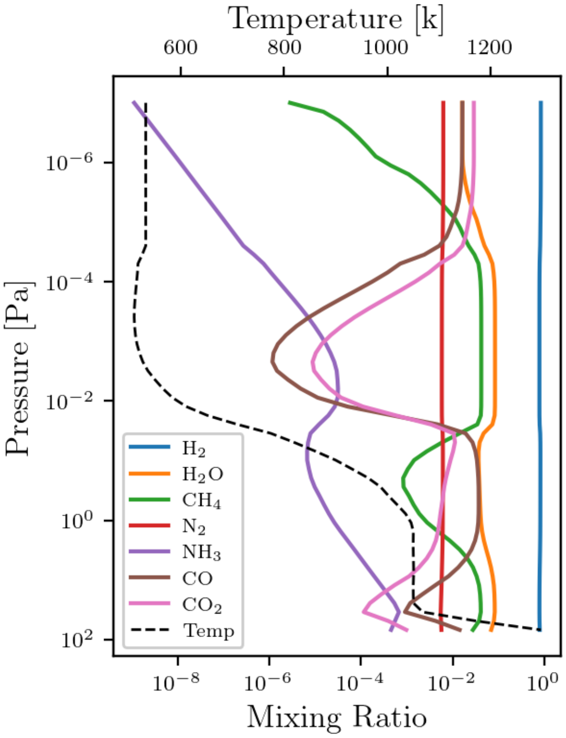

Figure 2.10 Mixing ratios for the major molecular species in the sub-Neptune atmosphere, and the atmospheric temperature profile.

Table 2.6. Host star and planetary companion properties for the terrestrial atmospheres in this study

| | M2V host | M3V host | M4V host | M6V host | M8V host |
|---|---|---|---|---|---|
| $R_*$ | $0.499^a$ | $0.464^b$ | $0.376^c$ | $0.141^d$ | $0.114^e$ |
| $m_I$ (5pc) | 6.2 | 6.8 | 7.1 | 10.7 | 12.2 |
| $m_J$ (5pc) | 5.0 | 5.4 | 7.1 | 10.7 | 12.2 |
| $R_p$ | 1 | 1 | 1 | 1 | 1 |
| P [day] | 48 | 33 | 29 | 6.4 | 6.0 |
| a [AU] | 0.24 | 0.19 | 0.16 | 0.041 | 0.027 |

References. — [a]Houdebine (2010), [b]Torres (2007), [c]von Braun et al. (2014), [d]Bonfils et al. (2005), [e]Filippazzo et al. (2015)

Table 2.7. Molecular bands explored for the atmospheres in this study

| | Molecule | Bands [$\mu m$] |
|---|---|---|
| Terrestrial | $O_2$ | 0.69, 0.76, 1.27 |
| | $CH_4$ | 0.89, 1.1, 1.3, 1.6 |
| | $CO_2$ | 1.59, 2.0 |
| | $H_2O$ | 0.94, 1.1, 1.3 |
| | $O_3$ | 0.63, 0.65, 3.2 |
| | CO | 1.55, 2.3 |
| Sub-Neptune | $CH_4$ | 0.89, 1.1, 1.3, 1.6 |
| | $CO_2$ | 1.59, 2.0 |
| | CO | 1.55, 2.3 |
| | $H_2O$ | 0.94, 1.1, 1.3 |
| | $H_2$ | 0.78, 1.2 |
| | $NH_3$ | 1.43, 1.9, 2.15 |

a more detailed description and figures related to the planetary and stellar parameters. In summary, for each spectral type, we use publicly available synthetic high-resolution stellar spectra for the stars GJ832, GJ436, GJ876, Proxima Centauri, and TRAPPIST-1 (Peacock et al. (2019a,b, 2020), Davis et al. in prep.), serving as analog examples for M2V, M3V, M4V, M6V, and M8V dwarf stars, respectively. To simulate habitable zone targets, the planet is placed at an orbital radius such that it receives 0.66 times the irradiance that Earth receives, which in the M6V example is similar to the radiation received by Proxima Centauri b Anglada-Escudé et al. (2016). In the GJ 1214 b case, we assume the planet has a radius of $\sim 2.68$ Earth radii, and a semi major axis of 0.0143 au (Charbonneau et al., 2009).

After compiling our library of terrestrial planet atmospheres, we calculate high-resolution reflectance spectra of our planet atmospheres using LBLABC/SMART, a 1D, line-by-line radiative transfer model (Stamnes et al., 1988; Meadows & Crisp, 1996; Crisp, 1997). LBLABC calculates the absorption coefficients for each molecule in the atmosphere, then SMART calculates the optical properties of the atmosphere at a given wavelength and atmospheric layer. In each layer of the atmosphere, SMART calculates extinction due to vibrational and rotational transitions, and collisionally-induced absorption for each absorbing gas. It also calculates the effects of aerosols, Rayleigh scattering, and wavelength-dependent surface albedo. SMART outputs top-of-atmosphere planetary radiances and transmission spectra, and has been validated for Earth in reflected light at low-resolution in Robinson et al. (2011), and for Earth in transmission at high-resolution in Lustig-Yaeger et al. (2022). We calculated each spectrum at a resolution of $R = 1,000,000$ and convolved with a Gaussian profile to achieve a spectral resolution of $R = 100,000$ for this study.

### *2.2.2 Synthesizing Observations with SPECTR*

We convert our high-resolution planetary spectra into synthetic observations using the Spectral Planetary ELT Calculator for Terrestrial Retrieval (SPECTR) detectability pipeline, which is described in detail in Chapter 3 and Currie et al. (2023). SPECTR is a comprehensive, sophisticated noise model for ground-based telescopes and instrumentation that is

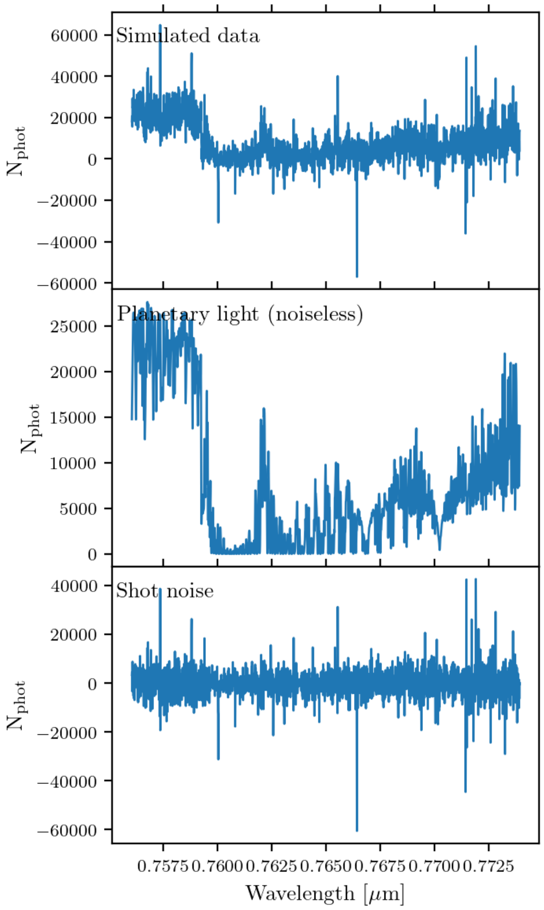

Figure 2.11 Example of simulated data for a 1000 hour observation of the $O_2$ A-band (upper). The simulated data is constructed with two components, the light reflected from the planet and the shot noise, plotted in the middle and lower panels, respectively.

based on the `coronagraph` noise model for space-based telescopes (Robinson et al., 2016; Lustig-Yaeger et al., 2019b). SPECTR takes high resolution spectra as input, adds the appropriate noise associated with user-specified observing parameters as well as the effects of the Earth's telluric contamination, and finally applies a cross-correlation analysis to determine the detectability of spectral features.

#### *2.2.2.1 Upgrading SPECTR to simulate reflected light observations*

SPECTR was initially developed to simulate transit transmission spectroscopy (Chapter 3; Currie et al., 2023), and in this work, we have developed new features to upgrade SPECTR with the capability to make detectability estimates for non-transiting planets in reflected light. We now provide a simplistic stellar suppression model for high-contrast imaging by allowing the user to multiply the stellar light by a specified contrast value, $C$, which parameterizes the level of stellar suppression for a given observational configuration, as in e.g. Wang et al. (2017); Hawker & Parry (2019); Zhang et al. (2023). We note that this is a simplistic way to model contrast, as this value does not depend on wavelength. To support reflected light simulations, the code has been modified to calculate the planet's observable illumination fraction as a function of viewing geometry, taking into account system orientation and the planet's phase. The detectability of the molecules in the planetary atmosphere is also dependent on the its radial velocity (Section 4.2.2.2). This upgrade is necessary because, unlike a transiting planet, a non-transiting planet can be observed at the range of positions in its orbital path that is not limited by inner working angle constraints. SPECTR calculates the planet's RV according to the observing geometry using the following equation:

$$\mathrm{RV}_p = K_p(\cos(\phi + \omega) + e\cos(w)), \tag{2.8}$$

where $\mathrm{RV}_p$ is the planetary RV, $K_p$ is the planetary semi-amplitude, $\phi$ is the planetary phase, $\omega$ is the argument of periastron, and $e$ is the orbital eccentricity. The planetary semi-amplitude encodes inclination ($i$), orbital radius ($a$), and orbital period ($P$) and is given by

$$K_p = 2\pi \frac{a \sin(i)}{P\sqrt{1-e^2}}. \tag{2.9}$$

For this work, we assume the planet is on a circular orbit aligned with the midplane of the host star where $e$ is 0 and $\omega$ is 90°; however, we included functionality in SPECTR to model eccentric orbits for future work.

#### *2.2.2.2 Observational assumptions*

Because we are testing the relative detectability of molecular features, and not the efficiency of instrumentation or telluric removal algorithms, we make several simplifications to our observational configuration. We assume that all observations occur at the planet's maximum separation (quadrature). For telluric line removal, we assume that the Earth's telluric contribution to the spectrum is known (Section 2.2.2.3) and can thus be removed from the data via a cross-correlation analysis between the template spectrum and the known telluric transmittance (Section 2.2.3.1). Additionally, we assume shot noise only for the simulated spectra. We note that these assumptions result in optimistic detectability estimates, and quoted observation times should be interpreted as lower limits.

We also do not take into account whether the angular separation of the planet and star is sufficient to avoid inner working angle (IWA) constraints in the imaging instrumentation, but for the nearby targets discussed in this work, that is unlikely to be an issue for the shorter wavelength bands we target. One of the top-level requirements of the RISTRETTO instrument concept on the VLT is that it have an IWA of $\sim 2\lambda/D$ (Lovis et al., 2022). While the final specifications of the ELT instruments are not yet known, if they are designed to achieve a similar IWA requirement as RISTRETTO the typical angular separation limit as a function of wavelength will be $\sim 5-20$ mas in the 0.5–2.0 $\mu$m wavelength range for the E-ELT's 39 m diameter. The nearby (1.3 pc) Proxima Centauri b target, which orbits an M6V star, would have the entire 0.5–2.0 $\mu$m wavelength range accessible near quadrature (Figure 2.12), but planets in the habitable zones of late-type M dwarf targets farther away

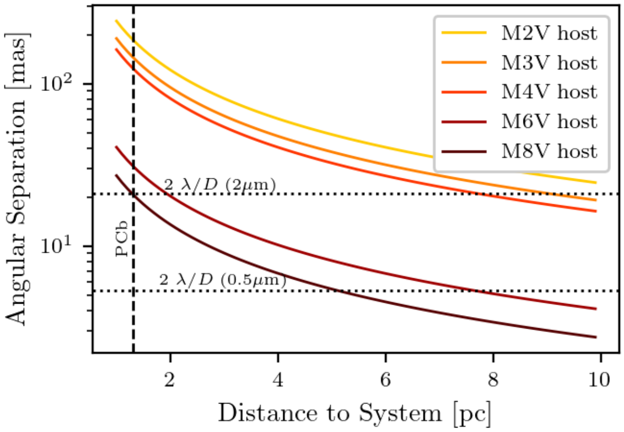

Figure 2.12 Angular separation at quadrature as a function of distance to the system for planets receiving 67% of Earth's instellation in the habitable zones of a range of host star types. The habitable zones of earlier type M-dwarfs reside at larger orbital radii than later type systems, thus are less affected by observational configurations limited by coronagraphic IWA.

(e.g. GJ 1061 d and GJ 1002 b/c at $\sim$ 4pc) may become challenging because the longer wavelength molecular bands will not be accessible. For example, the 1.6 $\mu$m bands will begin to become inaccessible at a distance of $\sim$ 2.5 and 1.6 pc for the M6V and M8V hosts, respectively (Figure 2.12). However, we may not be as limited by IWA constraints when observing planets orbiting early type M dwarfs, whose habitable zones are farther from the star— a planet in the habitable zone of an M4V star may be accessible in the 0.5–2.0 $\mu$m wavelength range out to $\sim$ 7pc, and out to $\sim$ 10pc for an M2V planet. We plot the angular separations for our planets as a function of distance in Figure 2.12 for comparison with future instrument design specifications.

#### *2.2.2.3 Telluric Contamination and Noise Sources*

To simulate sources of noise and signal attenuation associated with the sky and background, SPECTR interfaces with the Cerro Paranal Advanced Sky Model (SkyCalc Noll et al., 2012;

Jones et al., 2013) to incorporate signal extinction due to telluric spectral contamination into our simulated observations. For all telescope configurations considered here, we use Paranal as our observatory site for all three ELTs simulated (see below), as a proxy for the similar dry, high altitude sites identified for the ELTs. We assume a precipitable water vapor column of 3.5 mm, and do not include scattered moonlight.

We simulate high spectral resolution observations for European ELT (E-ELT), Thirty Meter Telescope (TMT), and Giant Magellan Telescope (GMT) configurations, with collecting areas of and 978 $m^2$, 707 $m^2$, and 368 $m^2$, respectively. These collecting areas correspond to a 39 m E-ELT with a central hole to accommodate its secondary mirror[4], a 30 m diameter TMT, and the total expected collecting area of all mirror segments of the GMT[5]. The ELTs will be equipped with high-resolution spectrometers capable of R $\sim$ 100,000 in visible and/or near-infrared wavelengths with estimated throughputs of 10%, typical dark current values of 0.0002 $e^-$/pix/s and 0.015 $e^-$/pix/s for the visible and NIR, respectively, and read noise of 3 $e^-$/pix (Szentgyorgyi et al., 2014, GMT) (Marconi et al., 2022, E-ELT) (Mawet et al., 2019, TMT). We use these values for our E-ELT, TMT, and GMT configurations for this study, and assume 10 detector pixels per resolution element, which is on the order of magnitude for the default value of the E-ELT ANDES Exposure Time Calculator[6]. The observation is synthesized using the following equation:

$$\text{data} = c_p + \mathcal{N}(0,1)\sqrt{c_p + c_s + c_n}, \tag{2.10}$$

where $c_p$ and $c_s$ are the planet and stellar photon counts observed by the telescope, and $c_n$ encompasses the sky background and detector noise contributions outlined above. See Chapter 3 or Currie et al. (2023) for a more detailed description of how SPECTR handles $F_n$. Examples of our simulated data, planetary light, and shot noise are plotted in Figure 2.11.

---

[4] `https://elt.eso.org/about/facts/`

[5] `https://giantmagellan.org/explore-the-design/`

[6] `http://tirgo.arcetri.inaf.it/nicoletta/etc_andes_sn_com.html`

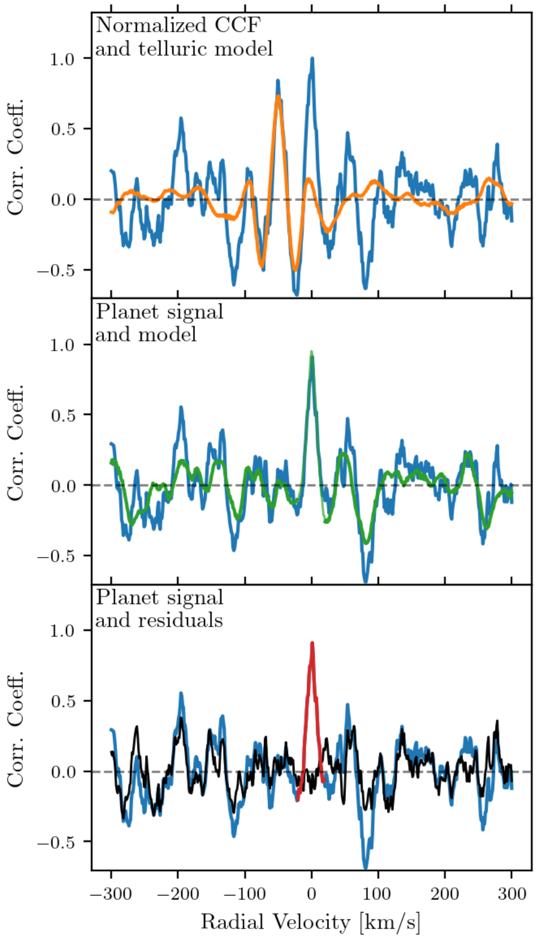

Figure 2.13 Stages of cross-correlation analysis, including telluric line removal (upper), alias detrending (middle), and S/N estimation (lower). The data cross-correlation function (CCF) is shown in blue, and the model telluric and planet CCFs are in orange and green, respectively. The upper panel shows the telluric CCF fit to the raw data CCF, which is subtracted off to remove the tellurics from the observation. The middle panel shows the telluric-subtracted data CCF as well as the planetary model CCF, which is used for detrending the aliasing patterns. The lower panel shows the detrended CCF residuals in black and the planetary signal in red. The S/N is calculated by dividing the maximum signal coefficient by the standard deviation of the detrended CCF residuals.

### *2.2.3 Cross-correlation Analysis*

To estimate the detectability of the molecular absorption bands in our simulated data, we employ a cross-correlation technique similar to that described in Brogi et al. (2016). This technique includes sensitivity to line locations, line shapes, relative line depths, and robustness against small perturbations to the radial velocity due to stellar or planetary processes when applied to real data. We cross-correlate our simulated reflected light spectra with a model template of the molecular absorption band based on the techniques tested and used by similar studies (e.g. Snellen et al., 2010, 2013; Rodler & López-Morales, 2014; Brogi et al., 2016; Serindag & Snellen, 2019; López-Morales et al., 2019; Spring et al., 2022; Currie et al., 2023) or Chapter 3 of this work, and report detections as the significance at the expected signal location in the resulting cross-correlation functions.

To reduce contamination from other spectral features within the observed wavelength range during the cross-correlation, we use a model template spectrum containing only the molecular species of interest, even though the simulated data will include features from all species modeled in the atmosphere. This reduces contamination in the cross-correlation function and extracted S/N measurement. The Doppler velocity of the template spectrum is allowed to vary over ±300 km/s on an evenly spaced grid of 301 elements.

#### *2.2.3.1 Telluric line removal*

Because we make the simplistic assumption that all observations occur at quadrature, it is straightforward to directly remove telluric line contamination from the raw cross-correlation function of the data itself. This is achieved by first cross-correlating our model template spectrum with the telluric line SkyCalc model assumed for the observations, resulting in a telluric model cross-correlation function. We then fit this telluric model CCF to the raw data CCF, and subtract the telluric contribution from the data CCF. This process is illustrated in the top panel of Figure 2.13, and the residual telluric-free data CCF is plotted in blue in the middle panel.

However, we note that in a realistic observing scenario, more advanced techniques will be employed to remove telluric contamination because the planet will not be stationary for the duration of the observation when it moves along a finite portion of its orbit. These methods will separate the planetary signal from the stationary telluric lines as the planet moves along its orbital path using PCA techniques (e.g. Brogi et al., 2018), or by modeling the atmospheric contamination itself (e.g. Allart et al., 2017; Smette et al., 2015; Bertaux et al., 2014). More recent advancements show that removing tellurics on a sub-pixel level may also be possible with increased spectral resolution and knowledge of the stellar spectrum (Cheverall & Madhusudhan, 2024). In this work, we have opted to simplify telluric contamination and removal to focus on the relative detectability of molecular features, and do not explore these advanced techniques.

#### *2.2.3.2 Alias Detrending*

The off-peak values of cross-correlation functions include predictable patterns due to the structure of the molecular band that can introduce systematic noise into the cross-correlation S/N estimate (e.g. Wang et al., 2017; Hawker & Parry, 2019; Currie et al., 2023). A common practice to reduce the effect of these patterns is to apply a high-pass filter to flatten the off-peak CCF coefficients (e.g. Hawker & Parry, 2019; Currie et al., 2023). However, the filter size that optimally reduces these effects can vary with observation, and may be unknown. In this work, we instead use our knowledge of the model spectrum to predict the shape of the aliasing pattern by cross-correlating our single molecule template spectrum with a noiseless model of the planetary spectrum that includes all molecules. In a similar process to the telluric removal step (Section 2.2.3.1), this planetary model CCF is then fit and subtracted from the observed data CCF, which leaves a set of residuals, sans aliasing pattern. This process is shown in the middle and lower panels of Figure 2.13, where the green CCF is the planetary model CCF, and the black curve shows the detrended residuals. We use the standard deviation of the off-peak detrended residuals as an estimate for noise in the CCF S/N calculation (Section 2.2.3.3).

#### *2.2.3.3 S/N estimation*

Finally, we measure the S/N of the telluric-free, detrended cross-correlation function by dividing the correlation coefficient at 0 km/s (red region in the lower panel of Figure 2.13) by the standard deviation of the detrended residuals (black CCF in the lower panel of Figure 2.13). For N hours observed, we integrate N hours of data with random noise, and calculate the cross-correlation detection significance. We then repeat this process for 1000 iterations, enough to ensure the median S/N changes by $< 1\%$ with additional iterations. We report the median detection significance for a range of observational scenarios in Section 4.2.

## 2.3 Implementing a High-Resolution Cross-correlation Spectroscopy Retrieval Framework

To test our ability to retrieve the abundance of $O_2$ in simulated ELT observations of terrestrial atmospheres, we upgraded an existing terrestrial planet retrieval model (Lustig-Yaeger et al., 2023a) to include the capability to analyze multi-epoch high-resolution (R∼100,000) spectra. Below, we describe the experiments we selected to run, our process for simulating the data, the upgrades to the retrieval framework, and the application of the retrieval framework to our simulated data.

### *2.3.1 Planetary Atmospheres and System Properties*

In this work, we explore the accuracy with which we can potentially retrieve the abundance of $O_2$ in a selection of terrestrial exoplanetary atmospheres that are representative of biological, uninhabitable and false positive atmospheres. We consider a total of five terrestrial exoplanet atmospheres orbiting in the habitable zone of Proxima Centauri with levels of $O_2$ ranging from 1% to 21% in a 1 bar atmosphere (biological/false positive), 50% in a 1 bar atmosphere (uninhabitable) and 95% in a 10 bar atmosphere (false positive) (Figure 2.14 and Table 2.8). We choose these $O_2$ mixing ratios to sample the plausible range of $O_2$ abundances due to both abiotic and biological $O_2$ generation mechanisms working in terrestrial environments, and to test the limits of our ability to measure $O_2$ abundances with the ELTs

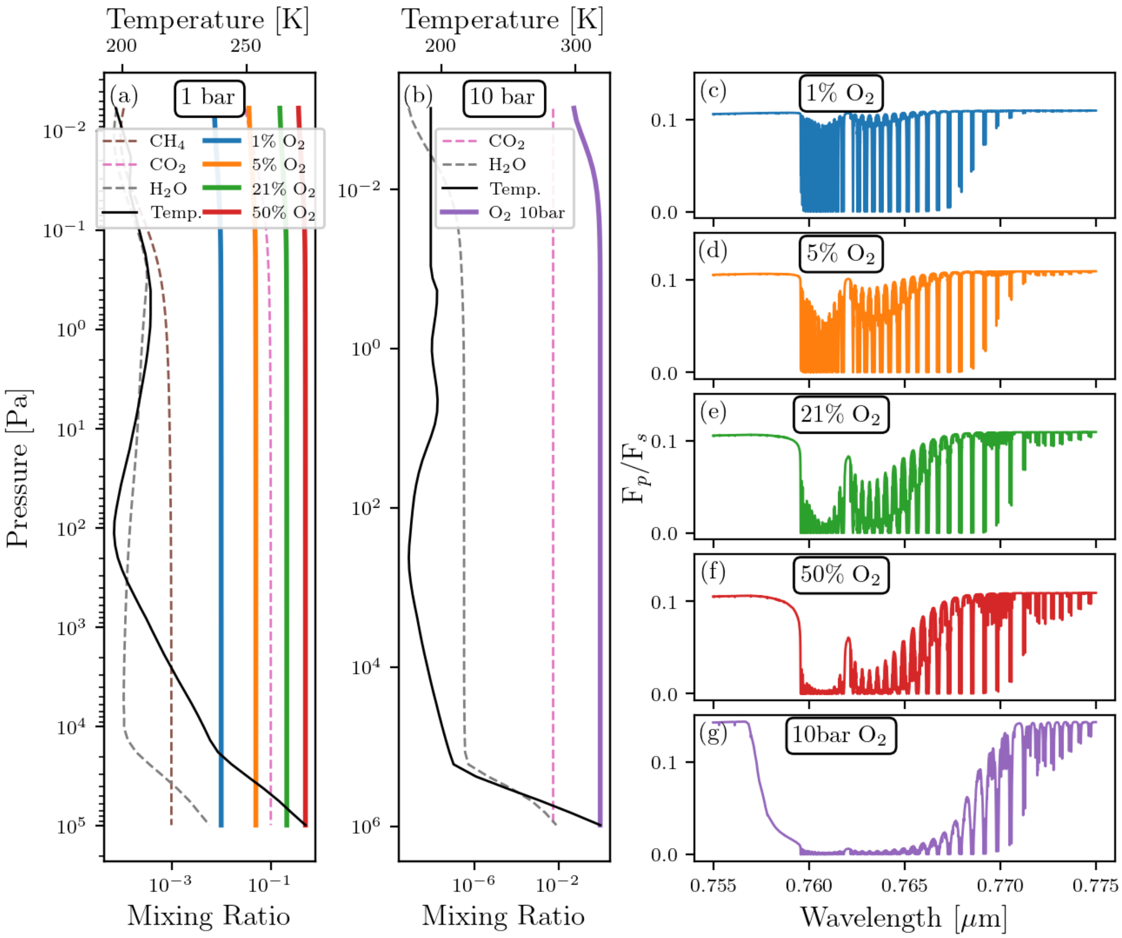

Figure 2.14 Molecular mixing ratios, temperature–pressure profiles, and spectra of the $O_2$ 0.76 $\mu$m band for the atmospheres considered in this study. The 1 bar atmosphere profiles (a) show 1, 5, 21, and 50 % $O_2$ in bold curves, with the corresponding spectra shown in the same color in panels c–f. The mixing ratio profiles for $CH_4$, $CO_2$, and $H_2O$ remain constant with varying $O_2$, and the atmospheres are filled with enough $N_2$ to create a 1 bar surface pressure. The 10 bar atmosphere (panel b) contains $CO_2$, $H_2O$, and nearly 10 bars of $O_2$; the corresponding spectrum is shown in panel g. As more $O_2$ is added to the atmosphere, the $O_2$ absorption spectrum becomes saturated, potentially masking high-resolution spectral features that may be critical for $O_2$ detection.

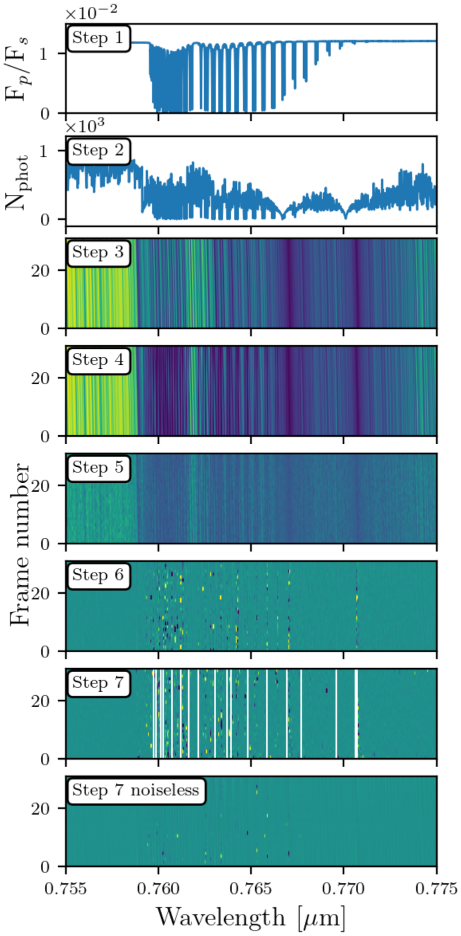

Figure 2.15 Steps for simulating and processing ELT spectra of a terrestrial exoplanet atmosphere. After calculating the high-resolution spectrum (Step 1) and the number of planetary photons that hit the detector (Step 2), we simulate a multi-epoch observation of the planetary spectrum by Doppler shifting the spectrum to realistic radial velocities over the course of an observation (Step 3). Next we simulate telluric attenuation (Step 4) and add noise (Step 5). Finally, we remove the tellurics (Step 6) and flag noisy spectral channels (Step 7). The Step 7 spectra are then analyzed by our retrieval framework. We show a noiseless version of this data simulation pipeline in the final panel. We describe each step in detail in Section 2.3.2. We note that these panels show a small snippet of the full spectrum for illustrative purposes, but this process is performed on the full 0.5–2.0 $\mu$m spectrum.

for the nearest potentially terrestrial exoplanet target. Earth's atmosphere through time has undergone fluctuations in its $O_2$ abundance, ranging from a trace gas in the Archean Eon (Catling & Zahnle, 2020), to $1 - 21\%$ in the post-Archean to modern Earth atmosphere (e.g. Lyons et al., 2014). Additionally, theoretical studies have predicted that $O_2$ can be generated abiotically via $CO_2$ photolysis, but this results in only trace $O_2$ abundances $< 0.4\%$(e.g. Ranjan et al., 2023). We also consider a photochemically self-consistent 10 bar atmosphere with a 95% $O_2$ mixing ratio (Meadows et al., 2018) to simulate the outcome of an ocean loss scenario (Luger & Barnes, 2015; Tian, 2015), where $H_2O$ can be photolyzed to produce significant $O_2$, including $O_2$–$O_2$ collisionally induced absorption that can suppress the high-resolution structure of the $O_2$ bands (Leung et al., 2020). The temperature profiles, molecular abundances, and spectra for the atmospheres we consider in this work are plotted in Figure 2.14.

Since we are examining only the $O_2$ band, we start with a photochemically self-consistent Earth-like atmosphere, and scale the $O_2$ profile as needed. Specifically, we use a template of a photochemically self-consistent pre-industrial Earth-like atmosphere (with 21% $O_2$) calculated by (Davis et al. in prep.), and we create three additional atmospheres with 1%, 5%, and 50% $O_2$ mixing ratios for a 1 bar atmosphere by scaling the $O_2$ profile appropriately. We note that these atmospheres are not photochemically self-consistent with the Proxima Centauri host star spectrum— as altering only the $O_2$ concentration will likely affect the photochemically dependent $O_3$ concentration (Grenfell et al., 2007). However, this will have negligible effects on the $O_2$ absorption spectrum because the $O_3$ spectral features are outside the range of the $O_2$ spectral features we are investigating in this work. We also assume the altered $O_2$ profiles remain evenly mixed, which is reasonable because the modern Earth lacks significant sinks that allow the $O_2$ profile to be evenly mixed (e.g. Lyons et al., 2014; Meadows, 2017).

We assume that each planet is Earth-like in size and mass, and that the planet orbits in the habitable zone of Proxima Centauri at an orbital radius of 0.049 au (the location of Proxima Centauri b), orbital period of 12 days, and receives 66% of the insolation that Earth

Table 2.8. Atmospheric test cases

| | 1% $O_2$ | 5% $O_2$ | 21% $O_2$ | 50% $O_2$ | 95% $O_2$ |
|---|---|---|---|---|---|
| $O_2$ Mixing Ratio | 0.01 | 0.05 | 0.21 | 0.5 | 0.95 |
| Surface Pressure | 1 bar | 1 bar | 1 bar | 1 bar | 10 bar |

receives (Anglada-Escudé et al., 2016). We use realistic literature values for the properties of the Proxima Centauri system, including a distance of 1.3 pc from Earth Anglada-Escudé et al. (2016), a system radial velocity of -22 km/s Kervella et al. (2017), stellar radius of 0.15 $R_\odot$ (Kervella et al., 2017), and stellar mass of 0.12 $M_\odot$ (Kervella et al., 2017). Because the Proxima Centauri system does not have a well known system inclination, we assume an inclination of 60° as in Vaughan et al. (2024); this is statistically the median inclination for stellar systems of unknown orientation. For the stellar spectrum, we use the HAZMAT high-resolution Proxima Centauri spectrum calculated by Davis et al. (in prep.).

### *2.3.2 Data simulation*

Following the prescription of Brogi & Line (2019), we simulate our ELT data in a series of discrete steps, outlined as follows:

**Step 1:** Compute spectra

**Step 2:** Calculate photon counts

**Step 3:** Simulate multi-epoch observations

**Step 4:** Include telluric extinction

**Step 5:** Add noise

**Step 6:** Normalize spectra and remove tellurics

**Step 7:** Mask noisy spectral channels

Each step is described in the following sections and illustrated in Figure 2.15.

#### *2.3.2.1* ***Step 1:*** *Compute Spectra*

We compute high-resolution (R=500,000) spectra of the atmospheres described in Section 2.3.1 using the LBLABC and Spectral Mapping Atmospheric Radiative Transfer (SMART) models (Meadows & Crisp, 1996; Crisp, 1997). We use LBLABC to calculate the absorption coefficients at each pressure level in the atmosphere for each atmospheric constituent, then use SMART to solve the radiative transfer equation. For this study, we use only the $O_2$ A-band at 0.76 $\mu$m, as this is the most well-studied $O_2$ band for previous ELT simulations (e.g. Rodler & López-Morales, 2014; Snellen et al., 2015; López-Morales et al., 2019; Hardegree-Ullman et al., 2023; Currie et al., 2023) and it is less affected by contamination by other molecules and pressure effects than the 1.27$\mu$m $O_2$ band. SMART produces the planet and stellar fluxes, $F_{\mathrm{p}}$ and $F_{\mathrm{s}}$, respectively, at the top of the planet atmosphere. We plot the reflectance spectrum of the 21% $O_2$ case computed with SMART in the "Step 1" panel of Figure 2.15, and use this case as the example for illustrating the subsequent data simulation steps.

#### *2.3.2.2* ***Step 2:*** *Calculate photon counts*

Using the Spectral Planetary ELT Calculator for Terrestrial Retrieval (SPECTR) developed in this work (Section 2.1; Currie et al., 2023; Currie & Meadows, submitted), we simulate the photon counts on the detector for an ELT observation. The flux for each target system calculated in Step 1 (§ 2.3.2.1) is scaled to a distance of 1.3 pc away from the observatory, and photon count rates for the star and planet are calculated via the following equations, respectively:

$$c_{\mathrm{p}} = T\frac{\lambda\Delta\lambda}{hc}F_{\mathrm{p}}A \tag{2.11}$$

and

$$c_{\mathrm{s}} = T\frac{\lambda\Delta\lambda}{hc}F_{\mathrm{s}}A, \tag{2.12}$$

where T is total throughput, $\lambda$ is wavelength grid, h is Planck's constant, c is the speed of light, A is total collecting area, and $\mathrm{F_p}$ and $F_{\mathrm{s}}$ are the planet and stellar fluxes scaled to the distance of the target from Earth. We assume the targets are observed with the 39 m E-ELT (987 $\mathrm{m}^2$ collecting area Ramsay et al., 2020), and the total throughput T is 10% across all wavelengths. The total observation time we use in this study is $t_{\mathrm{obs}} = 100$ hrs worth of E-ELT time. For simplicity, we assume that the total time spent observing is coadded and spread evenly across a series of 30 exposures taken between planetary phase angles 30° and 60° to maximize the change in Doppler velocity over the course of the observation. Maximizing the change in Doppler velocity frame-to-frame is essential for separating the telluric lines from the planetary spectrum (e.g. Birkby, 2018), which is later performed in Step 4 (§ 2.3.2.4). The assumption that our observations night-to-night are uniform allows us to easily co-add spectra to simulate a simple dataset, although we note that realistically observers may not be able to obtain observations between our phase angle bounds on any given night. We also note that observing a planet at different phases may affect our ability to remove tellurics night-to-night (López-Morales et al., 2019; Hardegree-Ullman et al., 2023; Currie & Meadows, submitted) and therefore retrieve molecular abundances.

To calculate a full dataset of co-added observations, we multiply Equations 2.11 and 2.12 by $t_{\mathrm{obs}}$ in seconds to simulate the total number of photons collected per frame. An example of the result of this calculation is given in the "Step 2" panel of Figure 2.15.

#### *2.3.2.3* ***Step 3:*** *Simulate multi-epoch observations*

Next, we apply Doppler shifts to each frame of our dataset. Because our observations take place between planetary phase angles 30° and 60°, we calculate and apply a Doppler velocity shift to each frame given by (Lovis et al., 2010):

$$V_p = V_{\mathrm{sys}} + V_{\mathrm{bary}}(t) + K_p \sin\phi(t), \tag{2.13}$$

where $V_{\text{sys}}$ is the radial velocity of the system, $V_{\text{bary}}$ is the barycentric radial velocity, $\phi$ is the planetary phase angle, and $K_p$ is the planetary radial velocity semi-amplitude given by

$$K_p = 2\pi \frac{a_p \sin i}{P}, \tag{2.14}$$

where $a_p$ is the planet's orbital radius, $i$ is the system inclination, and $P$ is the planet's orbital period. We note that the barycentric velocity $V_{\text{bary}}(t)$ will vary between observations over the course of seasons and may significantly impact our ability to detect molecular features (López-Morales et al., 2019; Hardegree-Ullman et al., 2023; Currie & Meadows, submitted); however, for simplicity we assume this variable is zero for this study. Finally, we convolve each frame with a Gaussian profile to downbin to a wavelength grid with resolution R=100,000. The Doppler shifted spectra are plotted in the "Step 3" panel of Figure 2.15.

#### *2.3.2.4* ***Step 4:*** *Include telluric extinction*

We use the Cerro Paranal Advanced Sky Model (SkyCalc; Noll et al., 2012; Jones et al., 2013) to simulate telluric signal attenuation associated with the Earth's atmosphere. We use Paranal as our observatory site, and specify a precipitable water vapor depth of 3.5 mm. We assume the observations are taken in dark time, and do not include scattered moonlight in these simulations. The telluric transmittance spectrum we obtained from SkyCalc is interpolated onto our native wavelength grid, and multiplied by each frame to simulate telluric spectral contamination. This step is illustrated in the "Step 4" panel of Figure 2.15.

#### *2.3.2.5* ***Step 5:*** *Add noise*

Next, we add Poisson noise to our simulated observations. We calculate simulated noise for the spectrum in each frame via the following equation:

$$\text{data}_i = c_{\text{p,i}} t_{\text{obs,i}} + \mathcal{N}(0,1)\sqrt{(c_{\text{p,i}} + C c_{\text{s},i}) t_{\text{obs,i}}}, \tag{2.15}$$

where $\mathcal{N}(0,1)$ represents randomly selected numbers from a normal distribution, and C represents the contrast achieved by the instrument (Robinson et al., 2016; Lustig-Yaeger et al., 2019b). For this study, we assume an instrument contrast of $10^{-4}$, which is considered achievable for the next generation ELT instrumentation (Snellen et al., 2015; Marconi et al., 2022; Palle et al., 2023). An example of a grid of noisy spectra is plotted in the “Step 5” panel of Figure 2.15.

#### *2.3.2.6* ***Step 6:*** *Normalize spectra and remove tellurics*

The final steps (Step 6 and Step 7) follow Brogi & Line (2019) to prepare the simulated data for atmospheric retrieval. After we add noise to the spectra, we normalize each spectrum and remove telluric contamination, following the method of Brogi & Line (2019). For each frame, we normalize the spectrum by the median of the largest 300 values. For a real dataset, this ensures any frame-to-frame variation in detector response is removed. While this step is not necessary for our simulated data, which does not simulate detector response variations, we nevertheless include it for posterity. We then compute the average spectrum in time across all frames, and fit the average spectrum to each frame with a second order polynomial, and divide the fit from the frame. This removes the bulk of the telluric lines and stellar background, leaving only the planet spectrum behind plotted in the “Step 6” panel of Figure 2.15.

#### *2.3.2.7* ***Step 7:*** *Mask noisy spectral channels*

Finally, we perform an outlier rejection routine to reduce noise in the final spectra, as in Brogi & Line (2019). We first remove variations in each spectral channel by fitting a second order polynomial to each column of the data Step 6 dataset and subsequently dividing these columnar variations out. These columnar variations can include remnants of water vapor telluric lines that are not fully removed in Step 6 (Brogi & Line, 2019), and must be divided out; however there is no significant water vapor absorption in the wavelength region we test in this work. We include this feature for future studies investigating wavelength regions that may be more impacted by telluric water vapor. After removing the columnar variations, we perform a simple outlier rejection routine, where we mask columns with standard deviations greater than 3x the standard deviation of the full dataset. The “Step 7” panel of Figure 2.15 illustrates the output of our outlier rejection step, and is the data that will be passed to the retrieval framework in Section 2.3.3. For comparison, we also include the outcome of applying Steps 5-7 for a noiseless dataset (bottom panel of Figure 2.15).

### *2.3.3 Retrieval Framework*

In this work, we upgrade the Spectral Mapping Atmospheric Radiative Transfer for Exoplanet Retrieval (SMARTER) framework (Lustig-Yaeger, 2020; Lustig-Yaeger et al., 2023a), which was originally designed for space-based observations of terrestrial exoplanets, to include the functionality to analyze multi-epoch high-resolution ground-based data. SMARTER is used to solve the Bayesian inverse problem, where, given a dataset, we infer the parameters of a model, such as molecular abundance, that best describes the dataset. At the core of SMARTER is the SMART model (Meadows & Crisp, 1996; Crisp, 1997) (Section 2.3.2), which is paired with a Bayesian estimator to generate a suite of models that describe the observed spectrum. SMARTER has been validated on a high-resolution Earth transmission spectrum (Lustig-Yaeger et al., 2023a), and has been used to retrieve molecular abundances in simulated (Lustig-Yaeger et al., 2022, 2023a) and observed (Lustig-Yaeger et al., 2023b) JWST data. We upgrade SMARTER with a forward model and log likelihood function tailored specifically for high-resolution cross-correlation spectroscopy (Brogi & Line, 2019), and describe our upgrades in Sections 2.3.3.1 and 2.3.3.2.

#### *2.3.3.1 Forward Model*

The forward spectral model is used in the retrieval framework to estimate atmospheric parameters by comparing to the simulated observed spectrum. We fit the data with one-dimensional atmospheres, and for simplicity, assume evenly mixed molecular abundances and an isothermal temperature–pressure profile. We specify the atmosphere is composed of $O_2$, $CO_2$, $CH_4$, $H_2O$, and $O_3$, and has a 1 bar surface pressure for the 1%, 5%, 21%, and 50% $O_2$ cases, or a 10 bar surface pressure for the 95% $O_2$ ocean loss case (Table 2.8), with $N_2$ as a filler gas

(Figure 2.14). This combination of gases encompasses the major atmospheric constituents in an Earth-like terrestrial exoplanet atmosphere.In the forward model, we allow the $\log_{10} f$ volume mixing ratio of $O_2$ to vary, and force the mixing ratio of $N_2$ to fill the space needed to create a surface pressure of 1 bar for the 1%, 5%, 21%, and 50% cases and 10 bar for the 95% case. In these experiments, we focus principally on the accuracy of the retrieved $O_2$ abundance, and do not simultaneously retrieve atmospheric pressure as a free parameter, although SMARTER does have this capability. Additionally, we allow the total gray surface albedo of the planet ($A_s$) to vary in the forward model. Using SMART (Meadows & Crisp, 1996; Crisp, 1997) (see Section 2.3.2.1), the forward model computes a high-resolution (R=500,000) spectrum of the atmosphere with these parameters, then creates a time-series observation of the exoplanet with the same number of frames and phases as the simulated data. Each frame is then Doppler shifted according to the radial velocity semi-amplitude of the planetary orbit $K_p$ and the total radial velocity of the system $V_{\text{sys}}$ using Equation 2.13. In addition to the $f_{O_2}$ and $A_s$ parameters, we also allow the retrieval to explore the $K_p$ and $V_{\text{sys}}$ parameter spaces to constrain the radial velocity of the planet. Finally, each frame is convolved with a Gaussian to downbin to the native resolution of the instrument used in the simulated observations (R=100,000). This forward model is used in the retrieval framework to constrain the parameters that describe the simulated observed spectra.

#### *2.3.3.2 SMARTER Upgrades and the Inverse Model*

At the core of our upgrades to SMARTER is the inclusion of a log-likelihood equation tailored for high-resolution cross-correlation spectroscopy derived by Brogi & Line (2019), which we then pair with the Bayesian estimator `dynesty` (Skilling, 2004; Speagle, 2020) to perform atmospheric retrievals. The `dynesty` nested sampling code is used to solve the Bayesian inverse problem for the posterior probability distribution functions of our forward model parameter state vector $\omega$ given simulated planetary data. In total, we use a four-parameter state vector $\omega$, for our forward model with the following uninformative priors on the four parameters:

$$\mathcal{P}(\omega) = \begin{cases} f_{\mathrm{O}_2} & \sim \mathcal{U}(-12, 0) \quad [log_{10}(\mathrm{VMR})] \\ A_s & \sim \mathcal{U}(-2, 0) \quad [log_{10}(A_s)] \\ K_p & \sim \mathcal{U}(-50, 50) \quad [\mathrm{km/s}] \\ V_{\mathrm{sys}} & \sim \mathcal{U}(0, 100) \quad [\mathrm{km/s}], \end{cases} \tag{2.16}$$

where $\mathcal{U}(\mathrm{lower}, \mathrm{upper})$ represents uniform distribution with finite probability between the lower and upper bounds, and the units for each parameter are in brackets. We note that in future iterations of this analysis we plan to also include the surface pressure ($P_0$) and temperature ($T_0$) because the shape of the absorption lines are sensitive to these parameters, and we could potentially probe the pressure as another way to constrain $O_2$ abundance for 1 bar vs. 10 bar cases; however, the months-long timescale to run the four parameter state vector in this work limited the scope of this initial analysis. The present work serves as a proof of concept for this retrieval framework, and we outline our plans to improve the analysis before submission for publication in Section 5.3.3.

Because our simulated observations are composed of a time series of high-resolution spectra, where each individual spectrum is relatively low S/N and has lost its continuum information after post-processing (see Section 2.3.2), the standard $\chi^2$ log-likelihood function used in many retrieval frameworks for space-based data (e.g. Lustig-Yaeger et al., 2022) is not optimal (Brogi & Line, 2019). Instead, we opt to use a log-likelihood formalism derived by Brogi & Line (2019) that uses a cross-correlation technique which enhances the S/N by a factor of the square root of the number of resolved spectral lines (Snellen et al., 2010). This enhancement is especially important for terrestrial planets observed in reflected light, whose signals will be at the very limit of upcoming observational capabilities (Snellen et al., 2015). The log-likelihood formalism derived by Brogi & Line (2019) tailored for high-resolution ground based observations is given by:

$$\log(L) = -\frac{N}{2} \log[s_f^2 - 2R(s) + s_g^2], \tag{2.17}$$

where $s_f^2$ is the variance of the data, $s_g^2$ is the variance of the model, and $R(s)$ is the cross-covariance, defined as

$$R(s) = \frac{1}{N} \sum_{n} f(n) g(n-s), \tag{2.18}$$

where $n$ is the bin or pixel number, $s$ is a bin or wavelength shift due to the relative velocity, $N$ is the total number of pixels, $f(n)$ is the synthetic observed spectrum, and $g(n-s)$ is the model spectrum with a wavelength shift of $s$. We create an unnormalized log-posterior that can be sampled with `dynesty` by adding this log-likelihood function to the logarithm of our uninformative priors given in Equation 2.16. We run dynesty with 1000 live points and take model convergence to be achieved when the estimated contribution of the remaining prior volume to the total evidence $\hat{\mathcal{Z}}$ falls below 0.5 between consecutive iterations. We then apply our upgraded retrieval model to the data simulated in Section 2.3.2, and present the results of the converged retrievals in Section 5.2.

# Part I

# MOLECULAR DETECTABILITY IN GROUND-BASED HIGH-RESOLUTION SPECTRA OF TERRESTRIAL EXOPLANETS

## Chapter 3

# A STRATEGY FOR CHARACTERIZING TRANSITING TERRESTRIAL EXOPLANET TARGETS WITH GROUND-BASED HIGH-RESOLUTION OBSERVATIONS

*Portions of this chapter were originally published in collaboration with Victoria S. Meadows and Kaitlin C. Rasmussen in the May 2023 edition of The Planetary Science Journal (Currie et al., 2023a, PSJ, Vol. 4, 5; DOI: 10.3847/PSJ/accf86), and is reproduced below with the permission of the American Astronomical Society.*

## ***Summary***

Within the next decade, atmospheric $O_2$ on Earth-like M dwarf planets may be accessible with visible–near-infrared, high spectral resolution extremely large ground-based telescope (ELT) instruments. However, the prospects for using ELTs to detect environmental properties that provide context for $O_2$ have not been thoroughly explored. Additional molecules may help indicate planetary habitability, rule out abiotically generated $O_2$, or reveal alternative biosignatures. To understand the accessibility of environmental context using ELT spectra, we simulate high-resolution transit transmission spectra of previously-generated evolved terrestrial atmospheres. We consider inhabited pre-industrial and Archean Earth-like atmospheres, and lifeless worlds with abiotic $O_2$ buildup from $CO_2$ and $H_2O$ photolysis. All atmospheres are self-consistent with M2V–M8V dwarf host stars. Our simulations include explicit treatment of systematic and telluric effects to model high-resolution spectra for GMT, TMT, and E-ELT configurations for systems 5 and 12 pc from Earth. Using the cross-correlation technique, we determine the detectability of major species in these atmospheres: $O_2$, $O_3$, $CH_4$, $CO_2$, CO, $H_2O$, and $C_2H_6$. Our results suggest that $CH_4$ and $CO_2$ are the most accessible molecules for terrestrial planets transiting a range of M dwarf hosts using an E-ELT, TMT, or GMT sized telescope, and that the $O_2$ NIR and $H_2O$ 0.9 $\mu$m bands may also be accessible with more observation time. Although this technique still faces considerable challenges, the ELTs will provide access to the atmospheres of terrestrial planets transiting earlier-type M-dwarf hosts that may not be possible using JWST.

## 3.1 Brief Introduction

In this chapter, we explore the potential for using the ELTs to detect a number of molecules expected in transiting terrestrial planetary atmospheres, and their application for biosignature interpretation. We use previously-generated simulations of self-consistent inhabited environments for Earth throughout its history transiting five M dwarf spectral types from M2V-M8V. We apply cross-correlation techniques to simulated spectra of these environments to determine the number of transits needed to detect the molecules. Additionally, we explore two lifeless, but habitable, atmosphere types that may also exhibit abiotically-generated $O_2$ from processes such as significant $CO_2$ photolysis, complete ocean loss, and ongoing ocean outgassing, to understand how we can potentially discriminate these atmospheres from those influenced by life. Refer to Chapter 1 for a thorough introduction of this subject, and Section 2.1 for an overview of the methods used in this specific chapter. In Section 3.2, we present the results of our detectability calculations, which inform future observations of transiting terrestrial exoplanets. In Section 3.3, we discuss the significance of detections and non-detections of molecular bands in the context of habitability and life, and propose an observational strategy for characterizing terrestrial atmospheres in transit. We summarize our findings in Section 3.4.

## 3.2 Results

Using our cross-correlation pipeline, we estimate the detectability of molecular bands in terrestrial planet atmospheres transiting M2V through M8V host star types. The atmosphere classes included in our study are self-consistent PIE and ARE atmospheres which contain true biosignatures, and abiotically-generated $O_2$ via $CO_2$ photolysis (Harman et al., 2018) and ocean-loss/outgassing (Leung et al., 2020) atmospheres (see Table 2.2). Selected high-resolution spectra of the most detectable molecular absorption bands are presented in Figure 2.7, and the results for all molecular absorption bands are available as an accompanying data product for this chapter. We calculate molecular detectability for these atmospheres for clear- and cloudy-sky scenarios, for GMT, TMT, and E-ELT configurations, and at distances of 5 and 12 pc away from Earth. Although it is unlikely that we find a transiting terrestrial planet at 5 pc, we include simulations of these systems at this distance for direct comparison with previous results that have used 5 pc as a point of reference.

A comparison of detectability for the most sensitive bands of specific molecules in a given atmosphere is summarized in Figure 3.1, the effects of clouds for the most sensitive bands are summarized in Figure 3.2. Detailed results on molecular detectability as a function of stellar type, atmosphere type, and number of transits are presented in Figure 3.3 for targets 5 pc away observed using a TMT configuration and Figure 3.4 for targets 12 pc away using an E-ELT configuration. Similarly, we present molecular detectability using an E-ELT configuration for our simulated TRAPPIST-1 e clear-sky atmospheres in Figure 3.5. Each plot shows the detection significance vs. number of observed transits for a molecular absorption band in an atmosphere, orbiting M2V through M8V host stars. Missing lines signify the molecule is not present in the atmosphere, or that the atmosphere is only self-consistent with one host star type, as in the case of the $CO_2$ photolysis and ocean-loss/outgassing atmospheres (M4V and M6V, respectively). Values for number of transits required for 3- and 5-$\sigma_{\mathrm{det}}$ detections of molecular bands are given in Tables 3.2 through 3.7. Although the collecting area of the GMT is much smaller than the E-ELT and TMT, our simulations suggest that some molecular targets, namely $CO_2$, will still be feasible to observe with the GMT, and we present these targets in Table 3.8 for systems 12 pc away. The addition of clouds in our atmospheres increases the number of transits required by 2-4x on average (Figure 3.2).

We apply the same noise properties to an 8.2 m diameter mirror telescope and find that the number of transits required to achieve a similar detection significance increases by at least an order of magnitude. The distance dependence tracks with the inverse-square law: a target at 10 pc from Earth requires 4 times the number of transits to obtain a 3-$\sigma_{\mathrm{det}}$ significance detection for a target 5 pc away from Earth.

The most detectable molecules are $CH_4$ and $CO_2$, with their most detectable absorption features residing in the 1.6 $\mu$m region. We find that the 1.27$\mu$m, 0.9$\mu$m, and 1.55$\mu$m bands

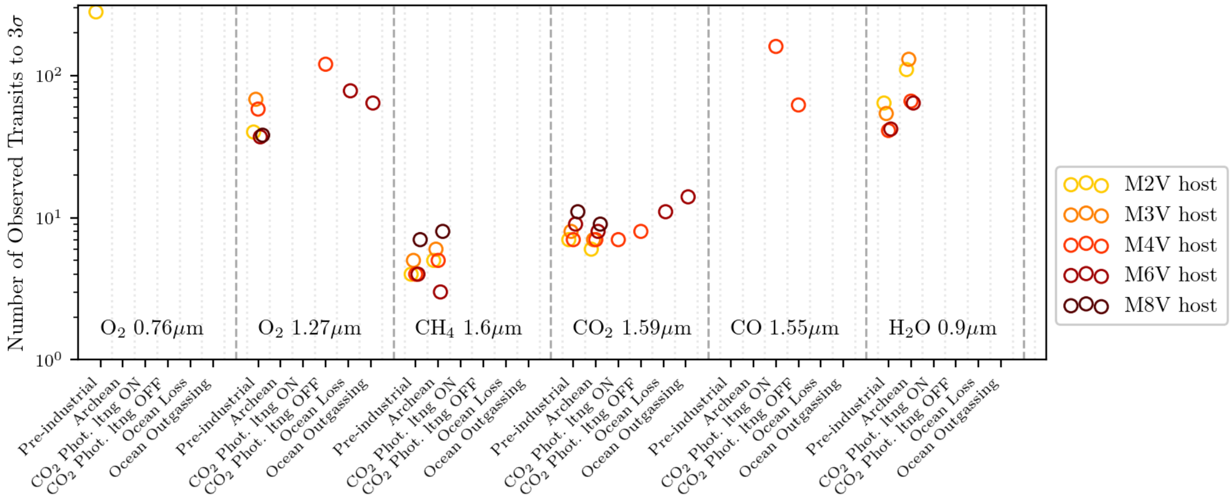

Figure 3.1 Total observed transits required for a 3-$\sigma_{\mathrm{det}}$ significance detection using an E-ELT sized telescope for selected bands in all atmosphere classes orbiting a range of host stars at a distance of 12 pc from the observer. A marker is missing either where the atmosphere does not contain a molecule or $> 300$ observed transits are required to detect the molecular band.

are the most detectable $O_2$, $H_2O$, and CO features, respectively. $O_3$ and $C_2H_6$ were not detectable in any case in this study.

### *3.2.1 Dependence on stellar type*

In nearly all cases, the molecular detectability is dependent on the host star type. We identify an interplay between physical and chemical effects of the host star on the detectability of molecular bands in an exoplanet atmosphere. In addition to photochemical effects in the exoplanet atmosphere, the wavelength-dependent brightness and physical size of the stellar disk can influence detectability.

#### *3.2.1.1 Photochemistry*

As discussed in Section 3.1, the SED of the host star affects both the abundance and distribution of molecules in an exoplanet atmosphere through photochemical processes. A higher

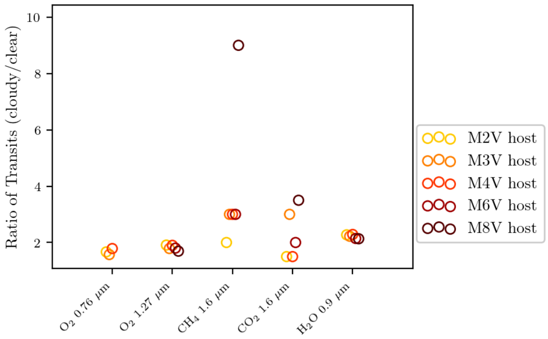

Figure 3.2 Ratios of the number of transits required to detect the most sensitive molecular bands in our study for cloudy to clear sky pre-industrial Earth-like atmospheres. Missing markers signify that cloudy spectra require $> 300$ transits to detect the molecular feature.

molecular abundance absorbs more photons from the star, creating deeper transits, and leading to stronger detectability. This effect is clearly seen when comparing the $CH_4$ profiles of self-consistent PIE to true Earth (Figure 2.3). Variable UV activity of M dwarf stars allows for the buildup of $CH_4$, while $CH_4$ in the true Earth atmosphere is photochemically destroyed more rapidly (Segura et al., 2005).

#### *3.2.1.2 Stellar brightness and size*

Photochemical effects aside, the wavelength-dependent brightness of the host star SED also impacts the detection significance of individual molecular bands. The incident SED on the planet atmosphere can have wavelength-dependent effects on detectability. For example, molecules that absorb in the region of peak flux in the host star SED have the advantage of more available photons to absorb when compared to an off-peak molecular absorption band, thus producing deeper transits. This effect is illustrated in our results by comparing the $0.76\mu m$ and $1.27\mu m$ bands of $O_2$ in Figure 3.3. Since the earlier type M dwarf host SEDs peak closer to the $0.76\mu m$ band, they have an observational advantage over later-type stars: they require fewer transits to achieve the same detection significance for this band (see Figure 3.3). Conversely, later type M dwarf SEDs peak closer to the $1.27\mu m$ $O_2$ band, and

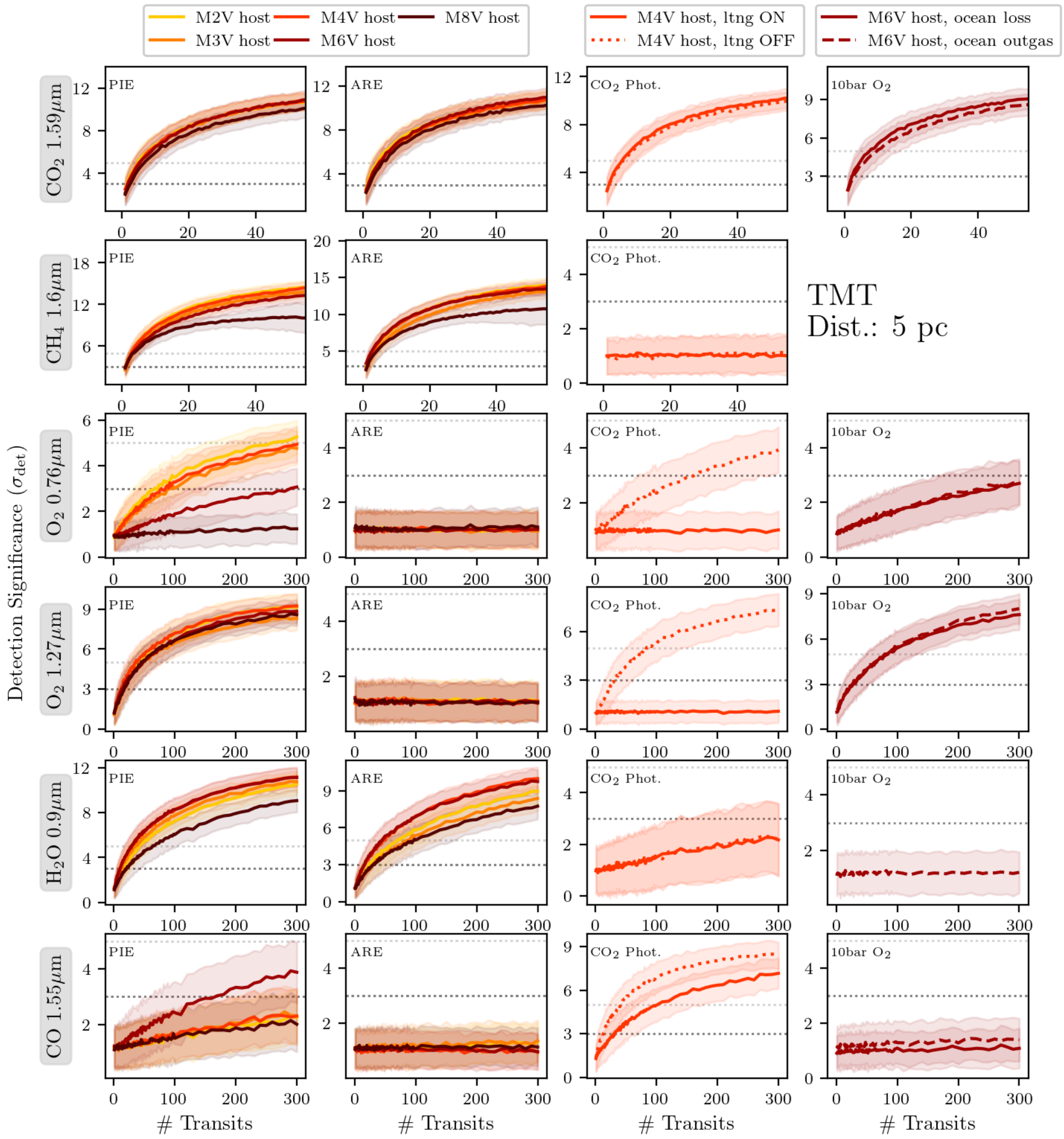

Figure 3.3 Detection significance as a function of total integration time for the most detectable molecular bands in photochemically self-consistent pre-industrial Earth-like (PIE) atmospheres, Archean Earth-like (ARE) atmospheres, $CO_2$ photolysis atmospheres (lightning on/off), and 10 bar $O_2$ worlds (ocean-loss/outgassing) (columns left to right) at distances of 5 pc from Earth observed with a TMT sized telescope. The shaded regions are the 1-$\sigma_{\mathrm{det}}$ uncertainties on detection significance. The dark and light gray dotted lines mark the 3- and 5-$\sigma_{\mathrm{det}}$ thresholds, respectively.

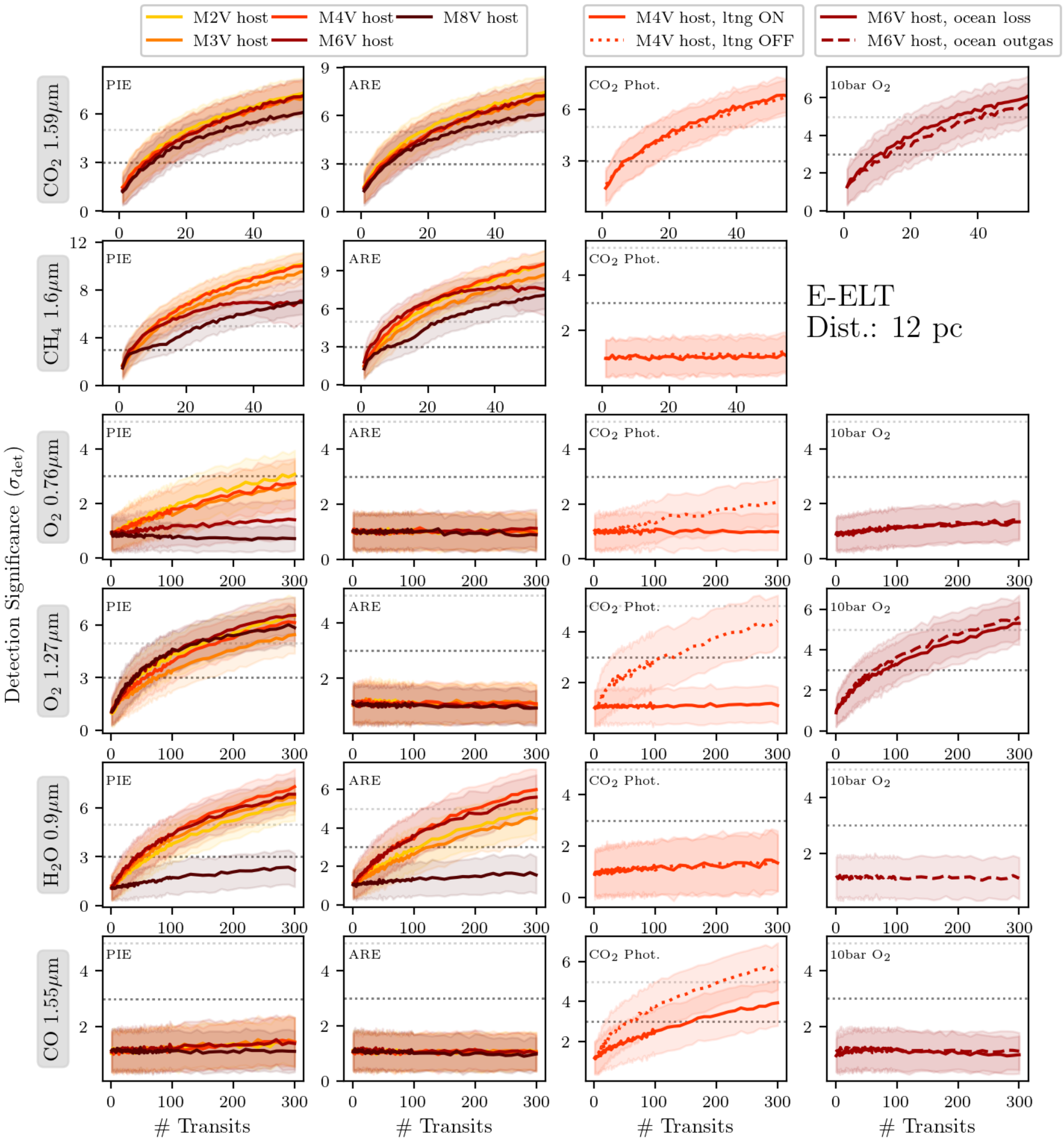

Figure 3.4 Detection significance as a function of total integration time for the most detectable molecular bands in photochemically self-consistent pre-industrial Earth-like (PIE) atmospheres, Archean Earth-like (ARE) atmospheres, $CO_2$ photolysis atmospheres (lightning on/off), and 10 bar $O_2$ worlds (ocean-loss/outgassing) (columns left to right) at distances of 12 pc from Earth observed with an E-ELT sized telescope. The shaded regions are the 1-$\sigma_{\rm det}$ uncertainties on detection significance. The dark and light gray dotted lines mark the 3- and 5-$\sigma_{\rm det}$ thresholds, respectively.

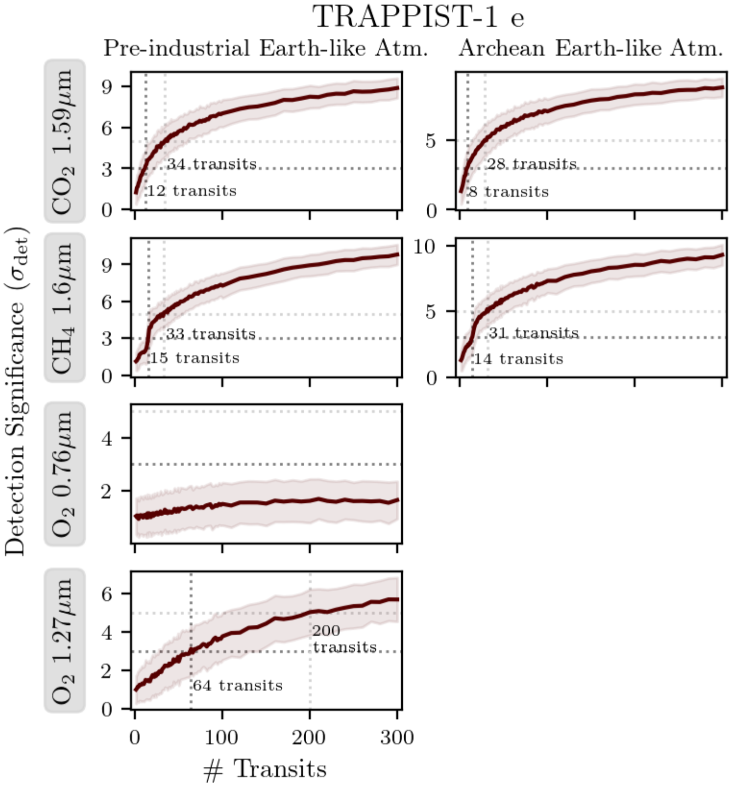

Figure 3.5 Detection significance as a function of number of observed transits for four molecular bands in our simulated TRAPPIST-1 e atmospheres observed with the E-ELT. The shaded regions are the 1-$\sigma_{\mathrm{det}}$ uncertainties on detection significance. The horizontal dark and light gray dotted lines mark the 3- and 5-$\sigma_{\mathrm{det}}$ thresholds, respectively. The vertical dotted dark and light gray lines, and corresponding labels to their right, denote the precise integration time required for 3- and 5-$\sigma_{\mathrm{det}}$ detections. Note that the transit duration is 0.99 hr, so integration time required is nearly the same as number of observed transits required.

$O_2$ is equally or more detectable in this region for late-type hosts. However, in many cases the flux of the host star at the observer due either to intrinsic brightness or proximity (lower panel of Figure 2.2) can compete with any wavelength-dependent effects due to the number of photons that are incident on the detector. This effect can be seen in the 1.6 $\mu$m $CH_4$ band in Figure 3.4, where the larger, earlier-type hosts may require fewer transits to achieve a 3- or 5-$\sigma_{\mathrm{det}}$ detection significance, even though the later type host SEDs peak closer to this region.

Transit depth is also inversely proportional to the radius of the star squared, and so larger stars can reduce the detectability of molecules in the atmospheres of exoplanets transiting them, while smaller stars will enhance the detectability of planetary atmospheric absorption. Deeper transits are easier to distinguish from the surrounding noise, thus are more detectable. This is an important factor working to increase the detectability of molecules in planets transiting late-type hosts.

In summary, detectability is proportional to transit depth and the square root of stellar luminosity, which both depend on the size of the host star. Additionally, stellar luminosity depends on the effective temperature of the star. Detectability is also highly variable for different wavelength regions in a transit spectrum due to photochemical effects in the exoplanet atmosphere and telluric effects in the Earth's atmosphere.

### *3.2.2 Favorable targets for the ELTs*

In terms of the fewest number of transits required to detect a molecule, the best overall stellar host targets for characterizing terrestrial-sized exoplanets for habitability and life are M dwarf stars earlier than M6V; however, it is important to note that in terms of least total observing time and opportunities to obtain transmission spectra, later-type M dwarf hosts have the advantage (see Section 3.3.4 for a discussion). Since the transit duration of a planet increases with earlier-type hosts and surface brightness increases, early-type systems require fewer observed transits, while later-type hosts require less overall observation time to achieve the same detection significance. The best targets will depend on the priorities and limitations of the observer. Figure 3.1 provides a summary of the number of transits required to detect the most accessible molecular bands for each self-consistent atmosphere transiting M dwarf hosts in our study.

The $CH_4$ $1.6\mu m$ and $CO_2$ $1.59\mu m$ bands stand out as being the most accessible bands for the ELTs (see Figures 3.3 and 3.4), requiring the fewest number of observed transits (see also Figure 3.1). If a planet atmosphere contains both species, such as our PIE and ARE atmospheres, a $>$5-$\sigma_{\rm det}$ detection can be achieved for both $CH_4$ and $CO_2$ by observing $\sim 20-30$ transits for all stellar host types at a distance of 12 pc for the E-ELT. If abundant $O_2$ is present in an atmosphere, the band requiring the fewest number of observed transits is the $1.27\mu m$ band for all stellar host types (see Figure 3.3), and can be detected at a detection significance of 5-$\sigma_{\rm det}$ for PIE atmospheres 12 pc away in $> 300$ transits for the GMT, 230 or more transits for the TMT, and 140–180 transits for the E-ELT. The $0.76\mu m$ A-band may be accessible with significantly more observation time, requiring three or more times the number of observed transits to detect at the same significance as the $1.27\mu m$ band. We note that this differs from the results of Rodler & López-Morales (2014); López-Morales et al. (2019); Wunderlich et al. (2020), and attribute the differences to their inclusion of red noise sources as 20% and 50% of the white noise in the visible and NIR, respectively. Here we choose not to model red noise in this way to simulate an idealistic scenario. $H_2O$ may also be accessible for planets around any M dwarf host, with the $0.9\mu$m band as the most detectable feature in all cases, requiring 140–180 transits for a 5-$\sigma_{\rm det}$ detection for a pre-industrial Earth-like planet transiting an M6V 12 pc away observed with the E-ELT. CO may be detectable for mid-type M dwarf hosts in the $1.55\mu m$ region if sufficient CO is available in the atmosphere (i.e. only for the $CO_2$ photolysis atmospheres), and is accessible at a 3-$\sigma_{\rm det}$ level in 160 and 62 transits for scenarios with and without lightning, respectively, for targets 12 pc away observed with the E-ELT. The next most detectable $H_2O$ and CO bands may require an order of magnitude or more observed transits, and may be inaccessible for targets at 12 pc. $O_3$ and $C_2H_6$ are not detectable with our simulated observational setups.

#### *3.2.2.1 TRAPPIST-1 e with the ELTs*

To better understand the detectability of molecular bands for a promising known target, we simulate transit transmission observations of PIE and ARE planets transiting TRAPPIST-1 at an orbital geometry analogous to the planet TRAPPIST-1 e. We report the number of transits to 5-$\sigma_{\mathrm{det}}$ for the most detectable molecules in the atmosphere of TRAPPIST-1 e in Table 3.1, and include detectability estimates for an M4V at 12 pc in the table for comparison. In Figure 3.5, we show that $CO_2$ and $CH_4$ are detectable in 34 and 33 observed transits, respectively, at a 5-$\sigma_{\mathrm{det}}$ significance with the E-ELT for a PIE atmosphere, and 28 and 31 transits, respectively, for an ARE atmosphere. Detecting $O_2$ in a PIE atmosphere will be challenging, requiring 200 observed transits for a 5-$\sigma_{\mathrm{det}}$ significance detection, and 64 transits for a 3-$\sigma_{\mathrm{det}}$ significance detection. $H_2O$ may be extremely challenging, requiring more than 300 transits.

### *3.2.3 Molecular targets requiring other observation techniques*

The most difficult molecules to detect with transit transmission spectroscopy using ground-based ELTs are $O_3$ for all atmospheres, CO for PIE and ARE atmospheres, and $C_2H_6$ for ARE atmospheres. The only $O_3$ bands with wavelength accessibility for the ELTs are the Chappuis band and $3.2\mu m$ band, and the features do not have sufficient high-resolution structure to use this detection method. CO, which can be an indicator of abiotic generation of $O_2$, is most prominent in the $CO_2$ photolysis atmosphere and may be possible to detect in $< 100$ transits in certain scenarios, but in all other cases is not reliably detectable with the ELTs. These molecules may be better observed using space-based telescopes, which can probe other molecular bands, or ground-based reflected light spectroscopy, which can probe deeper into the atmosphere.

### *3.3 Discussion*

We have identified multiple molecular bands, including $CO_2$, $CH_4$, $O_2$, $H_2O$, and CO, that could be detectable using the ELTs for terrestrial planet atmospheres transiting a range of M dwarf host stars. The suite of molecules accessible to ground-based observatories could aid in searching for environmental clues that point to life, habitability, and biosignature false-positive mechanisms. Additionally, the factors that affect the detectability of a molecule reach beyond photochemistry and instrument sensitivity, and we note the importance of the host star's physical characteristics, such as size and wavelength-dependent/overall brightness, for selecting ideal systems and molecular bands to observe in the future. We present a recommended observing protocol for discriminating possible terrestrial planet environments below in Section 3.3.1

Our results suggest that there are many molecular bands that may be accessible with the ground-based ELTs, and these bands may be able to provide environmental context for an $O_2$ detection, or point to other outcomes of atmospheric evolution. With our novel cross-correlation pipeline, we estimated the detectability of $O_2$, $CH_4$, $CO_2$, CO, $H_2O$, $O_3$, and $C_2H_6$ in the atmospheres of pre-industrial Earth-like, Archean Earth-like, $CO_2$ photolysis, and 10 bar ocean-loss/outgassing atmospheres, all photochemically self-consistent with M2 through M8 host stars. We found that $CO_2$ and $CH_4$ are excellent targets to search for in suspected habitable Earth-like atmospheres orbiting any type of M dwarf host, taking just a few observed transits for initial discovery. Additionally, $O_2$ may be detectable for a pre-industrial Earth-like world at both 0.76 and $1.27\mu m$, with the $1.27\mu m$ band having a distinct observational advantage. An atmosphere that builds up abiotic $O_2$ from $CO_2$ photolysis may not be able to accumulate detectable levels of $O_2$ for the more unrealistic case of no lightning in an atmosphere, therefore discrimination from atmospheres influenced by life may not be a problem. However, if $O_2$ is detected, detection of both $CO_2$ in 28 transits, and strong CO in 84 transits would strongly suggest an abiotic buildup scenario from $CO_2$ photolysis in the case of a target 12 pc away observed with the E-ELT.

We compare our $O_2$ results to previous literature (e.g. Rodler & López-Morales, 2014; López-Morales et al., 2019; Leung et al., 2020; Wunderlich et al., 2020), and find that our detectability estimates for planets transiting late-type hosts are in agreement, while our estimates for early-type M dwarf planets differ. We overestimate the 1.27 um detectability, and underestimate the 0.76 um detectability, for early type hosts. We agree on the late-type detectability estimates for both the 0.76 and 1.27 $O_2$ bands (López-Morales et al., 2019). We hypothesize that this is due to a difference in how we added noise to our simulations: we use ESO SkyCalc to generate realistic wavelength-dependent background noise, while Rodler & López-Morales (2014) and López-Morales et al. (2019) approximate red noise as 20% and 50% of the white noise in the visible and NIR, respectively, therefore differences in our detectability estimates are expected. For planets with significant $O_2$ buildup due to $H_2O$ photolysis, Leung et al. (2020) predicts suppression in the 1.27 $\mu$m $O_2$ band, which we do not see in our results. This is likely explained by a difference in observational methods: we test transmission spectra only, which are more sensitive to the upper layers of the atmosphere and less susceptible to saturate, while Leung et al. (2020) tests reflected light spectra, which probe to the surface and can saturate and suppress the 1.27 $\mu$m $O_2$ feature. Wunderlich et al. (2020) investigate the detectability of a similar suite of molecules in Earth-like TRAPPIST-1 e atmospheres with similar abundances for $CH_4$ and $CO_2$ to our study using a simple SNR-estimation approach, and they find $CH_4$ and $CO_2$ are detectable in 26 and 33 transits, respectively, which are consistent with our estimates of 34 and 33 transits, respectively. However, the $O_2$ abundance for the Wunderlich et al. (2020) "wet and alive" case is 35%, compared with our 21% $O_2$ abundance. Therefore, we cannot directly compare $O_2$ detectability results, however our results suggest that the $1.27 \mu m$ $O_2$ band can be detected in 200 transits, a factor of 4.5 less than Wunderlich et al. (2020), and we attribute our enhanced $O_2$ sensitivity to our more rigorous application of the cross-correlation technique, and our "perfect" telluric line removal step.

Using the ground-based ELTs, we may have the capacity to search for two biosignature pairs. $O_2$, $CH_4$, and $CO_2$ are all detectable within the lifetime of these telescopes at multiple absorption bands, and the $O_2$–$CH_4$ and $CO_2$–$CH_4$ biosignature pairs are potentially accessible. In the most optimistic scenario of a transiting target 12 pc away, both biosignature pairs could be found in as few as 140 observed transits with the E-ELT at 5-$\sigma_{\rm det}$ significance. The ELTs will require fewer transits to obtain both biosignature pairs than than using JWST, which will require approximately 278 transits for a 5-$\sigma$ detection of the $O_2$ 1.27 $\mu$m band on TRAPPIST-1 e at 12pc using NIRSpec PRISM (Meadows et al., 2023). However, the GMT will require >300 transits for the $O_2$ 1.27 $\mu$m, and in this case JWST NIRSpec PRISM may be marginally better. However, the higher-resolution JWST/NIRSpec G140H mode or the NIRISS spectrograph may enhance sensitivity to $O_2$ alone, albeit with a truncated wavelength range, that may compete with or exceed the capabilities of ground-based observing.

Furthermore, we may be able to discriminate abiotic $O_2$ buildup scenarios from an Earth-like atmosphere influenced by biology. A detection of CO would indicate that the abiotic $O_2$ is due to $CO_2$ photolysis by detecting CO. A non-detection of $CH_4$ could also reveal that detected $O_2$ is abiotic from either $CO_2$ photolysis or $H_2O$ photolysis in ocean-loss/outgassing scenarios.

The degree to which it is possible to constrain gas abundances in high-resolution spectra depends on whether the chosen telluric line removal technique also removes continuum information from the observed spectrum (Birkby, 2018). See Section 2.1.3 for a discussion on telluric line removal techniques. One consequence of applying a PCA-like routine is the loss of continuum information, which can introduce degeneracies when comparing the observed spectrum to a grid of atmosphere models to determine molecular abundances. However, given simultaneous observations of multiple gases, it may be possible to infer the relative abundances of the gases since they would depend on the same pressure–temperature profile (de Kok et al., 2013). On the other hand, knowledge of the Earth's atmosphere during the observation can inform radiative transfer tools which can model the Earth's telluric transmission, and remove it from an observed spectrum, preserving the continuum and absolute line depths. Another proposed pathway for preserving the continuum is to combine both low- and high-resolution observations of the same target to break abundance degeneracies (De

Kok et al., 2014). The power of multi-resolution observations is demonstrated in Pino et al. (e.g. 2018), where a more sophisticated atmosphere model for HD 189733 b was developed to reconcile the sharp features seen in high-resolution observations with the relatively flat spectrum seen at low-resolution. Abundance determination for terrestrial planets, however, is still an open question to be explored in future work.

### *3.3.1 Recommended observing protocol*

To discriminate terrestrial atmosphere types and characterize planetary environments, we recommend prioritizing specific molecular bands to maximize the information gained in as little observation time as possible. Although future designs for high-resolution spectrographs on the ELTs may allow for simultaneous wavelength coverage in the visible (G-CLEF, 0.35-0.95 $\mu$m Szentgyorgyi et al., 2014), NIR (MOHDIS, 0.95-2.4 $\mu$m Mawet et al., 2019), or both (ANDES, 0.4-1.8 $\mu$m Marconi et al., 2022), some of the details of these instruments have not yet been finalized; we therefore treat each molecular band in this study individually in an effort to inform the development of these instruments. In order from highest to lowest priority, we recommend that observers target $CO_2$, $CH_4$, $O_2$, $H_2O$, and CO. In all cases, there are no detectable $O_3$ or $C_2H_6$ bands with the ELTs, and $O_3$ will likely be best detected using the lower-resolution methods of space-based missions. We preface this discussion with the caveat that this study is limited to a handful of planetary atmospheres, and there are many possible outcomes of planetary evolution; detections and non-detections of molecules discussed below should therefore be treated as additional pieces evidence that can increase the probability of certain evolutionary outcomes. Below we synthesize information about each molecule with its relative detectability to justify its placement in our observing protocol priority list.

#### *3.3.1.1 $CO_2$*

A detection of $CO_2$ can help rule out larger $H_2$-dominated atmospheres by indicating that the atmosphere is primarily the result of planetary outgassing rather than accretion during formation. $CO_2$ is readily detectable for all of the atmospheres in this work, requiring 20–30 observed transits for a target 12 pc away and 5–10 transits for a target 5 pc away to reach a 5-$\sigma_{\rm det}$ detection with the E-ELT.

Additionally, the presence of $CO_2$ could help constrain planetary climate. $CO_2$ is a greenhouse gas tightly coupled to geologic processes on our planet. A planet with significant $CO_2$ may have an active carbonate–silicate cycle (Walker et al., 1981; Kasting et al., 1993; Kopparapu et al., 2013), which may help buffer the planetary climate through geologic time (Walker et al., 1981). $CO_2$ could be a useful habitability indicator, however its presence alone is not indicative of an inhabited planet.

#### *3.3.1.2 $CH_4$*

A $CH_4$ detection can help discriminate ocean-loss/outgassing and $CO_2$ photolysis scenarios from Earth-like atmospheres, and provide clues that can point to habitability and life. If a $CO_2$ detection is made with an accompanying $CH_4$ detection, the resulting $CH_4/CO_2$ disequilibrium pair (Krissansen-Totton et al., 2016) may be the most efficient way to search for biosignatures on both PIE and ARE planets, requiring only $\sim 5$ and $\sim 20$ transits in the most optimistic scenarios for transiting Earth-like planets 5 and 12 pc away, respectively.

#### *3.3.1.3 $O_2$*

Our simulations indicate that the NIR band requires fewer transits to detect $O_2$ than the A-band for most targets with $O_2$ in their atmospheres by factors of four or more. A non-detection of $O_2$ could help rule out PIE and 10 bar $O_2$ atmospheres, and, if $CO_2$ is also present, could point to a $CO_2$ photolysis atmosphere or Archean Earth scenario, although a full suite of gases would be needed to specify the atmosphere type with more certainty. Conversely, a detection of $O_2$ could provide evidence for a post-ocean-loss, ongoing ocean outgassing, or PIE atmosphere. Furthermore, a simultaneous detection of $CH_4$ would constitute the $O_2/CH_4$ disequilibrium biosignature in a PIE atmosphere. Given that the Archean $CH_4/CO_2$ disequilibrium pair is also potentially detectable (Meadows et al., 2023), this means that two potential biosignature disequilibrium pairs, spanning early Earth to modern Earth atmospheres, could be acquired in as few as $\sim 39$ transits in the most optimistic scenario of an Earth-like planet transiting a star 5 pc away.

#### *3.3.1.4* $H_2O$

A detection of $H_2O$ can help strengthen the case for a PIE, ARE, or ocean outgassing world, and, conversely, a non-detection can strengthen the case for an ocean-loss or $CO_2$ photolysis atmosphere. $H_2O$ detection typically requires a comparable number of transits to the $O_2$ NIR band to achieve a 3-$\sigma_{\mathrm{det}}$ detection, and a factor of 5–10 or more transits than $CO_2$ and $CH_4$, and for that reason we recommend prioritizing $H_2O$ after $CO_2$, $CH_4$, and $O_2$. Although the 1-D atmosphere models in our study cannot self-consistently account for 3D effects typically included in 3-D global circulation models (GCMs), the $H_2O$ profiles are similar enough to first order for reliable detectability estimates (Meadows et al., 2023).

The 0.9 um band is the most detectable $H_2O$ band despite the fact that it is weaker than the other bands we tested. Although the $H_2O$ absorption at 1.1 and 1.3 $\mu$m may be stronger than the 0.9 $\mu$m band in the planet atmosphere, they are also stronger in the telluric transmission spectrum. Compared with the 0.9 $\mu$m region, these longer wavelength regions are dense with $H_2O$ and overlapping $CH_4$ lines that saturate to nearly 0% atmospheric transmission, and effectively block our ability to observe these molecular bands, even at a resolving power of $R = 100,000$. Additionally, transmission spectroscopy is limited in the regions of the atmosphere it can probe; namely, it is more sensitive to upper regions of the atmosphere. To detect strongly absorbing molecules that mainly reside near the surface of an Earth-like planet, like $H_2O$, the observer must also overcome this additional challenge, and different techniques such as reflected light observations, which can probe deeper into the atmosphere, may be better suited for detecting $H_2O$.

Because an $H_2O$ detection would be crucial evidence for the presence of liquid water on an exoplanet, we re-ran our analysis combining of all three $H_2O$ bands in a single spectrum in an attempt to glean any information that may be suppressed in the 1.1 and 1.3 $\mu$m bands.

After examining the resulting cross-correlation function, we find that H2O is marginally more detectable with the combined bands, requiring 60 transits for a 3-$\sigma_{\mathrm{det}}$ detection, compared with 64 transits using only the 0.9 $\mu$m $H_2O$ band. Additionally, the 1.1 and 1.3 $\mu$m bands are out of the nominal GMT G-CLEF wavelength range (0.35-0.95 $\mu$m Szentgyorgyi et al., 2014), and the 0.9 $\mu$m band will be the most suitable target in that case.

#### *3.3.1.5 CO*

A CO detection can help identify a world with abiotic $O_2$ buildup due to $CO_2$ photolysis, requiring 42 transits for a planet 5 pc away from Earth. However, CO will not be present at significant levels on a planet with life, and should only be prioritized for ruling out an $O_2$ biosignature false positive scenario.

#### *3.3.1.6 $O_3$ and $C_2H_6$*

$O_3$ and $C_2H_6$ are not accessible using ground-based high-resolution transit transmission spectroscopy.

### *3.3.2 Effects of clouds*

We investigate the effects of adding Earth-like clouds to our pre-industrial Earth-like atmospheres. While in most cases we are still able to detect the molecular features in a cloudy spectrum, we find that between two and four times the transits required to detect molecules in the clear sky scenario are required to achieve the same detection significance for cloudy sky scenarios. This is an effect of the clouds suppressing some of the high-resolution features by both raising the spectral continuum in altitude and reducing the relative transit depths (Fauchez et al., 2019). The increase in the number of transits required to detect a molecular feature is a direct consequence of the level of suppression in the spectral features. Of particular note is the $CH_4$ 1.6$\mu$m band for the PIE atmosphere orbiting the M8V host, which requires nearly 9 times the number of transits to detect this feature than for a clear-sky

Table 3.1. Number of transits required for 5-$\sigma_{\mathrm{det}}$ detection in modern Earth-like clear-sky atmospheres on TRAPPIST-1 e and around an M4V at 12 pc with the ELTs

| | TRAPPIST-1 e | | | | M4V at 12 pc | | |
|---|---|---|---|---|---|---|---|
| | GMT | TMT | E-ELT | W20 E-ELT | GMT | TMT | E-ELT |
| $CO_2$ (1.56 $\mu$m) | 240 | 62 | 34 | 33 | 60 | 33 | 25 |
| $CH_4$ (1.6 $\mu$m) | $> 300$ | 56 | 33 | 26 | $> 300$ | 14 | 11 |
| $H_2O$ (0.9 $\mu$m) | $> 300$ | $> 300$ | $> 300$ | 1224 | $> 300$ | 180 | 130 |
| $O_2$ (1.27 $\mu$m) | $> 300$ | 300 | 200 | 910 | $> 300$ | 240 | 180 |

Note. — The W20 column presents ELT detectability results from Wunderlich et al. (2020).

scenario.

### *3.3.3 Observing protocol applied to TRAPPIST-1 e*

To better understand how our observing protocol can be used in practice, we apply it to PIE and ARE planets orbiting the M8V host star TRAPPIST-1, simulating transit transmission spectroscopy of TRAPPIST-1 e. In Figure 3.5 and Section 3.2.2.1, we show that $CO_2$ and $CH_4$ are potentially accessible for a TRAPPIST-1 e planet with either a PIE or ARE atmosphere in 12 and 8 transits, respectively, for a 3-$\sigma_{\mathrm{det}}$ detection, and 34 and 28 transits, respectively for a 5-$\sigma_{\mathrm{det}}$ detection. With sufficient observation time, $O_2$ may be accessible for PIE atmospheres, but would likely require a multi-year observing strategy, even in the most ideal conditions. Similarly, $H_2O$ would require significant observation time to detect, and may be extremely challenging for the ELTs, even in the case of water vapor transport due to synchronous rotation, as described above in Section 3.3.1.4. Given the most favorable weather, telescope availability, and seasonal observability, an observer could detect $CO_2$ and $CH_4$ in a relatively short timescale, pointing to an Earth-like atmosphere and revealing a biosignature pair.

#### *3.3.3.1 Complementarities to space-based missions*

The ELTs may be powerful tools for terrestrial exoplanet characterization, and complementary to current and future space-based missions. JWST can be used to characterize transiting rocky exoplanets for the biosignature gases $CO_2$ and $CH_4$, but $O_2$ will be more challenging (Lustig-Yaeger et al., 2019a; Pidhorodetska et al., 2020; Krissansen-Totton et al., 2018a; Wunderlich et al., 2019).

We compare our ELT detectability results to similar studies for an Earth-like TRAPPIST-1 e observed with JWST, and find that JWST detectability results vary depending on whether the atmospheric composition used was photochemically and climatically self-consistent with the parent star. While it is not straightforward to compare our results to current estimates for JWST detectability due to the different specified atmospheres for these studies (e.g.

$CO_2$ abundances that span 400 ppm to 10%) we can look at the broad range of estimated detectability anticipated over a broad range of atmospheric gas abundances. Studies with photochemically self-consistent TRAPPIST-1 e Earth-like atmospheres (e.g. Lustig-Yaeger et al., 2019a; Krissansen-Totton et al., 2018a; Pidhorodetska et al., 2020; Gialluca et al., 2021; Wunderlich et al., 2019; Wunderlich et al., 2020) use a range of $CO_2$ abundances, and estimate that in atmospheres with 400 ppm of $CO_2$, it is detectable in $\sim 10$ transits (Lustig-Yaeger et al., 2019a), while a more analogous atmosphere to our study with 10% $CO_2$ may be detectable in 5 transits (Wunderlich et al., 2020), roughly 7 times fewer transits than for the ELTs. One consequence of studies that consider non-photochemically self-consistent atmospheres is that even biological amounts of $CH_4$ may not reach high enough abundances to be readily detectable, requiring $\sim 55$ or more transits to reach a detection (Fauchez et al., 2019; Tremblay et al., 2020), compared with 34 transits for our self-consistent E-ELT results. Therefore, while there are relatively few studies which provide direct comparisons between JWST and ELT capabilities, it is apparent that the ELTs will be powerful tools for followup or simultaneous observations to confirm detections of $CO_2$ or $CH_4$, or to dedicate significant ELT resources to search for molecules like $O_2$ that may be out of reach for JWST.

Ground-based high-resolution spectroscopy is additionally more sensitive to line cores higher in the atmosphere, and may be used to probe above the cloud deck (Gandhi et al., 2020), while low-to-mid resolution space-based instruments will be limited to relatively few spectral features for cloudy atmospheres (Fauchez et al., 2019). Compared to low-resolution observations, the cross-correlation technique is uniquely sensitive to both the relative depths and spacing of individual absorption lines as well as the high-resolution structure of the lines in the full molecular band, potentially enhancing our ability to break degeneracies due to overlapping absorption bands in low-resolution observations. Without a coronagraph designed for terrestrial exoplanet characterization, JWST observations will be limited to transmission spectroscopy only. Conversely, terrestrial exoplanets are being considered in the design for the ELT coronagraphs, and the ELTs will have access to a larger number of targets with the addition of reflected light spectroscopy as a capability, a topic we leave for future work.

Looking ahead to the next generation of space-based instruments, the Astro2020 Decadal Survey recommended a 6 m class space mission capable of directly imaging terrestrial-sized exoplanets as a top science priority (Decadal Survey on Astronomy and Astrophysics 2021). Obtaining a direct spectrum of a terrestrial exoplanet will require a coronagraph designed for high-contrast imaging of habitable zone exoplanets, and the technology requirements set by this goal can be implemented and tested with the current designs for ELT high-contrast imaging capabilities in the near term. The lessons learned from the ground will be crucial in the design process for a space-based direct imaging mission, and may help inform future observing strategies.

### *3.3.4 Observing logistics and caveats*

Although seasonal observability is a constraint for any observatory, space-based telescopes are unencumbered by factors that limit ground-based observing programs, including variation in the weather and the day-to-night cycle, and may allow more opportunities to observe a transiting planet. However, Lovis et al. (2017) estimate that despite the restrictions of ground-based observing, it may be possible to detect $O_2$ in the atmosphere of the non-transiting Proxima Centauri b at $3.6\sigma$ in 60 nights spread over three years using the Very Large Telescope, assuming observations are obtained twice per orbit at approaching and receding quadrature. For comparison with this non-transiting planet at 1.3 pc from Earth using an 8.2 m telescope, we have calculated the feasibility of detecting $O_2$ from the ground for the transiting HZ planet, TRAPPIST-1 e at 12 pc with an ELT, where 64 transits are needed for a 3-$\sigma_{\rm det}$ detection. TRAPPIST-1 e undergoes transit once every 6.1 days, corresponding to 60 transits per year; however, using the Exoplanet Archive transit observability prediction tool with a maximum airmass of 3 predicts that only $\sim$ 10 of these (17%) are observable from the ground (Akeson et al., 2013). If 35% of a semester's observing time is also lost to weather[1], this means that only $\sim$ 6 transits can be observed per year. Thus a 3-$\sigma_{\rm det}$ detection of $O_2$ in the PIE scenario of TRAPPIST-1 e will take $\sim$ 10 years, and $\sim$ 33 years for a 5-$\sigma_{\rm det}$ detection. If this system was instead at a distance of 5 pc, these estimates would improve to $\sim$ 2 years and $\sim$ 6.5 years for 3- and 5-$\sigma_{\rm det}$ detections, respectively. This real-time estimate potentially increases for habitable zone planets transiting early type hosts, where orbital periods can reach 30 days or more, and the resulting increased transit durations for early-type M dwarf planets may not fully compensate for the decreased number of opportunities to observe a transit. Consequently, while likely possible from the ground, high-resolution spectral exploration of transiting HZ terrestrial exoplanet atmospheres for the known planets at 12 pc will remain challenging, and will require a significant investment in observing time over several years, and possibly decades. In comparison, the closer, non-transiting planets may provide faster access to adequate S/N for HZ exoplanet atmospheres, and we will explore these in subsequent work.

## 3.4 Conclusion

The ELTs will be capable of detecting other molecules that can help place detected $O_2$ in its environmental context, including $CO_2$, $CH_4$, $H_2O$, and CO. For the terrestrial planets considered here, $CO_2$ and $CH_4$ stand out as the best molecular targets for the ELTs. In particular, a $CO_2$ detection can increase the likelihood that a planet is terrestrial, and searching for $CO_2$ may also reveal biological levels of $CH_4$ (if present), constituting a biosignature pair. A non-detection of $CH_4$ may point to an abiotic environment. Additionally, detecting Earth-like levels of $O_2$ in an atmosphere will be challenging, but not impossible for the known transiting targets at 12 pc, and more feasible for any transiting M dwarf planets found at closer distances. However, since $O_2$ is likely not accessible with JWST, ground-based searches for $O_2$ provide the best possible means of detecting this important molecule, which can potentially identify an Earth-like planet with oxygenic photosynthesis,

---

[1] https://www.gemini.edu/observing/science-operations-statistics

and reveal a second biosignature pair ($O_2/CH_4$) if $CH_4$ can also be detected. This pair will help to rule out a scenario where abiotic $O_2$ has built up to detectable levels. A simultaneous non-detection of $H_2O$ or $CH_4$ may also help discriminate an abiotic $O_2$ scenario from a planet with biogenic $O_2$. Furthermore, a detection of CO may help discriminate abiotic $O_2$ buildup via $CO_2$ photolysis from $O_2$ buildup via ocean loss or outgassing.

The ELTs have the potential to be used to reveal two biosignature pairs, and detect the molecules necessary to discriminate biological and false positive origins for $O_2$. They will be even more powerful when techniques for telluric line subtraction are improved, and if transiting targets are found closer than the existing ones at 12 pc. In addition to testing and demonstrating technology that will be crucial to the success of future space-based direct imaging missions, their versatility and relatively near-term availability is complementary to current space-based missions, and they will provide opportunities to observe planetary targets and spectral features that are otherwise inaccessible in the near term.

## *3.5 Acknowledgments*

The authors thank our anonymous reviewers for their comments and suggestions that substantially improved the clarity and robustness of the paper. We would also like to thank Motohide Tamura (University of Tokyo) for reading an early version of this chapter and providing valuable comments that helped to strengthen the chapter. M.C. also thanks Michael Line (Arizona State University) and Matteo Brogi (University of Warwick) for helpful discussions on the capabilities and limitations of high-resolution spectroscopy. This work was performed by the Virtual Planetary Laboratory Team, a member of the NASA Nexus for Exoplanet System Science (NExSS), funded via NASA Astrobiology Program Grant No. 80NSSC18K0829, and this work benefited from our participation in the NExSS research coordination network. This work was also partly supported by the Astrobiology Center, Japan. The simulations in this work were facilitated though the use of advanced computational, storage, and networking infrastructure provided by the Hyak supercomputer system at the University of Washington.

### *3.6 Chapter Appendix*

Below we include detailed tables for the detectability estimates of each atmosphere type in our study for the configurations of observing targets 5 pc away with the TMT, and targets 12 pc away with the E-ELT. Tables 3.2 through 3.7 show exact values for the number of transits required to detect each molecule at detection significances of 3-$\sigma_{\mathrm{det}}$ and 5-$\sigma_{\mathrm{det}}$. Table 3.8 shows the targets at 12 pc away that will be accessible to the GMT. Ellipses are given for molecular bands not detectable with the ELTs.

Table 3.2. Detectability results for clear sky pre-industrial Earths at 12 pc with an E-ELT sized telescope. Missing values indicate that the molecular band was not detectable at the missing significance level in less than 300 transits.

| Molecule | Band | M2V | M3V | M4V | M6V | M8V |
|---|---|---|---|---|---|---|
| | | # transits to 3-$\sigma_{\mathrm{det}}$ (5-$\sigma_{\mathrm{det}}$) detection | | | | |
| $O_2$ | $0.69\mu m$ | ··· | ··· | ··· | ··· | ··· |
| | $0.76\mu m$ | 280 | ··· | ··· | ··· | ··· |
| | $1.27\mu m$ | 40(160) | 68(240) | 58(180) | 37(140) | 38(150) |
| $CH_4$ | $0.89\mu m$ | 210 | 250 | 220 | ··· | ··· |
| | $1.1\mu m$ | ··· | ··· | ··· | ··· | ··· |
| | $1.3\mu m$ | 48(140) | 68(210) | 64(200) | 80(220) | 120 |
| | $1.6\mu m$ | 4(11) | 5(12) | 4(11) | 4(12) | 7(25) |
| $CO_2$ | $1.59\mu m$ | 7(20) | 8(24) | 7(25) | 9(25) | 11(32) |
| | $2.0\mu m$ | 12(35) | 16(52) | 20(62) | ··· | ··· |
| $H_2O$ | $0.9\mu m$ | 64(180) | 54(160) | 41(130) | 42(140) | ··· |
| | $1.1\mu m$ | ··· | ··· | ··· | ··· | ··· |
| | $1.3\mu m$ | ··· | ··· | ··· | ··· | ··· |
| CO | $1.55\mu m$ | ··· | ··· | ··· | ··· | ··· |
| | $2.3\mu m$ | ··· | ··· | ··· | ··· | ··· |
| $O_3$ | $0.63\mu m$ | ··· | ··· | ··· | ··· | ··· |
| | $0.65\mu m$ | ··· | ··· | ··· | ··· | ··· |
| | $3.2\mu m$ | ··· | ··· | ··· | ··· | ··· |

Table 3.3. Detectability results for clear sky pre-industrial Earths at 5 pc with a TMT sized telescope. Missing values indicate that the molecular band was not detectable at the missing significance level in less than 300 transits.

| Molecule | Band | M2V | M3V | M4V | M6V | M8V |
|---|---|---|---|---|---|---|
| | | # transits to 3-$\sigma_{\rm det}$ (5-$\sigma_{\rm det}$) detection | | | | |
| $O_2$ | 0.69$\mu m$ | 180 | 280 | 230 | ⋯ | ⋯ |
| | 0.76$\mu m$ | 68(260) | 88 | 78 | 290 | ⋯ |
| | 1.27$\mu m$ | 15(39) | 17(47) | 13(37) | 13(48) | 18(45) |
| $CH_4$ | 0.89$\mu m$ | 49(150) | 62(180) | 50(160) | 96 | ⋯ |
| | 1.1$\mu m$ | ⋯ | ⋯ | ⋯ | ⋯ | ⋯ |
| | 1.3$\mu m$ | 12(34) | 19(52) | 17(48) | 21(68) | 37(110) |
| | 1.6$\mu m$ | 1(3) | 2(4) | 2(3) | 1(4) | 2(4) |
| $CO_2$ | 1.59$\mu m$ | 2(5) | 2(6) | 2(6) | 2(6) | 3(7) |
| | 2.0$\mu m$ | 3(7) | 3(9) | 3(9) | ⋯ | ⋯ |
| $H_2O$ | 0.9$\mu m$ | 15(42) | 13(36) | 11(31) | 11(29) | 21(64) |
| | 1.1$\mu m$ | ⋯ | ⋯ | ⋯ | ⋯ | ⋯ |
| | 1.3$\mu m$ | 120 | 130 | 140 | 58(180) | 140 |
| CO | 1.55$\mu m$ | ⋯ | ⋯ | ⋯ | 170 | ⋯ |
| | 2.3$\mu m$ | ⋯ | ⋯ | ⋯ | ⋯ | ⋯ |
| $O_3$ | 0.63$\mu m$ | ⋯ | ⋯ | ⋯ | ⋯ | ⋯ |
| | 0.65$\mu m$ | ⋯ | ⋯ | ⋯ | ⋯ | ⋯ |
| | 3.2$\mu m$ | ⋯ | ⋯ | ⋯ | ⋯ | ⋯ |

Table 3.4. Detectability results for clear sky Archean Earths at 12 pc with an E-ELT sized telescope. Missing values indicate that the molecular band was not detectable at the missing significance level in less than 300 transits.

| Molecule | Band | M2V | M3V | M4V | M6V | M8V |
|---|---|---|---|---|---|---|
| | | # transits to 3-$\sigma_{\rm det}$ (5-$\sigma_{\rm det}$) detection | | | | |
| $O_2$ | 0.69$\mu m$ | $\cdots$ | $\cdots$ | $\cdots$ | $\cdots$ | $\cdots$ |
| | 0.76$\mu m$ | $\cdots$ | $\cdots$ | $\cdots$ | $\cdots$ | $\cdots$ |
| | 1.27$\mu m$ | $\cdots$ | $\cdots$ | $\cdots$ | $\cdots$ | $\cdots$ |
| $CH_4$ | 0.89$\mu m$ | $\cdots$ | $\cdots$ | 300 | $\cdots$ | $\cdots$ |
| | 1.1$\mu m$ | $\cdots$ | $\cdots$ | $\cdots$ | $\cdots$ | $\cdots$ |
| | 1.3$\mu m$ | 58(170) | 82(240) | 70(190) | 68(190) | 150 |
| | 1.6$\mu m$ | 5(13) | 6(16) | 5(12) | 3(10) | 8(23) |
| $CO_2$ | 1.59$\mu m$ | 6(18) | 7(23) | 7(21) | 8(22) | 9(29) |
| | 2.0$\mu m$ | 12(34) | 16(50) | 18(62) | $\cdots$ | $\cdots$ |
| $H_2O$ | 0.9$\mu m$ | $\cdots$ | $\cdots$ | 66(210) | 64(240) | $\cdots$ |
| | 1.1$\mu m$ | $\cdots$ | $\cdots$ | $\cdots$ | $\cdots$ | $\cdots$ |
| | 1.3$\mu m$ | $\cdots$ | $\cdots$ | $\cdots$ | $\cdots$ | $\cdots$ |
| CO | 1.55$\mu m$ | $\cdots$ | $\cdots$ | $\cdots$ | $\cdots$ | $\cdots$ |
| | 2.3$\mu m$ | $\cdots$ | $\cdots$ | $\cdots$ | $\cdots$ | 41 |
| $O_3$ | 0.63$\mu m$ | $\cdots$ | $\cdots$ | $\cdots$ | $\cdots$ | $\cdots$ |
| | 0.65$\mu m$ | $\cdots$ | $\cdots$ | $\cdots$ | $\cdots$ | $\cdots$ |
| | 3.2$\mu m$ | $\cdots$ | $\cdots$ | $\cdots$ | $\cdots$ | $\cdots$ |
| $C_2H_6$ | 3.33$\mu m$ | $\cdots$ | $\cdots$ | $\cdots$ | $\cdots$ | $\cdots$ |

Table 3.5. Detectability results for clear sky Archean Earths at 5 pc with a TMT sized telescope. Missing values indicate that the molecular band was not detectable at the missing significance level in less than 300 transits.

| Molecule | Band | M2V | M3V | M4V | M6V | M8V |
|---|---|---|---|---|---|---|
| | | # transits to 3-$\sigma_{\mathrm{det}}$ (5-$\sigma_{\mathrm{det}}$) detection | | | | |
| $O_2$ | $0.69\mu m$ | ··· | ··· | ··· | ··· | ··· |
| | $0.76\mu m$ | ··· | ··· | ··· | ··· | ··· |
| | $1.27\mu m$ | ··· | ··· | ··· | ··· | ··· |
| $CH_4$ | $0.89\mu m$ | 78(220) | 130 | 74(220) | 160 | ··· |
| | $1.1\mu m$ | ··· | ··· | ··· | ··· | ··· |
| | $1.3\mu m$ | 16(44) | 23(60) | 18(45) | 21(62) | 46(140) |
| | $1.6\mu m$ | 2(4) | 2(5) | 2(4) | 1(3) | 2(5) |
| $CO_2$ | $1.59\mu m$ | 2(5) | 2(6) | 2(5) | 2(5) | 3(6) |
| | $2.0\mu m$ | 3(7) | 3(8) | 3(9) | 36 | ··· |
| $H_2O$ | $0.9\mu m$ | 24(72) | 30(90) | 17(48) | 17(45) | 31(98) |
| | $1.1\mu m$ | ··· | ··· | ··· | ··· | ··· |
| | $1.3\mu m$ | 260 | 240 | 220 | 160 | ··· |
| CO | $1.55\mu m$ | ··· | ··· | ··· | ··· | ··· |
| | $2.3\mu m$ | ··· | ··· | ··· | ··· | ··· |
| $O_3$ | $0.63\mu m$ | ··· | ··· | ··· | ··· | ··· |
| | $0.65\mu m$ | ··· | ··· | ··· | ··· | ··· |
| | $3.2\mu m$ | ··· | ··· | ··· | ··· | ··· |
| $C_2H_6$ | $3.33\mu m$ | ··· | ··· | ··· | ··· | ··· |

Table 3.6. Detectability results for clear sky $O_2$ false positive cases with an E-ELT sized telescope at 12 pc. Missing values indicate that the molecular band was not detectable at the missing significance level in less than 300 transits.

| Molecule | Band | M4V host<br>$CO_2$ Phot.<br>ltng. ON | M4V host<br>$CO_2$ Phot.<br>ltng. OFF | M6V host<br>10 bar $O_2$<br>ocean outgas | M6V host<br>10 bar $O_2$<br>ocean-loss |
|---|---|---|---|---|---|
| | | # transits to 3-$\sigma_{\rm det}$ (5-$\sigma_{\rm det}$) detection | | | |
| $O_2$ | $0.69\mu m$ | $\cdots$ | $\cdots$ | $\cdots$ | $\cdots$ |
| | $0.76\mu m$ | $\cdots$ | $\cdots$ | $\cdots$ | $\cdots$ |
| | $1.27\mu m$ | $\cdots$ | 120 | 64(240) | 78(270) |
| $CH_4$ | $0.89\mu m$ | $\cdots$ | $\cdots$ | $\cdots$ | $\cdots$ |
| | $1.1\mu m$ | $\cdots$ | $\cdots$ | $\cdots$ | $\cdots$ |
| | $1.3\mu m$ | $\cdots$ | $\cdots$ | $\cdots$ | $\cdots$ |
| | $1.6\mu m$ | $\cdots$ | $\cdots$ | $\cdots$ | $\cdots$ |
| $CO_2$ | $1.59\mu m$ | 7(25) | 8(28) | 14(40) | 11(34) |
| | $2.0\mu m$ | 21(86) | 21(84) | $\cdots$ | $\cdots$ |
| CO | $1.55\mu m$ | 160 | 62(210) | $\cdots$ | $\cdots$ |
| | $2.3\mu m$ | $\cdots$ | $\cdots$ | $\cdots$ | $\cdots$ |
| $H_2O$ | $0.9\mu m$ | $\cdots$ | $\cdots$ | $\cdots$ | $\cdots$ |
| | $1.1\mu m$ | $\cdots$ | $\cdots$ | $\cdots$ | $\cdots$ |
| | $1.3\mu m$ | $\cdots$ | 210 | $\cdots$ | $\cdots$ |

Table 3.7. Detectability results for clear sky $O_2$ false positive cases with a TMT sized telescope at 5 pc. Missing values indicate that the molecular band was not detectable at the missing significance level in less than 300 transits.

| Molecule | Band | M4V host<br>$CO_2$ Phot.<br>ltng. ON | M4V host<br>$CO_2$ Phot.<br>ltng. OFF | M6V host<br>10 bar $O_2$<br>ocean outgas | M6V host<br>10 bar $O_2$<br>ocean-loss |
|---|---|---|---|---|---|
| | | # transits to 3-$\sigma_{\text{det}}$ (5-$\sigma_{\text{det}}$) detection | | | |
| $O_2$ | 0.69$\mu m$ | ⋯ | ⋯ | ⋯ | ⋯ |
| | 0.76$\mu m$ | ⋯ | 170 | ⋯ | ⋯ |
| | 1.27$\mu m$ | ⋯ | 31(84) | 29(80) | 27(86) |
| $CH_4$ | 0.89$\mu m$ | ⋯ | ⋯ | ⋯ | ⋯ |
| | 1.1$\mu m$ | ⋯ | ⋯ | ⋯ | ⋯ |
| | 1.3$\mu m$ | ⋯ | ⋯ | ⋯ | ⋯ |
| | 1.6$\mu m$ | ⋯ | ⋯ | ⋯ | ⋯ |
| $CO_2$ | 1.59$\mu m$ | 2(6) | 2(6) | 3(10) | 3(8) |
| | 2.0$\mu m$ | 3(10) | 3(10) | ⋯ | ⋯ |
| CO | 1.55$\mu m$ | 32(110) | 14(42) | ⋯ | ⋯ |
| | 2.3$\mu m$ | ⋯ | ⋯ | ⋯ | ⋯ |
| $H_2O$ | 0.9$\mu m$ | ⋯ | ⋯ | ⋯ | ⋯ |
| | 1.1$\mu m$ | ⋯ | ⋯ | ⋯ | ⋯ |
| | 1.3$\mu m$ | 78(270) | 52(170) | ⋯ | ⋯ |

Table 3.8. Detectability results for all favorable targets at 12 pc using a GMT sized telescope. Missing values indicate that the molecular band was not detectable at the missing significance level in less than 300 transits.

| Star | Atm. | Molecule | [$\mu$m] | $N_{\rm trans}$ ($3\sigma_{\rm det}$) | $N_{\rm trans}$ ($5\sigma_{\rm det}$) |
|---|---|---|---|---|---|
| M2V | ARE | $CO_2$ | 1.59 | 17 | 54 |
| M2V | ARE | $H_2O$ | 0.9 | 270 | ··· |
| M2V | PIE | $CH_4$ | 1.6 | 54 | ··· |
| M2V | PIE | $CO_2$ | 1.59 | 22 | 58 |
| M2V | PIE | $H_2O$ | 0.9 | 150 | ··· |
| M2V | PIE | $O_2$ | 1.27 | 120 | ··· |
| M3V | ARE | $CO_2$ | 1.59 | 16 | 62 |
| M3V | PIE | $CH_4$ | 1.6 | 56 | ··· |
| M3V | PIE | $CO_2$ | 1.59 | 23 | 62 |
| M3V | PIE | $H_2O$ | 0.9 | 150 | ··· |
| M3V | PIE | $O_2$ | 1.27 | 190 | ··· |
| M4V | ARE | $CH_4$ | 1.6 | 54 | ··· |
| M4V | ARE | $CO_2$ | 1.59 | 16 | 60 |
| M4V | ARE | $H_2O$ | 0.9 | 200 | ··· |
| M4V | $CO_2$ ltng ON | $CO_2$ | 1.59 | 18 | 60 |
| M4V | $CO_2$ ltng OFF | $CO_2$ | 1.59 | 22 | 70 |
| M4V | $CO_2$ ltng OFF | CO | 1.55 | 150 | ··· |
| M4V | PIE | $CH_4$ | 1.6 | 37 | ··· |
| M4V | PIE | $CO_2$ | 1.59 | 23 | 60 |
| M4V | PIE | $H_2O$ | 0.9 | 130 | ··· |
| M4V | PIE | $O_2$ | 1.27 | 150 | ··· |
| M6V | ARE | $CH_4$ | 1.6 | 6 | 140 |
| M6V | ARE | $CO_2$ | 1.59 | 21 | 62 |
| M6V | ARE | $H_2O$ | 0.9 | 270 | ··· |
| M6V | Ocean Loss | $CO_2$ | 1.59 | 30 | 96 |
| M6V | Ocean Loss | $O_2$ | 1.27 | 150 | ··· |
| M6V | Ocean Outgas | $CO_2$ | 1.59 | 29 | 140 |
| M6V | Ocean Outgas | $O_2$ | 1.27 | 110 | ··· |
| M6V | PIE | $CH_4$ | 1.6 | 8 | ··· |
| M6V | PIE | $CO_2$ | 1.59 | 20 | 60 |
| M6V | PIE | $H_2O$ | 0.9 | 180 | ··· |
| M6V | PIE | $O_2$ | 1.27 | 76 | ··· |
| M8V | ARE | $CH_4$ | 1.6 | 31 | ··· |
| M8V | ARE | $CO_2$ | 1.59 | 26 | 290 |
| M8V | PIE | $CH_4$ | 1.6 | 10 | ··· |
| M8V | PIE | $CO_2$ | 1.59 | 30 | 240 |
| M8V | PIE | $O_2$ | 1.27 | 58 | ··· |

## Chapter 4

# PROBING DEEPER INTO TERRESTRIAL EXOPLANET ATMOSPHERES WITH HIGH RESOLUTION REFLECTED LIGHT OBSERVATIONS

*Portions of this chapter have been submitted for publication in collaboration with Victoria S. Meadows on June 19, 2024 in The Planetary Science Journal, and is reproduced below with the permission of the American Astronomical Society.*

## *Summary*

The upcoming extremely large telescopes will provide the first opportunity to search for signs of habitability and life on non-transiting terrestrial exoplanets using high-contrast, high-resolution instrumentation. However, the suite of atmospheric gases in terrestrial exoplanet environments that are accessible to ground-based reflected light observations has not been thoroughly explored. In this work, we use an upgraded ELT detectability pipeline to simulate the detectability of gases that can serve as habitability markers, potential biosignatures and false positive discriminants in the atmospheres of Earth-sized and sub-Neptune planets. We calculate molecular detectability for five photochemically self-consistent atmosphere types, including the modern and Archean Earth, uninhabited biosignature "false positive" environments, and a sub-Neptune, over a grid of observational configurations for non-transiting targets within 10pc of Earth. We include known targets within $\sim$ 5 pc such as Proxima Centauri b, GJ1061 d, Teegarden's Star c, and GJ1002 b and c. For the most accessible nearby target, Proxima Centauri b, our results suggest that we may be able to rule out a sub-Neptune atmosphere in as little as a single hour of observing, and two biosignature disequilibrium pairs ($O_2$/$CH_4$ and $CO_2$/$CH_4$) may be accessible in $\sim$ 10 hours. It may also be possible to discriminate uninhabited worlds, and rule out biosignature false positives by identifying contextual indicators (CO and $H_2O$) of abiotic $O_2$ and/or $CH_4$ buildup on similar timescales. In the near term, ELT reflected light observations will likely allow us to characterize multiple nearby terrestrial atmospheres, and search for signs of habitability and life.

## *4.1 Brief Introduction*

In this chapter, we investigate the detectability of a wide range of molecular features in simulated spectra of photochemically self-consistent terrestrial and sub-Neptune atmospheres orbiting M dwarf stars to prepare for future ELT observations of non-transiting terrestrial exoplanet atmospheres and better understand biosignature detection and interpretation using the ELTs. Refer to Chapter 1 for a thorough introduction of this subject, and Section 2.2 of Chapter 2 for an overview of the methods used in this specific chapter. We present our results in Section 4.2, discuss the meaning of our results in an astrobiological context in Section 4.3, and conclude in Section 4.4.

## *4.2 Results*

Using our updated SPECTR pipeline, we estimate the detectability of a range of molecular features in spectra of terrestrial planet atmospheres on Earth-sized planets orbiting M dwarf stars, and for a sub-Neptune. We calculate the detectability of molecular features as a function of a grid of relevant parameters, including the observed molecular band, the distance to the system, the performance of the instrumentation, the radial velocity of the star/planet, and the total collecting area of the observatory. Finally, we estimate the accessibility of the most detectable molecular features in a variety of atmospheres for planets in systems analogous to the closest known stellar targets. These targets have a habitable zone planet with a radial velocity minimum mass in the terrestrial range, and include Proxima Centauri (Anglada-Escudé et al., 2016), GJ 1061 (Dreizler et al., 2020), Teegarden's Star (Zechmeister et al., 2019), and GJ 1002 (Mascareño et al., 2023).

### *4.2.1 Molecular Detectability*

We test the detectability of the major molecular species with spectral features between 0.5–2.0 $\mu m$ (see Table 2.7) for self-consistent atmospheres of Earth through time, biosignature false positive worlds, and a sub-Neptune atmosphere. Figure 4.1 shows the exposure time in hours required to obtain a $3\sigma$ detection of each molecular band for terrestrial atmosphere types orbiting M2V-M8V host stars, including both the Earth through time and biosignature false positive scenarios. The observational configuration assumed for Figure 4.1 includes instrumentation capable of achieving $10^{-4}$ contrast and R=100,000 resolving power, which will be achievable and is included in the technology goals for the next generation of instruments for the ELTs (Snellen et al., 2015) including the GMT (Szentgyorgyi et al., 2014), TMT (Mawet et al., 2019), and ELT (Marconi et al., 2022), and the VLT (Lovis et al., 2022). Figure 4.2 similarly shows molecular detectability for the major species in the sub-Neptune atmosphere. We also test the detectability of a range of molecules for analogs of nearby habitable zone targets with atmosphere types including Earth through time, biosignature false positive cases, and a sub-Neptune, and we present the results in Figure 4.3 and associated IWA limitations in Figure 4.4. Finally, we test molecular detectability for grids of distance to the system (Figure 4.5), instrument contrast (Figure 4.7), system RV (Figure 4.6), and total collecting area (Figure 4.8).

#### *4.2.1.1 Inhabited Worlds and Biosignatures*

Examining the detectability of molecular bands for different, yet equidistant, stellar hosts reveals that molecular features are more detectable around later type stars overall, and that the most sensitive band for a given molecule can change with host star spectral type. Figure 4.1 presents the detectability of selected molecular features for planets in systems at 1.3pc, for the inhabited pre-industrial Earth-like planet (circles) and its ocean loss false positives for an M6V planet ("X" markers) (upper panel) and for the Archean Earth-like planet (triangles) and its M8V prebiotic high-volcanism false positive ("+" markers) (lower panel) atmospheres, respectively. Except for the 0.69um $O_2$ band, all the molecular features are easier to detect for later type stars, due to the more favorable contrast between planet and star. We note that since these targets are at a distance of 1.3 pc, all planets fall outside the IWA for the molecular bands presented; however, this begins to become a concern for planets farther away as the apparent separation between the planet and host star becomes smaller, especially for later type hosts. For the pre-industrial Earth-like atmospheres, $O_2$, $CO_2$, $CH_4$ are all detectable in $< 100$ hours for late-type hosts, and between 100–1000 hours for early type hosts. For the M6V host at 1.3 pc (analogous to Proxima Centauri b), our results suggest that the most detectable bands of $O_2$, $CO_2$, $CH_4$, and $H_2O$ are the 1.27, 1.59, 1.6, and 0.9 $\mu$m bands, respectively. At the minimum, $O_2$, $CO_2$, $CH_4$, and $H_2O$ will require approximately 10, 13, 5, and $\leq 1$ hours to detect, respectively. $H_2O$ is the most accessible molecule for pre-industrial Earth-like cases in our work. In cases with early-type hosts, the $O_2$ A-band at 0.76 $\mu$m is more accessible than the 1.27 $\mu$m NIR band because the SED of the host star peaks at shorter wavelengths, and there are more reflected photons in the 0.76 $\mu$m range than for the 1.27$\mu$m range. Similarly, for late-type hosts the NIR band may be the more detectable target because the SED of the host star peaks at longer wavelengths, and there are more NIR photons than visible. A similar effect was highlighted for transiting planets in Chapter 3 and Currie et al. (2023). CO may be challenging due to its low abundance ($< 1$ ppm) in this atmosphere type, requiring $> 10^3$ hours to detect. $O_3$ does not have the high-resolution structure required for detection via cross-correlation in the wavelengths we tested, as discussed in Chapter 3 and Currie et al. (2023).

The molecular features in the Archean Earth atmospheres we tested have similar detectablity when compared to the pre-industrial Earth cases, with the exception of $O_2$ which is at sufficiently low abundance that it is not detectable in the Archean atmosphere, and $CH_4$, whose higher abundance is more detectable. The lower panel of Figure 4.1 (triangular markers) shows that for an Archean Proxima Centauri b, $CO_2$ and $CH_4$ are detectable in approximately 20 and 2 hours, respectively, and $H_2O$ is accessible in an hour of observation. CO is challenging due to a low abundance, and the Archean atmospheres have little to no $O_2$ and $O_3$ to detect.

#### *4.2.1.2 Uninhabited Worlds and False Positive Discriminants*

In addition to the inhabited planet results, the upper and lower panels of Figure 4.1 also show detectability results for two biosignature false positive scenarios, including an ocean loss world (Luger & Barnes, 2015; Meadows et al., 2018; Leung et al., 2020) (upper panel, "X" markers) and a prebiotic Earth atmosphere (Krissansen-Totton et al., 2018b; Wogan et al., 2020; Meadows et al., 2023) (lower panel, "+" markers). These biosignature false positive scenarios can build up potentially detectable levels of abiotically generated $O_2$ in the case of the ocean loss world, and $CO_2$ and $CH_4$ in the prebiotic Earth scenario. Our results suggest that for the ocean loss scenario, $CO_2$ is accessible in $\sim 17$ hours, similar to the pre-industrial Earth case because of the strong absorption of the $CO_2$ band. While the pre-industrial Earth around an M6V star had an $O_2$ A-band at 0.76 $\mu$m that was less detectable than the 1.27 $\mu$m $O_2$-band, its ocean-loss false positive has an $O_2$ A-band at 0.76 $\mu$m is approximately two orders of magnitude more detectable than the 1.27 $\mu$m band (380 and 60,000 hours for the 0.76 and 1.27 $\mu$m bands, respectively). Our results confirm those of Leung et al. (2020), who also modeled massive 10-bar $O_2$-dominated post-ocean-loss atmospheres, and showed that the 1.27 $\mu$m $O_2$ band will be suppressed due to $O_2$–$O_2$ collisionally-induced absorption. However, we note that all $O_2$ bands, except for the weaker 0.69 $\mu$m band, will be more challenging to detect than for the pre-industrial Earth case. Water vapor is also more challenging to detect for the ocean loss world, despite comparable surface water abundances, requiring 11 hrs for water detection to the pre-industrial Earth-like case's 1 hr. This is due primarily to $H_2O$ line broadening in the dense $O_2$ atmosphere, which reduces the effective number of absorption lines accessible to the cross-correlation, as well as some suppression of the 0.94 $\mu$m $H_2O$ band due to $O_2$–$O_2$ collisionally-induced absorption.

In summary, our results suggest the "false positive" $O_2$ in the ocean loss case may be more challenging to detect than the biological $O_2$ in the pre-industrial Earth case, with the characteristic that the 0.76 $\mu$m band is easier to detect than the 1.27 $\mu$m band, and $H_2O$ may not be as readily detectable for this $O_2$ false positive scenario.

The prebiotic Earth scenario (lower panel, "+" markers in Figure 4.1), can generate detectable $CH_4$ and $CO_2$ in its atmosphere, which can be a false positive for the $CH_4/CO_2$ biosignature pair (Krissansen-Totton et al., 2018b; Meadows et al., 2023). Both $CH_4$ and

$CO_2$ are similarly detectable near 1.6 $\mu$m in the prebiotic Earth case as in the Archean Earth case, requiring approximately 3 and 12 hours of observation, respectively, and $H_2O$ is similarly detectable in both cases and accessible within a few hours of observing. The discriminant between the two cases is the significantly more detectable CO in the prebiotic Earth case, which requires only 13 hours of observing time, as opposed to $\sim 10^4$ hours in the inhabited Archean case. This high abundance of CO relative to $CO_2$ and $CH_4$ is an indicator that the $CH_4$ could be volcanic (Wogan et al., 2020). We discuss the implications of molecular detections and non-detections for both the inhabited and uninhabited worlds in Section 4.3.

#### *4.2.1.3 Sub-Neptune type atmosphere*

For our simulations of Proxima Centauri b as a sub-Neptune (using GJ1214 b as an analog atmosphere), we find that both the E-ELT and the VLT need of the order of an hour to make a 3-$\sigma$ detection of at least one band of several molecules (Figure 4.2), including $NH_3$, which can be diagnostic of an H-dominated atmosphere. In particular, multiple bands of $CH_4$, $CO_2$, CO, and $H_2O$, as well as the 0.78 $\mu$m $H_2$ feature and the 1.43 $\mu$m band of $NH_3$, may be detectable in as little as an hour or less of observation time using the E-ELT or VLT. We tested the detectablity of these molecular features for both the cloudy and clear cases simulated by Charnay et al. (2015), and find that the detectability of most of the molecules in the cloudy atmosphere are within a few percent— cloudiness does not significantly impact molecular detectability in most cases. This is because high-resolution spectroscopy is sensitive to line cores that allow us to probe higher altitudes above the cloud deck, an improvement over low-resolution spectroscopy where the clouds can raise the spectral continuum and obscure spectral features (Gandhi et al., 2020). The high detectability of species in the GJ 1214 b atmosphere is likely due to two main factors: 1) GJ 1214 b's roughly 3x larger diameter than Earth, which increases the flux of reflected photons, 2) the higher abundances of H-bearing species in the sub-Neptune atmosphere (e.g. $\sim 10^4$ ppm $CH_4$, vs. $\sim 100$ ppm $CH_4$ and little to no $H_2$ and $NH_3$ in the Archean atmosphere) (Charnay et al., 2015).

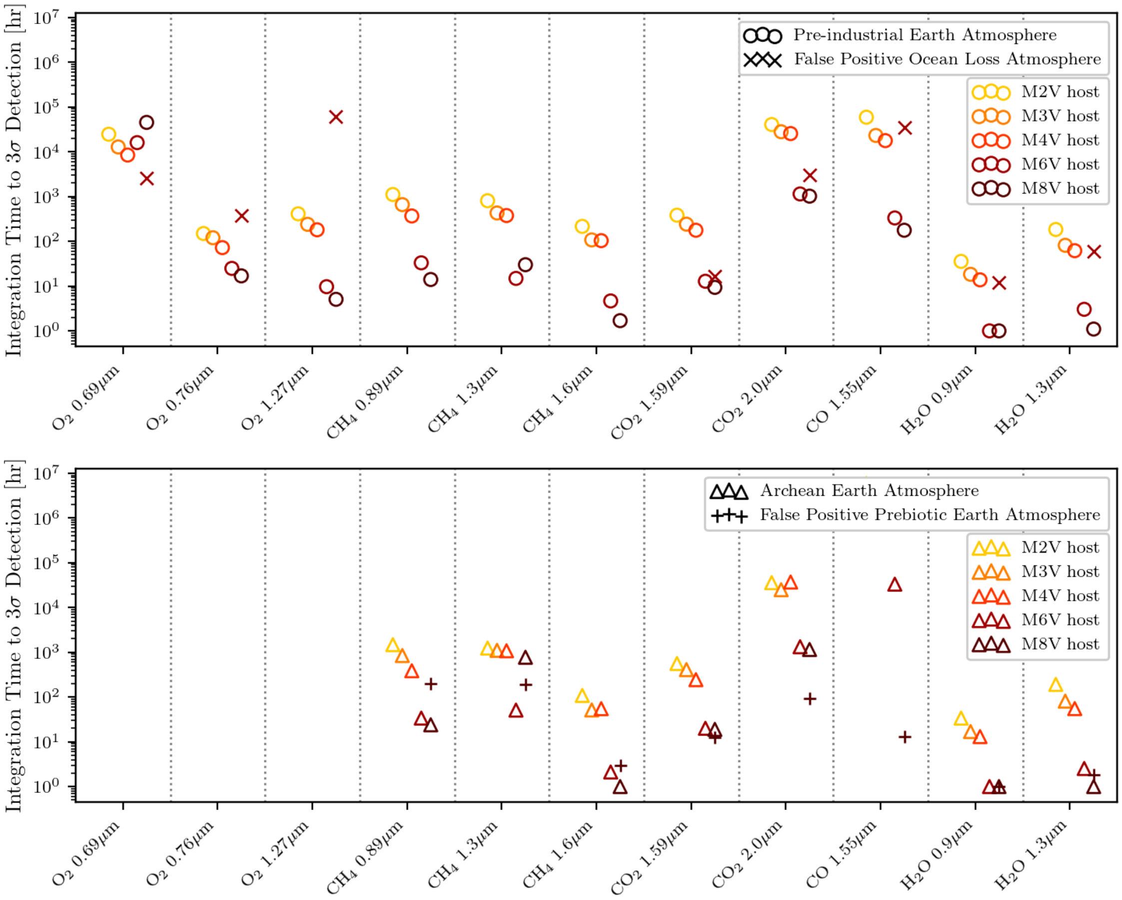

Figure 4.1 ELT integration time required to obtain a $3\sigma$ detection of a range of molecular bands for terrestrial atmospheres orbiting hypothetical 1.3 pc distant M2V–M8V host stars. Circular and triangular markers represent pre-industrial and Archean Earth-like atmospheres, respectively. “X” and “+” markers represent uninhabited ocean loss and prebiotic Earth atmospheres, respectively. This observational scenario assumes each planet receives 66% of Earth’s insolation, the system has a radial velocity of 20 km/s and is 1.3 pc away from Earth, and the observations are made with the E-ELT with an instrument capable of R=100,000 observations with a contrast of $10^{-4}$. While the biosignature disequilibrium pairs $O_2/CH_4$ and $CO_2/CH_4$ are potentially accessible for inhabited worlds, the abiotic gases $O_2$ and $CH_4$ in the uninhabited worlds may also be detectable in false positive scenarios.

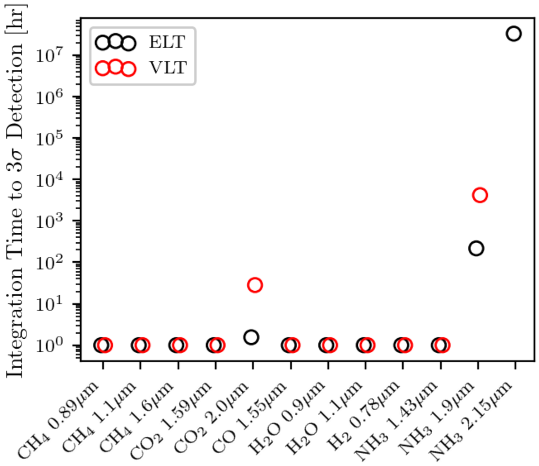

Figure 4.2 Integration time required to obtain a $3\sigma$ detection of a range of molecular bands for a sub-Neptune atmosphere (Charnay et al., 2015) orbiting Proxima Centauri b using simulated E-ELT and VLT observations. The molecules in this atmosphere are highly detectable with the ELT, requiring less than a few hours for most molecular species. The overall high detectability of all molecules, including H-bearing species, may help to identify the atmosphere of Proxima Centauri b as more likely to be sub-Neptune-like, rather than terrestrial, and this may be possible in the near term with smaller aperture observatories.

#### *4.2.1.4 Nearby Target Analogs*

Our previous simulations compared a suite of simulated planetary systems at a fixed systemic radial velocity (20 km/s) and distance (1.3 pc) from Earth, and we now simulate a suite of habitable zone planets with the same planetary system distances and systemic radial velocities, as well as host stars analogous to the nearby stars Proxima Centauri, GJ 1061, Teegarden's Star, and GJ 1002. We present our assumed planetary and stellar properties for these analog targets in Table 4.1, and show the time to a $3\sigma$ detection for our analog targets in Figure 4.3. Although the spectra of these host stars are not included in our suite of self-consistent atmosphere calculations, our range of M dwarf host types includes analogs to these nearby targets. With the exception of Proxima Centauri, which is used as the M6V host for the self-consistent atmospheres in this study, for planets orbiting the other target stars we choose to use atmospheres that are self consistent with the stellar type that is most similar to GJ 1061, Teegarden's Star, and GJ 1002. For Proxima Centauri, GJ 1061, Teegarden's Star, and GJ 1002, we assume system distances of 1.3, 3.67, 3.83, and 4.85 pc, respectively, and system RVs of -22, 1, 68, and -40 km/s, respectively (Anglada-Escudé et al., 2016; Kervella et al., 2017; Dreizler et al., 2020; Vallenari et al., 2023; Zechmeister et al., 2019; Tanner et al., 2012; Mascareño et al., 2023). Note that these atmospheres are for a planet placed in the host star's habitable zone at 67% of Earth's insolation, and so do not necessarily match the orbital distance of the known planets orbiting these stars, although this is a good approximation for Proxima Centauri b (Anglada-Escudé et al., 2016). For the other targets, this approximation may lead to under or overestimates of abundances of photochemically and climatically controlled gases such as $CH_4$, $O_3$, and $H_2O$ (Grenfell et al., 2006).

We find that our Proxima Centauri b analog is likely the best target for atmospheric characterization using the ELTs, followed by the analogs systems for GJ 1061, Teegarden's Star, and GJ1002 with generic habitable zone planets receiving 67% instellation. With the E-ELT, it may be possible to detect $H_2O$ in as little as an hour for a terrestrial atmosphere on the planet Proxima Centauri b (Figure 4.3). This is comparable to the time required to detect $H_2O$ and many other species for a sub-Neptune atmosphere(Figure 4.2). Other molecular species in terrestrial atmospheres such as $O_2$, $CO_2$, $CH_4$, and $H_2O$ may be detectable on the order of $\sim$ 10 hours of observing. For targets in the 3–5 pc range, such as GJ 1061, Teegarden's Star, and GJ 1002, the molecules $O_2$, $CO_2$, $CH_4$, and $H_2O$ may require on the order of 10–100 hours of observing, but will likely still be detectable within a few real-time years when the ELTs come online.

### *4.2.2 Systemic, Instrument and Observatory Dependencies*

We now test the dependence of molecular detectability on four key parameters, including the distance and radial velocity of the exoplanetary system, stellar light suppression efficiency, and the total collecting area of the observatory. In addition to IWA considerations, which are presented broadly in Figure 2.12 and more specifically in Figure 4.4, molecular detectability is most sensitive to these four variables, and by testing how detectability scales with these parameters we can predict the first-order performance of the ELTs to characterize terrestrial exoplanet atmospheres in a range of observational scenarios. To illustrate these effects, we present detectability as a function of these four parameters for only pre-industrial Earth like atmospheres in Figures 4.5, 4.6, 4.7, and 4.8. Molecular detectability will ultimately be limited by the number of target photons we are able to collect on the detector, a prime motivation to construct the ELT class of observatories.

#### *4.2.2.1 Distance Dependence*

In Figure 4.5, we plot the observing time required for a $3\sigma$ detection of select molecular bands from Section 4.2.1 as a function of distance. We assume these pre-industrial Earth-like atmospheres orbit M2V–M8V host stars with 20 km/s systemic RVs, and are observed using E-ELT instrumentation capable of R=100,000 and a contrast ratio (C) of $10^{-4}$. For each host star curve, we compute the time to detection for a grid of 20 evenly-spaced distance values between 1 and 10 pc, then fit these values to a curve, which is ultimately plotted in

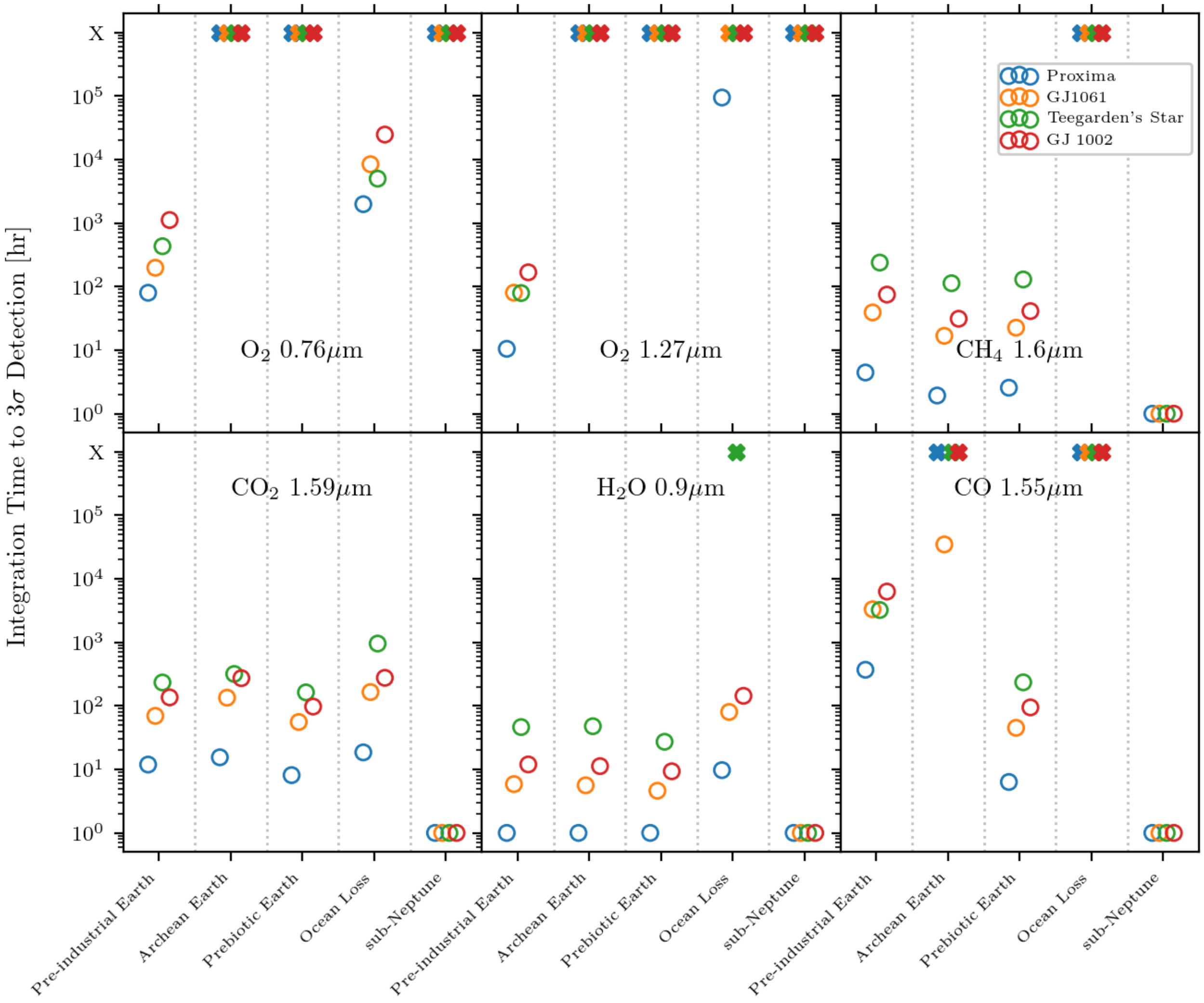

Figure 4.3 Integration time to a $3\sigma$ detection for a range of terrestrial atmosphere types on Earth-sized planets orbiting analog nearby targets. Each panel represents a different molecular band, and each colored ring represents a different nearby host star/planet analog. A sub-Neptune version of Proxima Centauri b is included for comparison. The most favorable terrestrial target will be Proxima Centauri b due to its close proximity to Earth, followed by planets orbiting GJ 1061, Teegarden's Star, and GJ 1002. An "X" symbol at the top of the panel indicates an undetectable molecular feature. We may be able to detect several molecules within 100 hours of observing each target.

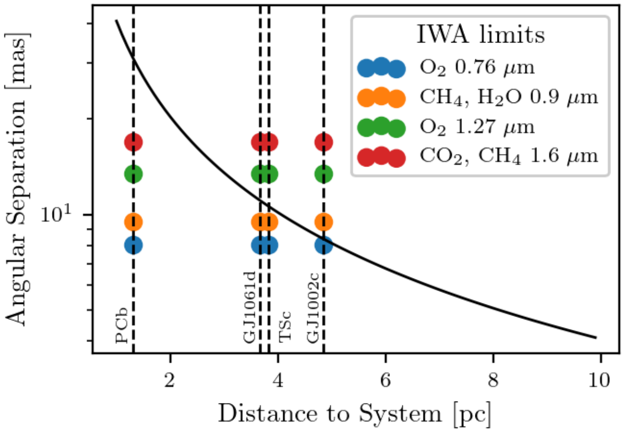

Figure 4.4 Angular separation as a function of distance for a mid-type M-dwarf planet in the HZ (black curve), and 39 m ELT IWA limits for most detectable molecular species (colored markers) for each of the case study analog systems in this work, assuming an IWA of 2 $\lambda/D$. For each case, if the IWA limit marker falls below the black curve, the associated molecular bands are outside of the IWA and are therefore potentially accessible to the ELT. Markers that fall above the black curve represent molecular bands that fall inside of the IWA, and are therefore not accessible.

the panels. As expected, the curves in Figure 4.5 suggest that time to detection scales as $d^2$, where $d$ is distance to the system. For early-type hosts, it may be challenging to detect molecular features in planetary atmospheres beyond 5 pc away from Earth. Planets around late type hosts may be amenable to characterization beyond 5 pc, but obtaining multiple molecular species detections beyond 10 pc may be challenging, some requiring $> 10^3$ hours; however, we note that the IWA limit will significantly hinder our ability to characterize later type M dwarf hosts beyond 5 pc (see Figure 2.12). For example, at 5 pc, $O_2$, $CH_4$, and CO require $> 10^3$ hours and $H_2O$ requires $> 10^2$ hours for early type systems, while these molecules are all still accessible to late type systems, barring IWA constraints. At 10 pc, late type systems require $10^3$ hours for $O_2$ (0.76 $\mu$m) and CO, $> 10^2$ hours for $O_2$ (1.27 $\mu$m), $CH_4$, and $CO_2$, and $> 10$ hours for $H_2O$. However, late type hosts have habitable zones that are closer to the star, and IWA constraints may begin to limit our ability to resolve the planet signal for $>$ 5pc distant targets (Figure 2.12).

#### *4.2.2.2 System RV Dependence*

Following López-Morales et al. (2019) and Hardegree-Ullman et al. (2023), we explore the impact of system RV on integration time. Figure 4.6 shows the number of hours to a $3\sigma$ detection as a function of system RV for pre-industrial Earth-like planets around M2V–M8V host stars at quadrature. This simulation assumes that the target system is at a distance of 1.3 pc, and is observed with the E-ELT with instrumentation capable of R=100,000 and C=$10^{-4}$. The total RV of the planet can play a large role in the detectability of a molecular feature because it controls the degree of separation or overlap between the target and telluric features, which can prevent planet/telluric line separation (López-Morales et al., 2019; Hardegree-Ullman et al., 2023). In practice, the instantaneous RV of the planetary target will depend not only on the intrinsic radial velocity of the host system, but also the barycentric radial velocity, i.e. the radial velocity due to the Earth's position around the Sun relative to the target, and the RV of the planet as a function of its orbital position. The planet's instantaneous radial velocity can be on the order of the host star's radial velocity,

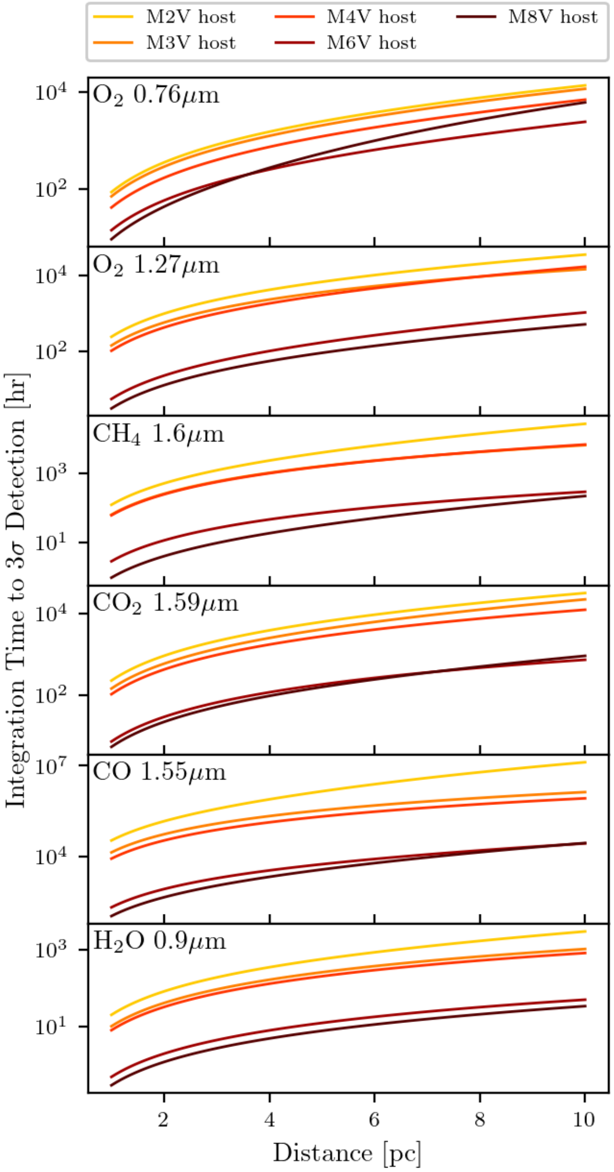

Figure 4.5 Time to a $3\sigma$ detection as a function of distance to the system for pre-industrial Earth atmospheres orbiting M dwarf hosts with systemic RVs of 20 km/s, observed with the E-ELT with instrumentation capable of R=100,000 and C=$10^{-4}$. Time to detection scales as $d^2$. Early type targets beyond 5 pc away may not have readily accessible molecular features, but late-type targets may be reasonably accessible for up to 10 pc. For this plot, the effects of telescope inner working angle have been neglected.

especially at quadrature, and our ability to separate the telluric and target spectra will depend strongly on both the host star and planetary RVs.

While the planetary RV changes as it orbits its host star, the host star RV (systemic RV), is fixed. To illustrate the dependency on the system RV of the host star, we hold the planet at quadrature where its maximum RV occurs and test the molecular detectability over a grid of host star system RVs in Figure 4.6. In most panels of Figure 4.6, a spike in observation time occurs near $\sim$ 50km/s and spans $\sim$ 10 km/s, due to significant line blending between the telluric and target spectra that significantly hinders detection, a result also seen by López-Morales et al. (2019) and Hardegree-Ullman et al. (2023). The spikes in observation time for the different host stars are slightly offset from one another because the planet's orbital distance, and thus its RV at quadrature, is set according to the position of the habitable zone— the habitable zones of late type stars are closer in than early type stars. Note that the panel in Figure 4.6 showing CO detectability does not show maxima near 50 km/s as in the other panels—any line blending that occurs due to the systemic RV does not significantly affect its detectability, because of the low telluric CO abundance ($\sim 50 - 100$ ppb). In summary, as in López-Morales et al. (2019) and Hardegree-Ullman et al. (2023), we find that total observation time may be reduced by minimizing the level of line blending for a given target. This can be achieved by using a higher spectral resolution instrument, selecting for targets with optimal systemic velocities, observing the planet at different orbital positions that minimize the amount of line blending, or observing the target seasonally if the barycentric RV has a significant Doppler shifting effect on the target.

#### *4.2.2.3 Stellar Suppression Performance*

We also explore the impact of instrument starlight suppression (contrast ratio) on exposure time needed to achieve a $3\sigma$ detection, and plot exposure time as a function of contrast ratios spanning $10^{-5}$ and $10^{-3}$ in Figure 4.7 for pre-industrial Earth-like atmospheres orbiting a range of M dwarf hosts. As expected, increasing the contrast ratio (smaller values) decreases the time required to reach the 3-$\sigma$ detection because this significantly reduces the stellar

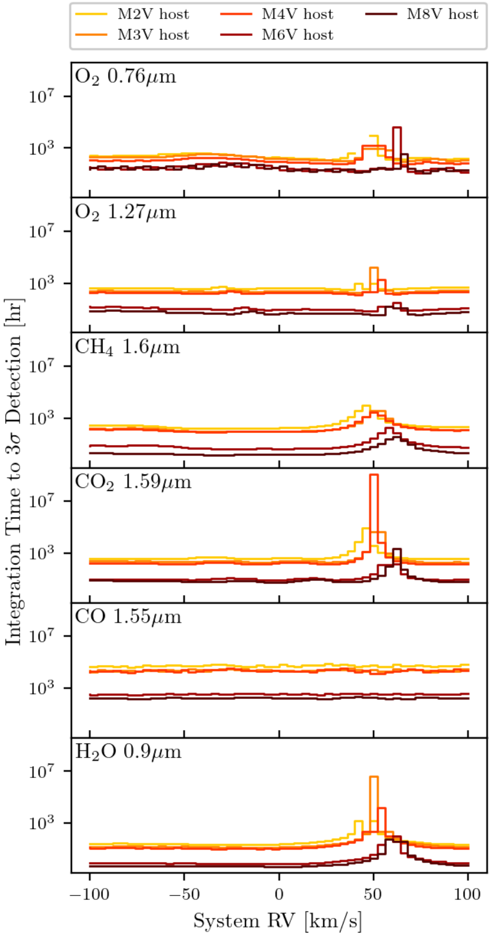

Figure 4.6 Time to a 3$\sigma$ detection as a function of system RV for pre-industrial Earth atmospheres orbiting M dwarf hosts. The host star is assumed to be 1.3 pc away, and observed with E-ELT instrumentation capable of R=100,000 and C=$10^{-4}$. Our ability to detect molecular features depends strongly on the degree of telluric/target line blending, and will be a consideration for minimizing the total observation time to detect molecular features in future observing campaigns by either vetting targets for non-optimal systemic velocities, observing the planet at orbital positions that minimize line blending, or taking into account observational seasonality if the barycentric velocity plays a significant role for a particular target.

component of the noise budget. Improvements in time to detection are up to two orders of magnitude better for $10^{-5}$ as opposed to $10^{-3}$ contrasts.

#### *4.2.2.4 Observatory Dependence*

Here, we simulate the detectability of select molecular features as a function of telescope collecting area, and in Figure 4.8 we report the time to $3\sigma$ detection for pre-industrial Earth atmospheres orbiting a range of M dwarf hosts. We compute the time to detection for a suite of 10 collecting areas ranging from the VLT (8.2 m diameter, 53 $\mathrm{m}^2$ collecting area) to a hypothetical 100 m diameter ($\sim$ 7900$\mathrm{m}^2$ collecting area) telescope (e.g. Dierickx & Gilmozzi, 2000). The diameters of current and future observatories, as well as a calculation for simplistically combining observations using all three planned ELTs, are shown as vertical lines in Figure 4.8, and are labeled in the top panel. Increasing the collecting area from a VLT-sized telescope to the ELT class yields an improvement in time to detection by at least an order of magnitude in all cases. Combining ELT observations for a single target can decrease overall time to molecular detection by up to about an order of magnitude in some cases.

## ***4.3 Discussion***

Our results show that a range of molecular features that can be used to identify terrestrial planets, and that serve as signs of habitability, biosignatures and abiotic processes, may be detectable in ELT reflected light observations of nearby exoplanets. Here we discuss what could be learned about terrestrial exoplanets from these observations, as well as recommendations for optimal targets and observing considerations and protocols.

### *4.3.1 Characterizing Terrestrial Exoplanets in Reflected Light From the Ground*

The ELTs will provide the first opportunity to identify and study the atmospheres of non-transiting terrestrial exoplanets, thereby enabling the search for atmospheres, habitability

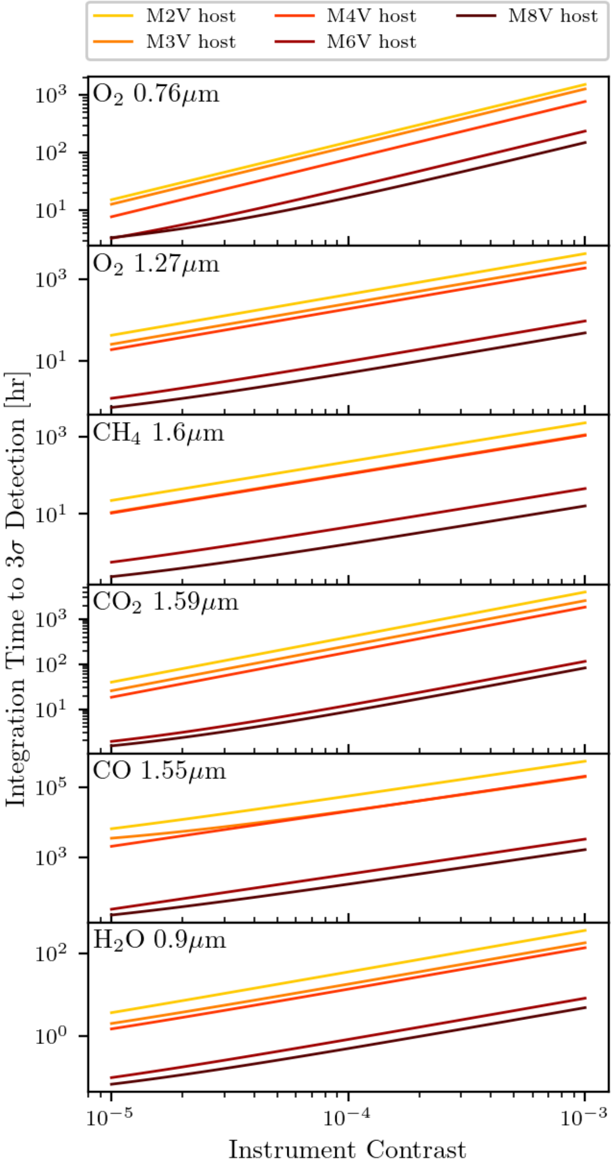

Figure 4.7 Time to a $3\sigma$ detection as a function of instrumental contrast for pre-industrial Earth atmospheres orbiting M dwarf hosts for an E-ELT with instrumentation capable of spectral resolution R=100,000. The M dwarf hosts are assumed to be 1.3 pc and have systemic RVs of 20 km/s.

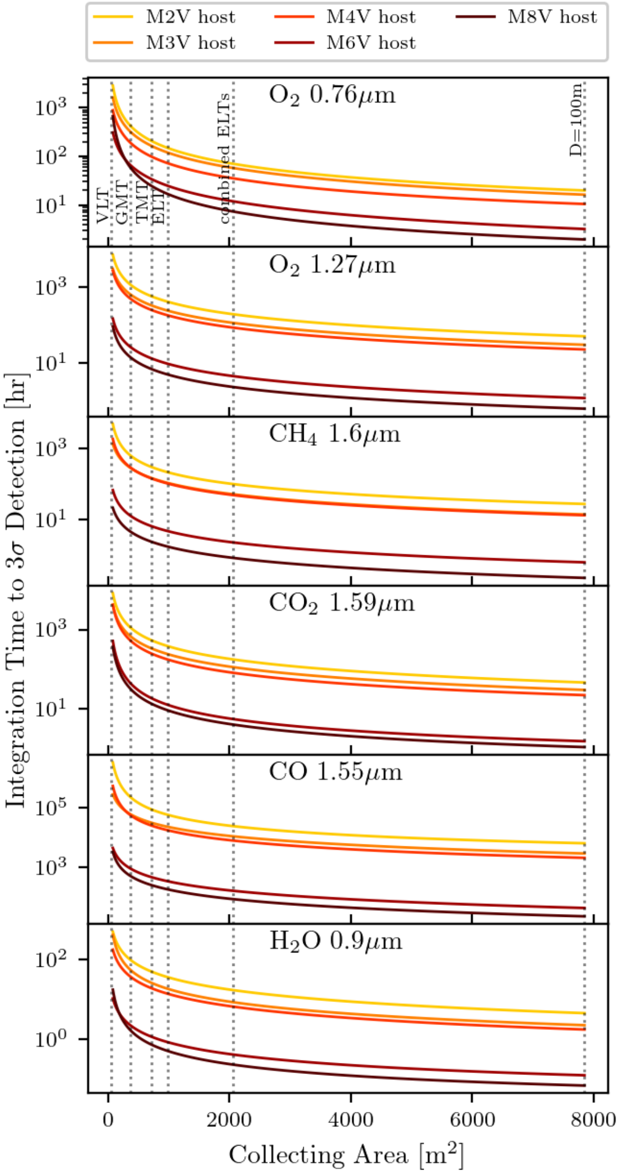

Figure 4.8 Time to a 3$\sigma$ detection as a function of telescope collecting area for pre-industrial Earth atmospheres orbiting M dwarf hosts 4.0 pc away with systemic RVs of 20 km/s, observed with with instrumentation capable of R=100,000 and C=$10^{-4}$. Current or planned telescopes are shown as dashed lines and labeled in the top panel. As expected, larger apertures improve the time to detection in all cases.

Table 4.1. Nearby analog habitable zone planet system properties

| Target | Distance [pc] | System RV [km/s] | Analog Stellar Host Type | Separation at quadr |
|---|---|---|---|---|
| Proxima b | 1.3[a] | -22[b] | M6V | 31 |
| GJ 1061 d | 3.67[c] | 1[d] | M6V | 11 |
| Teegarden's Star c | 3.83[e] | 68[f] | M4V | 11 |
| GJ 1002 b/c | 4.85[g] | -40[h] | M6V | 8.4 |

References. — [a]Anglada-Escudé et al. (2016), [b]Kervella et al. (2017), [c]Dreizler et al. (2020), [d]Vallenari
[e]Zechmeister et al. (2019), [f]Tanner et al. (2012), [g]Mascareño et al. (2023), [h]Vallenari et al. (2023),

and life. These near-term observations will yield valuable lessons learned for the development of future instrumentation and the upcoming Habitable Worlds Observatory NASA flagship mission.

#### *4.3.1.1 Discriminating Terrestrials and Sub-Neptunes*

Determining whether a planet is in fact terrestrial and not a sub-Neptune is the first step in terrestrial exoplanet characterization, and this process will not necessarily be straightforward for direct imaging targets, whose size and true mass may be unknown. Transit observations are potentially less ambiguous, as they can provide precise measurements of a planet's size (e.g. Seager & Mallen-Ornelas, 2003), and statistical arguments based on the known properties of similar sized planets can then be used to infer whether or not a planet is terrestrial (e.g. Rogers, 2015; Martínez et al., 2021). However, for direct imaging targets in reflected light, the size of the planet will be degenerate with its albedo, and although extremely large targets can likely be ruled out, planetary brightness alone will likely lack the precision needed to discriminate between terrestrial and sub-Neptune sized planets for directly imaged targets (e.g. Feng et al., 2018; Carrión-González et al., 2020). Similarly many non-transiting, direct imaging targets are discovered with radial velocity, which can only return a mass that is a lower limit, due to the unknown inclination and therefore observed radial velocity component of the planet's orbit (Hatzes, 2016). However, it has been proposed that determining the planetary mass and inclination through high-resolution spectral observations could be achieved by either monitoring the planetary orbit via molecular detections over a timeseries of observations and fitting an orbital model (e.g. Rodler et al., 2012), or observing the planet at quadrature to measure the planetary semi-amplitude and using the RV-measured stellar semi-amplitude to solve for the planetary mass and inclination (Lovis et al., 2017). However, a measured mass, or mass range, that spans the two planetary populations may leave these measurements ambiguous as to the nature of the planet. Here, we instead investigate discriminating terrestrials from sub-Neptunes by characterizing the atmosphere via spectroscopy to more definitively confirm or rule out a sub-Neptune.

Our results show that sub-Neptunes may be readily discriminated from potentially terrestrial planets with high-resolution direct imaging spectroscopic observations of reduced gases, and that the ambiguous nature of RV-detected Proxima Centauri b could be conclusively resolved in as little as a night of observing. We also show that $CO_2$ and $H_2O$ are comparatively detectable in sub-Neptune and terrestrial atmospheres, and so are poor discriminants for terrestrial worlds. For the sub-Neptune atmosphere used in this study, which is shown in Figure 2.10 (Charnay et al., 2015), our results show that the molecular bands of reduced gases including $NH_3$, $CH_4$, $H_2$ and CO may be detectable at a 3-$\sigma$ level in as little as an hour of observation for bands between 0.7 and 1.4 $\mu$m (Figure 4.2). Moreover, reduced gases such as $NH_3$ and $H_2$ are much less likely to be seen in an oxidizing terrestrial atmosphere, such as the Earth's atmosphere throughout time, and the detection of reduced gases may allow us to discriminate an atmosphere with a primarily reducing atmosphere from one with a primarily oxidizing atmosphere. We also found that $CO_2$ was more detectable in the sub-Neptune atmosphere, as its lower abundance was more than compensated by the size of the sub-Neptune. Water vapor was also comparably detectable for both the sub-Neptune and the 1.3 pc distant terrestrials, requiring as little as an hour of observing time (Figure 4.3), or significantly more detectable in the sub-Neptune than in more distant terrestrials. Searching for molecules indicating a sub-Neptune atmosphere could also be done in the near term using a VLT-sized observatory also for relatively little observing time (Figure 4.2), and ruling out a sub-Neptune atmosphere before the ELTs come online may be a strong observing strategy (see Section 4.3.2). Since abundant water vapor may be a common feature of most sub-Neptune type atmospheres (e.g. Bean et al., 2021), our results suggest that $H_2O$ and $CO_2$ are very poor discriminants for terrestrial vs sub-Neptune exoplanet identification in reflected light observations. Given that the inclination ambiguity in the RV mass means that there may be at least a 10% likelihood that Proxima Centauri b is a sub-Neptune (Bixel & Apai, 2017), the high detectability of the sub-Neptune atmosphere type should allow us to conclusively rule out the sub-Neptune nature of Proxima b with only a few hours of observing. This approach could also be considered for other targets with ambiguous masses.

#### *4.3.1.2 Habitability assessment*

For a terrestrial exoplanet the presence of greenhouse gases can provide insight into its climate and habitability, and we find that the greenhouse gases $H_2O$, $CO_2$ and $CH_4$ are likely accessible to the ELTs for nearby non-transiting targets. Sufficient atmospheric water vapor can contribute to the greenhouse warming needed to maintain liquid surface water (Kasting et al., 1993), and our results show that 0.9 $\mu$m $H_2O$ is the most accessible band for most terrestrial targets (Figure 4.3), needing only $\leq 1$ hr of integration time for a 3-$\sigma$ detection on a terrestrial Proxima Centauri b. Additionally, an $H_2O$ detection, while not guaranteeing surface liquid water, could make surface liquid water more likely, and liquid water is thought to be critical for developing and supporting life (e.g. Ball, 2008; Pohorille & Pratt, 2012). Given its relative ease of detection, we recommend the 0.9 $\mu$m $H_2O$ band as a prime target for initial terrestrial atmosphere characterization efforts using the ELTs. However, as described in the previous section, considering $H_2O$ as a habitability indicator necessitates a degree of caution until the terrestrial/sub-Neptune degeneracy can be broken.

$CO_2$ and $CH_4$ are also powerful greenhouse gases that both impact planetary climate and support biosignature detection, and these are likely accessible to the ELTs for approximately 3–10x more observing time than $H_2O$ (on the order 10 of hours for Proxima Centauri b). In particular, in Earth-like environments $CO_2$ may be strongly tied to geological processes and so may also be indicative of an active carbonate–silicate cycle (Walker et al., 1981; Kasting et al., 1993; Kopparapu et al., 2013), which could buffer the planetary climate through geologic time. As is the case for water though, $CO_2$ may also be readily detectable in sub-Neptune atmospheres (Figure 4.3), and so it is important to discriminate terrestrial from sub-Neptune atmospheres (see Section 4.3.1.1) before attempting to interpret a $CO_2$ detection.

#### *4.3.1.3 Biosignatures*

We find that two biosignature disequilibrium pairs, $O_2/CH_4$ and $CO_2/CH_4$, may be accessible to the ELTs. Detecting both $O_2$ and $CH_4$ would reveal the canonical $O_2$–$CH_4$ biosignature pair, indicating a chemical disequilibrium and evidence for active fluxes from both oxygenic photosynthetic, and methanogenic organisms (Hitchcock & Lovelock, 1967; Meadows et al., 2018). The presence of both $CO_2$ and $CH_4$ may reveal an active flux of $CH_4$ that is likely higher than expected for Earth-like geological activity alone (Krissansen-Totton et al., 2016, 2018b). Our reflected light results show that the biologically-mediated $CO_2/CH_4$ disequilibrium is comparably detectable in both the Archean and PIE atmospheres (within a factor of 2–3) making it a long-lived biosignature, a similar result to that of Meadows et al. (2023) for simulations of JWST transmission observations of TRAPPIST-1. The $O_2/CH_4$ disequilibrium is only detectable in the PIE case, which has a photosynthetic biosphere. $O_2$, $CH_4$, and $CO_2$ may require more observation time than $H_2O$, but are still accessible within approximately 100 hours for most nearby targets with a pre-industrial Earth-like atmosphere. For Proxima b, $\sim 10$ hours of observing would be needed to detect these biosignature pairs if the molecules can be observed simultaneously, with more distant planets requiring either more time, or the coaddition of data from multiple observatories. The most accessible spectral features for these molecules will be $O_2$ at both 0.76 $\mu$m and 1.27 $\mu$m, $CH_4$ at 0.89, 1.3, and 1.6 $\mu$m, and $CO_2$ at 1.59 $\mu$m.

#### *4.3.1.4 Biosignature False Positive Discrimination*

To study our ability to gather environmental context to identify false positives for biosignatures we also examined two worlds that may produce false positive biosignatures similar to the true biosignatures seen in our inhabited Archean-like and modern pre-industrial Earth-like planets. These false positive worlds include a prebiotic Earth-like world with high-volcanic outgassing from a more reducing mantle, which produces a false positive for the $CH_4/CO_2$ disequilibrium pair (Meadows et al., 2023), and a habitable zone world with a dense ocean-loss $O_2$ atmosphere and volcanic outgassing that retained an ocean, and that produces a strong abiotic $O_2$ signal (Meadows et al., 2018).

Our results show that for reflected light observations, the false positive case for the $CO_2/CH_4$ pair is more readily confirmed than the $O_2$ false positive case considered, which is instead much harder to detect than the true inhabited case. For the prebiotic Earth-like world, the $CO_2$ was comparably detectable to the Archean-like Earth for the Proxima b case, and the $CH_4$ was only a factor of $\sim 5$ less detectable, constituting a plausible false positive. However, the CO discriminant that would indicate vigorous volcanic outgassing from a more reducing mantle (Krissansen-Totton et al., 2018b; Thompson et al., 2022) is detectable with only 10 hours of observing for the prebiotic Earth atmosphere modeled here, allowing us to confirm the likelihood that we are observing a $CO_2/CH_4$ false positive atmosphere relatively quickly.

In comparison, for the post-ocean-loss planet, we find that the 10 bars of $O_2$ in its atmosphere are significantly less detectable than the 0.2 bars of photosynthetically-generated $O_2$ in the pre-industrial Earth atmosphere, confirming similar results from (Leung et al., 2020). In the case of the 0.76 $\mu$m band, 20 times more observing time would be needed to detect this $O_2$ band in the ocean-loss vs inhabited case, and four orders of magnitude more observing time would be needed for the 1.27$\mu$m $O_2$ band making it basically undetectable. This perhaps counterintuitive behavior is due to strong absorption in the bands and additionally strong $O_2$-$O_2$ collisionally-induced absorption at wavelength coinciding with the 1.27$\mu$m $O_2$ band (Leung et al., 2020) which suppresses the high-resolution structure of these bands. This makes $O_2$ in the false positive atmosphere less detectable than that for the pre-industrial Earth modern photosynthetic biosphere, and reduces the likelihood that a false positive is detected, but if it is, the much stronger suppression of the 1.27$\mu$m band is diagnostic of a multi-bar $O_2$ atmosphere. In addition, pressure-broadened water bands in the 10 bar post-ocean-loss environment require $\sim$ 10 more hours to detect than the $\sim$ 1 hr needed for the Proxima b habitable environments, and the highly-oxidizing post-ocean-loss atmosphere also has undetectable $CH_4$. Therefore, even if the weaker signals from the ocean-loss atmosphere are detected, detection of the $O_2$ 0.76$\mu$m band, but not 1.27$\mu$m band, plus lack of or severe depletion of $CH_4$ and $H_2O$ observed in a comparable exposure time, would make biological processes as the origin of the observed $O_2$ much less likely.

### *4.3.2 Recommendations for an Observing Protocol*

Given the detectability of molecular features in terrestrial and sub-Neptune atmospheres, we have developed an observing protocol detailing our recommendations for characterizing terrestrial planets and searching for signs of habitability and life with the ELTs, with particular emphasis on Proxima Centauri b since this is likely the most amenable to thorough atmospheric characterization. The first step in our observing protocol is to discriminate a terrestrial atmosphere from a sub-Neptune atmosphere via the detection of $NH_3$ or other reduced and/or H-bearing species, such as $H_2$,$CH_4$ and CO, which can be optimized if the detector has an extended wavelength range between 0.5 and 2.0 $\mu$m— if the planet is more sub-Neptune-like, the atmosphere will likely be highly detectable, and many species, may be accessible in a single night of observing, allowing us to rapidly and conclusively identify the atmosphere as that of a sub-Neptune. If $NH_3$ or other reduced species are not readily detected, this makes a terrestrial nature more likely, and we recommend followup observations to search for $H_2O$ since it is likely detectable in about an hour of observation if Proxima Centauri b has a terrestrial atmosphere. A detection of water vapor could help establish habitability and serve as a false positive indicator for a photochemical production of $O_2$, especially because the $H_2O$ band probes almost the entire atmospheric column, down to the very near surface.

Next, $CH_4$, $CO_2$, and $O_2$ can all be observed simultaneously within about 10 hours of observation time if it is possible to observe a broad 0.5–2.0 $\mu$m wavelength range— otherwise, choosing to search for only two, either $CO_2/CH_4$ or $O_2/CH_4$, could provide pathways for detecting biosignatures or ruling out false positive cases. Searching for $CO_2$ and $CH_4$, which absorb in a similar wavelength range, may be convenient if the instrument only has a narrow NIR bandpass. If $CH_4$ and $CO_2$ are positively identified in an atmosphere, we recommend searching for CO next. A detection of CO is possible in $\sim$ 10 hours for Proxima Centauri b for only the prebiotic Earth scenario in this work, and could indicate that the $CH_4$ is abiotic (volcanically-produced) and that this is a false positive atmosphere. Conversely, a non-detection of CO in $>$ 10 hours could help rule out the biosignature false positive for Proxima Centauri b.

Searching for $O_2$, and the $O_2/CH_4$ biosignature pair, may also be possible simultaneously, however this would require the broader 0.5–2.0$\mu$m wavelength coverage because the absorption bands span the visible and NIR, respectively. Nevertheless, this biosignature pair may be more accessible for M dwarf systems than for G-dwarf systems (Gilbert-Janizek et al., 2024) due to the enhanced buildup of $CH_4$ in M dwarf planet atmospheres (Segura et al., 2005). If $O_2$ is detected in the visible, and not in the NIR, this could indicate that the atmosphere is an uninhabited ocean loss type world (Leung et al., 2020), and we find that a non-detection of $CH_4$ and weak detection of $H_2O$ would support this interpretation. Conversely, a strong detection of $H_2O$ and the $O_2$ 1.27 $\mu$m band rules out a massive $O_2$ atmosphere; however, determining the absolute abundance of $O_2$ would allow for a more definitive interpretation.

### *4.3.3 Realistic Observing Considerations*

Here we have given detectability in total observing time in hours, but real-world consideration of observatory overheads, scheduling, telluric subtraction and weather, mean that hours of observing may take days to years of real-world time to complete. We use a simplistic parameterization to model detectability as a function of time, and we do not include time lost due to observatory overhead such as slew and readout time, or other weather-related phenomena that can reduce the total available observation time on a given night. Additionally, we have assumed that all observations in this study occur at or near quadrature, which will not always be the case for real observations because of planet phase variability night-to-night, and from the beginning to the end of the night, especially for these M dwarf planets where the orbital period is measured in days. Removing telluric lines will also be a major challenge to overcome for real observations, and our results assume that we can model out the telluric lines. While we make this assumption for our work, there has been significant progress toward understanding how to optimally remove telluric lines (e.g. Cheverall & Madhusudhan, 2024). Additionally, seasonal observability can limit us to certain optimal observing windows. Therefore, our results reflect the most optimistic observational conditions.

#### *4.3.3.1 Nearby Targets*

If we take these realistic observing considerations into account then the hours required to detect molecules transforms into days and years. We use an estimate for the total number of nights available to observe Proxima Centauri b calculated by Lovis et al. (2017): considering the contribution of weather, seasonal observability, and planetary phase, Lovis et al. (2017) estimate that $\sim 20$ nights are available to observe Proxima Centauri b per year. We note $\sim 20$ nights/year is likely a lower limit for 30 m class telescopes because of the $\lambda/D$ advantage gained with a larger telescope. Nevertheless, using this estimate and assuming a 30 year ELT operation lifetime, we will likely have at least 600 nights available to observe Proxima

Table 4.2. Configurations for Figure 4.9 detectability comparison

| Reference | Figure 4.9 panel | Telescope | Resolution | Contrast | Instrument/Background Noise |
|---|---|---|---|---|---|
| Lovis et al. (2017) | a | VLT (8.2m) | 220,000 | $10^{-4}$ | On |
| Vaughan et al. (2024) | b | ELT (39m) | 17,385 | $10^{-4}$ | On |
| Hawker & Parry (2019) | c | ELT (39m) | 150,000 | $10^{-4}$ | Off |
| Wang et al. (2017) | d | TMT (30m) | 100,000 | $10^{-6}$ | On |
| Zhang et al. (2023) | e | ELT (39m) | 1,000 | $10^{-4}$ | On |

Centauri b over 30 years. If we assume 8 hr can be observed in a given night, Figure 4.3 suggests that many molecular targets will likely require less than a few years of operation time with the ELTs. Proxima b may be characterized within days to weeks, and targets further away will likely take weeks to years. Following the suggestion of Hardegree-Ullman et al. (2023), an observing strategy that uses simultaneous observations of a target with more than one ELT could significantly reduce the time to detection, and maximize the molecular features that are accessible (Figure 4.8).

### *4.3.4 Comparison with other work*

Here we compare the results of this study to previous work that predicts the performance of current and future ground-based observatories to characterize terrestrial exoplanets in both reflected light and transit transmission observations.

#### *4.3.4.1 Reflected light observations*

The results of this study are largely consistent with previous work presenting detectability estimates for molecules in an Earth-like atmosphere on Proxima Centauri b. To optimally compare our work to previous work, we simulate molecular detectability by running our detectability pipeline customized with the same or similar observing conditions and modes used in Lovis et al. (2017), Wang et al. (2017), Hawker & Parry (2019), Zhang et al. (2023),

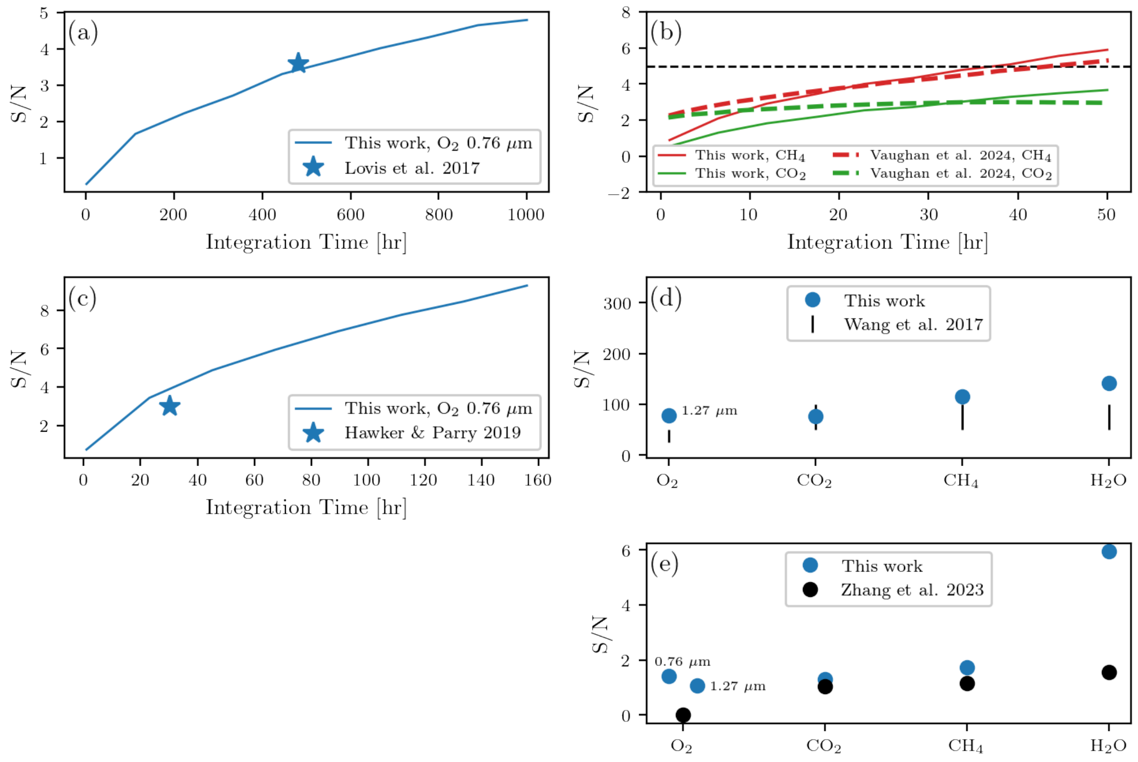

Figure 4.9 Comparison with previous work investigating the detectability of molecular features in an Earth-like atmosphere of Proxima Centauri b. Panels a, b, c, d, and e correspond to comparisons with Lovis et al. (2017), Vaughan et al. (2024), Hawker & Parry (2019), Wang et al. (2017), and Zhang et al. (2023), respectively. The studies we compare with use a variety of observing modes and configurations, which we attempt to control for in our comparisons by using the same or similar input parameters, and we list our assumptions for observing conditions and configurations in Table 4.2. Our results are largely consistent with those of others, with the exception of more optimistic $O_2$ and $H_2O$ detection when compared to Zhang et al. (2023).

and Vaughan et al. (2024). The observing configurations we assume include custom configurations of telescope size, spectral resolution, coronagraphic contrast and instrument and background noise, and are documented in Table 4.2, and the results of our comparison are plotted in Figure 4.9. The panels in Figure 4.9 represent comparisons to the works of Lovis et al. (2017), Vaughan et al. (2024), Hawker & Parry (2019), Wang et al. (2017), and Zhang et al. (2023) (panels a, b, c, d, and e, respectively). We note however that our comparison input spectra were not standardized for abundances with published results, and so discrepancies in the more photochemically-active or variable molecules, such as methane and water vapor, is to be expected.

Lovis et al. (2017) simulate VLT observations of Proxima b, and we find that similar simulations using our detectability pipeline are consistent with their $O_2$ result (see panel a of Figure 4.9), but our work is more optimistic for $H_2O$. Lovis et al. (2017) estimate that a $3.6\sigma$ detection of $O_2$ would require 480 hr of observing, and we match this estimate to within 10%. However, we estimate that it will take a factor of $\sim 10$ less time ($\sim 50$ hr vs. $\sim 480$ hr) to detect $H_2O$ than Lovis et al. (2017) predict because they test only $H_2O$ bands in the 0.6–0.7 $\mu$m region, where $H_2O$ absorption is much weaker than in the 0.9 $\mu$m region where our estimates are made.

Vaughan et al. (2024) simulate ELT HARMONI observations of Proxima Centauri b and target the molecular species $CO_2$ and $CH_4$, and we find that an analogous observational configuration using our pipeline is consistent with their results. In panel b of Figure 4.9, we present this comparison showing very similar trends for both $CO_2$ and $CH_4$. The results of Vaughan et al. (2024) indicate the possibility of some systematics that affect the shape of the curves, which our model does not reproduce— Vaughan et al. (2024) use a highly sophisticated HARMONI noise model, which includes components that can introduce instrument-specific systematics, and this is neglected in our model.

Hawker & Parry (2019) present a range of estimates for the $O_2$ A-band detectability in the atmosphere of Proxima Centauri b using the ELT, and our estimates are within these ranges when using a similar observing configuration. In panel c of Figure 4.9, we plot the estimate of Hawker & Parry (2019), where $O_2$ is detectable at 3 $\sigma$. Our results are plotted as a curve of S/N as a function of integration time, which is within $\sim 30\%$ of the Hawker & Parry (2019) estimate.

Wang et al. (2017) simulate 100 hr observations of Proxima Centauri using a NIR detector on a 30 m telescope, and we find that our results are roughly consistent with their predictions for $O_2$, $CO_2$, $CH_4$, and $H_2O$ detectability (see panel d of Figure 4.9). Since precise values for molecular detectability were not presented in Wang et al. (2017), we compare to detectability limits estimated from their figures. Since Wang et al. (2017) only simulate NIR observations, we only include an estimate for the 1.27 $\mu$m $O_2$ band in our comparison. The black markers in panel d of Figure 4.9 represent an estimated lower bound on S/N gained from a 100 hr observation using a 30 m telescope, and the top of the arrows represent an upper bound. We find that our results are consistent with the credible detectability regions estimated from Wang et al. (2017).

Zhang et al. (2023) simulate medium resolution (R=1,000) observations of Proxima Centauri b using the ELT, and using a similar configuration, we find that our results are slightly more optimistic by factors of up to 3. Panel e of Figure 4.9 shows this comparison. Because Zhang et al. (2023) simulate a broad wavelength range that covers both the 0.76 $\mu$m and 1.27 $\mu$m $O_2$ bands, we include estimates for both these bands in Figure 4.9. Our results are most consistent for $CH_4$ and $CO_2$. We find major discrepancies when comparing $O_2$ and $H_2O$ detectability. Zhang et al. (2023) report that $O_2$ is undetectable in 10 hrs of observing, while our results show that $O_2$ is detectable using their observational configuration. We also report that $H_2O$ is a factor of 3 more detectable than Zhang et al. (2023). These discrepancies may be due to differences in S/N calculations: our detectability pipeline performs a cross-correlation analysis for many realizations of noise for simulated observations, while the S/N calculations of Zhang et al. (2023) rely on the analytical S/N equation, but identifying a precise cause is challenging without comparing input planetary spectra and analysis pipelines in depth.

We also confirm the results of Leung et al. (2020), who investigated the relative detectability of $O_2$ bands in scenarios with thick post-ocean-loss $O_2$ atmospheres. They and we both find that suppression is expected in the 1.27 $\mu$m $O_2$ band due $O_2$–$O_2$ collisionally induced absorption, while the 0.76 $\mu$m A-band should remain more detectable. This mechanism is an $O_2$ false positive discriminant. While Leung et al. (2020) did not simulate observations with realistic noise, we can confirm that this false positive discriminant is still valid, and possibly detectable, using our more realistic observation simulation and analysis pipeline. We indeed find that the detectability of the 1.27 $\mu$m $O_2$ band is suppressed compared to the A-band, which indicates the dense post-ocean-loss $O_2$ biosignature false positive atmosphere. Further evidence for this case could be gathered by attempting to retrieve the abundance of $O_2$, however we leave this to future work.

#### *4.3.4.2 Transit transmission observations*

In this work, we considered several of the atmospheres used as input for the transit transmission calculations of Chapter 3 and Currie et al. (2023), allowing us to directly assess the benefits and complementarity when observing equidistant targets in reflected light vs. transmission. Observing in reflected light allows us to sample the atmospheric column down to the surface or near surface of a planet, thereby enhancing sensitivity to gases that may be confined to the near-surface, such as $H_2O$. On the other hand, transit transmission observations are sensitive primarily to the upper troposphere and stratosphere of a terrestrial planet, and are not as susceptible to molecular band saturation as in reflected light. Below, we compare the molecular detectability for reflected light (this study) to those we previously calculated for transit transmission (Chapter 3; Currie et al., 2023).

We find that direct imaging targets require an additional step to rule out the planet being a sub-Neptune, as typically a lower limit on the mass is all that is known, compared to usually well-known radii and radius/density relations for transiting exoplanets. However, this additional step will likely only take a handful of observing hours per planet, and so is relatively inexpensive.

Overall the transit transmission technique is more sensitive to most molecules in ter-

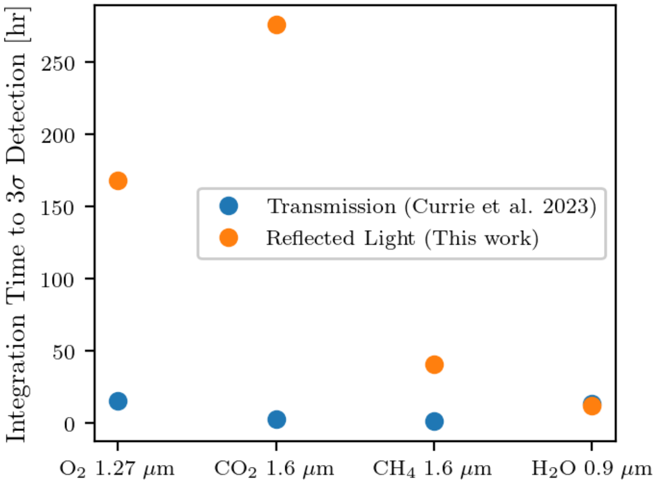

Figure 4.10 Integration time to detect $O_2$, $CO_2$, $CH_4$, and $H_2O$ in a pre-industrial Earth-like atmosphere orbiting an M6V host star 5 pc away using both transmission and reflected light techniques. The transit transmission technique is overall more efficient for detecting $O_2$, $CO_2$, and $CH_4$, but these techniques yield comparable results for $H_2O$ because reflected light observations are able to probe deeper into the atmosphere than in transmission and can detect the more abundance near-surface water.

restrial planet atmospheres when compared to the reflected light technique, for equidistant targets, with the exception of water vapor, which is equally as detectable with the two techniques. Figure 4.10 presents a comparison between the detectability of molecules in a hypothetical pre-industrial Earth-like atmosphere orbiting an M6V star at 5 pc away. We find that significantly more time is required to detect $O_2$, $CO_2$, and $CH_4$ in reflected light for such a target than for transmission observations. To obtain a $3\sigma$ detection for $O_2$, $CO_2$, and $CH_4$, an observer would need to integrate for approximately 13/168, 2/276, and 1/41 hours for transmission/reflected light, respectively. Transmission observations require $\sim 10-100$x less observation time than reflected light observations to detect $O_2$, $CO_2$, and $CH_4$ for a planet at 5 pc away.However, $H_2O$ does not follow this trend for reflected light because reflected light observations are able to probe deeper into the atmosphere to reach the near-surface water, requiring nearly the same amount of observing time (12 hours for reflected light as opposed to 11 hours in transmission).

We also note that because of the drop-off in reflected light sensitivity with planetary system distance, there will likely be very few habitable zone exoplanetary targets for which both transit and reflected light observations will be possible, unless a new transiting M dwarf HZ planet is discovered within 5 pc. Overall, the $CO_2/CH_4$ and $O_2/CH_4$ biosignature disequilibrium pairs may be more accessible in transmission than in reflected light for a planet where both observational techniques are viable, but transiting terrestrial targets closer than 12 pc are unlikely. We are likely to have more and closer targets targets amenable to reflected light studies than transiting targets, and several direct imaging targets within 5pc are already known.

If we compare instead the two best targets with each technique—TRAPPIST-1 e (at 12 pc) for transmission and Proxima Centauri b (at 1.3 pc) for direct imaging—we find that the reflected light technique allows us to access more molecules with fewer observational resources. $O_2$ is more detectable for Proxima Centauri b, requiring at minimum 10 hours, while TRAPPIST-1 e may require 60–100 hours. $CO_2$ and $CH_4$ will likely require a similar time investment for Proxima Centauri b and TRAPPIST-1 e, requiring $\sim$ 5 and $\sim$ 10 hours for each, respectively. However, we note that the $CO_2/CH_4$ biosignature pair is likely readily detectable for both of these targets, but the $O_2/CH_4$ pair is likely best detected for non-transiting planets in reflected light. Finally, $H_2O$ will likely be much more detectable for Proxima Centauri b, requiring nearly 100x less observation time than for TRAPPIST-1 e. Overall, characterizing the nearest non-transiting target Proxima Centauri b will likely require fewer resources than the nearest transiting target, TRAPPIST-1 e.

## *4.4 Conclusions*

In this work, we upgraded the existing SPECTR ELT detectability pipeline to include functionality for high spectral resolution observations of terrestrial exoplanets in reflected light, and applied SPECTR to estimate the detectability of molecular features in simulated observations of five exoplanet atmosphere types, including pre-industrial Earth-like, Archean Earth-like, prebiotic Earth-like, an ocean loss scenario, and a sub-Neptune atmosphere. We find that $O_2$, $CO_2$, $CH_4$, and $H_2O$ may be detectable for nearby non-transiting targets in as little as a few hours of observing with an ELT, and we may be able to readily search for signs of habitability and life, or rule out habitable but uninhabited environments that include biosignature false positive gases, and sub-Neptune like atmospheres. In particular, we show that $CO_2$ and $H_2O$ are comparatively detectable in sub-Neptune and terrestrial atmospheres, and so are poor discriminants for terrestrial worlds. For Proxima Centauri b, which is the prime target for highly detailed atmospheric characterization in the ELT era, if it is a sub-Neptune, this will be readily apparent via detection of reducing molecules like $NH_3$ and $H_2$ which is feasible in approximately an hour of observing with the ELT. For a terrestrial Proxima Centauri b, two biosignature disequilibrium pairs are potentially accessible in $\sim 10$ hours with broad wavelength coverage (0.5–2.0 $\mu$m), including $O_2/CH_4$ and the $CO_2/CH_4$ pairs. We may be able to discriminate biosignature false positives via detection of CO and failure to detect $H_2O$ or $CH_4$ in a comparable amount of observation time.

Multiple other targets within 5 pc away will likely be amenable to atmospheric characterization using this technique at the cost of approximately an order of magnitude more observation time. We compared the efficacy of transmission vs reflected light observations for characterizing terrestrial exoplanets, and while transmission observations were more sensitive to molecular bands for a hypothetical equidistant target, in reality direct imaging has more and closer targets to study. While terrestrial exoplanet characterization is inherently challenging, the ELT era will likely offer the first opportunities to study the atmospheres of non-transiting terrestrial exoplanet targets, and search for signs of habitability and life on our nearest exoplanetary neighbors.

## *4.5 Acknowledgements*

The authors thank Andrew Lincowski and Drake Deming for helpful discussions during the writing phase that improved the quality of this work, and C. Evan Davis, who ran the original climate–photochemistry calculations for the the pre-industrial Earth and Archean Earth atmospheres used here. This work was performed by the Virtual Planetary Laboratory Team, a member of the NASA Nexus for Exoplanet System Science (NExSS), funded via the NASA Astrobiology Program grant No. 80NSSC18K0829. This work was also partially supported by the Astrobiology Center, Japan. The simulations in this work were facilitated though the use of advanced computational, storage, and networking infrastructure provided by the Hyak supercomputer system at the University of Washington.

# Part II

# RETRIEVING MOLECULAR ABUNDANCES WITH THE ELTS

# Chapter 5

# DEVELOPING AND DEMONSTRATING A NOVEL RETRIEVAL FRAMEWORK FOR SIMULATED HIGH RESOLUTION OBSERVATIONS OF TERRESTRIAL EXOPLANETS

*Portions of this chapter are being prepared for submission for publication in collaboration with Victoria S. Meadows and Jacob Lustig-Yaeger. The results in this study are preliminary.*

## ***Summary***

The upcoming ground-based extremely large telescopes (ELTs) will have the sensitivity to characterize the atmospheres of nearby terrestrial exoplanets, and will be powerful near-term tools for searching for signs of habitability and life outside of the Solar System. Previous work has suggested that the ELTs will be sensitive to a range of molecular features, including $O_2$, but our ability to constrain the abundance of molecules in spectra of terrestrial atmospheres is currently untested. In particular, determining the abundance and total pressure of $O_2$ can provide clues as to its abiotic or biological origin. In this work, we simulate 100 hr ELT observations of a range of terrestrial atmospheres for Proxima Centauri b, with $O_2$ abundances ranging from 1% to 50% in a 1 bar atmosphere, and 95% in a 10 bar atmosphere, and then apply an upgraded retrieval framework to test how sensitive the ELTs will be to $O_2$ abundance. We find that our retrieval framework can constrain the $O_2$ abundance for concentrations $\leq$ 21% in a 1 bar atmosphere, however measuring $O_2$ abundances for cases with greater than 21% in 1-bar and 10-bar atmospheres may be challenging. Using the retrieved abundance information, we may be able to discriminate modern Earth-like biological $O_2$ from $O_2$ generated via mechanisms that may produce less than 21%, abiotic $O_2$. However, discriminating $O_2$ buildup in a post ocean loss atmosphere may be challenging due to significant saturation in the $O_2$ bands, and other methods for discriminating this scenario may be required. While previous work has shown that a range of molecular features may be detected in terrestrial exoplanet atmospheres, this study demonstrates for the first time that it may be possible to determine their abundances, providing an avenue for highly detailed atmospheric characterization studies for terrestrial, potentially habitable worlds within the next decade.

## *5.1 Brief Introduction*

In this chapter, we upgrade an existing retrieval framework to include cross-correlation capabilities for high-resolution ground-based observations. We simulate ELT data for a range of terrestrial atmospheres orbiting Proxima Centauri with varying levels of $O_2$ abundance. Applying our retrieval framework to the simulated data, we attempt to retrieve atmospheric properties in our simulated data. Refer to Chapter 1 for a thorough introduction of this subject, and Section 2.3 for an overview of the methods used in this specific chapter. We present our results in Section 5.2 and highlight insights gleaned from this study in Section 5.3 before concluding in Section 5.4.

## *5.2 Results*

Using the SMARTER pipeline upgraded for this work to analyze high-resolution spectra via cross-correlation, we examine simulated ELT observations of terrestrial Earth-like atmospheres on Proxima Centauri b with different abundances of $O_2$ (Table 2.8) and we retrieve these abundances using SMARTER. We allow our high-resolution retrieval framework to converge for each case, and present the posterior distributions of each retrieved $O_2$ abundance in Figure 5.1. We show the spectra corresponding to the retrieved parameters plotted against the input spectra for the 21% $O_2$ 1-bar and 95% $O_2$ 10-bar cases in Figure 5.2. We also present the posterior distributions and correlations for all retrieved parameters in Figures 5.4, 5.5, 5.6, 5.7, and 5.8 for the 1%, 5%, 21%, 50% and 10 bar $O_2$ cases (Table 2.8), respectively. The retrieved parameters with 95% credibility intervals are presented in Table 5.2. Below we describe our results for all test cases (Table 2.8).

### *5.2.1 1-bar cases*

Our results show that we may be able to accurately retrieve the true abundance of $O_2$ in the inhabited modern Earth-like case with 21% $O_2$, assuming the atmospheric pressure is known or can be retrieved. This result is shown in panel c of Figure 5.1, where the median

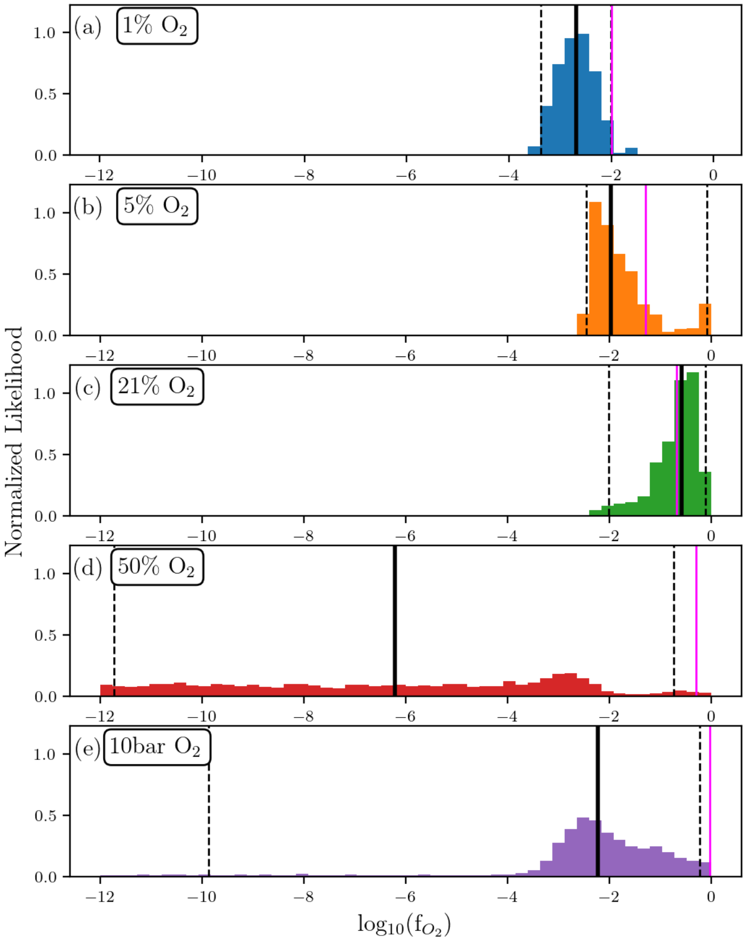

Figure 5.1 Posterior distributions of retrieved $O_2$ abundances for the 1%, 5%, 21%, 50%, and 10 bar $O_2$ cases (panels a, b, c, d and e, respectively). Our retrieval analysis retrieves the 21% $O_2$ modern Earth case to high accuracy, and the true value for the 1% $O_2$ case is within the 95% credible region (i.e. 2-$\sigma$) for its retrieval. The retrieved posterior distributions are unconstrained for the 5% and 50% cases. We are unable to retrieve the $O_2$ abundance in the 10 bar case.

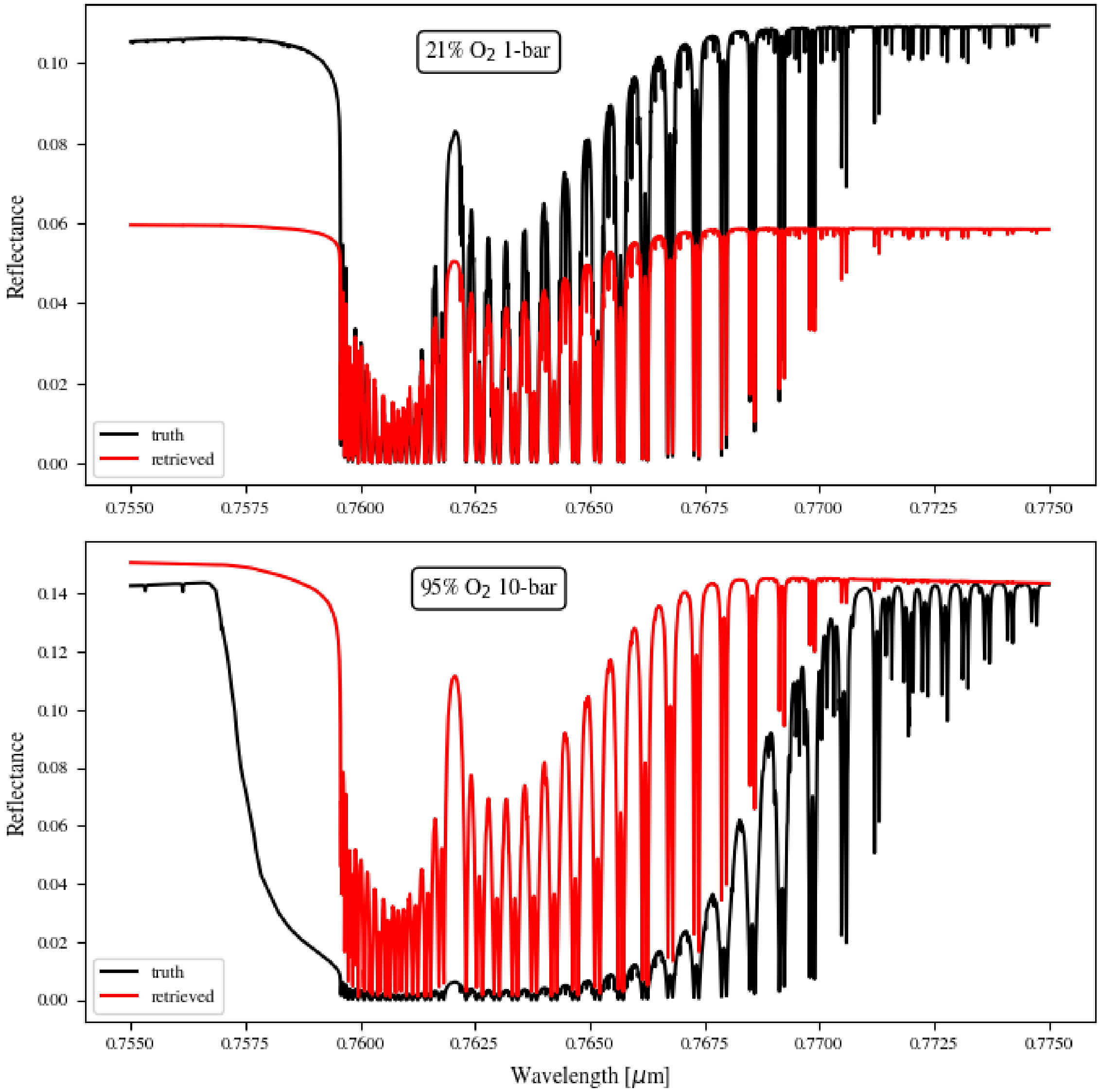

Figure 5.2 Retrieved spectra (red) for the 21% and 10 bar $O_2$ cases. We calculate the retrieved spectra for the 21% 1-bar (upper) and 95% 10-bar (lower) atmospheres using the forward model, assuming the retrieved $O_2$ abundance is the weighted median of the retrieved $O_2$ posteriors. The true spectra are plotted in red for comparison.

Table 5.1. Retrieved parameters with 95% credibility interval uncertainties

| | 1-bar atm. | | | | 10-bar atm. |
|---|---|---|---|---|---|
| Parameter | 1% $O_2$ | 5% $O_2$ | 21% $O_2$ | 50% $O_2$ | 95% $O_2$ |
| $f_{O_2}$ | $2.0^{+7.6}_{-1.6} \times 10^{-3}$ | $1.0^{+79}_{-0.7} \times 10^{-2}$ | $0.26^{+0.51}_{-0.25}$ | $\cdots$ | $6.0^{+590}_{-6.0} \times 10^{-3}$ |
| $A_s$ | $0.10^{+0.83}_{-0.088}$ | $0.17^{+0.83}_{-0.16}$ | $0.034^{+0.50}_{-0.023}$ | $0.088^{+0.78}_{-0.077}$ | $0.12^{+0.75}_{-0.11}$ |
| $K_p$ | $80^{+20}_{-32}$ | $67^{+28}_{-58}$ | $54^{+21}_{-34}$ | $54^{+43}_{-51}$ | $61^{+36}_{-51}$ |
| $V_{\mathrm{sys}}$ | $-33^{+20}_{-14}$ | $-34^{+20}_{-14}$ | $-18^{+35}_{-13}$ | $-3.1^{+49}_{-44}$ | $-26^{+54}_{-22}$ |

of the retrieved posterior distribution (black vertical line) for the 21% $O_2$ case is $f_{O_2} = 0.26$, which is within 25% of the true value (pink vertical line) of $f_{O_2} = 0.21$. Although the 95% credibility (i.e. 2-$\sigma$) region (vertical dashed lines in Figure 5.1) spans $f_{O_2} = 9.8 \times 10^{-3}$ to 0.77, nearly two orders of magnitude.

For the 21% $O_2$ world, we also find that the other retrieved parameters $V_{\mathrm{sys}}$ and $K_p$ can also be constrained to within 20% of their true values, and $A_s$ can be constrained to an upper limit of approximately 0.16 (see Figure 5.6). Accurately retrieving $V_{\mathrm{sys}}$ and $K_p$ shows that the radial velocity of the planet was retrieved, and that the $O_2$ was detected in the target atmosphere at the radial velocity of the planet, and not in the rest frame of the Earth's telluric spectrum. Retrieving the gray surface albedo $A_s$ is inherently challenging for cross-correlation spectroscopy because by removing telluric lines in the data pre-processing step the spectral continuum information is lost (Section 2.3.2.6). Regardless, our retrieval framework is able to put an upper limit constraint of 0.16 on the surface albedo, and the true value from the model spectrum is 0.16 at and around 0.76$\mu$m (Meadows et al., 2018), so is within this upper limit constraint.

Our results suggest that it may be possible to retrieve the $O_2$ abundance with 1% and

5% $O_2$, however retrieving the $O_2$ abundance in the 50% $O_2$ 1-bar or 95% $O_2$ 10 bar cases may be challenging. We present the $O_2$ abundance posteriors for the cases with 1%, 5%, 50% $O_2$ 1-bar and 95% $O_2$ 10 bar cases in panels a, b, d, and e, respectively, of Figure 5.1. The corresponding corner plots for all parameters are shown in Figures 5.4, 5.5, 5.7, and 5.8 for the 1%, 5%, 50%, and 95% $O_2$ abundance cases, respectively. Below we describe the 1 bar and 10 bar cases separately.

We find that we are able to retrieve the $O_2$ abundances for the 1% and 5% $O_2$ 1 bar atmospheres to within 80% and 50% of their true values, respectively, but we are not able to constrain the abundance in the 50% $O_2$ case due to the increased saturation of the band (see Section 5.3.1). However we note that the uncertainties on the retrieved values for the 1% and 5% $O_2$ cases are larger than the deviation of the median retrieved value from the true value (see Table 5.2). Furthermore, our retrieval framework was not able to constrain the parameters $A_s$, $K_p$, and $V_{\mathrm{sys}}$ to high precision. We show the $f_{\mathrm{O_2}}$ posteriors for the 1%, 5%, and 50% $O_2$ cases in panels a, b, and d of Figure 5.1, respectively, and all parameters in the corner plots shown in Figures 5.4, 5.5, and 5.7. Our retrieval analysis for the 1%, 5%, and 50% $O_2$ cases results in median retrieved $O_2$ abundances of $f_{\mathrm{O_2}} = 2.0 \times 10^{-3}$, $2.6 \times 10^{-2}$, and $6.2 \times 10^{-7}$, respectively. These retrieved abundances differ from the true $O_2$ mixing ratios of $f_{\mathrm{O_2}} = 0.01$, 0.05, and 0.5 by factors of 5, $\sim 2$, and $\sim 10^6$, respectively. The 95% credibility region (i.e. 2-$\sigma$) spans two orders of magnitude for the 1% ($\sim 10^{-4} - 10^{-2}$) and 5% ($\sim 10^{-2} - 10^{0}$) $O_2$ cases, and 11 orders of magnitude ($\sim 10^{-11} - 10^{0}$) for the 50% case, suggesting that the 1% and 5% $O_2$ abundances are relatively well constrained compared to the 50% $O_2$ case. Furthermore, the current implementation of this retrieval framework suggests the parameters $A_s$, $K_p$, and $V_{\mathrm{sys}}$ are largely unconstrained for all the non 21% $O_2$ 1-bar cases, suggesting that any retrieved $O_2$ abundance for these cases may be contaminated by other regions in RV space that may correlate with the $O_2$ template, such as telluric artifacts left over from the telluric removal step (Section 2.3.2.6). In summary, while our framework can retrieve the $O_2$ abundances for the 1% and 5% $O_2$ atmospheres to reasonable accuracy, our inability to accurately and precisely retrieve the RV parameters would make these detections

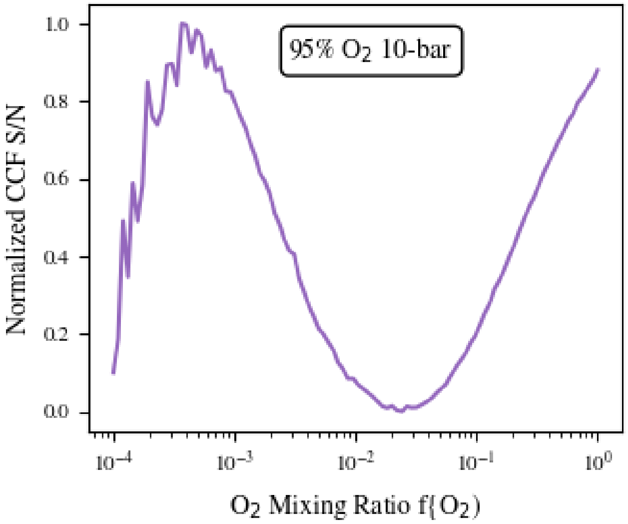

Figure 5.3 Normalized S/N for the cross-correlation between the noiseless true spectrum and a noiseless forward model as a function of $O_2$ mixing ratio. While the cross-correlation S/N appears to increase near the true $O_2$ mixing ratio of 95%, suggesting a strong correlation, the high saturation of this band in the simulated data prevents this trend from manifesting in the posterior distribution. Instead, the depth of the absorption lines in low-$O_2$ spectra enhances the cross-correlation S/N enough to be apparent in the posterior distribution.

difficult to interpret; furthermore, we find that retrieving any parameters, including $O_2$, in the 50% $O_2$ case may be challenging with the current framework because of saturation in the $O_2$ band and relatively low S/N throughout the band (see Section 5.3.1).

### *5.2.2 10-bar case*

For the 10 bar atmosphere with 95% $O_2$, we find that we are unable to retrieve the true value of $O_2$ for this atmosphere, and the parameters $A_s$, $K_p$, and $V_{\text{sys}}$ are also not well constrained (Figure 5.8). The retrieved $O_2$ abundance is $f_{O_2} = 6.0 \times 10^{-3}$, which is three orders of magnitude less than the true value of $f_{O_2} = 0.95$ in the 10 bar atmosphere. While we are not able to retrieve the true abundance of $O_2$ in this case, the posterior is not entirely unconstrained, and the true value is within 3 sigma of the median. Although our framework retrieved median values for the RV parameters $K_p$ and $V_{\rm sys}$ that are within 2% and 20% of the true values, respectively, the 95% credibility regions span nearly 80 km/s for both parameters, indicating that these parameters are not well constrained. Additionally, the shape of the retrieved posterior distributions, and their correlation, suggests a bimodal distribution for the RV of the planet, with the true values in the valley between the peaks. Finally, the surface albedo $A_s$ remains largely unconstrained due to the removal of the spectral continuum when subtracting telluric lines in the data pre-processing step.

Our inability to retrieve the atmospheric properties for the 10 bar case may be due to the substantial saturation across the entirety of the band, and to test this we ran a sensitivity test for the $O_2$ mixing ratio for the 10 bar atmosphere. Figure 5.3 shows the normalized cross-correlation S/N as a function of $O_2$ mixing ratio for the 10 bar case. We find that S/N peaks at $f_{O_2} \sim 10^{-3}$ and then again at nearly 100% $O_2$, indicating that template spectra corresponding to these mixing ratios maximize the cross-correlation S/N in the retrieval, which explains the relatively low $O_2$ abundance retrieved for the 10 bar case. We discuss the implications of this bimodal structure in Section 5.3.1.

## *5.3 Discussion*

The techniques and algorithm used here on simulated 100 hr ELT spectroscopic observations were able to retrieve close to the true $O_2$ abundance for Earth-like atmospheres with up to 21% $O_2$, but in atmospheres with higher levels of $O_2$, saturation of the band makes accurate retrieval challenging . While previous work has shown that we may be able to detect the presence of $O_2$ in the atmospheres of Earth-like (Snellen et al., 2015; Hawker & Parry, 2019; Currie & Meadows, submitted) and other habitable but uninhabited worlds (Chapter 4; Currie & Meadows, submitted), and retrieval of molecular abundances has been shown to be possible for high-resolution spectra of K2-18 b, a temperate sub-Neptune sized planet (Cabot et al., 2024). We have shown for the first time that it may be possible in some cases to also determine the abundance of $O_2$ in Earth-like atmospheres detected with the ELTs. A retrieved abundance is an additional critical piece of information that can inform planetary habitability, and help us assess the relative likelihood of a biological or abiotic source for the observed $O_2$ Below we discuss our findings in the context of discriminating worlds that generate $O_2$ biologically vs. abiotically.

### *5.3.1 High Oxygen Abundances and Cross-correlation Analysis Sensitivity*

To first order, our ability to retrieve the $O_2$ abundance is a function of the mixing ratio of $O_2$ in the simulated observed atmosphere, as well as pressure, which alters the structure of the $O_2$ bands. At the core of our upgraded retrieval framework is a cross-correlation analysis—performed between the SMARTER-generated template spectra and the simulated observation—that is sensitive to individually resolved absorption lines in a given molecular band. The degree of correlation is therefore a function of the number of resolved lines, the depth of the lines relative to the continuum and relative to other lines, and the shape of the band (e.g. Birkby, 2018). An increase or decrease in the number of lines or relative depth of the lines can significantly affect detectability, and this effect can be seen in our results: We are able to retrieve the $O_2$ abundances for the $f_{O_2} \leq 0.21$ cases to within a few factors of the true value for the 1% and 5% $O_2$ cases, and within a factor of 0.25 for the 21% $O_2$ case, because the resolved absorption lines are deep and distinctive (see panels c, d, and e of Figure 2.14). However, increasing the $O_2$ abundance to concentrations of $f_{O_2} \geq 0.5$ introduces significant saturation in the absorption bands (see panels f and g of Figure 2.14), decreasing the relative depth of the absorption lines at 0.76 $\mu$m and extending to 0.762 $\mu$m and 0.766 $\mu$m for the 50% 1-bar and 95% 10 bar $O_2$ cases, respectively— at these high $O_2$ concentrations, over half of the absorption lines become nearly completely saturated, and therefore provide little benefit to the cross-correlation calculation. What few clean absorption lines that remain can be enhanced by cross-correlating with spectra that have clear and distinctive absorption lines, which explains why the retrieval for the 10 bar case provides either upper limits or median $f_{O_2}$ values on the order of a tenth of a percent $O_2$ abundance. Figure 5.3 illustrates this by showing the normalized correlation between the noiseless true spectrum and the noiseless forward model as a function of $O_2$ fraction for the 95% 10-bar case. The cross-correlation S/N peaks with very low ($f_{O_2} = 10^{-3}$) $O_2$ abundances, which is consistent with the retrieved value of $6 \times 10^{-3}$, but discrepant from the true value by several orders of magnitude, $O_2$ abundance for the 10-bar case. This test has shown that the error is clearly in the cross-correlation, but it is currently unclear exactly why this fit is so discrepant and what causes the double-peaked structure. Further experiments will be needed to improve the accuracy of the retrieval for saturated bands, and a possible tests/workaround includes exploring cross correlation over a narrower (unsaturated) segment of the band, or on a less saturated band of the same molecule (see below). Furthermore, because we are measuring the reflectance of the planet, molecular absorption manifests itself as an absence of photons, and the S/N of the absorption lines themselves will be low. The cross-correlation analysis for the 10-bar case will therefore not be as sensitive to the absorption lines because of the high saturation that reduces the entire continuum, lowering the S/N throughout the majority of the band (see panel g of Figure 2.14). We note that while the noiseless cross-correlation S/N appears to increase as the $O_2$ mixing ratio approaches unity in Figure 5.3, this trend is not seen in the retrieval posterior distributions for the 10-bar case because of the low S/N in this region. In practice, if saturation or pressure effects are suspected, observation of a weaker band of the same molecule (e.g. the 0.69 $\mu$m $O_2$ band) may provide a less saturated, more resolved band for retrieval purposes. If the low abundance observed in the first band is the reality, then that lower abundance will be confirmed by, or there will be a non-detection, of the second band. If the low abundance in the first band is instead due to saturation and/or pressure-mediated effects, the second, weaker band may then return a higher, and potentially closer to true, abundance.

### *5.3.2 Abundance Measurements as Biosignature Discriminants*

Being able to constrain the abundance of oxygen in a planetary atmosphere will provide critical clues to the likelihood that any detected oxygen is in fact due to life, and it will guide and augment observations needed for false positive discrimination (Meadows, 2017; Meadows et al., 2018; Schwieterman et al., 2018). While nearly all of the $O_2$ in Earth's atmosphere is biologically generated (Lyons et al., 2014), there are known abiotic mechanisms that can also generate $O_2$ on worlds in the habitable zone, especially for planets orbiting M dwarfs (e.g. Luger & Barnes, 2015; Gao et al., 2015; Wordsworth & Pierrehumbert, 2014). For $O_2$ in atmospheres with retrieved $f_{\mathrm{O}_2} \leq 0.21$, the retrieval would provide evidence that the $O_2$ was either generated biologically, via analogy with the modern Earth atmosphere (Lyons et al., 2014) for the $f_{\mathrm{O}_2} = 0.21$ case, or by some other mechanism that may produce $< 21\%$ $O_2$, either biologically as in the pre-great oxidation event Earth atmosphere with an early photosynthetic biosphere (Lyons et al., 2014), or by an abiotic mechanism like $CO_2$ or $H_2O$ photolysis; however currently known $CO_2$ photolysis mechanisms can only build up trace levels of $O_2$ (Ranjan et al., 2023), which are under the 1% $O_2$ level we tested and may not be detectable at all (Ranjan et al., 2023). However, our inability to retrieve the $O_2$ abundance in the $f_{\mathrm{O}_2} > 0.21$ cases suggests that these biosignature false positive atmospheres will need to be ruled out via other methods, such as the detection of other molecules that can provide additional clues to understand the planetary environment.

Our ability to retrieve the $O_2$ abundances of $f_{\mathrm{O}_2} \leq 0.21$ for 1-bar atmospheres may also indicate a more hospitable environment for life by decreasing the likelihood of combustion on the surface. In brief periods of Earth's history, the $O_2$ abundance may have risen above $f_{\mathrm{O}_2} = 0.24$, which is also associated with evidence of widespread wildfires (Lenton, 2013; Glasspool et al., 2015) that likely created an inhospitable environment for life on land to thrive. Our ability to retrieve $O_2$ abundances at the modern Earth abundance and lower would allow an assessment of how atmospheric $O_2$ abundance impacts the likelihood that a planet's land surfaces are habitable.

If the retrieved $O_2$ is measured to be at the $\sim 20\%$ level, this could indicate an Earth-like environment with oxygenic photosynthesis, a desiccated $O_2$ false positive planet (Gao et al., 2015), or a false positive planet with abiotic $O_2$ generated in a low non-condensable gas inventory scenario (Wordsworth & Pierrehumbert, 2014), and additional information would be needed to discriminate between these possibilities. In the Earth-like case, searching for

$CH_4$, which is likely detectable in $\sim 10$ hours with the ELTs (Chapter 4; Currie & Meadows, submitted), could strengthen the interpretation that the $O_2$ is generated via life by indicating an atmospheric disequilibrium (Hitchcock & Lovelock, 1967; Meadows, 2017; Meadows et al., 2023), and helping to rule out a massively $O_2$-dominated atmosphere (Domagal-Goldman et al., 2014). On the other hand, models suggest that for an M dwarf planet $O_2$ could be generated abiotically at the 20% level for a desiccated world (Gao et al., 2015), where the lack of $H_2O$ would prevent the recombination of $CO_2$, allowing $O_2$ and CO to build up in the atmosphere. However, this desiccated false positive world could be identified by its abundant (0.1-0.3 bars) of CO, which is likely detectable with the ELTs within the 10 hrs of observing it would take to detect $O_2$ (Chapter 4; Currie & Meadows, submitted). Finally, Wordsworth & Pierrehumbert (2014) predict that an atmosphere with a low non-condensable gas inventory may allow water to enter the upper atmosphere, where it can be photolyzed into $\leq 15\%$ atmospheric $O_2$. While the discriminant for this case may be confirming that the non-condensable gas inventory is low by also measuring the abundance of $N_2$ via $N_2$–$N_2$ collisionally induced absorption at 4.2 $\mu$m (Schwieterman et al., 2015), this measurement is likely extremely challenging for the ELTs due to enhanced sky brightness at these wavelengths and lack of high-resolution band structure for this spectral feature; however, this remains untested. For a transiting target, this scenario could also potentially be ruled out by looking for abundant $N_2$–$N_2$ collisionally induced absorption at lower resolution from a space-based platform (e.g. Schwieterman et al., 2015), or for direct imaging, potentially from a future NIR-MIR direct imaging space-based telescope (Quanz et al., 2022).

While the 21% $O_2$ in the modern Earth is directly an effect of the development of oxygenic photosynthesis, an atmosphere with $O_2$ abundances at the 1% and 5% level, which we are also able to retrieve to within a factor of 5 of their true values, would also potentially indicate the presence of life. After the evolution of oxygenic photosynthesis, the $O_2$ inventory has ranged from 1% to over 21% throughout Earth's inhabited history (Lyons et al., 2014), and may have been very low ($< 0.1\%$ PAL) during the Proterozoic (Planavsky et al., 2014). Detecting $CH_4$ in addition to $O_2$—an atmospheric disequilibrium biosignature that in this case may indicate that two metabolisms (oxygenic photosynthesis and methanogenesis) are active (Hitchcock & Lovelock, 1967; Meadows, 2017)—would provide stronger evidence for life in this case. However, we note that the $CH_4$ abundance throughout Earth's history has also varied, and detecting both $O_2$ and $CH_4$ together may have been challenging in the last 2.5 billion years (Reinhard et al., 2017) However, the Reinhard et al. (2017) study calculated detectability for low to medium spectral resolution observations with a space telescope, and not for the high-resolution capabilities of the ELTs. As we have shown, the ELTs may be able to detect $O_2$ abundances as low as 1%, potentially allowing detection of Earth's photosynthetic biosphere throughout the Phanerozoic (543-0 Ma), and for 200 My in the Paleoproterozoic (Reinhard et al., 2017). The detectability of $CH_4$ at the abundances throughout Earth's history remains to be tested using this retrieval framework. False positives for these lower abundances may be more straightforward to generate photosynthetically, but after initial results that appeared to show possible build up of abiotic $O_2$ at the 6% level via $CO_2$ photolysis (e.g. Harman et al., 2015), other and more recent analyses refute this result, and show that this is not possible for greater than $f_{\mathrm{O}_2} = 0.4\%$ (Tian et al., 2014; Harman et al., 2018; Ranjan et al., 2023) , ruling out this possibility for a 5% retrieved $O_2$ abundance.

If the $O_2$ abundance cannot be well constrained (i.e. the 95% credibility region spans $> 3$ orders of magnitude), as we find for the 50% and 10 bar case, additional environmental context can be gained by searching for indicators of a thick atmosphere, such as a detectable 0.76 $\mu$m band, and a missing 1.27 $\mu$m band due to saturation and $O_2$–$O_2$ collisionally-induced absorption features (Leung et al., 2020). This measurement will also likely be possible with the ELTs even without running a retrieval (Chapter 4; Currie & Meadows, submitted).

### *5.3.3 Future Directions*

This study demonstrates the use of our updated retrieval framework for measuring molecular abundances in simulated high-resolution ELT observations of terrestrial exoplanets, and we note that this work is still ongoing. The time required for retrieval convergence exceeds one month for the minimum set of parameters used in this study ($A_s$, $f_{\mathrm{O}_2}$, $K_p$, and $V_{\mathrm{sys}}$) due to the increased computational demands of the upgraded high-resolution analysis component that includes expensive cross-correlation calculations. Although we have presented some preliminary results in this chapter, we aim to continue refining this analysis in the future. In particular, several outstanding items require further investigation, including the addition of more atmospheric parameters (including other molecules) and wider wavelength coverage to the analysis.

Before submitting this work for publication in the Planetary Science Journal, we plan to run similar retrievals with an updated list of parameters to additionally include $CH_4$, as well as the surface temperature ($T_0$) and pressure ($P_0$). If time permits, we will also explore our retrieval sensitivity to different abundances of $CO_2$, $H_2O$, and $O_3$ mixing ratios. In particular, including the surface pressure parameter is important because the shape of the absorption lines and total abundance are sensitive to pressure, and this could help to discriminate between the 1-bar and 10-bar atmospheres if the surface pressure can be constrained.

Critically, including $CH_4$ in the retrieval could provide additional avenues for directly assessing the origin of the $CH_4$, strengthening its interpretation as a biosignature or false positive. Measuring the $CH_4$ abundance and running photochemical models will allow us to provide constraints on its surface flux. This flux range can then be compared to the known limits of abiotic $CH_4$ surface fluxes (Guzmán-Marmolejo et al., 2013; Krissansen-Totton et al., 2018b) to determine if it exceeds these and is more likely to be due to life (Krissansen-Totton et al., 2018b).

Another limitation of this study, also constrained by the speed of the cross-correlation computations, is the operating wavelength range used for the retrievals. This work focused solely on analyzing the $O_2$ A-band between 0.755 and 0.775 $\mu$m. In the future, we plan to apply the retrieval framework to a broader wavelength range (0.5–2.0 $\mu$m) to capture multiple $O_2$ bands and the spectral features of other molecules, which can possibly help to constrain the $O_2$ abundance, especially for the saturated $O_2$ A-band in the 10 bar case. This broader range will enhance our ability to constrain the $O_2$ abundance as well as gain further environmental context by detecting molecules that can support the interpretation of an $O_2$

detection, and more comprehensively characterize the atmosphere.

## *5.4 Conclusions*

In this work, we upgraded the SMARTER retrieval framework to analyze ground-based high-resolution ELT observations, and performed atmospheric retrievals on simulated ELT observations to investigate our ability to measure the abundance of $O_2$ in the atmosphere of a terrestrial Proxima Centauri b. We tested Earth-like atmospheres with $O_2$ abundances spanning 1% to 50% for 1 bar atmospheres, and a 95% $O_2$ 10 bar atmosphere, and found that while it may be possible to constrain the $O_2$ abundance for atmospheres with $f_{O_2} \leq 0.21$, atmospheres with higher $O_2$ abundances may be challenging to retrieve due to saturation in the $O_2$ bands. We find that we are able to retrieve a biologically generated $O_2$ abundance in a simulated spectrum to within 25% of its true value, and to within a factor of 5 for lower abundances, and these lower values may increase the likelihood that an environment is habitable by preventing the possibility of widespread fires common for $O_2$ concentrations greater than 24% (Lenton, 2013; Glasspool et al., 2015). Constraining the $O_2$ abundance can be a critical piece of evidence for determining its origin, and we find that this analysis can enhance the likelihood that $O_2$ was generated via either biology or other mechanisms that build up $O_2$ at the $\leq 21\%$ level. Discriminating biological from abiotic sources of $O_2$ may be achieved by searching for other molecules that can give context to the detected $O_2$; however we leave this to future work. Additionally, identifying that detected $O_2$ is the result of ocean outgassing and $H_2O$ photolysis may be challenging with this technique, and may be better achieved by searching for signs of $O_2$–$O_2$ collisionally induced absorption using reflected light spectroscopy with the ELTs (Chapter 4; Currie & Meadows, submitted). In summary, the upcoming ELTs will provide the only near term way to detect $O_2$, and may also be promising tools for measuring the abundance of $O_2$ to support our search for signs of habitability and life.

## *5.5 Supplemental Corner Plots for Retrievals*

Here we include the full corner plots showing the nested sampling posterior distributions and parameter correlations in Figures 5.4, 5.5, 5.6, 5.7, and 5.8.

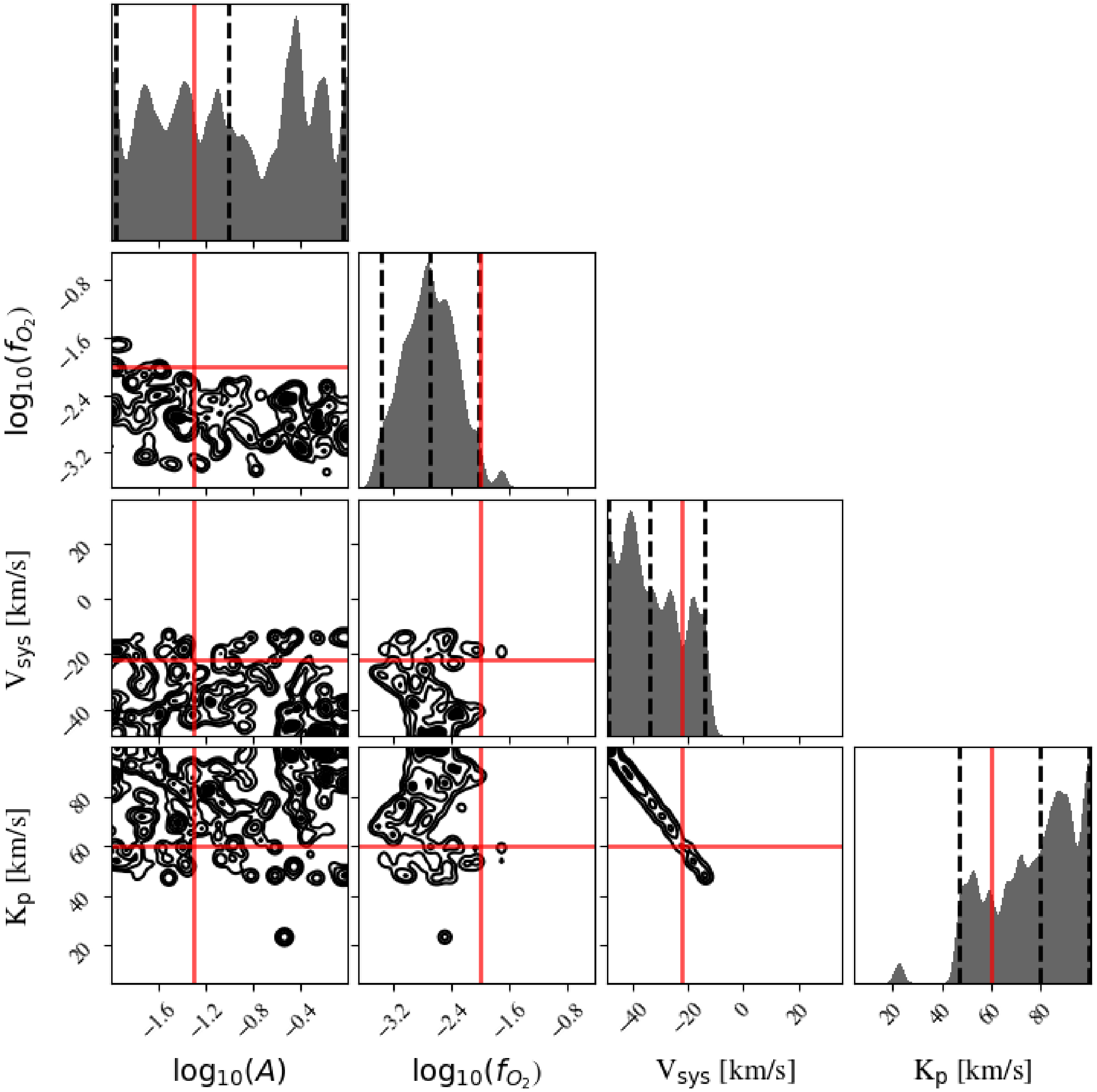

Figure 5.4 Corner plot presenting the posterior distributions and correlations between the retrieved parameters $f_{\mathrm{O}_2}$, $K_p$, and $V_{\mathrm{sys}}$ for the Earth-like atmosphere with 1% O2.

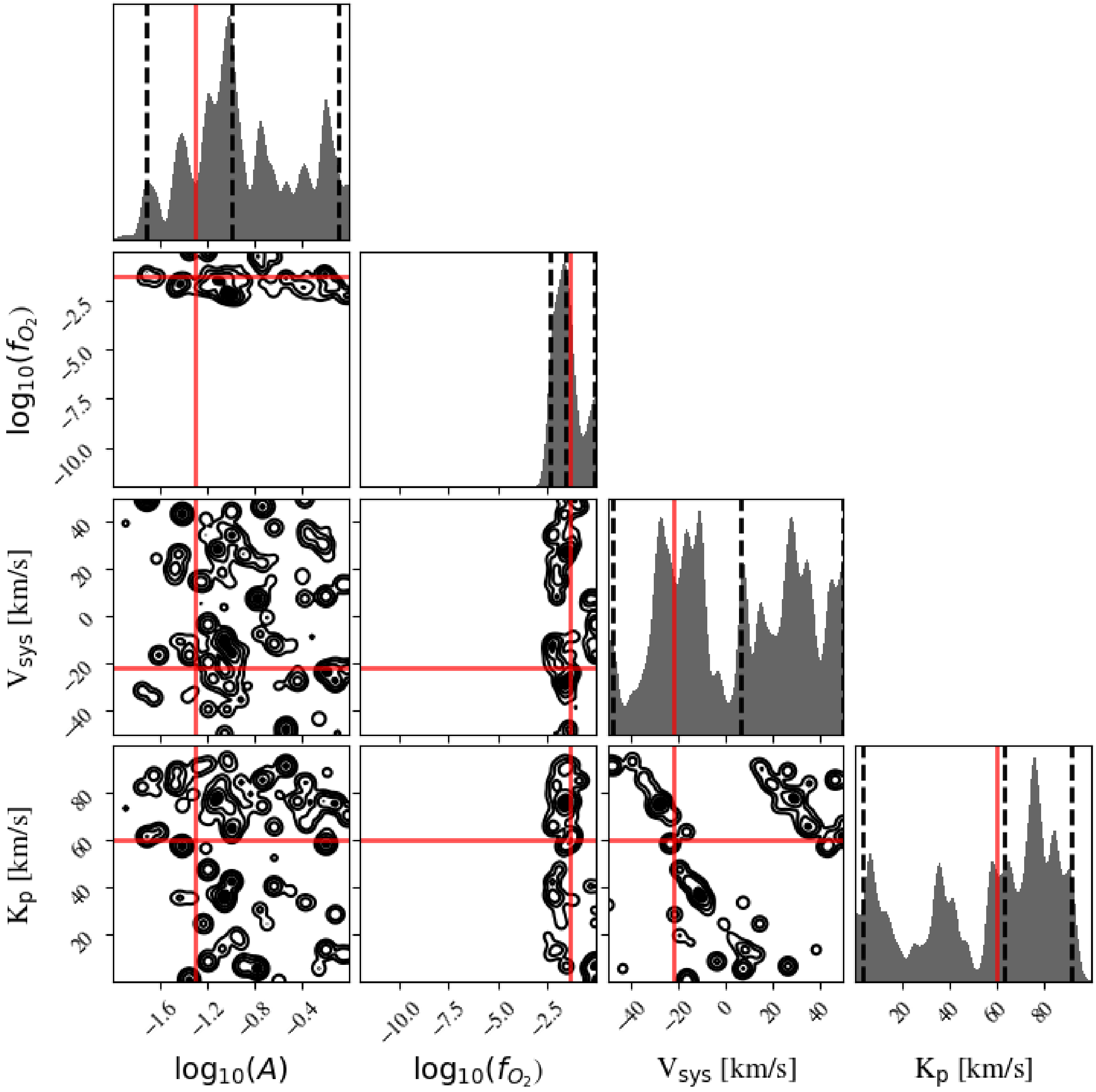

Figure 5.5 Same as Figure 5.4, but for the 5% $O_2$ atmosphere.

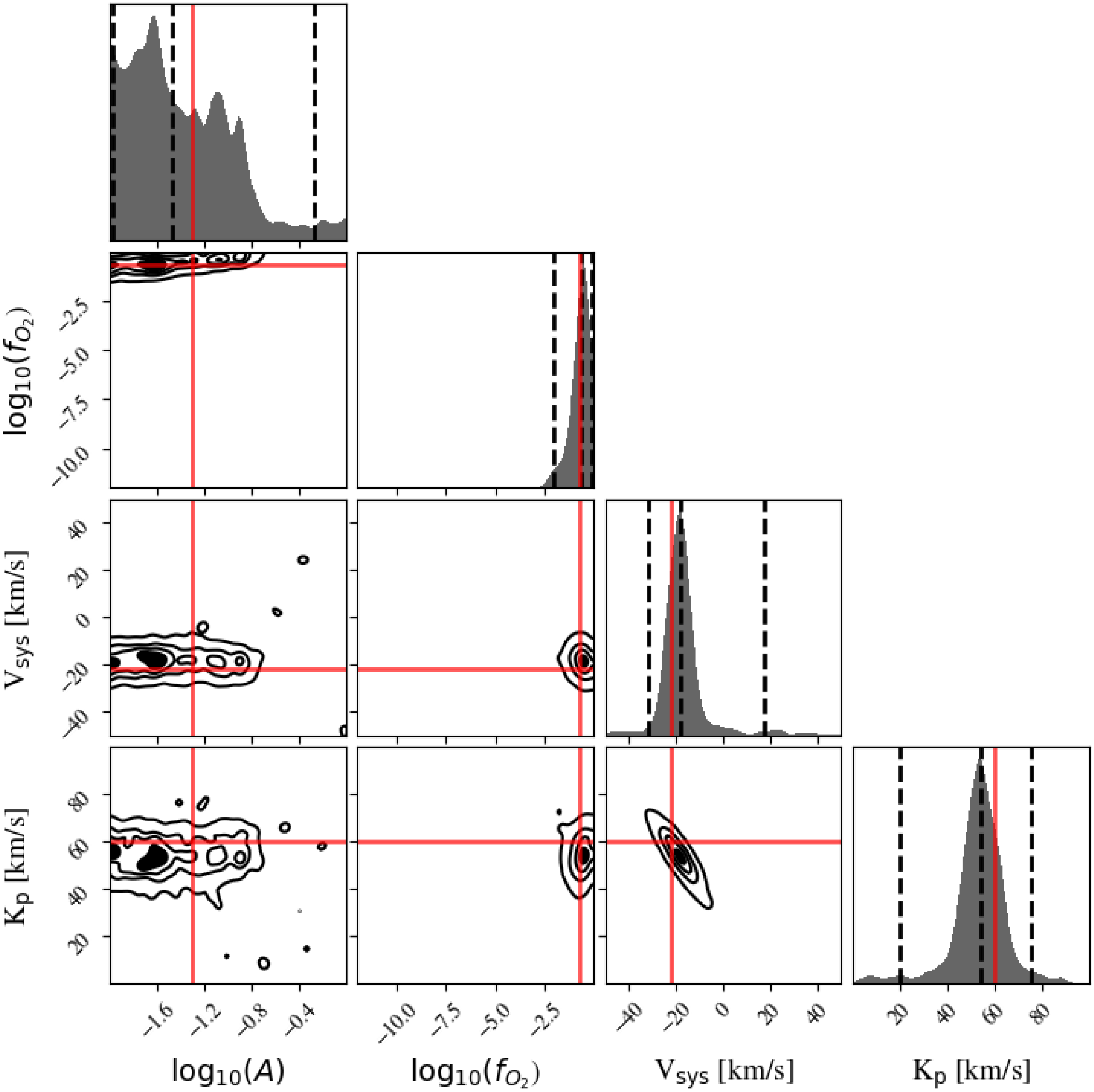

Figure 5.6 Same as Figure 5.4, but for the 21% $O_2$ atmosphere.

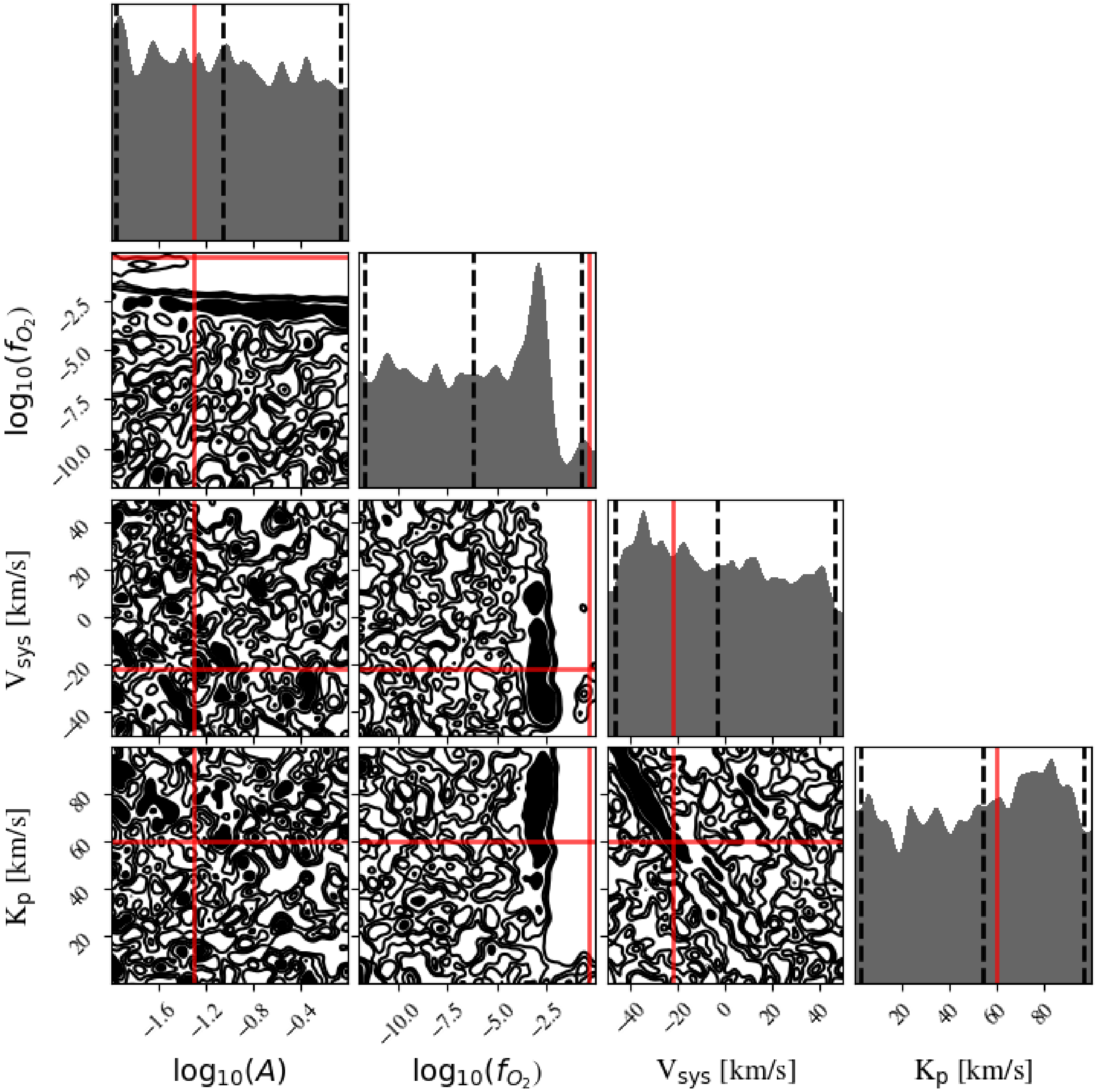

Figure 5.7 Same as Figure 5.4, but for the 50% $O_2$ atmosphere.

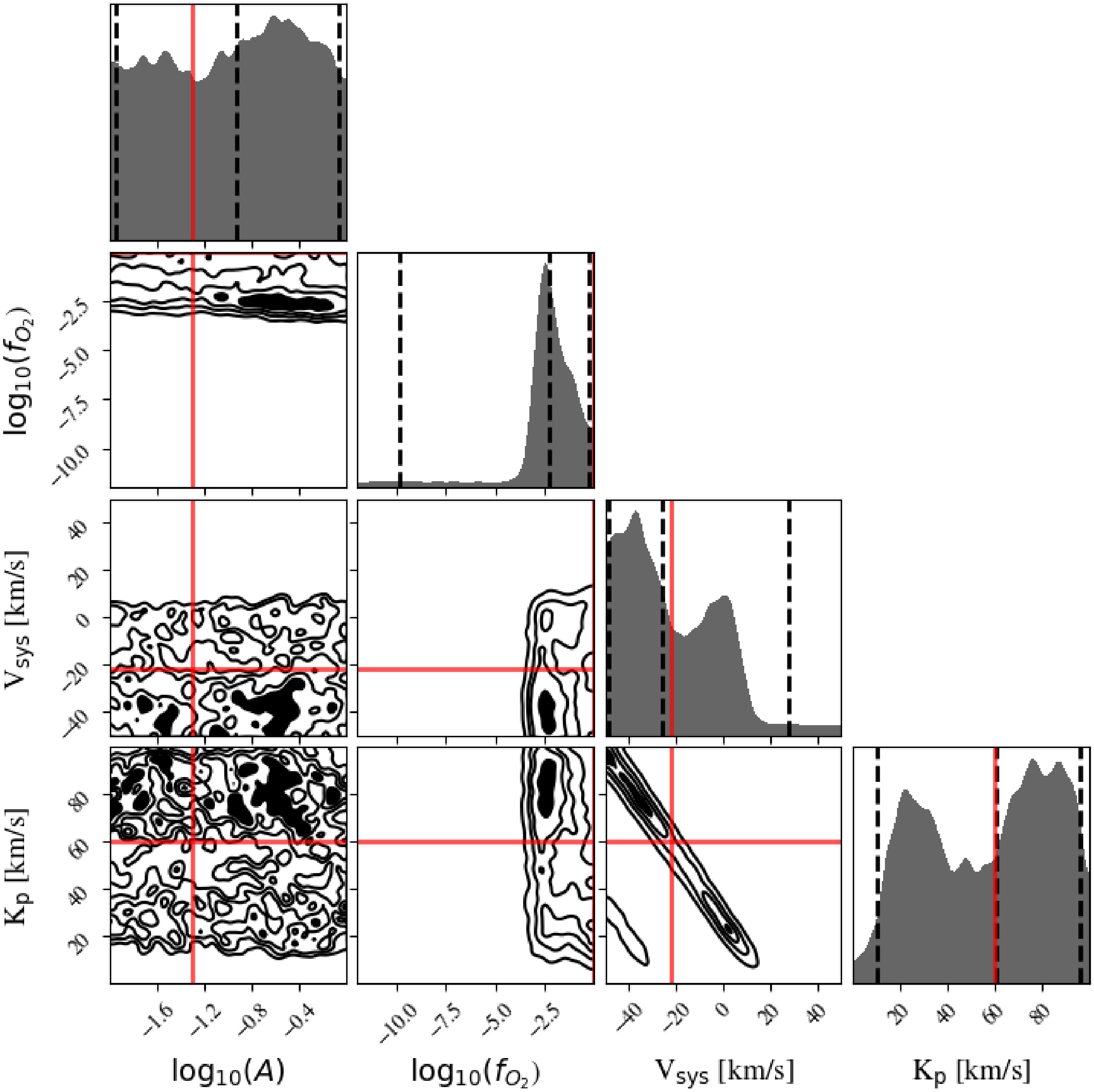

Figure 5.8 Same as Figure 5.4, but for the 10 bar $O_2$ atmosphere.

# Part III

# INSIGHTS ON SEARCHING FOR SIGNS OF HABITABILITY AND LIFE IN THE ELT ERA AND BEYOND

# Chapter 6

# SUMMARY AND INSIGHTS: USING NEXT-GENERATION OBSERVATORIES FOR TERRESTRIAL EXOPLANET CHARACTERIZATION

By the end of this decade, the ELTs will begin to come online, and will provide unprecedented opportunities for studying both transiting and non-transiting terrestrial exoplanet atmospheres in high spectral resolution from the ground. In the meantime, significant work is ongoing to begin preparing for the advent of the ELTs, including instrument development (e.g. Jensen-Clem et al., 2021; Males et al., 2022; Marconi et al., 2022; Palle et al., 2023), and modeling and simulations (e.g. Chapters 3, 4, 5; Wang et al., 2017; Hawker et al., 2018; López-Morales et al., 2019; Hardegree-Ullman et al., 2023; Zhang et al., 2023; Currie et al., 2023; Vaughan et al., 2024; Currie & Meadows, submitted; Currie et al., in prep.). Previous work simulating biosignature detectability using the ELTs has focused on the detection of $O_2$ (e.g. Rodler & López-Morales, 2014; Snellen et al., 2015; Hawker et al., 2018; López-Morales et al., 2019; Hardegree-Ullman et al., 2023), a capability that is complementary to JWST, which will not be able to detect $O_2$ (Pidhorodetska et al., 2020; Meadows et al., 2023). However, in this dissertation I have expanded on these early studies to answer targeted questions about the nature of terrestrial exoplanet atmospheres, and to aid in the development of ELT instrumentation to achieve these goals. By considering the detectability of molecules beyond $O_2$ for the unique capabilities of ground-based high-contrast, high-resolution spectroscopy, we can begin to understand atmospheric composition and provide environmental context to more robustly search for habitability and life. In this chapter, I discuss the insights we gained from completing this work, and their impacts on the field.

## *6.1 State of the Field Prior to This Work*

Because the large abundance of $O_2$ in Earth's atmosphere is a direct byproduct of oxygenic photosynthesis, previous work has placed significant emphasis on simulating the ability of the ELTs to detect $O_2$ in terrestrial exoplanet atmospheres to begin to understand if the ELTs will be able to detect life (e.g. Snellen et al., 2013; Rodler & López-Morales, 2014; Snellen et al., 2015; Hawker et al., 2018; Serindag & Snellen, 2019; López-Morales et al., 2019; Hardegree-Ullman et al., 2023). $O_2$ is a strong absorber in the visible and near-infrared wavelengths, and its high abundance in Earth's atmosphere as well as the structure of its molecular bands make it a high-priority target amenable to high-resolution cross-correlation spectroscopy studies. The ELTs will have enhanced sensitivity due to mirror size and instrumentation designed for characterizing the atmospheres of smaller terrestrial exoplanets, and early studies have found that $O_2$ is likely detectable for nearby exoplanets if they have Earth-like atmospheres (e.g. López-Morales et al., 2019). However, $O_2$ does not solely originate from oxygenic photosynthesis, and its detection alone is not a robust indicator of life, especially if its abundance cannot be determined (Meadows, 2017). Photochemical pathways exist that can generate potentially detectable levels of abiotic $O_2$ via the photolysis of $CO_2$ or $H_2O$ (e.g. Luger & Barnes, 2015; Gao et al., 2015; Wordsworth & Pierrehumbert, 2014; Meadows, 2017). Therefore, we will need to understand the exoplanet environment as a whole to place a potential $O_2$ detection in context before making conclusions about its origin. While early work has shown promise for using ground-based observations to detect other molecules that can give further environmental context (e.g. Wang et al., 2017; Lovis et al., 2017); the goal of this dissertation work is to provide a broader overview of molecular detectability, and a novel in-depth analysis on how we can use the detection of these other molecules, and the retrieval of their abundances, to either directly support a biosignature claim, or confirm or rule out biosignature false positive environments.

## *6.2 Detecting Molecular Features Beyond Oxygen with ELT Observations*

Detecting other molecules beyond $O_2$ will be vital to understand the origin of a potential $O_2$ detection in the context of the exoplanet environment. A rich library of exoplanet atmosphere models predict that gaining environmental context via the detection of molecules beyond $O_2$ can help to provide clues to the habitability of the environment, and evidence that can either support or rule out the hypothesis of abiotically produced $O_2$ "false positive" atmospheres (Meadows, 2017; Meadows et al., 2018) (also see Section 1.3.2). Additionally, biosignature pairs can indicate an atmospheric disequilibrium, providing strong evidence for life processes that influence the atmosphere like oxygenic photosynthesis and/or methanogenesis (e.g. Hitchcock & Lovelock, 1967; Meadows, 2017; Meadows et al., 2018; Schwieterman et al., 2018). Supplemental context can be gained from analyzing the habitability of an exoplanet environment, and searching for signs of water and other greenhouse gases that can control the climate (Walker et al., 1981; Kasting et al., 1993; Kopparapu et al., 2013), providing additional evidence to support a given interpretation of a potential biosignature. Therefore, future observing campaigns targeting only $O_2$ may provide inconclusive evidence for a planet's ability to host life, or for the presence of extant life.

### *6.2.1 A Novel Suite of ELT Detectability Tools*

In Chapter 2, I describe a novel suite of software tools developed over the course of this work to simulate ELT observations, estimate the detectability of molecules in the atmosphere, and finally retrieve molecular abundances. The Spectral Planetary ELT Calculator for Terrestrial Retrieval (SPECTR) tool[1] is a comprehensive pipeline that broadly consists of two major parts: simulating observations, and estimating molecular detectability. To simulate ELT observations, the inputs to SPECTR include spectra calculated with a 1D radiative transfer model (e.g. SMART (Meadows & Crisp, 1996; Crisp, 1997)) and a suite of user-defined parameters that describe the planetary system and observational properties. SPECTR is based

---

[1] https://github.com/curriem/spectr

on the `coronagraph` pipeline (Robinson et al., 2016; Lustig-Yaeger et al., 2019b), which models instrument noise. Through this work we have added an interface to the ESO SkyCalc (Noll et al., 2012; Jones et al., 2013) to model the wavelength-dependent telluric contamination for our simulated observations. SPECTR is a comprehensive and flexible model to simulate observations of any custom exoplanet system for any specified telescope/instrument parameters, and can reproduce results to agree with previous work (see Figure 4.9). Then, SPECTR applies a cross-correlation analysis to estimate the detectability of a molecule at a particular band, or for a broad wavelength range. SPECTR is available to the community[2], with regular support and updates to improve its performance. As part of this dissertation, I also created and implemented a new module to the SMARTER framework for retrieving molecular abundances from high-resolution ground-based observations, using an algorithm centered around a cross-correlation analysis and based on the work of Brogi & Line (2019). These upgrades will soon be available to the public as part of the SMARTER retrieval framework suite[3].

### 6.2.2 *Brief Summary of Results*

In Part I of this dissertation, we have explored the detectability of a range of molecular species in M dwarf terrestrial exoplanet atmospheres, examining scenarios where nearby exoplanets have atmospheres similar to the Earth through time, habitable but uninhabited environments, and sub-Neptune compositions. Because the observing technique for transiting and non-transiting planets differ in instrumentation and logistics, we investigate these two geometries separately. In Chapter 3 Currie et al. (2023), we simulate ELT observations of terrestrial exoplanets transiting M dwarf host stars, and calculate the detectability of molecular species present in their atmospheres. For these transit transmission observations, we find that both $CO_2$ and $CH_4$ are detectable within $\sim$ 10 observed transits, and may be top priority targets for searching for biosignatures as well as indicators of the climate

---

[2] https://github.com/curriem/spectr

[3] https://github.com/jlustigy/smarter

(Section 6.3.1). Additionally, we find that it may take 3–5x or more observation time to detect $O_2$, $H_2O$, and CO if these molecules are present in terrestrial atmospheres, but may still be achievable within the lifetime of the ELTs given a strategic multi-year observing campaign with one or more ELTs (Currie et al., 2023). $O_3$ is not detectable using cross-correlation, due to its lack of high-resolution line structure in the visible–NIR wavelengths (Gorshelev et al., 2014). To date, the best known transiting terrestrial exoplanet targets belong to the TRAPPIST-1 system (Gillon et al., 2016, 2017), which is 12 pc distant from Earth, and our work predicts that while $CO_2$ and $CH_4$ will likely be accessible with the ELTs in this system, $O_2$, $H_2O$, and CO may be more challenging. However, there are non-transiting targets that are closer ($< 5$ pc away), which may provide better opportunities to detect the full range of atmospheric species.

In Chapter 4, we have investigated our ability to use the ELTs to detect molecules in the atmospheres of nearby non-transiting small exoplanets (Currie & Meadows, submitted). We find that optimal non-transiting targets amenable to atmospheric characterization with the ELTs will be within 5 pc away and orbit mid-type M dwarfs, and several known potentially terrestrial targets meet these criteria, including Proxima Centauri b (Anglada-Escudé et al., 2016), GJ1061 d (Dreizler et al., 2020), Teegarden's Star c (Zechmeister et al., 2019), and GJ1002 b and c (Mascareño et al., 2023). For these targets, we predict that $H_2O$ will be accessible in just a few hours of observing, owing to the ability of reflected light observations to probe deep into the near-surface region of the atmosphere where water resides (Gilbert-Janizek et al., 2024). However, we note that the final IWA of the ELT coronagraphs may limit this ability— for example, if we assume an IWA of 2 $\lambda/D$, $H_2O$ may only be accessible for Proxima Centaur b, Teegarden's Star c, and GJ 1002 c (see Figure 4.4). Additionally, $O_2$, $CH_4$, $CO_2$, and/or CO may also be accessible to in Earth-like and abiotic atmospheres, requiring $\sim 10$ hours of observing for the most nearby potentially terrestrial target Proxima Centauri b. For the planets GJ 1061 d, Teegarden's star c, and GJ1002 b/c, only molecules $< 1\mu$m may be accessible due to IWA limitations (see Figure 4.4). Finally, non-transiting targets are primarily discovered via radial velocity observations, which are unable to constrain the inclination (i) of the system, leaving an $M \sin i$ ambiguity in the mass (M) of the planet. The atmosphere of a planet is influenced by the mass, and larger mass planets tend to keep their primordial H/He atmospheres (e.g. Inaba & Ikoma, 2003), while smaller terrestrial planet atmospheres expel this primary envelope over a period of time and largely consist of oxidizing species from geologic outgassing (e.g. Kite & Barnett, 2020). This ambiguity in the planet mass, and therefore atmospheric composition, is particularly relevant for planet mass uncertainties that straddle the line between terrestrial and sub-Neptune (e.g. Fulton et al., 2017). In particular, the closest and likely best target for ELT atmospheric characterization, Proxima Centauri b, has at least a 10% likelihood that its atmosphere may be sub-Neptune-like (Bixel & Apai, 2017), with reduced H-bearing molecular species (Charnay et al., 2015). However, Lovis et al. (2017) argue that even detecting a non-transiting exoplanet in reflected light allows a unique determination of the mass and inclination by observing the planet at quadrature to measure the planet semi-amplitude, and our work shows that observing Proxima b for just a few hours with the ELTs can also detect characteristic molecules in a sub-Neptune atmosphere, conclusively discriminating it from a terrestrial counterpart. More substantially, several H-bearing molecules such as $NH_3$, $CH_4$, and $H_2$ are likely highly accessible in these few hours for a sub-Neptune atmosphere, providing evidence that the atmosphere is reduced and more sub-Neptune-like as opposed to terrestrial. For ELT simulations that are closest to ours in instrument parameters and noise treatments, we find that we are consistent with the results to within $\sim 10\%$ (Vaughan et al., 2024). Our work shows that a wealth of information is accessible in just a few hours of observing non-transiting exoplanet atmospheres, and a $\leq 100$ hr investment in observation time for multiple targets $< 5$ pc away may allow us to characterize their atmospheres by detecting the presence of molecules and searching for signs of habitability and life.

In Part II, we have investigated our ability to retrieve the abundance of $O_2$ in terrestrial atmospheres on Proxima Centauri b, and found that it may be possible to retrieve up to Earth-like abundances of $O_2$ (1 to 21% of the atmosphere) in 100 hr of observing with an ELT, vs. the 10 hr to detection that we found in Chapter 4. We tested $O_2$ retrieval for

1-bar atmospheres containing between 1% and 50% $O_2$ to sample the plausible range of $O_2$ in terrestrial atmospheres that may be generated via either biology or abiotic mechanisms. Additionally, we tested our ability to retrieve $O_2$ in a post-ocean-loss scenario, where up to 10 bars of abiotic $O_2$ may be generated, but we find that retrieving $O_2$ in a thick atmosphere may be challenging with the current implementation of our retrieval framework, due to significant saturation, and subsequent destruction of the high-resolution band structure, for the $O_2$ band we tested.

These studies are the first to thoroughly examine and predict our ability to use the ELTs to characterize the atmospheres of terrestrial exoplanets in the near future, which may provide context to analyze the presence of a potential biosignature or determine the habitability of an atmosphere. Below we discuss the implications and synthesize our results for nearby transiting and non-transiting targets.

## *6.3 Astrobiology in the ELT Era*

In this section, we discuss the interpretation of the detections described in the previous sections in the context of searching for signs of habitability and life. Additionally, we present a set of ELT observing protocols that can be used in the future for planning observing campaigns that aim to characterize nearby known terrestrial exoplanet atmospheres.

### *6.3.1 Habitability Indicators, Biosignature Pairs, and False Positive Environments*

Using the ELTs, we may be able to characterize a range of terrestrial atmosphere types, not just Earth-like atmospheres. In this work, we consider five examples of habitable terrestrial atmospheres, including the Earth through time (Archean and pre-industrial), a prebiotic Earth-like uninhabited atmosphere, and abiotic atmospheres that can generate potentially detectable levels of $O_2$ via $CO_2$ or $H_2O$ photolysis. These atmospheres all have different mixing ratio profiles for the ELT-detectable gases $O_2$, $CO_2$, $CH_4$, $H_2O$, and CO. We can leverage the presence or absence of these gases to assess the atmospheric environment of an exoplanet, and determine if the planet is habitable or if it supports life. One of the major findings of this work is that we may be able to use the ELTs to identify the origin of the $O_2$ as biological or abiotic in some cases— this can be done by either ruling out biosignature false positive scenarios, searching for other gases that can indicate atmospheric disequilibria indicative of life, or determining its abundance. The inclination of a target system (i.e. whether or not the planet transits its host star) may play a large role in the observational method we are able to use to obtain data, and below we discuss assessments of habitability and the presence of life while synthesizing and comparing transmission observations for transiting planets vs. reflected light observations for non-transiting planets.

#### *6.3.1.1 Habitability Indicators*

The ELTs will likely be sensitive to several greenhouse gases that can control the climate of an exoplanet atmosphere, and indicate whether the planet may be habitable (Houghton, 2002). These gases include $CO_2$, $H_2O$, and $CH_4$, and detecting these gases can allow us to determine the climate of a terrestrial atmosphere because they are greenhouse gases that can absorb infrared radiation to insulate the planet and act as a thermostat if the planet has an active carbonate–silicate cycle (e.g. Walker et al., 1981; Kasting et al., 1993; Kopparapu et al., 2013).

In both transit transmission and reflected light observations, $CO_2$ and $CH_4$ are likely highly detectable with the ELTs— for the nearest transiting terrestrial targets in the TRAPPIST-1 system, these gases may be accessible in $\sim 10$ or fewer transits (Chapter 3; Currie et al., 2023), and for the nearest non-transiting target Proxima Centauri b, these gases may be accessible on a similar timescale ($\sim 10$ hr) (Chapter 4; Currie & Meadows, submitted). $CO_2$ is the most universally detectable molecules for all atmospheres we tested, regardless of whether or not the planet is transiting. In general, $CO_2$ in particular likely originates from planetary outgassing, and its presence alone can provide evidence that (1) the planet is terrestrial and has a secondary outgassed atmosphere (e.g. Kite & Barnett, 2020) and (2) the planet's atmosphere is likely warmed to some degree due to its presence (e.g. Kopparapu et al., 2013).

However, transit observations are less sensitive to lower parts of the atmosphere where $H_2O$ resides, and detecting $H_2O$ in transmission may take at least an order of magnitude more time to detect for transiting planets than in reflected light. Because we are able to probe deeper into the atmosphere with reflected light observations of non-transiting planets, $H_2O$ becomes more readily detectable relative to the other molecules, and can likely be obtained in just a few hours of observing for targets less than 5 pc away from Earth. Detecting water vapor may only be feasible for reflected light observations of nearby Earth-like atmospheres because of the 12 pc distance to the nearest transiting target and the lack of $H_2O$ in the post-ocean loss atmosphere.

Unlike $CH_4$ and $H_2O$, which are only accessible for the Earth-like worlds, $CO_2$ is likely the best probe for determining whether an atmosphere is terrestrial (Chapter 3; Currie et al., 2023), and whether it has the ability to warm itself via the greenhouse effect, for any potentially terrestrial target observed with the ELTs. On Earth, the effect of $CO_2$ on the climate is tightly coupled to the global carbon cycle (Walker et al., 1981; Kasting et al., 1993; Kopparapu et al., 2013), which can buffer the planetary climate to keep it habitable for a range of distances from the host star (Kopparapu et al., 2013). The global carbon cycle also requires liquid $H_2O$, and detecting water vapor in the atmosphere could be also be indicative of liquid surface water supporting this weathering process. Probing the habitability of non-transiting planets may be less challenging than for planets transiting their host stars due to the accessibility of both $CO_2$ and $H_2O$ for reflected light observations, vs. just $CO_2$ for transiting planets.

#### *6.3.1.2 Biosignatures*

The $O_2/CH_4$ disequilibrium has been a topic of discussion for over 60 years (e.g. Lovelock, 1965), and our work suggests that the ELTs may be the first ever observatories with the sensitivity to search for and detect this biosignature pair. Moreover, we have shown that the biosignature pair is probably more accessible in reflected light, rather than transmission observations. While $CH_4$ is likely readily detectable in transit transmission observations of

Earth-like exoplanets, $O_2$ may be more challenging (Currie et al., 2023; Hardegree-Ullman et al., 2023). The nearest transiting terrestrial target is in the TRAPPIST-1 system, and the 12 pc distance to the system as well as limitations in how often it is possible to observe the planet transiting its host star from the ground may make an $O_2$ detection difficult in the lifetime of the ELTs (Currie et al., 2023; Hardegree-Ullman et al., 2023).

Although detecting $O_2$ in the atmospheres of transiting exoplanets may be challenging (Currie et al., 2023; Hardegree-Ullman et al., 2023), $O_2$ may be more accessible for non-transiting planets. In Chapter 4 of this work, we find that both $O_2$ and $CH_4$ may be accessible by directly imaging nearby ($< 5$ pc away) terrestrial exoplanets in reflected light observations. With 10 hours of observing, it may be possible to achieve a robust detection of the $O_2/CH_4$ biosignature pair for nearby non-transiting planets with modern Earth-like atmospheres. In particular, Proxima Centauri b will be the prime target for such an observing campaign because of its close proximity to Earth (1.3 pc away), but other nearby potentially terrestrial exoplanets will also be amenable to atmospheric characterization with this technique.

The $CO_2/CH_4$ biosignature pair is hypothesized to reveal the presence of a methanogenic biosphere (Krissansen-Totton et al., 2016; Meadows et al., 2023), and it is potentially accessible with the ELTs for both transiting and non-transiting terrestrial planets. In transit transmission observations, we find that the ELTs will be highly sensitive to both $CO_2$ and $CH_4$ for both ancient and modern Earth-like biospheres, requiring as few as 10 transits to detect for Earth-like atmospheres through time orbiting a star 12 pc away (i.e. the TRAPPIST-1 system). For non-transiting targets, the $CO_2/CH_4$ biosignature pair will be detectable on similar timescales as the $O_2/CH_4$ biosignature pair, requiring on the order of 10 hours of observing to detect for the nearest non-transiting target Proxima Centauri b, and may be an additional readily detectable measurement to support a search for life on an Earth-like planet. Our work suggests that prioritizing observations that target the $CO_2/CH_4$ biosignature pair may be the best way to search for signs of life with the ELTs, regardless of whether or not the planet transits its host star.

#### *6.3.1.3 Discriminating Biosignature False Positives*

While the $O_2/CH_4$ and $CO_2/CH_4$ biosignature pairs may be detectable for nearby targets using the ELTs, there exist uninhabited environments for planets within the habitable zone that may also be capable of building up these gases to detectable levels, and we find that we may be able to discriminate these cases from biological cases using the ELTs. In particular, throughout this work we have tested three distinct scenarios that can build up detectable amounts of $O_2$ and/or $CH_4$ via either $CO_2$ photolysis in a $CO_2$ rich environment[4], $H_2O$ photolysis in an ocean loss scenario (Luger & Barnes, 2015; Meadows et al., 2018), or volcanism in a prebiotic Earth environment (Meadows et al., 2023). The $CO_2$ and $H_2O$ photolysis environments can build up detectable levels of $O_2$, which can be a false positive for biological $O_2$, but discriminants for these cases would also include detectable CO (Krissansen-Totton et al., 2018b; Meadows et al., 2023) and enhanced suppression of the NIR $O_2$ band compared to the $O_2$ A-band (Leung et al., 2020), respectively. We tested the $CO_2$ and $H_2O$ photolysis environments for observations using the transit transmission technique in Chapter 3 and Currie et al. (2023), and the $H_2O$ photolysis and prebiotic Earth environments using the reflected light method in Chapter 4 and Currie & Meadows (submitted). We discuss the detectability of the gases in these environments and their discriminants below.

Discriminating biosignature false positive scenarios using transmission spectroscopy was challenging for the false positive scenarios we modeled. For planets with significant $O_2$ buildup due to $H_2O$ photolysis, as in an ocean loss case (Luger & Barnes, 2015), Leung et al. (2020) used noiseless reflected light observations to identify, and we quantify and confirm (Chapter 4; Currie & Meadows, submitted) the diagnostic suppression of the 1.27 $\mu$m $O_2$ band for high-pressure $O_2$ atmospheres, there is no significant suppression of the 1.27 $\mu$m $O_2$ band in transmission, and so the origin of the detected $O_2$ cannot be conclusively determined with the transmission observations alone. This discrepancy is because the Chapter 3

---

[4] We note that this case may be moot because of modeling artifacts in the original climate–photochemical calculations for this environment, and recent estimates show that $O_2$ does not build up to the level previously predicted in this scenario(Ranjan et al., 2023)

and Currie et al. (2023) transmission result for the ocean loss case is not as sensitive as reflected light observations to the higher density lower layers of the atmosphere where the $O_2$-$O_2$ collisionally induced absorption that suppresses the 1.27$\mu$m band is generated. This result suggests that ocean loss scenarios that build up $O_2$ cannot be ruled out with transit transmission observations with the ELTs, although reflected light observations of a transiting target would provide that additional piece of information. Unfortunately, the known transiting targets are so distant that ELT reflected light observations would be challenging (Chapter 4; Currie & Meadows, submitted).

For planets with $O_2$ buildup due to $CO_2$ photolysis, a predicted byproduct that could indicate this abiotic mechanism is abundant CO (e.g. Harman et al., 2018), however we note that more recent studies show that this case may not build up detectable levels of $O_2$ at all (Ranjan et al., 2023). Nevertheless, we examine the detectability of the CO discriminant gas, and find that it may be challenging with the ELTs for planets in transmission, requiring 100s of transits for the closest transiting terrestrial target TRAPPIST-1 e. For the transit transmission technique, while the ELTs may be sensitive to the $O_2/CH_4$ biosignature pair, it may be challenging to rule out false positive cases that can build up these gases abiotically via the detection of the indicator gases such as CO and $O_4$, and the origin of these gases if detected may remain ambiguous. For the $CO_2/CH_4$ biosignature pair, which is highly detectable in transmission, we did not test the most likely false positive, the volcanic production of $CH_4$ from a planet with a more reducing mantle (Krissansen-Totton et al., 2016; Wogan et al., 2020; Thompson et al., 2022). However, recent work has modeled this false positive for transmission observations with JWST, and shown that the resulting CO buildup from production of large amounts of abiotic $CH_4$ is likely detectable in a similar number of transits to the $CO_2$ and $CH_4$ itself (Meadows et al., 2023). However, JWST can access longer wavelengths and stronger CO bands, so this result still needs to be tested for high-resolution simulations at shorter wavelengths.

Discriminating biosignature false positive scenarios using the reflected light technique may be considerably less challenging than for transmission. Our results from Chapter 4

(Chapter 4; Currie & Meadows, submitted) show that for reflected light observations, we may be able to readily rule out the biosignature false positives in the prebiotic Earth case and the ocean loss case with less than 100 hours of observing for nearby targets. We find that the false positive case for the $CO_2/CH_4$ pair (prebiotic Earth) is more readily ruled out than the $O_2$ false positive case (ocean loss) considered.

For the prebiotic Earth-like world, the $CO_2$ was comparably detectable to the Earth-like atmospheres for the Proxima b case, requiring $\sim 10$ hr of observation, and the $CH_4$ was only a factor of $\sim 5$ less detectable at $\sim 50$ hrs, making this a plausible false positive that may be detected with the ELTs. However, the prebiotic Earth-like atmosphere that builds up volcanic $CH_4$ would also build up significant CO, and detecting CO would be the discriminant that indicates that the $CH_4$ is from volcanic outgassing from a reducing mantle (Krissansen-Totton et al., 2018b; Thompson et al., 2022; Meadows et al., 2023). We find that this CO discriminant is readily detectable at $\sim 10$ hours of observing for the prebiotic Earth atmosphere for the nearest non-transiting target Proxima Centauri b, allowing us to rule out this $CO_2/CH_4$ false positive atmosphere with relatively few observational resources.

In comparison, for the 10 bar $O_2$-dominated post-ocean-loss planet, the abiotically-generated $O_2$ is less detectable than for the pre-industrial Earth photosynthetic biosphere, reducing the likelihood that a false positive is detected. The ocean loss atmosphere contains 10 bars of $O_2$, which both saturates the $O_2$ bands, and creates strong suppression of the high-resolution structure of $1.27\mu$m $O_2$ band due to $O_2$-$O_2$ collisionally-induced absorption (Leung et al., 2020). In addition, the post-ocean-loss environment $O_2$–$O_2$ collisionally-induced absorption works to suppress the water vapor bands we tested, requiring $\sim 10$ more hours to detect than the $\sim 1$ hr needed for the Proxima b habitable environments, and has undetectable $CH_4$. Therefore detection of the $O_2$ $0.76\mu$m band, but no detection of the $1.27\mu$m band, plus the lack of or severe depletion of $CH_4$ and $H_2O$, signs of which are detectable in a comparable exposure time, would make it less likely that the origin of the observed $O_2$ is biological. Comparing this result to the transit transmission case, where it may be challenging to rule out the ocean loss case, reveals that the reflected light method is much more sensitive to discriminating inhabited from uninhabited worlds. This result suggests that the reflected light technique is more robust to biosignature false positive environments, owing to both the accessibility of the molecular features and that the targets amenable to this technique are closer than known transiting terrestrial planets.

#### *6.3.1.4 Transmission vs. reflected light spectroscopy: A synthesis*

Overall, we find that observing terrestrial exoplanet atmospheres using either transmission or reflected light spectroscopy, can provide different advantages, including the number of systems available to observe, the accessibility of biosignatures, and our ability to rule out false positive mechanisms. Systems with transiting exoplanets are relatively rare because of the edge-on orientation required (e.g. Basri et al., 2005), and, despite the abundance of nearby M dwarf stars (e.g. Bochanski et al., 2010), the closest known system with transiting terrestrial HZ targets is the TRAPPIST-1 system at 12 pc away (Gillon et al., 2016, 2017). On the other hand, systems with non-transiting potentially terrestrial planets are more numerous and nearby, with several known systems with habitable zone planets within 5 pc: Proxima Centauri b (1.3 pc distant, M6V host Anglada-Escudé et al., 2016), GJ 1061 d (3.67 pc, M5.5V host Dreizler et al., 2020), Teegarden's Star c (3.83 pc, M7V host Zechmeister et al., 2019), and GJ 1002 b and c (4.85 pc, M5.5V host Mascareño et al., 2023). We may be able to characterize atmospheres for planets in the habitable zones of these stars, but the IWA of the ELTs may limit our ability to do so for later type hosts at 5 pc (see Figures 2.12 and 4.4). In particular, the full 0.5–2.0 $\mu$m wavelength range, along with the molecular features that we found to be detectable in this work, are accessible for Proxima Centauri b, but only molecular features $< 1\mu$m may be accessible to the GJ 1061 and Teegarden's Star targets (i.e. $CH_4$, $CO_2$, and $O_2$). For GJ 1002c, only the $O_2$ A-band may be accessible due to its distance and the IWA limit. Therefore, we will likely have more opportunities to characterize non-transiting planets than transiting planets with the ground-based ELTs, potentially providing near-term avenues for comparative studies of terrestrial atmospheres in different systems. Finally, while we find that the $CH_4/CO_2$ biosignature disequilibrium pair is potentially detectable for both transiting and non-transiting Earth-like Archean and modern atmospheres, but the $O_2/CH_4$ biosignature pair may be more detectable for reflected light observations. Based on current knowledge of biosignature false positives, we are more likely able to rule out false positive scenarios using reflected light spectroscopy than transmission spectroscopy, making reflected light observations the more robust technique for searching for signs of habitability and life.

### *6.3.2 Additional Insights via Molecular Retrieval*

Retrieving the abundance of $O_2$ may also provide a way to determine its origin, and this may be possible with the ELTs for both inhabited and uninhabited worlds by applying an atmospheric retrieval framework. For our retrieval study we specifically focused on $O_2$ because the ELTs are likely the only near term facilities that have the sensitivity to detect $O_2$ (Snellen et al., 2015; López-Morales et al., 2019; Lustig-Yaeger et al., 2019a; Hawker & Parry, 2019; Currie et al., 2023, in prep.) until the HWO launch planned for the 2040s (National Academies of Sciences, Engineering, and Medicine, 2021). Our results suggested that we may be able to retrieve the $O_2$ abundance for Proxima Centauri b atmospheres with 21% $O_2$ or less, to within a factor of 5 of the true value in the simulated ELT spectra when retrieving $O_2$ abundances of 1% and 5%, and within a factor of 1.25 for the 21% $O_2$ case. This provides a range of abundances for $O_2$ that are plausibly produced by life, and can support the interpretation that a planet is habitable due to reduced atmospheric flammability. For $O_2$ abundances over 24%, which we are currently not able to retrieve due to significant saturation in the band, fire activity could be catalyzed on the land surface of the planet, as has been seen in the Phanerozoic geological record (Lenton, 2013; Glasspool et al., 2015).

Using this abundance information gained from applying our upgraded retrieval framework, we may be able to further narrow the origin of the detected $O_2$ and identify the possible false positive mechanisms that may be at work. Specifically, if we are able to retrieve a $\sim 20\%$ $O_2$ abundance, this could point to either biologically-produced $O_2$ or abiotic

$O_2$ generated in a desiccated environment (Gao et al., 2015) or an atmosphere with low non-condensable gas inventory (Wordsworth & Pierrehumbert, 2014). To confirm the biological origin of $O_2$, we can additionally search for the presence of $CH_4$, which would reveal a biosignature disequilibrium pair. However, to rule out a desiccated false positive environment, we could also search for the presence of CO, which should be detectable in this environment (Chapter 4; Currie & Meadows, submitted). Finally, ruling out a low non-condensable gas inventory would require measuring the abundance of $N_2$, which is typically only seen as an $N_2$-$N_2$ collisionally induced absorption band near 4.2 $\mu$m (Schwieterman et al., 2015), and the lack of high-resolution and the long wavelength may make this challenging with the ELTs.

Additionally, identifying a post-ocean-loss environment by retrieving the high abundance of $O_2$ (Luger & Barnes, 2015; Meadows et al., 2018; Gialluca et al., 2024) may be challenging with the current implementation of the retrieval framework due to significant saturation of the bands, and we may need to rely on the Leung et al. (2020) method of looking for suppression of the 1.27 $\mu$m vs the 0.76 $\mu$m band for discriminating this case, which is achievable with the ELTs (Chapter 4; Currie & Meadows, submitted). Although we investigated our ability to measure the abundance for only a single molecule in a limited set of simulated atmospheres, this was the first time current state-of-the-art retrieval techniques were applied to simulated ELT observations, and the framework we developed is flexible to additionally test other molecules or atmospheric parameters in future studies, such as $CH_4$ for determining its surface flux. The advancements made in this study make a foundational step toward analyzing the first real ELT spectra of terrestrial exoplanet atmospheres in the near future, allowing us to search for signs of habitability and life from the ground.

### *6.3.3 Available Nearby Targets and Observing Protocols*

Given the detectability of a range of molecules in the atmospheres of terrestrial exoplanets using the ELTs, we have designed a recommended observing protocol to aid in observation planning in the near future when the ELTs begin to come online. We intend for this to be used as a guide for prioritizing spectral features when observing, if a choice between molecules or bandpasses is necessary. Figure 6.1 shows a visualization of the observing protocols for both transiting (upper) and non-transiting (lower) planets, and we describe each sequence below.

The best known terrestrial targets for transmission spectroscopy are in the TRAPPIST-1 system at 12 pc away from Earth and the size and terrestrial densities (Agol et al., 2021) of these planets are already confirmed (Gillon et al., 2016, 2017). For planets that transit their host star, prioritizing $CO_2$ first may indicate a terrestrial secondary atmosphere that is oxidized, and its high detectability ($<$ 10 transits for the target TRAPPIST-1 e) may provide a quick avenue for determining whether or not it has an atmosphere, and additionally it can be a habitability indicator controlling the climate and its ability to host liquid surface water (Walker et al., 1981; Kasting et al., 1993; Kopparapu et al., 2013). If $CO_2$ is detected, relatively low effort would be required to additionally search for the presence of $CH_4$, which is detectable in the same $\sim$ 10 hr timeframe and in the same wavelength region. A $CH_4$ detection in addition to $CO_2$ could immediately indicate a biosignature disequilibrium pair (Krissansen-Totton et al., 2018b,a; Meadows et al., 2023). Next, $O_2$ requires considerably more (>3x higher) observation time for transiting targets, and may be quite challenging to detect (Hardegree-Ullman et al., 2023; Currie et al., 2023), potentially making a $O_2/CH_4$ disequilibrium pair detection difficult (Currie et al., 2023), and should be prioritized later. Additionally, since transmission observations have much higher sensitivity to the upper layers of the atmosphere, $H_2O$ may be less accessible, and similar to $O_2$ we recommend prioritizing a search for this gas later in the sequence. Finally, CO may be challenging or even undetectable, and falls last on our list of gas priorities.

The best targets amenable to observations in reflected light will be targets $<$ 5 pc away from Earth (Chapter 4; Currie & Meadows, submitted), and there are several known systems that meet these requirements, including Proxima Centauri b (1.3 pc distant, M6V host Anglada-Escudé et al., 2016), GJ 1061 d (3.67 pc, M5.5V host Dreizler et al., 2020), Teegarden's Star c (3.83 pc, M7V host Zechmeister et al., 2019), and GJ 1002 b and c (4.85 pc, M5.5V host Mascareño et al., 2023). For reflected light observations, since planet size and true mass are unknown—the latter due to the unknown inclination of the system—we include the added step of discriminating a terrestrial atmosphere from a sub-Neptune by searching for H-bearing reduced species detectable within a few hours of observing. In the reflected light priority sequence, $H_2O$ is more detectable than both $CO_2$ and $CH_4$— the resources required to detect $H_2O$ in direct imaging are almost negligible ($\sim$ 1hr for the closes target, Proxima Centauri b) compared to those required of the other molecules ($\sim$ 10 hr or more), and an $H_2O$ detection could readily indicate the habitability of a target, prompting further followup. For $\sim$ 10 hr of observing Proxima Centauri b, $CO_2$, $CH_4$, $O_2$, and CO are all potentially accessible depending on the terrestrial atmosphere type. We recommend searching for $CO_2$ and $CH_4$ first because the most detectable bands of these molecules overlap in wavelength space, and a simultaneous detection could readily indicate a disequilibrium pair (e.g. Krissansen-Totton et al., 2016, 2018b,a; Meadows et al., 2023). $CO_2$ can also indicate the habitability of the atmosphere, as discussed in the previous paragraph. Furthermore, $O_2$ is also readily detectable ($\sim$ 10 hr) in the same NIR wavelength range, providing an opportunity to search for the $O_2/CH_4$ disequilibrium pair (Hitchcock & Lovelock, 1967; Meadows, 2017), which likely also requires $\sim$ 10 hr for Proxima Centauri b. For Proxima Centauri b it is likely possible to rule out a post ocean-loss $O_2$ false positive scenario if $O_2$ is detectable in the visible but not in the NIR $O_2$, and a lack of $H_2O$ and/or $CH_4$ is observed. Finally, ruling out abiotically-generated $CH_4$ may be possible by additionally detecting the presence of CO within the 10 hours required to detect $CH_4$— CO is not expected to be readily detectable for Earth-like atmospheres, so its presence can indicate an abiotic mechanism for the origin of detected $CH_4$.

Furthermore, the detectability framework built for these studies can help to inform future trade studies on the resolution, contrast, IWA, and wavelength range. Our results provide an initial look at the impact of some of these parameters, including resolution, contrast, and wavelength range. We found that spectrometers with R$>100,000$ resolving power will likely be optimal for these observations, with R$=300,000$ as the upper limit resolving power where photons begin to become spread too thin over the detector (Chapter 3). As expected, our

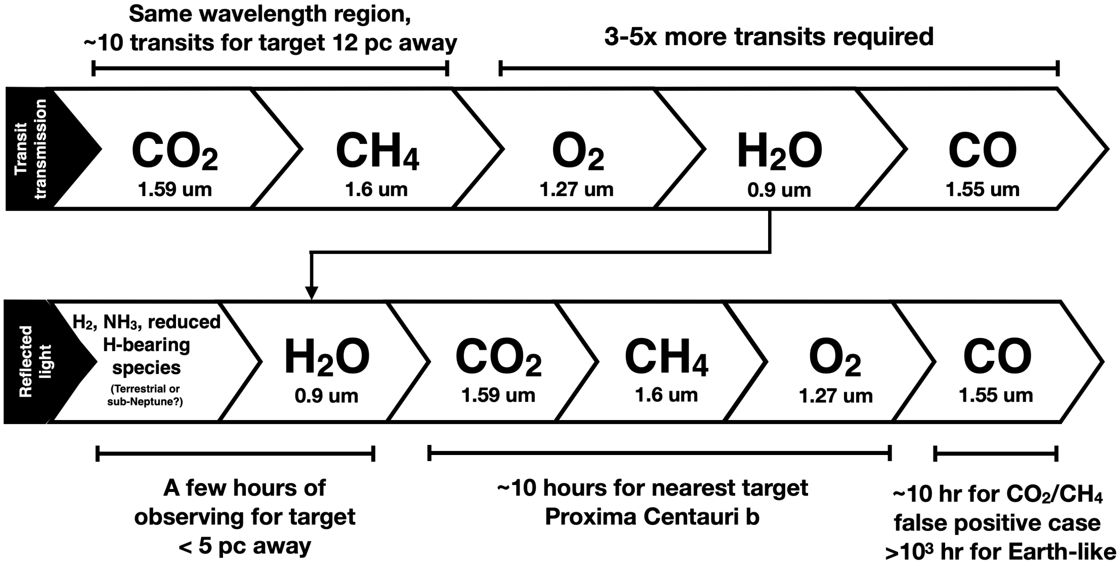

Figure 6.1 Observing protocols for characterizing the atmospheres of terrestrial planets using the transit transmission (upper) and reflected light (method).

ability to suppress stellar light to $< 10^{-4}$ will be critical to characterize nearby non-transiting terrestrial atmospheres (Chapter 4). Finally, we considered a range of molecular features between 0.5 and 2.0 $\mu$, and found that prioritizing the longer wavelength optical and the NIR (0.7–1.8 $\mu$m) will be necessary to detect multiple molecules, allowing us to search for signs of both habitability and life. Our observing protocol (described above and Figure 6.1) highlights the utility of these wavelength ranges and detecting individual molecules for atmospheric characterization. With our detectability pipeline, we are equipped to run more detailed ELT trade studies for instrument development purposes in the future.

## *6.4 Complementarities to Current and Future Space-based Missions*

The TRAPPIST-1 system is likely the best overlapping target for the ELTs and JWST, and observations of this system with the ELTs with transmission spectroscopy may be complementary to JWST observations. While JWST is more sensitive to the NIR, the ELTs will provide access to the visible wavelengths, with the potential to detect $O_2$ (Chapter 3;

Currie et al., 2023), which, for an Earth-like atmosphere is considered impossible for JWST by multiple research groups (Gialluca et al., 2021; Pidhorodetska et al., 2020; Lustig-Yaeger et al., 2019a; Wunderlich et al., 2020; Meadows et al., 2023). Additionally, constraints on the presence of other molecules detected with the JWST can be enhanced by following up with ELT observations, especially for $CO_2$ and $CH_4$, which are highly detectable with the ELTs for TRAPPIST-1 e (Chapter 3; Currie et al., 2023).

The ELTs will also be a proving ground for advanced coronagraphic instrumentation that will demonstrate critical technology to be incorporated into the future direct imaging NASA flagship mission, the Habitable Worlds Observatory (HWO) (National Academies of Sciences, Engineering, and Medicine, 2021). Our ability to suppress stellar light to directly image exoplanets is deeply rooted in ground-based observing (e.g. Guyon, 2018), and with goals of directly imaging Earth-like exoplanets around Sun-like stars at $\sim 10^{-10}$ contrast, the technology developed for HWO will be one of the most exciting engineering feats to date. In the near-term, ELT instrumentation will continue to push to lower contrasts (e.g. Palle et al., 2023), demonstrating both the coronagraphic instrumentation and our ability to directly image smaller planets for characterization studies. Furthermore, the ELTs will be operational in the years leading up to the 2040s launch of HWO, and can potentially provide precursor observations for the few M and potentially K dwarf targets that the ELTs and HWO will both be sensitive to (Currie et al., 2019; Mamajek & Stapelfeldt, 2023). These studies may include constraining the orbits of potentially terrestrial targets, or vetting the targets for terrestrial vs. sub-Neptune-like atmospheres (Chapter 4; Currie & Meadows, submitted), however a comprehensive study on the complementary science of the ELTs and HWO has not yet been completed. When the ELTs and HWO are both operational, their shared visible-NIR wavelength regime will also allow for space-based followup of some ELT targets to enhance ELT science. The ELTs will be most sensitive to M dwarf terrestrial planets (López-Morales et al., 2019), which potentially have very different evolutionary outcomes (e.g. Lincowski et al., 2018) than those of the more Sun-like stars that will be observed by HWO, allowing for a detailed comparative study for the outcomes of planetary evolution around stars of very different spectral types. Additionally, the ELTs will likely have a larger target overlap with the proposed ESA LIFE mission, which will also have a target list composed primarily of nearby M dwarf stars (Quanz et al., 2022).

## *6.5 Ongoing and Future Work*

In this work, we have addressed pressing issues in the field of terrestrial exoplanet characterization using future ground-based observatories that will help to drive the science goals and observing strategies of new ground and space-based telescopes. Although we made a promising leap forward in our understanding of the capabilities of these future facilities, there are many opportunities to build upon this work, and below we outline some of the challenges we plan to address in the near future.

### *6.5.1 Refining Approaches for Molecular Abundance Retrieval with the ELTs*

In Part I of this work, we have shown that is likely possible to detect a range of molecules in the atmospheres of terrestrial exoplanets orbiting in the habitable zones of nearby M dwarf stars, and in Part II, we have shown that it may be possible to constrain the abundance of one of these molecules, $O_2$, providing enhanced ability to characterize the exoplanet environment. However, there are many opportunities to investigate our ability to retrieve the abundances of other supporting gases in terrestrial atmospheres, such as the also detectable $CH_4$, $CO_2$, and $H_2O$. By determining the abundance of these other gases, we can further understand the planetary environment, and perhaps provide complementarity to future HWO observations of M dwarf planets by constraining the $CH_4$ abundance and therefore the surface flux, which HWO will be less sensitive to (The LUVOIR Team, 2019). Probing the limits of the habitable zone may also be possible by constraining the $CO_2$ abundance and climate of the planet. With the retrieval framework developed in Chapter 5 of this work, we have the mechanics in hand to address these questions to further understand the science that will be possible with the ELTs. These are projects that will soon be underway to help inform the instrumentation that is currently being developed for the ELTs and HWO. Additionally, in the near future, the analyses developed in this work can be used as the baseline for analyzing the first ELT spectra of terrestrial exoplanets to search for signs of habitability and life. Proxima Centauri b may also be a high-priority target for ground-based spectroscopy in the near term with Keck or the VLT (8–10 m class) with upcoming instrumentation, which may be able to either confirm or rule out a sub-Neptune atmosphere.

### *6.5.2 Combining Ground- and Space-based Observations to Retrieve More Precise Atmospheric Constraints*

Observations of terrestrial exoplanet atmospheres will be at the very limit of telescope capability, and to best characterize we must understand how the sensitivities, wavelength ranges, IWA, contrast, and spectral resolution of current and future telescopes can be combined to maximize our ability to study the limited number of targets. These telescopes include the James Webb Space Telescope (JWST), the upcoming extremely large ground-based telescopes (ELTs), the Habitable Worlds Observatory (HWO) flagship mission, and the Large Interferometer For Exoplanets (LIFE) mission concept. Each observatory will use different observing techniques in wavelength ranges spanning the UV-MIR, allowing them to probe different atmospheric parameters, such as temperature, pressure, and composition, and for different regions of the planetary atmosphere from the near-surface through the stratosphere. By simultaneously considering both ground- and space-based datasets, we can (1) access a broader wavelength range to search for novel molecules and observe multiple bands of a molecule, (2) maintain the continuum to determine absolute molecular abundance with ELT spectra, and (3) determine temperature structure from transmission and thermal emission, complementing the molecular detection and Rayleigh scattering in the visible-NIR. Using the expertise developed in this work, we will be poised to develop the first retrieval framework that simultaneously considers multiple datasets from future ground- and space-based telescopes to enhance the science of Earth-like exoplanet characterization beyond the individual capabilities of these observatories. The synergies defined by this framework will enhance our ability to explore nearby Earth-like exoplanet environments, and increase the likelihood of finding signs of habitability and life. This work can also inform the development of the HWO mission and aid in the design of second-generation ELT instrumentation.

# Chapter 7

# CONCLUSION

In this dissertation, we developed a novel detectability pipeline that simulates ELT observations of terrestrial exoplanet atmospheres and applies a cross-correlation technique to analyze the high-resolution simulated spectra for molecular features. We considered a range of atmosphere types around M dwarf stars, including inhabited pre-industrial Earth-like and Archean Earth-like atmospheres, uninhabited but habitable biosignature false positive environments, and a sub-Neptune atmosphere. We found that the ELTs will be sensitive to a range of molecular species between 0.5 and 2.0 $\mu$m, including $O_2$, $CO_2$, $CH_4$, $H_2O$, and CO, in both transiting and non-transiting nearby terrestrial exoplanet atmospheres within $\sim 10$ hours of observing time for the best case scenarios. Additionally, we may be able to discriminate terrestrial from sub-Neptune atmospheres by detecting $H_2$ and/or $NH_3$ within a single hour of observing using reflected light spectroscopy for nearby potentially terrestrial planets, including Proxima Centauri b, breaking the mass–inclination degeneracy for non-transiting targets and confirming an $H_2$-dominated atmosphere. For terrestrial targets, we found that the $CO_2/CH_4$ biosignature pair is readily accessible for the nearest habitable transiting target TRAPPIST-1 e, as well as the nearest potentially habitable non-transiting target Proxima Centauri b. We may also be able to detect the $O_2/CH_4$ biosignature disequilibrium pair in 10 hours for Proxima Centauri b, and $< 100$ hours for other non-transiting targets $< 5$ pc away. Furthermore, while our results suggest that it may be challenging to discriminate biosignature false positive atmospheres in transit transmission observations, the molecules needed may be readily detectable in reflected light for non-transiting targets, and we find that we are able to discriminate abiotic from biological $CH_4$ and $O_2$ generated in prebiotic Earth and ocean loss scenarios, respectively. Additionally, the prospects for determining the abundance of $O_2$ for Proxima Centauri b are promising, and we may be able to retrieve the abundance of $O_2$ to within a few factors of its true abundance for both inhabited and uninhabited worlds with Earth-like $O_2$ abundance or less ($\leq 21\%$ $O_2$), providing supplementary evidence pointing to either an abiotic or biological mechanism for generating $O_2$. In the near term, the ELTs will be more than just a telescope to detect $O_2$— they will be powerful astrobiological tools that we can use to characterize both inhabited and uninhabited terrestrial atmospheres and more critically discriminate between these scenarios to enable the first search for signs of habitability and life in the atmospheres of multiple nearby exoplanets.

# BIBLIOGRAPHY

Agol, E., Dorn, C., Grimm, S. L., et al. 2021, Planet. Sci. J., 2, 1

Aime, C., Soummer, R., & Ferrari, A. 2002, A&A, 389, 334, doi: `10.1051/0004-6361:20020419`

Akeson, R. L., Chen, X., Ciardi, D., et al. 2013, PASP, 125, 989, doi: `10.1086/672273`

Allard, F., Hauschildt, P. H., Alexander, D. R., & Starrfield, S. 1997, Annu. Rev. Astron. Astrophys., 35, 137

Allart, R., Lovis, C., Pino, L., et al. 2017, Astron. Astrophys. Suppl. Ser., 606, A144

Angelo, I., & Hu, R. 2017, AJ, 154, 232, doi: `10.3847/1538-3881/aa9278`

Anglada-Escudé, G., Amado, P. J., Barnes, J., et al. 2016, Nature, 536, 437

Arney, G., Domagal-Goldman, S. D., & Meadows, V. S. 2018, Astrobiology, 18, 311, doi: `10.1089/ast.2017.1666`

Arney, G. N., Meadows, V. S., Domagal-Goldman, S. D., et al. 2017, ApJ, 836, 49, doi: `10.3847/1538-4357/836/1/49`

Ball, P. 2008, Chem. Rev., 108, 74

Basri, G., Borucki, W. J., & Koch, D. 2005, New Astronomy Reviews, 49, 478

Bean, J. L., Raymond, S. N., & Owen, J. E. 2021, Journal of Geophysical Research (Planets), 126, e06639, doi: `10.1029/2020JE006639`

Bell, T. J., Crouzet, N., Cubillos, P. E., et al. 2024, Nature Astronomy, 1

Ben-Ami, S., López-Morales, M., Garcia-Mejia, J., Abad, G. G., & Szentgyorgyi, A. 2018, The Astrophysical Journal, 861, 79, doi: `10.3847/1538-4357/aac835`

Berta-Thompson, Z. K., Irwin, J., Charbonneau, D., et al. 2015, Nature, 527, 204

Bertaux, J. L., Lallement, R., Ferron, S., Boonne, C., & Bodichon, R. 2014, A&A, 564, A46, doi: `10.1051/0004-6361/201322383`

Beust, H., Lagrange-Henri, A. M., Vidal-Madjar, A., & Ferlet, R. 1990, A&A, 236, 202

Birkby, J. L. 2018, arXiv e-prints, arXiv:1806.04617, doi: `10.48550/arXiv.1806.04617`

Birkby, J. L., de Kok, R. J., Brogi, M., et al. 2013, Mon. Not. R. Astron. Soc. Lett., 436, L35

Birkby, J. L., de Kok, R. J., Brogi, M., Schwarz, H., & Snellen, I. A. G. 2017a, The Astronomical Journal, 153, 138, doi: `10.3847/1538-3881/aa5c87`

Birkby, J. L., Kok, R. J. d., Brogi, M., Schwarz, H., & Snellen, I. A. G. 2017b, Astron. J., 153, 138

Bixel, A., & Apai, D. 2017, The Astrophysical Journal Letters, 836, L31

Bochanski, J. J., Hawley, S. L., Covey, K. R., et al. 2010, The Astronomical Journal, 139, 2679

Bonfils, X., Delfosse, X., Udry, S., et al. 2005, Astron. Astrophys. Suppl. Ser., 442, 635

Bourrier, V., Dumusque, X., Dorn, C., et al. 2018, A&A, 619, A1, doi: `10.1051/0004-6361/201833154`

Brandl, B. R., Feldt, M., Glasse, A., et al. 2014, in Ground-based and Airborne Instrumentation for Astronomy V, Vol. 9147, SPIE, 747–764

Brogi, M., de Kok, R. J., Albrecht, S., et al. 2016, The Astrophysical Journal, 817, 106, doi: `10.3847/0004-637x/817/2/106`

Brogi, M., de Kok, R. J., Birkby, J. L., Schwarz, H., & Snellen, I. A. G. 2014, A&A, 565, A124, doi: `10.1051/0004-6361/201423537`

Brogi, M., Giacobbe, P., Guilluy, G., et al. 2018, Astron. Astrophys. Suppl. Ser., 615, A16

Brogi, M., Line, M., Bean, J., Désert, J. M., & Schwarz, H. 2017, ApJL, 839, L2, doi: `10.3847/2041-8213/aa6933`

Brogi, M., & Line, M. R. 2019, The Astronomical Journal, 157, 114, doi: `10.3847/1538-3881/aaffd3`

Brogi, M., Snellen, I. A., De Kok, R. J., et al. 2012, Nature, 486, 502, doi: `10.1038/nature11161`

—. 2013, Astrophysical Journal, 767, doi: `10.1088/0004-637X/767/1/27`

Brown, A. G. A., Vallenari, A., Prusti, T., et al. 2018, Astron. Astrophys. Suppl. Ser., 616, A1

Brown, R. A. 2005, ApJ, 624, 1010, doi: `10.1086/429124`

Bruno, G., Deleuil, M., Almenara, J.-M., et al. 2016, Astron. Astrophys. Suppl. Ser., 595, A89

Bruno, G., Lewis, N. K., Alam, M. K., et al. 2020, Mon. Not. R. Astron. Soc., 491, 5361

Burrows, A. S. 2014, Proceedings of the National Academy of Sciences, 111, 12601

Butler, R. P., Marcy, G. W., Williams, E., Hauser, H., & Shirts, P. 1997, The Astrophysical Journal, 474, L115

Cabot, S. H., Madhusudhan, N., Constantinou, S., et al. 2024, The Astrophysical Journal Letters, 966, L10

Carrión-González, Ó., Muñoz, A. G., Cabrera, J., et al. 2020, Astronomy & Astrophysics, 640, A136

Catling, D. C., & Zahnle, K. J. 2020, Science advances, 6, eaax1420

Charbonneau, D., Brown, T. M., Noyes, R. W., & Gilliland, R. L. 2002, ApJ, 568, 377, doi: `10.1086/338770`

Charbonneau, D., Berta, Z. K., Irwin, J., et al. 2009, Nature, 462, 891, doi: `10.1038/nature08679`

Charnay, B., Meadows, V., & Leconte, J. 2015, ApJ, 813, 15, doi: `10.1088/0004-637X/813/1/15`

Cheverall, C., & Madhusudhan, N. 2024, arXiv preprint arXiv:2403.18894

Chisholm, E. M., Larkin, J. E., Wright, S. A., et al. 2020, in Ground-based and Airborne Instrumentation for Astronomy VIII, Vol. 11447, SPIE, 114471V

Christiansen, J. L. 2022, Nature Astronomy, 6, 516

Cockell, C. S., Bush, T., Bryce, C., et al. 2016, Astrobiology, 16, 89

Costa, E., Méndez, R. A., Jao, W.-C., et al. 2006, AJS, 132, 1234

Cowan, N. B., Greene, T., Angerhausen, D., et al. 2015, PASP, 127, 311, doi: `10.1086/680855`

Crass, J., Crepp, J., Sands, B., et al. 2023, in American Astronomical Society Meeting Abstracts, Vol. 55, American Astronomical Society Meeting Abstracts, 267.05

Crisp, D. 1997, Geophys. Res. Lett., 24, 571

Crossfield, I. J. 2016, arXiv preprint arXiv:1604.06458

Crossfield, I. J. M., Barman, T., & Hansen, B. M. S. 2011, ApJ, 736, 132, doi: `10.1088/0004-637X/736/2/132`

Currie, M. H., & Meadows, V. S. submitted

Currie, M. H., Meadows, V. S., & Lustig-Yaeger, J. in prep.

Currie, M. H., Meadows, V. S., & Rasmussen, K. C. 2023, PSJ, 4, 83, doi: `10.3847/PSJ/accf86`

Currie, M. H., Stark, C. C., Kammerer, J., Juanola-Parramon, R., & Meadows, V. S. 2023, The Astronomical Journal, 166, 197

Currie, T., Belikov, R., Guyon, O., et al. 2019, BAAS, 51, 154, doi: `10.48550/arXiv.1903.05468`

Czesla, S., Huber, K. F., Wolter, U., Schröter, S., & Schmitt, J. H. M. 2009, Astron. Astrophys. Suppl. Ser., 505, 1277

Damiano, M., & Hu, R. 2022, AJ, 163, 299, doi: `10.3847/1538-3881/ac6b97`

Damiano, M., Hu, R., & Hildebrandt, S. R. 2020, AJ, 160, 206, doi: `10.3847/1538-3881/abb76a`

Davis, C. E., Meadows, V. S., Lincowski, A. P., et al. in prep.

De Kok, R. J., Birkby, J., Brogi, M., et al. 2014, Astronomy and Astrophysics, 561, 1, doi: `10.1051/0004-6361/201322947`

de Kok, R. J., Birkby, J., Brogi, M., et al. 2014, a&a, 8, 1

de Kok, R. J., Brogi, M., Snellen, I. A. G., et al. 2013, Astron. Astrophys. Suppl. Ser., 554, A82

Defrère, D., Stark, C., Cahoy, K., & Beerer, I. 2012, in Society of Photo-Optical Instrumentation Engineers (SPIE) Conference Series, Vol. 8442, Space Telescopes and Instrumentation 2012: Optical, Infrared, and Millimeter Wave, ed. M. C. Clampin, G. G. Fazio, H. A. MacEwen, & J. Oschmann, Jacobus M., 84420M, doi: `10.1117/12.926324`

Deibert, E. K., de Mooij, E. J. W., Jayawardhana, R., et al. 2021, AJ, 161, 209, doi: `10.3847/1538-3881/abe768`

Deming, D., Harrington, J., Laughlin, G., et al. 2007, ApJL, 667, L199, doi: `10.1086/522496`

Demory, B.-O., Gillon, M., de Wit, J., et al. 2016, Nature, 532, 207, doi: `10.1038/nature17169`

Dermott, S. F., Jayaraman, S., Xu, Y. L., Gustafson, B. Å. S., & Liou, J. C. 1994, Nature, 369, 719

Dermott, S. F., Kehoe, T. J. J., Durda, D. D., Grogan, K., & Nesvorný, D. 2002, in ESA Special Publication, Vol. 500, Asteroids, Comets, and Meteors: ACM 2002, ed. B. Warmbein, 319–322

Dermott, S. F., Nicholson, P. D., Burns, J. A., & Houck, J. R. 1985, in IAU Colloq. 85: Properties and Interactions of Interplanetary Dust, ed. R. H. Giese & P. Lamy, 395, doi: `10.1007/978-94-009-5464-9_77`

Des Marais, D. J., Harwit, M. O., Jucks, K. W., et al. 2002, Astrobiology, 2, 153, doi: `10.1089/15311070260192246`

Des Marais, D. J., Nuth, Joseph A., I., Allamandola, L. J., et al. 2008, Astrobiology, 8, 715, doi: `10.1089/ast.2008.0819`

Désert, J.-M., Charbonneau, D., Demory, B.-O., et al. 2011, ApJS, 197, 14

Dierickx, P., & Gilmozzi, R. 2000, in Telescope Structures, Enclosures, Controls, Assembly/Integration/Validation, and Commissioning, Vol. 4004, SPIE, 290–299

Dittmann, J. A., Irwin, J. M., Charbonneau, D., et al. 2017, Nature, 544, 333

Domagal-Goldman, S. D., Segura, A., Claire, M. W., Robinson, T. D., & Meadows, V. S. 2014, ApJ, 792, 90

Draine, B. T., & Lee, H. M. 1984, ApJ, 285, 89, doi: `10.1086/162480`

Dreizler, S., Jeffers, S. V., Rodríguez, E., et al. 2020, Mon. Not. R. Astron. Soc., 493, 536

Ducrot, E., Lagage, P.-O., Min, M., et al. 2024, "Research Square preprint 10.21203/rs.3.rs-3706919/v1", doi: `10.21203/rs.3.rs-3706919/v1`

Ehrenreich, D., Lovis, C., Allart, R., et al. 2020, Nature, 580, 597, doi: `10.1038/s41586-020-2107-1`

Ertel, S., Defrère, D., Hinz, P., et al. 2020, AJS, 159, 177

Esteves, L. J., de Mooij, E. J. W., Jayawardhana, R., Watson, C., & de Kok, R. 2017, AJ, 153, 268, doi: `10.3847/1538-3881/aa7133`

Etiope, G., & Sherwood Lollar, B. 2013, Rev. Geophys., 51, 276

Fanson, J., Bernstein, R., Ashby, D., et al. 2022, in Ground-based and Airborne Telescopes IX, Vol. 12182, SPIE, 454–473

Fanson, J. L., Bernstein, R. A., Angeli, G. Z., et al. 2020, in Ground-based and Airborne Telescopes VIII, ed. H. K. Marshall, J. Spyromilio, & T. Usuda (SPIE)

Fauchez, T. J., Turbet, M., Villanueva, G. L., et al. 2019, ApJ, 887, 194

Feng, Y. K., Robinson, T. D., Fortney, J. J., et al. 2018, AJ, 155, 200, doi: `10.3847/1538-3881/aab95c`

Filippazzo, J. C., Rice, E. L., Faherty, J., et al. 2015, ApJ, 810, 158

Fischer, D., Jurgenson, C., McCracken, T., et al. 2017, in American Astronomical Society Meeting Abstracts, Vol. 229, American Astronomical Society Meeting Abstracts #229, 126.04

Follert, R., Dorn, R., Oliva, E., et al. 2014, in Ground-based and Airborne Instrumentation for Astronomy V, Vol. 9147, SPIE, 476–485

Fortney, J. J., Dawson, R. I., & Komacek, T. D. 2021, Journal of Geophysical Research (Planets), 126, e06629, doi: `10.1029/2020JE006629`

Franks, F., & Jones, M. 1987, FEBS Letters, 220, 391

Fulton, B. J., Petigura, E. A., Howard, A. W., et al. 2017, AJ, 154, 109, doi: `10.3847/1538-3881/aa80eb`

Gaidos, E. J., Nealson, K. H., & Kirschvink, J. L. 1999, Science, 284, 1631

Gandhi, S., Brogi, M., & Webb, R. K. 2020, Mon. Not. R. Astron. Soc., 498, 194

Gao, P., Hu, R., Robinson, T. D., Li, C., & Yung, Y. L. 2015, ApJ, 806, 249

Gao, P., Thorngren, D. P., Lee, E. K. H., et al. 2020, Nature Astronomy, 4, 951, doi: `10.1038/s41550-020-1114-3`

Gaudi, B. S., Seager, S., Mennesson, B., et al. 2020, arXiv e-prints, arXiv:2001.06683, doi: `10.48550/arXiv.2001.06683`

Gialluca, M. T., Barnes, R., Meadows, V. S., et al. 2024, The Planetary Science Journal, 5, 137

Gialluca, M. T., Robinson, T. D., Rugheimer, S., & Wunderlich, F. 2021, Publications of the Astronomical Society of the Pacific, 133, 054401

Gibson, N. P., Merritt, S., Nugroho, S. K., et al. 2020, Monthly Notices of the Royal Astronomical Society, 493, 2215, doi: `10.1093/mnras/staa228`

Gilbert-Janizek, S., Meadows, V. S., & Lustig-Yaeger, J. 2024, arXiv preprint arXiv:2404.01423

Gillon, M., Jehin, E., Lederer, S. M., et al. 2016, Nature, 533, 221

Gillon, M., Triaud, A. H. M. J., Demory, B.-O., et al. 2017, Nature, 542, 456

Gilmozzi, R., & Spyromilio, J. 2007, The Messenger, 127, 3

Gizis, J. E., Monet, D. G., Neill Reid, I., et al. 2007, AJS, 120, 1085

Glasspool, I. J., Scott, A. C., Waltham, D., Pronina, N., & Shao, L. 2015, Frontiers in Plant Science, 6, 756

Gorshelev, V., Serdyuchenko, A., Weber, M., Chehade, W., & Burrows, J. 2014, Atmospheric Measurement Techniques, 7, 609

Greaves, J. S., Holland, W. S., Moriarty-Schieven, G., et al. 1998, ApJL, 506, L133, doi: `10.1086/311652`

Greene, T. P., Bell, T. J., Ducrot, E., et al. 2023, Nature, 618, 39, doi: `10.1038/s41586-023-05951-7`

Grenfell, J. L., Lehmann, R., Mieth, P., Langematz, U., & Steil, B. 2006, Journal of Geophysical Research: Atmospheres, 111

Grenfell, J. L., Stracke, B., von Paris, P., et al. 2007, Planetary and Space Science, 55, 661

Guerrero, N. M., Seager, S., Huang, C. X., et al. 2021, The Astrophysical Journal Supplement Series, 254, 39

Guilluy, G., Sozzetti, A., Brogi, M., et al. 2019, Astronomy & Astrophysics, 625, A107

Guyon, O. 2018, Annu. Rev. Astron. Astrophys., 56, 315

Guzmán-Marmolejo, A., Segura, A., & Escobar-Briones, E. 2013, Astrobiology, 13, 550

Harada, C. K., Kempton, E. M.-R., Rauscher, E., et al. 2021, The Astrophysical Journal, 909, 85

Hardegree-Ullman, K. K., Apai, D., Bergsten, G. J., Pascucci, I., & López-Morales, M. 2023, AJ, 165, 267, doi: `10.3847/1538-3881/acd1ec`

Harman, C. E., Felton, R., Hu, R., et al. 2018, ApJ, 866, 56

Harman, C. E., Schwieterman, E. W., Schottelkotte, J. C., & Kasting, J. F. 2015, ApJ, 812, 137

Harrington, J., Hansen, B. M., Luszcz, S. H., et al. 2006, Science, 314, 623, doi: `10.1126/science.1133904`

Hatzes, A. P. 2016, Methods of detecting exoplanets: 1st advanced school on exoplanetary science, 3

Hawker, G. A., Madhusudhan, N., Cabot, S. H., & Gandhi, S. 2018, The Astrophysical Journal Letters, 863, L11

Hawker, G. A., & Parry, I. R. 2019, Mon. Not. R. Astron. Soc., 484, 4855

Hedelt, P., Von Paris, P., Godolt, M., et al. 2013, Astronomy and Astrophysics, 553, 1, doi: `10.1051/0004-6361/201117723`

Heng, K., & Showman, A. P. 2015, Annual Review of Earth and Planetary Sciences, 43, 509, doi: `10.1146/annurev-earth-060614-105146`

Hitchcock, D. R., & Lovelock, J. E. 1967, Icarus, 7, 149

Hoeijmakers, H., Cabot, S., Zhao, L., et al. 2020a, Astronomy & Astrophysics, doi: `10.1051/0004-6361/202037437`

Hoeijmakers, H. J., de Kok, R. J., Snellen, I. A. G., et al. 2015, A&A, 575, A20, doi: `10.1051/0004-6361/201424794`

Hoeijmakers, H. J., Snellen, I. A., & Van Terwisga, S. E. 2018a, Astronomy and Astrophysics, 610, 1, doi: `10.1051/0004-6361/201731192`

Hoeijmakers, H. J., Ehrenreich, D., Heng, K., et al. 2018b, Nature, 560, 453, doi: `10.1038/s41586-018-0401-y`

Hoeijmakers, H. J., Ehrenreich, D., Kitzmann, D., et al. 2019, Astronomy and Astrophysics, 627, doi: `10.1051/0004-6361/201935089`

Hoeijmakers, H. J., Seidel, J. V., Pino, L., et al. 2020b, Astronomy & Astrophysics, 641, A123

Holmberg, M., & Madhusudhan, N. 2022, The Astronomical Journal, 164, 79

Hood, C. E., Fortney, J. J., Line, M. R., et al. 2020, The Astronomical Journal, 160, 198

Houdebine, E. R. 2010, Mon. Not. R. Astron. Soc., 407, 1657

Houghton, J. T. 2002, The physics of atmospheres (Cambridge University Press)

Hu, R., Seager, S., & Bains, W. 2012, ApJ, 761, 166

Hu, R., Bello-Arufe, A., Zhang, M., et al. 2024, Nature, 1

Ih, J., Kempton, E. M. R., Whittaker, E. A., & Lessard, M. 2023, ApJL, 952, L4, doi: `10.3847/2041-8213/ace03b`

Inaba, S., & Ikoma, M. 2003, A&A, 410, 711, doi: `10.1051/0004-6361:20031248`

Irwin, P., Teanby, N., De Kok, R., et al. 2008, Journal of Quantitative Spectroscopy and Radiative Transfer, 109, 1136

Ivanova, A., Lallement, R., & Bertaux, J. L. 2023, arXiv e-prints, arXiv:2302.03897, doi: `10.48550/arXiv.2302.03897`

Jensen-Clem, R., Hinz, P., von Kooten, M., et al. 2021, in Society of Photo-Optical Instrumentation Engineers (SPIE) Conference Series, Vol. 11823, Techniques and Instrumentation for Detection of Exoplanets X, ed. S. B. Shaklan & G. J. Ruane, 1182309, doi: `10.1117/12.2594005`

Jindal, A., de Mooij, E. J., Jayawardhana, R., et al. 2020, arXiv preprint arXiv:2007.03115

John, C. E. S., & Nicholson, S. B. 1922, Phys. Rev., 19, 444, doi: `10.1103/PhysRev.19.444`

Johns, M., McCarthy, P., Raybould, K., et al. 2012, Ground-based and Airborne Telescopes IV, 8444, 526

Jones, A., Noll, S., Kausch, W., Szyszka, C., & Kimeswenger, S. 2013, Astron. Astrophys. Suppl. Ser., 560, A91

Jontof-Hutter, D. 2019, Annual Review of Earth and Planetary Sciences, 47, 141

Kaeufl, H.-U., Ballester, P., Biereichel, P., et al. 2004, in Proceedings of SPIE, Vol. 5492, Springer, 1218–1227

Kalas, P. 2005, ApJL, 635, L169, doi: `10.1086/499400`

Kalas, P., Graham, J. R., Chiang, E., et al. 2008, science, 322, 1345

Kaltenegger, L., & Lin, Z. 2021, ApJL, 909, L2

Kammerer, J., Stark, C. C., Ludwick, K. J., Juanola-Parramon, R., & Nemati, B. 2022, AJ, 164, 235, doi: `10.3847/1538-3881/ac97eb`

Kanodia, S., Mahadevan, S., Ramsey, L. W., et al. 2018, in Society of Photo-Optical Instrumentation Engineers (SPIE) Conference Series, Vol. 10702, Ground-based and Airborne Instrumentation for Astronomy VII, ed. C. J. Evans, L. Simard, & H. Takami, 107026Q, doi: `10.1117/12.2313491`

Kasdin, N. J., & Braems, I. 2006, ApJ, 646, 1260, doi: `10.1086/505017`

Kasting, J., & Walker, J. C. 1981, Journal of Geophysical Research: Oceans, 86, 1147

Kasting, J. F., Liu, S. C., & Donahue, T. M. 1979, J. Geophys. Res., 84, 3097

Kasting, J. F., Whitmire, D. P., & Reynolds, R. T. 1993, Icarus, 101, 108

Kawahara, H., Matsuo, T., Takami, M., et al. 2012, ApJ, 758, 13

Keles, E., Mallonn, M., Kitzmann, D., et al. 2022, MNRAS, 513, 1544, doi: `10.1093/mnras/stac810`

Kennedy, G. M., & Piette, A. 2015, MNRAS, 449, 2304, doi: `10.1093/mnras/stv453`

Kenner, R. D., & Ogryzlo, E. A. 1984, JChPh, 80, 1, doi: `10.1063/1.446479`

Kervella, P., Thévenin, F., & Lovis, C. 2017, Astron. Astrophys. Suppl. Ser., 598, L7

Khomich, V. Y., Semenov, A. I., & Shefov, N. N. 2008, Airglow as an indicator of upper atmospheric structure and dynamics (Springer Science & Business Media)

Kiang, N. Y., Domagal-Goldman, S., Parenteau, M. N., et al. 2018, Astrobiology, 18, 619

Kite, E. S., & Barnett, M. N. 2020, Proceedings of the National Academy of Sciences, 117, 18264

Knutson, H. A., Charbonneau, D., Allen, L. E., et al. 2007, Nature, 447, 183, doi: `10.1038/nature05782`

Koch, D. G., Borucki, W. J., Basri, G., et al. 2010, The Astrophysical Journal Letters, 713, L79

Konopacky, Q. M., Baker, A. D., Mawet, D., et al. 2023, in Techniques and Instrumentation for Detection of Exoplanets XI, Vol. 12680, SPIE, 50–74

Kopparapu, R. K., Ramirez, R., Kasting, J. F., et al. 2013, ApJ, 765, 131

Kotani, T., Tamura, M., Nishikawa, J., et al. 2018, in Society of Photo-Optical Instrumentation Engineers (SPIE) Conference Series, Vol. 10702, Ground-based and Airborne Instrumentation for Astronomy VII, ed. C. J. Evans, L. Simard, & H. Takami, 1070211, doi: `10.1117/12.2311836`

Krissansen-Totton, J., Bergsman, D. S., & Catling, D. C. 2016, Astrobiology, 16, 39

Krissansen-Totton, J., Garland, R., Irwin, P., & Catling, D. C. 2018a, AJS, 156, 114

Krissansen-Totton, J., Olson, S., & Catling, D. C. 2018b, Sci Adv, 4, eaao5747

Kuchner, M. J., & Holman, M. J. 2003, ApJ, 588, 1110, doi: `10.1086/374213`

Lagrange, A.-M., Bonnefoy, M., Chauvin, G., et al. 2010, Science, 329, 57

Landman, R., Stolker, T., Snellen, I., et al. 2024, Astronomy & Astrophysics, 682, A48

Lederberg, J. 1965, Nature, 207, 9

Lee, E., Wood, K., Dobbs-Dixon, I., Rice, A., & Helling, C. 2017, Astronomy & Astrophysics, 601, A22

Lee, J.-M., Fletcher, L. N., & Irwin, P. G. 2012, Monthly Notices of the Royal Astronomical Society, 420, 170

Lenton, T. M. 2013, Fire phenomena and the Earth system: an interdisciplinary guide to fire science, 289

Lesjak, F., Nortmann, L., Yan, F., et al. 2023, Astronomy & Astrophysics, 678, A23

Leslie, M. 2009, On the origin of photosynthesis, American Association for the Advancement of Science

Leung, M., Meadows, V. S., & Lustig-Yaeger, J. 2020, The Astronomical Journal, 160, 11, doi: `10.3847/1538-3881/ab9012`

Levine, M., Shaklan, S., & Kasting, J. 2006, Terrestrial Planet Finder Coronagraph Science and Technology Definition Team Report, Tech. Rep. D-34923, Jet Propulsion Laboratory

Lin, Z., & Kaltenegger, L. 2020, Monthly Notices of the Royal Astronomical Society, 491, 2845, doi: `10.1093/mnras/stz3213`

Lincowski, A. P., Meadows, V. S., Crisp, D., et al. 2018, ApJ, 867, 76

Lincowski, A. P., Meadows, V. S., Zieba, S., et al. 2023, ApJL, 955, L7, doi: `10.3847/2041-8213/acee02`

Line, M. R., Wolf, A. S., Zhang, X., et al. 2013, The Astrophysical Journal, 775, 137

Line, M. R., Stevenson, K. B., Bean, J., et al. 2016, The Astronomical Journal, 152, 203

Line, M. R., Brogi, M., Bean, J. L., et al. 2021, Nature, 598, 580

Lockwood, A. C., Johnson, J. A., Bender, C. F., et al. 2014, ApJL, 783, L29, doi: `10.1088/2041-8205/783/2/L29`

Lodders, K., & Fegley, B. 1998, The planetary scientist's companion (Oxford University Press, USA)

López-Morales, M., Ben-Ami, S., Gonzalez-Abad, G., et al. 2019, The Astronomical Journal, 158, 24, doi: `10.3847/1538-3881/ab21d7`

López-Morales, M., Currie, T., Teske, J., et al. 2019, arXiv preprint arXiv:1903.09523

Louden, T. M., & Wheatley, P. 2015, in AAS/Division for Extreme Solar Systems Abstracts, Vol. 47, AAS/Division for Extreme Solar Systems Abstracts, 111.28

Lovelock, J. E. 1965, Nature, 207, 568

Lovelock, J. E., & Kaplan, I. R. 1975, Proceedings of the Royal Society of London. Series B, Biological Sciences, 189, 167

Lovis, C., Fischer, D., et al. 2010, Exoplanets, 27

Lovis, C., Snellen, I., Mouillet, D., et al. 2017, Astronomy and Astrophysics, 599, doi: `10.1051/0004-6361/201629682`

Lovis, C., Blind, N., Chazelas, B., et al. 2022, in Society of Photo-Optical Instrumentation Engineers (SPIE) Conference Series, Vol. 12184, Ground-based and Airborne Instrumentation for Astronomy IX, ed. C. J. Evans, J. J. Bryant, & K. Motohara, 121841Q, doi: `10.1117/12.2627923`

Luger, R., & Barnes, R. 2015, Astrobiology, 15, 119

Lustig-Yaeger, J. 2020, PhD thesis, University of Washington, Seattle

Lustig-Yaeger, J., Meadows, V. S., Crisp, D., Line, M. R., & Robinson, T. D. 2023a, PSJ, 4, 170, doi: `10.3847/PSJ/acf3e5`

Lustig-Yaeger, J., Meadows, V. S., & Lincowski, A. P. 2019a, AJS, 158, 27

Lustig-Yaeger, J., Robinson, T. D., & Arney, G. 2019b, Journal of Open Source Software, 4, 1387, doi: `10.21105/joss.01387`

Lustig-Yaeger, J., Sotzen, K. S., Stevenson, K. B., et al. 2022, AJ, 163, 140, doi: `10.3847/1538-3881/ac5034`

Lustig-Yaeger, J., Fu, G., May, E. M., et al. 2023b, Nature Astronomy, 7, 1317, doi: `10.1038/s41550-023-02064-z`

Lyons, T. W., Reinhard, C. T., & Planavsky, N. J. 2014, Nature, 506, 307, doi: `10.1038/nature13068`

Lyons, T. W., Reinhard, C. T., & Planavsky, N. J. 2014, Nature, 506, 307

Lyu, Z., Shao, N., Akinyemi, T., & Whitman, W. B. 2018, Current Biology, 28, R727

Macdonald, E. J., & Cowan, N. B. 2019, Monthly Notices of the Royal Astronomical Society, 489, 196, doi: `10.1093/mnras/stz2047`

Madhusudhan, N., Agúndez, M., Moses, J. I., & Hu, Y. 2016, Space science reviews, 205, 285

Madhusudhan, N., & Seager, S. 2009, The Astrophysical Journal, 707, 24

Maimone, M., Brogi, M., Chiavassa, A., et al. 2022, Astronomy & Astrophysics, 667, A106

Malaterre, C., Ten Kate, I. L., Baqué, M., et al. 2023, Astrobiology, 23, 1213

Males, J. R., Close, L. M., Haffert, S. Y., et al. 2022, in Society of Photo-Optical Instrumentation Engineers (SPIE) Conference Series, Vol. 12185, Adaptive Optics Systems VIII, ed. L. Schreiber, D. Schmidt, & E. Vernet, 121854J, doi: `10.1117/12.2630619`

Mamajek, E., & Stapelfeldt, K. 2023, in American Astronomical Society Meeting Abstracts, Vol. 55, American Astronomical Society Meeting Abstracts, 116.07

Mansfield, M., Bean, J. L., Line, M. R., et al. 2018, The Astronomical Journal, 156, 10

Marais, D. D., & Walter, M. 1999, Annual review of ecology and systematics, 30, 397

Marconi, A., Di Marcantonio, P., D'Odorico, V., et al. 2016, Ground-based and Airborne Instrumentation for Astronomy VI, 9908, 990823, doi: `10.1117/12.2231653`

Marconi, A., Abreu, M., Adibekyan, V., et al. 2022, in Ground-based and Airborne Instrumentation for Astronomy IX, Vol. 12184 (SPIE), 720–735

Marley, M. S., Gelino, C., Stephens, D., Lunine, J. I., & Freedman, R. 1999, ApJ, 513, 879, doi: `10.1086/306881`

Marois, C., Macintosh, B., Barman, T., et al. 2008, science, 322, 1348

Martin, E. C., Fitzgerald, M. P., McLean, I. S., et al. 2018, in Society of Photo-Optical Instrumentation Engineers (SPIE) Conference Series, Vol. 10702, Ground-based and Airborne Instrumentation for Astronomy VII, ed. C. J. Evans, L. Simard, & H. Takami, 107020A, doi: `10.1117/12.2312266`

Martínez, R. R., Stevens, D. J., Gaudi, B. S., et al. 2021, The Astrophysical Journal, 911, 84

Mascareño, A. S., González-Álvarez, E., Osorio, M. Z., et al. 2023, Astronomy & Astrophysics, 670, A5

Matsuo, T., & Tamura, M. 2010, in Society of Photo-Optical Instrumentation Engineers (SPIE) Conference Series, Vol. 7735, Ground-based and Airborne Instrumentation for Astronomy III, ed. I. S. McLean, S. K. Ramsay, & H. Takami, 773584, doi: `10.1117/12.858323`

Matsuo, T., Kotani, T., Murakami, N., et al. 2012, in Society of Photo-Optical Instrumentation Engineers (SPIE) Conference Series, Vol. 8446, Ground-based and Airborne Instrumentation for Astronomy IV, ed. I. S. McLean, S. K. Ramsay, & H. Takami, 84461K, doi: `10.1117/12.926039`

Mawet, D., Serabyn, E., Liewer, K., et al. 2010, ApJ, 709, 53, doi: `10.1088/0004-637X/709/1/53`

Mawet, D., Milli, J., Wahhaj, Z., et al. 2014, ApJ, 792, 97, doi: `10.1088/0004-637X/792/2/97`

Mawet, D., Fitzgerald, M., Konopacky, Q., et al. 2019, in Bulletin of the American Astronomical Society, Vol. 51, 134. `https://arxiv.org/abs/1908.03623`

Mayor, M., & Queloz, D. 1995, Nature, 378, 355, doi: `10.1038/378355a0`

McCarthy, D. W., Burge, J. H., Angel, J. R. P., et al. 1998, in Society of Photo-Optical Instrumentation Engineers (SPIE) Conference Series, Vol. 3354, Infrared Astronomical Instrumentation, ed. A. M. Fowler, 750–754, doi: `10.1117/12.317340`

Meadows, V., Graham, H., Abrahamsson, V., et al. 2022, arXiv preprint arXiv:2210.14293

Meadows, V. S. 2017, Astrobiology, 17, 1022

Meadows, V. S., & Barnes, R. K. 2018, Handbook of exoplanets, 57

Meadows, V. S., & Crisp, D. 1996, J. Geophys. Res., 101, 4595

Meadows, V. S., Lincowski, A. P., & Lustig-Yaeger, J. 2023, PSJ, 4, 192, doi: `10.3847/PSJ/acf488`

Meadows, V. S., Arney, G. N., Schwieterman, E. W., et al. 2018, Astrobiology, 18, 133

Meadows, V. S., Reinhard, C. T., Arney, G. N., et al. 2018, Astrobiology, 18, 630, doi: `10.1089/ast.2017.1727`

Mobbs, C. V. 2016, Diabetes, 65, 2473, doi: `10.2337/dbi16-0027`

Morley, C. V., Kreidberg, L., Rustamkulov, Z., Robinson, T., & Fortney, J. J. 2017, ApJ, 850, 121

Mueller, M., Szentgyorgyi, A., McMuldroch, S., et al. 2022, in Ground-based and Airborne Instrumentation for Astronomy IX, Vol. 12184, SPIE, 1115–1133

National Academies of Sciences, Engineering, and Medicine. 2021, Pathways to Discovery in Astronomy and Astrophysics for the 2020s (Washington, DC: The National Academies Press), doi: `10.17226/26141`

Nayak, M., Lupu, R., Marley, M. S., et al. 2017, PASP, 129, 034401, doi: `10.1088/1538-3873/129/973/034401`

Nelson, J., & Sanders, G. H. 2008, in Ground-based and Airborne Telescopes II, Vol. 7012, SPIE, 504–521

Noll, S., Kausch, W., Barden, M., et al. 2012, Astron. Astrophys. Suppl. Ser., 543, A92

Nugroho, S. K., Gibson, N. P., de Mooij, E. J. W., et al. 2020, The Astrophysical Journal, 898, L31, doi: `10.3847/2041-8213/aba4b6`

Nugroho, S. K., Kawahara, H., Masuda, K., et al. 2017, The Astronomical Journal, 154, 221, doi: `10.3847/1538-3881/aa9433`

Oliva, E., Origlia, L., Baffa, C., et al. 2006, in Society of Photo-Optical Instrumentation Engineers (SPIE) Conference Series, Vol. 6269, Ground-based and Airborne Instrumentation for Astronomy, ed. I. S. McLean & M. Iye, 626919, doi: `10.1117/12.670006`

Orell-Miquel, J., Murgas, F., Palle Bago, E., Esparza-Borges, E., & Stangret, M. 2022, in Bulletin of the American Astronomical Society, Vol. 54, 102.83

Palle, E., Biazzo, K., Bolmont, E., et al. 2023, arXiv preprint arXiv:2311.17075

Park, C., Jaffe, D. T., Yuk, I.-S., et al. 2014, in Society of Photo-Optical Instrumentation Engineers (SPIE) Conference Series, Vol. 9147, Ground-based and Airborne Instrumentation for Astronomy V, ed. S. K. Ramsay, I. S. McLean, & H. Takami, 91471D, doi: `10.1117/12.2056431`

Peacock, S., Barman, T., Shkolnik, E. L., Hauschildt, P. H., & Baron, E. 2019a, ApJ, 871, 235

Peacock, S., Barman, T., Shkolnik, E. L., et al. 2019b, ApJ, 886, 77

—. 2020, ApJ, 895, 5

Pepe, F., Cristiani, S., Rebolo, R., et al. 2021, A&A, 645, A96, doi: `10.1051/0004-6361/202038306`

Perryman, M. 2011, The Exoplanet Handbook. Cambridge Univ, Press

Perryman, M. A., Lindegren, L., Kovalevsky, J., et al. 1997, Astronomy and Astrophysics, Vol. 323, p. L49-L52, 323, L49

Pidhorodetska, D., Fauchez, T. J., Villanueva, G. L., Domagal-Goldman, S. D., & Kopparapu, R. K. 2020, ApJL, 898, L33

Pino, L., Ehrenreich, D., Wyttenbach, A., et al. 2018, Astron. Astrophys. Suppl. Ser., 612, A53

Pino, L., Ehrenreich, D., Allart, R., et al. 2018, A&A, 619, A3, doi: `10.1051/0004-6361/201832986`

Piskorz, D., Benneke, B., Crockett, N. R., et al. 2016, ApJ, 832, 131, doi: `10.3847/0004-637X/832/2/131`

—. 2017, AJ, 154, 78, doi: `10.3847/1538-3881/aa7dd8`

Planavsky, N. J., Cole, D. B., Isson, T. T., et al. 2018, Emerging Topics in Life Sciences, 2, 149

Planavsky, N. J., Reinhard, C. T., Wang, X., et al. 2014, science, 346, 635

Pohorille, A., & Pratt, L. R. 2012, Origins of Life and Evolution of Biospheres, 42, 405

Pont, F., Knutson, H., Gilliland, R. L., Moutou, C., & Charbonneau, D. 2008, Mon. Not. R. Astron. Soc., 385, 109

Pont, F., Gilliland, R. L., Moutou, C., et al. 2007, Astron. Astrophys. Suppl. Ser., 476, 1347

Potier, A., Ruane, G., Stark, C., et al. 2022a, Journal of Astronomical Telescopes, Instruments, and Systems, 8, 035002, doi: `10.1117/1.JATIS.8.3.035002`

Potier, A., Ruane, G., Tajdaran, K., et al. 2022b, in Society of Photo-Optical Instrumentation Engineers (SPIE) Conference Series, Vol. 12180, Space Telescopes and Instrumentation 2022: Optical, Infrared, and Millimeter Wave, ed. L. E. Coyle, S. Matsuura, & M. D. Perrin, 121805D, doi: `10.1117/12.2629902`

Quanz, S. P., Ottiger, M., Fontanet, E., et al. 2022, Astronomy & Astrophysics, 664, A21

Quirrenbach, A., Amado, P. J., Caballero, J. A., et al. 2016, in Society of Photo-Optical Instrumentation Engineers (SPIE) Conference Series, Vol. 9908, Ground-based and Airborne Instrumentation for Astronomy VI, ed. C. J. Evans, L. Simard, & H. Takami, 990812, doi: `10.1117/12.2231880`

Rackham, B., Espinoza, N., Apai, D., et al. 2017, ApJ, 834, 151

Rackham, B. V., Apai, D., & Giampapa, M. S. 2018, ApJ, 853, 122

Ramsay, S., Amico, P., Bezawada, N., et al. 2020, in Advances in optical astronomical instrumentation 2019, Vol. 11203, SPIE, 1120303

Ranjan, S., Schwieterman, E. W., Leung, M., Harman, C. E., & Hu, R. 2023, The Astrophysical Journal Letters, 958, L15

Rasmussen, K. C., Currie, M. H., Hagee, C., et al. 2023, AJ, 166, 155, doi: `10.3847/1538-3881/acf28e`

Rayner, J., Tokunaga, A., Jaffe, D., et al. 2022, Publications of the Astronomical Society of the Pacific, 134, 015002

Reach, W. T., Franz, B. A., Weiland, J. L., et al. 1995, Nature, 374, 521, doi: `10.1038/374521a0`

Reidemeister, M., Krivov, A. V., Stark, C. C., et al. 2011, A&A, 527, A57, doi: `10.1051/0004-6361/201015328`

Reinhard, C. T., Olson, S. L., Schwieterman, E. W., & Lyons, T. W. 2017, Astrobiology, 17, 287

Richardson, L. J., Deming, D., & Seager, S. 2003, ApJ, 597, 581, doi: `10.1086/378390`

Ridden-Harper, A. R., Snellen, I. A. G., Keller, C. U., et al. 2016, A&A, 593, A129, doi: `10.1051/0004-6361/201628448`

Roberge, A., Chen, C. H., Millan-Gabet, R., et al. 2012, PASP, 124, 799

Robinson, T. D., & Catling, D. C. 2012, ApJ, 757, 104

Robinson, T. D., & Crisp, D. 2018, J. Quant. Spectrosc. Radiat. Transf., 211, 78

Robinson, T. D., Ennico, K., Meadows, V. S., et al. 2014, ApJ, 787, 171, doi: `10.1088/0004-637X/787/2/171`

Robinson, T. D., Stapelfeldt, K. R., & Marley, M. S. 2016, Publ. Astro. Soc. Pac., 128, 1

Robinson, T. D., Meadows, V. S., Crisp, D., et al. 2011, Astrobiology, 11, 393

Roche, S., Strong, K., Wunch, D., et al. 2021, Atmospheric Measurement Techniques, 14, 3087

Rodgers, C. D. 2000, Inverse methods for atmospheric sounding: theory and practice, Vol. 2 (World scientific)

Rodler, F., Kürster, M., & Barnes, J. R. 2013, MNRAS, 432, 1980, doi: `10.1093/mnras/stt462`

Rodler, F., & López-Morales, M. 2014, Astrophysical Journal, 781, doi: `10.1088/0004-637X/781/1/54`

Rodler, F., Lopez-Morales, M., & Ribas, I. 2012, ApJL, 753, L25, doi: `10.1088/2041-8205/753/1/L25`

Rogers, L. A. 2015, The Astrophysical Journal, 801, 41

Rugheimer, S., Kaltenegger, L., Segura, A., Linsky, J., & Mohanty, S. 2015, The Astrophysical Journal, 809, 57

Rugheimer, S., Kaltenegger, L., Zsom, A., Segura, A., & Sasselov, D. 2013, Astrobiology, 13, 251, doi: `10.1089/ast.2012.0888`

Rustamkulov, Z., Sing, D., Mukherjee, S., et al. 2023, Nature, 614, 659

Sagan, C., Thompson, W. R., Carlson, R., Gurnett, D., & Hord, C. 1993, Nature, 365, 715, doi: `10.1038/365715a0`

SANNA, N., OLIVA, E., & ORIGLIA, L. 2021, The Exposure Time Calculator for HIRES@ELT, Tech. rep., OA Arcetri

Saran, D. V., Slanger, T. G., Feng, W., & Plane, J. M. C. 2011, Journal of Geophysical Research (Atmospheres), 116, D12303, doi: `10.1029/2011JD015662`

Savransky, D., & Garrett, D. 2016, Journal of Astronomical Telescopes, Instruments, and Systems, 2, 011006, doi: `10.1117/1.JATIS.2.1.011006`

Schaefer, L., Wordsworth, R. D., Berta-Thompson, Z., & Sasselov, D. 2016, The Astrophysical Journal, 829, 63

Schwarz, H., Brogi, M., De Kok, R., Birkby, J., & Snellen, I. 2015, Astronomy and Astrophysics, 576, doi: `10.1051/0004-6361/201425170`

Schwieterman, E. W., Cockell, C. S., & Meadows, V. S. 2015, Astrobiology, 15, 341, doi: `10.1089/ast.2014.1178`

Schwieterman, E. W., Meadows, V. S., Domagal-Goldman, S. D., et al. 2016, Astrophys. J. Lett., 819

Schwieterman, E. W., Kiang, N. Y., Parenteau, M. N., et al. 2018, Astrobiology, 18, 663, doi: `10.1089/ast.2017.1729`

Seager, S. 2008, Space Science Reviews, 135, 345

Seager, S., & Deming, D. 2010, Annual Review of Astronomy and Astrophysics, 48, 631

Seager, S., & Mallen-Ornelas, G. 2003, The Astrophysical Journal, 585, 1038

Seager, S., & Sasselov, D. D. 2000, ApJ, 537, 916, doi: `10.1086/309088`

Seager, S., Schrenk, M., & Bains, W. 2012, Astrobiology, 12, 61, doi: `10.1089/ast.2010.0489`

Segura, A., Kasting, J. F., Meadows, V., et al. 2005, Astrobiology, 5, 706

Segura, A., Walkowicz, L. M., Meadows, V., Kasting, J., & Hawley, S. 2010, Astrobiology, 10, 751

Seidel, J., Borsa, F., Pino, L., et al. 2023, Astronomy & Astrophysics, 673, A125

Serindag, D. B., & Snellen, I. A. G. 2019, The Astrophysical Journal, 871, L7, doi: `10.3847/2041-8213/aafa1f`

Shields, A. L., Ballard, S., & Johnson, J. A. 2016, Physics Reports, 663, 1

Showman, A. P., Cho, J. Y., & Menou, K. 2010, Exoplanets, 526, 471

Showman, A. P., Cooper, C. S., Fortney, J. J., & Marley, M. S. 2008, ApJ, 682, 559, doi: `10.1086/589325`

Showman, A. P., Tan, X., & Parmentier, V. 2020, SSRv, 216, 139, doi: `10.1007/s11214-020-00758-8`

Silva-Valio, A., & Lanza, A. F. 2011, Astron. Astrophys. Suppl. Ser., 529, A36

Sing, D. K., Fortney, J. J., Nikolov, N., et al. 2016, Nature, 529, 59, doi: `10.1038/nature16068`

Skilling, J. 2004, in American Institute of Physics Conference Series, Vol. 735, Bayesian Inference and Maximum Entropy Methods in Science and Engineering: 24th International Workshop on Bayesian Inference and Maximum Entropy Methods in Science and Engineering, ed. R. Fischer, R. Preuss, & U. V. Toussaint, 395–405, doi: `10.1063/1.1835238`

Slipher, V. M. 1908, ApJ, 28, 397, doi: `10.1086/141609`

Smette, A., Sana, H., Noll, S., et al. 2015, Astron. Astrophys. Suppl. Ser., 576, A77

Snellen, I., de Kok, R., Birkby, J. L., et al. 2015, Astron. Astrophys. Suppl. Ser., 576, A59

Snellen, I. A., De Kok, R. J., De Mooij, E. J., & Albrecht, S. 2010, Nature, 465, 1049, doi: `10.1038/nature09111`

Snellen, I. A., De Kok, R. J., Le Poole, R., Brogi, M., & Birkby, J. 2013, Astrophysical Journal, 764, doi: `10.1088/0004-637X/764/2/182`

Snellen, I. A. G., Désert, J.-M., Waters, L. B. F. M., et al. 2017, The Astronomical Journal, 154, 77, doi: `10.3847/1538-3881/aa7fbc`

Solé, R. V., & Munteanu, A. 2004, EPL (Europhysics Letters), 68, 170, doi: `10.1209/epl/i2004-10241-3`

Soummer, R. 2005, ApJL, 618, L161, doi: `10.1086/427923`

Spake, J. J., Oklopčić, A., Hillenbrand, L. A., et al. 2022, ApJL, 939, L11, doi: `10.3847/2041-8213/ac88c9`

Speagle, J. S. 2020, MNRAS, 493, 3132, doi: `10.1093/mnras/staa278`

Spring, E. F., Birkby, J. L., Pino, L., et al. 2022, A&A, 659, A121, doi: `10.1051/0004-6361/202142314`

St. Laurent, K., Fogarty, K., Zimmerman, N. T., et al. 2018, in Society of Photo-Optical Instrumentation Engineers (SPIE) Conference Series, Vol. 10698, Space Telescopes and Instrumentation 2018: Optical, Infrared, and Millimeter Wave, ed. M. Lystrup, H. A. MacEwen, G. G. Fazio, N. Batalha, N. Siegler, & E. C. Tong, 106982W, doi: `10.1117/12.2313902`

Stamnes, K., Tsay, S. C., Jayaweera, K., & Wiscombe, W. 1988, ApOpt, 27, 2502, doi: `10.1364/AO.27.002502`

Stark, C. C. 2011, AJS, 142, 123

Stark, C. C. 2022, AJ, 163, 105, doi: `10.3847/1538-3881/ac45f5`

Stark, C. C., Dressing, C., Dulz, S., et al. 2020, The Astronomical Journal, 159, 286, doi: `10.3847/1538-3881/ab8f26`

Stark, C. C., & Kuchner, M. J. 2008, ApJ, 686, 637

Stark, C. C., & Kuchner, M. J. 2009, ApJ, 707, 543, doi: `10.1088/0004-637X/707/1/543`

Stark, C. C., Roberge, A., Mandell, A., & Robinson, T. D. 2014, ApJ, 795, 122

Stenborg, G., Gallagher, B., Howard, R. A., Hess, P., & Raouafi, N. E. 2021, ApJ, 910, 157, doi: `10.3847/1538-4357/abe623`

Stevenson, K. B., Line, M. R., Bean, J. L., et al. 2017, The Astronomical Journal, 153, 68

Szentgyorgyi, A., Barnes, S., Bean, J., et al. 2014, Ground-based and Airborne Instrumentation for Astronomy V, 9147, 914726

Szentgyorgyi, A., McMuldroch, S., Ben-Ami, S., et al. 2022, in Ground-based and Airborne Instrumentation for Astronomy IX, Vol. 12184, SPIE, 121841N

Tanner, A., White, R., Bailey, J., et al. 2012, ApJS, 203, 10

Thatte, N. A., Clarke, F., Bryson, I., et al. 2016, in Ground-based and Airborne Instrumentation for Astronomy VI, Vol. 9908, SPIE, 595–605

The LUVOIR Team. 2019, arXiv e-prints, arXiv:1912.06219, doi: `10.48550/arXiv.1912.06219`

Thibault, S., Rabou, P., Donati, J.-F., et al. 2012, in Society of Photo-Optical Instrumentation Engineers (SPIE) Conference Series, Vol. 8446, Ground-based and Airborne Instrumentation for Astronomy IV, ed. I. S. McLean, S. K. Ramsay, & H. Takami, 844630, doi: `10.1117/12.926697`

Thompson, M. A., Krissansen-Totton, J., Wogan, N., Telus, M., & Fortney, J. J. 2022, Proceedings of the National Academy of Sciences, 119, e2117933119

Tian, F. 2015, Earth Planet. Sci. Lett., 432, 126

Tian, F., France, K., Linsky, J. L., Mauas, P. J. D., & Vieytes, M. C. 2014, Earth Planet. Sci. Lett., 385, 22

Tilley, M. A., Segura, A., Meadows, V., Hawley, S., & Davenport, J. 2019, Astrobiology, 19, 64

Torres, G. 2007, ApJ, 671, L65

Traub, W. A., & Oppenheimer, B. R. 2010, Direct imaging of exoplanets (University of Arizona Press Tucson)

Tremblay, L., Line, M. R., Stevenson, K., et al. 2020, AJ, 159, 117, doi: `10.3847/1538-3881/ab64dd`

Tsiaras, A., Rocchetto, M., Waldmann, I. P., et al. 2016, ApJ, 820, 99, doi: `10.3847/0004-637X/820/2/99`

Ueno, Y., Yamada, K., Yoshida, N., Maruyama, S., & Isozaki, Y. 2006, Nature, 440, 516

Vallenari, A., Brown, A. G. A., Prusti, T., et al. 2023, Astron. Astrophys. Suppl. Ser., 674, A1

Vaughan, S. R., Birkby, J. L., Thatte, N., et al. 2024, Monthly Notices of the Royal Astronomical Society, 528, 3509

Vickers, P., Cowie, C., Dick, S. J., et al. 2023, Astrobiology, 23, 1202

von Braun, K., Boyajian, T. S., van Belle, G. T., et al. 2014, Mon. Not. R. Astron. Soc., 438, 2413

Wakeford, H. R., Lewis, N. K., Fowler, J., et al. 2018, AJS, 157, 11

Walker, J. C. G., Hays, P. B., & Kasting, J. F. 1981, J. Geophys. Res., 86, 9776

Walker, S. I., Bains, W., Cronin, L., et al. 2018, Astrobiology, 18, 779, doi: `10.1089/ast.2017.1738`

Wang, J., Mawet, D., Ruane, G., Hu, R., & Benneke, B. 2017, Astron. J., 153, 183

Weinberger, A. J., Becklin, E. E., Song, I., & Zuckerman, B. 2011, ApJ, 726, 72, doi: `10.1088/0004-637X/726/2/72`

Wilner, D. J., Holman, M. J., Kuchner, M. J., & Ho, P. T. P. 2002, ApJL, 569, L115, doi: `10.1086/340691`

Woese, C. R., & Fox, G. E. 1977, Proceedings of the National Academy of Sciences, 74, 5088

Wogan, N., Krissansen-Totton, J., & Catling, D. C. 2020, The Planetary Science Journal, 1, 58

Wong, M. L., Bartlett, S., Chen, S., & Tierney, L. 2022, Life, 12, 783

Wong, M. L., Prabhu, A., Williams, J., Morrison, S. M., & Hazen, R. M. 2023, Journal of Geophysical Research: Planets, 128, e2022JE007658

Wordsworth, R., & Pierrehumbert, R. 2014, ApJL, 785, L20

Wuebbles, D. J., & Hayhoe, K. 2002, Earth-Science Reviews, 57, 177

Wunderlich, F., Godolt, M., Grenfell, J. L., et al. 2019, A&A, 624, A49, doi: `10.1051/0004-6361/201834504`

Wunderlich, F., Scheucher, M., Godolt, M., et al. 2020, ApJ, 901, 126

Young, A. V., Crouse, J., Arney, G., et al. 2024, The Planetary Science Journal, 5, 7

Zahnle, K., Claire, M., & Catling, D. 2006, Geobiology, 4, 271

Zechmeister, M., Dreizler, S., Ribas, I., et al. 2019, Astron. Astrophys. Suppl. Ser., 627, A49

Zhang, H., Wang, J., & Plummer, M. K. 2023, The Astronomical Journal, 167, 37

Zhang, M., Knutson, H. A., Wang, L., et al. 2021, AJ, 161, 181, doi: `10.3847/1538-3881/abe382`

Zhang, X. 2020, Research in Astronomy and Astrophysics, 20, 099, doi: `10.1088/1674-4527/20/7/99`

Zieba, S., Kreidberg, L., Ducrot, E., et al. 2023, Nature, 620, 746, doi: `10.1038/s41586-023-06232-z`

# Appendix A

# LIST OF PUBLICATIONS

## *A.1 First-authored*

**Currie, M. H.**, V. S. Meadows, and J. Lustig-Yaeger. (2024, in prep). There's more to $O_2$ than life: Biosignature assessment via $O_2$ retrieval in simulated ELT spectroscopy. In prep.

> In this work, we simulated our ability to retrieve the abundance of $O_2$ for simulated reflected light observations of Proxima Centauri b. We found that we may be able to constrain the $O_2$ abundance for atmospheres with $\leq 21\%$ $O_2$, which may increase the likelihood that these atmospheres are habitable, and potentially provide evidence for the origin of $O_2$. Furthermore, we find it challenging to retrieve the $O_2$ abundance for a thick 10 bar post ocean loss atmosphere, and we may need to rely on other methods to discriminate this false positive atmosphere.

**Currie, M. H.** and V. S. Meadows. (2024, submitted). There's more to life in reflected light: Simulating the detectability of a range of molecules for high-contrast, high-resolution observations of non-transiting terrestrial exoplanets. Submitted to The Planetary Science Journal.

> In this work, we upgraded our ELT detectability pipeline to include the capability to simulate observations of non-transiting exoplanets. We found that the ELTs will likely be sensitive to $O_2$, $CH_4$, $CO_2$, $H_2O$, and CO for non-transiting planet atmospheres less than 5 pc away. We may be able to search for two biosignature pairs, and discriminate biosignature false positive scenarios, with ~ 10 hours of observing for the nearby target Proxima Centauri b. Addionally, we will be able to confirm or rule out a sub-Neptune atmosphere in a single hour of observing.

**Currie, M. H.**, Stark, C. C., Kammerer, J., Juanola-Parramon, R., & Meadows, V. S.

(2023). Mitigating Worst-case Exozodiacal Dust Structure in High-contrast Images of Earth-like Exoplanets. In The Astronomical Journal (Vol. 166, Issue 5, p. 197). American Astronomical Society. https://doi.org/10.3847/1538-3881/acfda7

In this work, we addressed exozodiacal dust contamination in Habitable Worlds Observatory images problem by simulating systems with significant exozodi structure, and developed a high-pass filter and PSF matching technique to minimize the exozodi contamination. This method successfully removed exozodi with structure for systems with moderate inclinations with little effect on planetary detectability. For systems with 3x the dust of the Solar System, which is the median of the habitable zones of nearby Sun-like stars, this method shows promising results for mitigating exozodiacal dust in future HWO observations.

Rasmussen, K. C. & **Currie, M. H.** (co-first author), Hagee, C., van Buchem, C., Malik, M., Savel, A. B., Brogi, M., Rauscher, E., Meadows, V., Mansfield, M., Kempton, E. M.-R., Desert, J.-M., Wardenier, J. P., Pino, L., Line, M., Parmentier, V., Seifahrt, A., Kasper, D., Brady, M., & Bean, J. L. (2023). A Nondetection of Iron in the First High-resolution Emission Study of the Lava Planet 55 Cnc e. In The Astronomical Journal (Vol. 166, Issue 4, p. 155). American Astronomical Society. https://doi.org/10.3847/1538-3881/acf28e

In this work, we applied high-resolution cross-correlation analysis methods to real observations of an extreme example of a terrestrial planet: 55 Cancri e. This planet, while not habitable, presents an interesting and accessible target that has been the subject of many characterization investigations. Its close proximity to its host star implies a global magma ocean; however, the existence and/or composition of its atmosphere is still up for debate. We took the first ever high-resolution emission spectra of 55 Cnc e with Gemini-N/MAROON-X to investigate the presence of an atmosphere. After applying a cross-correlation analysis, we were unable to detect the presence of an atmosphere, which is consistent with current crustal evaporation models for this planet. We estimate that if a mineral atmosphere is indeed present, the atmospheric pressure must have an upper limit of 100 mbar.

**Currie, M. H.**, Meadows, V. S., & Rasmussen, K. C. (2023). There's More to Life than $O_2$: Simulating the Detectability of a Range of Molecules for Ground-based, High-resolution Spectroscopy of Transiting Terrestrial Exoplanets. In The Planetary Science Journal (Vol. 4, Issue 5, p. 83). American Astronomical Society. https://doi.org/10.3847/psj/accf86

In this work, we explored the detectability of $CH_4$, $CO_2$, $H_2O$, CO, and $O_3$ in transiting terrestrial atmospheres using the ELTs. We developed a novel noise model for ELT observations, encompassing a cross-correlation analysis for high-resolution observations. We found that $CH_4$ and $CO_2$ are likely up to 3x more detectable than $O_2$ in these environments for transiting exoplanets (Figure 1), and detecting these two molecules would provide the fastest pathway to a biosignature pair detection in the TRAPPIST-1 system with the ELTs. This study showed that the ELTs will be powerful enough to search for more than just $O_2$, and may be essential to near-term terrestrial exoplanet characterization.

## *A.2 Co-authored*

Deming, D., **M. H. Currie**, V. S. Meadows, S. Peacock. (2024, in prep.). Bias-free Transit Spectroscopy of Terrestrial Exoplanets Using the ELTs. In prep.

In this work, we investigate the effect of star spots on our ability to detect molecular features for high-resolution observations. Left uncorrected, star spots will significantly degrade the detections of molecules not present in the spots (e.g., $CH_4$), and will produce spurious cross-correlation peaks for molecules (e.g.,$H_2O$) that are present in the star spot spectra.

Wong, M.L., V. S. Meadows, P. Gao, H Delgado Diaz, **M. H. Currie**, C. J. Bierson, X. Zhang. (2024, in prep.). Abiotic oxygen in the atmospheres of Venus-like exoplanets. In prep.

In this work, we study the ability of Venus-like exoplanets to build up $O_2$ in their atmospheres via $CO_2$ photolysis. We find that around late-type M dwarfs, such as TRAPPIST-1, it is possible to produce $O_2$ abundances of a few ppm and $O_3$ abundances of $\sim 10^{-10}$ $O_3$ above the main cloud/haze layer. This $O_2$ buildup is likely not detectable with the ELTs.

Rasmussen, K. C., Brogi, M., Rahman, F., Beltz, H., **Currie, M.**, Rauscher, E., & Ji, A. P. (2022). SPORK That Spectrum: Increasing Detection Significances from High-resolution Exoplanet Spectroscopy with Novel Smoothing Algorithms. In The Astronomical Journal (Vol. 164, Issue 2, p. 35). American Astronomical Society. https://doi.org/10.3847/1538-3881/ac6bfa

In this work, we demonstrate a novel smoothing algorithm for pre-processing observed high-resolution spectra. We find that this method improves the detection significance for HD 209458 b and HD 179949 b observations by up to 1.5x and 2x, respectively.

# Appendix B

# CURRICULUM VITAE

# Miles H. Currie

---

Email: mcurr@uw.edu
Website: milescurrie.com
Github: curriem
ORCID: 0000-0003-3429-4142

**Office Address**

Department of Astronomy, University of Washington
Box 351580
Seattle, WA 98195-1700

**Education**

PhD in Astronomy and Astrobiology (dual-title) 2018–2024
MS in Astronomy (2020)
University of Washington, Seattle, WA
*Thesis:* Searching for Signs of Habitability and Life in the Era of Extremely Large Observatories
*Advisor:* Prof. Victoria S. Meadows

BS in Physics & Astrophysics, *magna cum laude* 2013–2017
Florida State University, Tallahassee, FL

**Research Experience**

*Graduate Research Assistant:* Virtual Planetary Laboratory
**2018–present**
Terrestrial exoplanet atmospheres, ground-based high-res spectroscopy, space-based exoplanet characterization, astrobiology

*Post-baccalaureate Research Assistant:* Space Telescope Science Institute
**2017–2018**
Type 1a supernova cosmology, WFIRST science precursor study (advisors David Rubin, Susana Deustua, Andy Fruchter)

*Post-baccalaureate Research Assistant:* Geophysical Fluid Dynamics Institute
**2017**
Forest fire simulations (advisors Kevin Speer and Bryan Quaife)

*Undergraduate Research Assistant:* Florida State University, SETI Institute
**2013–2017**
Type 1a supernova cosmology (advisor David Rubin), Kepler/K2 exoplanet detection (advisors Susan Mullally and Fergal Mullally), particle physics collision simulations (advisor Todd Adams)

**Honors and Awards**

- NASA Postdoctoral Program Fellowship awarded Spring 2024, postdoc to begin September 2024
- The UW Astronomy Department Graduate Student Awards Research Prize, 2023

## Teaching Experience

*Research Mentor:* Department of Astronomy, University of Washington
**2020–2022**
Advised undergraduate students in exoplanet astronomy and astrobiology research

*Teaching Assistant:* Department of Astronomy, University of Washington
**2018–2020**
General Astronomy (ASTR 101) and The Solar System (ASTR 150)

## Observing Experience

*Co-I:* McDonald Observatory Observing Time Request McD22-c, "An Ancient Box of Chocolates: Follow-up of High-Priority Metal-Poor Stars Identified from S-PLUS Photometry" (50 hrs)

## Publications

*First-authored*

8. **Currie, M.H.**, V.S. Meadows, and J. Lustig-Yaeger. "There's more to $O_2$ than life: Biosignature assessment via $O_2$ retrieval in simulated ELT spectroscopy" 2024. In prep.
7. **Currie, M.H.** and V.S. Meadows. "There's more to life in reflected light: Simulating the detectability of a range of molecules for high-contrast, high-resolution observations of non-transiting terrestrial exoplanets" 2024. Submitted to PSJ.
6. **Currie, M.H.**, C.C. Stark, J. Kammerer, R. Juanola-Parramon, V.S. Meadows. "Mitigating Worst-Case Exozodiacal Dust Structure in Direct Images of Earth-like Exoplanets." 2023. The Astronomical Journal. 166 197.
5. Rasmussen, K.C. & **Currie, M.H.** (co-first author), C. Hagee, C. van Buchem, M. Malik et al. "A Non-Detection of Iron in the First High-Resolution Emission Study of the Lava Planet 55 Cnc e." 2023. The Astronomical Journal 166 155
4. **Currie, M.H.**, V.S. Meadows, and K.C. Rasmussen. "There's more to life than $O_2$: Simulating the detectability of a range of molecules for ground-based high-resolution spectroscopy of transiting terrestrial exoplanets." 2023. The Planetary Science Journal 4 83
3. **Currie, M.H.**, D. Rubin, G. Aldering, S. Deustua, A. Fruchter, S. Perlmutter. "Evaluating the Calibration of SN Ia Anchor Datasets with a Bayesian Hierarchical Model." 2020.
2. **Currie, M.H.**, K. Speer, J. K. Hiers, J. J. O'Brien, S. Goodrick, and B. Quaife. 2019. "Pixel-Level Statistical Analyses of Prescribed Fire Spread." Canadian Journal of Forest Research. Journal Canadien de La Recherche Forestiere 49 (1): 18–26.
1. **Currie, M.H.** and D. Rubin. 2018. "Characterization of Unstable Pixels Using a Mixture Model: Application to HST WFC3 IR." Research Notes of the AAS 2 (3): 141.

*Co-authored*

4. Rasmussen, K.C., M. Brogi, F. Rahman, H. Beltz, **M. Currie**, E. Rauscher, and A.P. Ji. 2022. "SPORK That Spectrum: Increasing Detection Significances from High-Resolution Exoplanet Spectroscopy with Novel Smoothing Algorithms." Astronomical Journal, 164 35.
3. V.S. Meadows, H. Graham et al. including **M. Currie**. "Community Report from the Biosignatures Standards of Evidence Workshop" 2023.
2. Hayden, B., D. Rubin, K. Boone, G. Aldering, J. Nordin, M. Brodwin, S. Deustua, et al. including **M. Currie** 2021. "The HST See Change Program.

I. Survey Design, Pipeline, and Supernova Discoveries*." The Astrophysical Journal 912 (2): 87.

1. Rubin, D., G. Aldering, K. Barbary, K. Boone, G. Chappell, **M. Currie**, S. Deustua, et al. 2015. "UNITY: CONFRONTING SUPERNOVA COSMOLOGY'S STATISTICAL AND SYSTEMATIC UNCERTAINTIES IN A UNIFIED BAYESIAN FRAMEWORK." The Astrophysical Journal 813 (2): 137.

**Presentations**

*Invited Talks*

6. Currie, M. and V. Meadows. ELSI/Tokyo Tech inaugural exoplanet observation discussion group, Tokyo, Japan. April 2024. "The Prospects for Characterizing Terrestrial Exoplanets with the ELTs."
5. Currie, M. and V. Meadows. NAOJ/ABC–UW/VPL collaboration meeting, Mitaka, Japan. April 2024. "Characterizing Earth-like Exoplanets in the Era of Extremely Large Telescopes."
4. Currie, M., C. Stark, J. Kammerer, R. Juanola-Parramon, V. Meadows. NASA Goddard Exoplanet Seminar. October 2023. "Detecting and Characterizing Earth-like Exoplanets in the Era of Next-Generation Observatories"
3. Currie, M., C. Stark, J. Kammerer, R. Juanola-Parramon, V. Meadows. UMD Exoplanets Journal Club. October 2023. "Detecting and Characterizing Earth-like Exoplanets in the Era of Next-Generation Observatories"
2. Currie, M., V. Meadows. UW Astrobiology Colloquium. October 2023. "There's more to life than $O_2$"
1. Currie, M., C. Stark, J. Kammerer, R. Juanola-Parramon, V. Meadows. UW Astrobiology Seminar. May 2022. "Mitigating Worst-case Exozodiacal Structure in High-contrast Images of Earth-like Exoplanets."

*Contributed Talks*

5. Currie, M. and V. Meadows. "Placing O2 in its environmental context with the extremely large telescopes" Astrobiology Science Conference 2024, AGU
4. Currie, M., C. Stark, J. Kammerer, R. Juanola-Parramon, V. Meadows. ExoPAG SAG 23 Workshop, Baltimore. 2023. "Mitigating Worst-case Exozodiacal Structure in High-contrast Images of Earth-like Exoplanets."
3. Currie, M., V. Meadows, and K. Rasmussen. AAS Winter Meeting, Seattle. 2023. "There's more to life than O2: Assessing the detectability of biosignatures and environmental context for high-resolution spectroscopy of terrestrial exoplanets"
2. Currie, M., V. Meadows, and K. Rasmussen. High-resolution spectroscopy thinkshop. Potsdam, Germany. 2022. "There's more to life than O2: Assessing the detectability of biosignatures and environmental context for high-resolution spectroscopy of terrestrial exoplanets"
1. Currie, M., V. Meadows, and K. Rasmussen. 2022. "Simulating ELT capabilities for terrestrial exoplanet characterization and biosignature detection and assessment." 2022 Astrobiology Science Conference. AGU, 2022.

*Posters*

8. Currie, M.H. and V. Meadows "Searching for signs of habitability and life on M-dwarf planets with next-generation ELTs." Extreme Solar Systems V, Christchurch, NZ. 2024.

7. Currie, M.H., C.C. Stark, J. Kammerer, R. Juanola-Parramon, V.S. Meadows. "Mitigating Worst-Case Exozodiacal Dust Structure in Direct Images of Earth-like Exoplanets." Science with the Habitable Worlds Observatory and Beyond, Baltimore. 2023.
6. Currie, M., and V. Meadows. 2021. "There's More to Life than O2: Simulating the Detectability of a Range of Molecules for Ground-Based High-Resolution Spectroscopy of Transiting Terrestrial Exoplanets." Habitable Worlds 2021, id. 1237. Bulletin of the American Astronomical Society, Vol. 53, No. 3 e-id 2021n3i1237
5. Currie, M., V.S. Meadows, and J. Lustig-Yaeger. "Detecting False Positives with O2: A Feasibility Study." In 2019 Astrobiology Science Conference. AGU, 2019.
4. Currie, M., and D. Rubin. 2019. "Automated Recognition of Transients with a Convolutional Neural Network." American Astronomical Society, AAS Meeting #233, id.349.05
3. Currie, M., and D. Rubin. 2018. "Improving the Calibration of the SN Ia Anchor Datasets with a Bayesian Hierarchal Model." AAS Meeting #231, id. 153.20
2. Currie, M., F. Mullally, and S.E. Thompson. 2017. "Finding Planets in K2: A New Method of Cleaning the Data." AAS Meeting #229, id.146.13
1. Currie, M., D. Rubin, G. Scott Aldering, C. Baltay, P. Fagrelius, D.R. Law, S. Perlmutter, and K. Pontoppidan. 2016. "Estimating the Supernova Cosmological Constraints Possible With the Wide-Field Infrared Survey Telescope." AAS Meeting #227, id.139.17

**Service and Outreach**

*Service*

- Member of Advisory Committee, NASA Habitable Worlds Observatory START/TAG Exoplanet Science Yield sub-Working Group, 2024–present
- Member, NASA ExoPAG SAG 26: Exoplanet Reflectance Spectroscopy for the Habitable Worlds Observatory, 2024–present
- Member, NASA ExoPAG SAG 23: Theory of Exozodi Sources and Dust Evolution, 2022–present
- Co-chair for NExSS Science Communication Working Group, 2020–2024
- Executive secretary for NASA ROSES panel, 2023
- Organizer/graphic designer for Astronomy on Tap Seattle, 2019–2022
- Graphic designer for Astronomy at Home public lecture series (University of Washington), 2020-2022

*Public Talks*

- "Searching for Life in a Pixel: The Challenge of Exoplanet Astrobiology", June 27, 2022, Science On Tap, Third Place Books, Seattle, WA
- "All About Venus", 2020, Pacific Crest School, Virtual, Seattle, WA